UNIVERSITY OF SOUTHAMPTON

FACULTY OF ENGINEERING AND THE ENVIRONMENT
Engineering Sciences

Assessment of welding induced plastic strain using the thermoelastic stress analysis technique

by

Elise Camille Chevallier

Thesis for the degree of Doctor of Philosophy

June 2017

UNIVERSITY OF SOUTHAMPTON

ABSTRACT

FACULTY OF ENGINEERING AND THE ENVIRONMENT

Engineering Sciences

Thesis for the degree of Doctor of Philosophy

ASSESSMENT OF WELDING INDUCED PLASTIC STRAIN USING THE THERMOELASTIC STRESS ANALYSIS TECHNIQUE

by Elise Camille Chevallier

The work presented in the thesis is dedicated to the development and validation of a new technique to assess plastic strain based on thermoelastic stress analysis (TSA). Welding induced plasticity (WIP) and welding residual stresses can negatively affect the structural integrity of welded structures as they can exacerbate creep and stress corrosion cracking and limit the structure’s resistance to failure. Moreover, WIP has been shown to negatively affect weld integrity, since the associated accumulation of defects (dislocations) in the material will accelerate the nucleation of macro-scale defects that lead to component failure.

There has been considerable amount of work published on determining the magnitude and distribution of the residual stresses both experimentally and by using numerical techniques. WIP can be predicted using finite element analysis (FEA), however, there is currently no standardised experimental method to characterise plastic strain and hence, model predictions are not readily validated with confidence. Recently, two techniques, based on electron backscatter diffraction and indentation respectively, were developed to assess WIP. However, both techniques are destructive and would not be applicable on in-situ components.

TSA is a non-contact stress analysis method which is quick to apply and fully portable. TSA is based on the measurement of a small temperature change that occurs as a result of a change in the stress. The small temperature change is measured using an infrared detector. A method for plastic strain assessment (PSA) using TSA has been proposed based on the change in the thermoelastic response due to the plastic strain a material has experienced during a process, e.g. deformation or welding. TSA has the potential to be the first non-destructive, non-contact plastic strain assessment technique, termed as TSA-PSA.

The aim of the PhD is to investigate the potential of using the TSA-PSA approach for assessing WIP in austenitic (AISI 316L) and ferritic (SA508 Gr.3 Cl.1) steels. The influence of welding induced microstructural changes on the thermoelastic response is investigated to establish any changes in the thermoelastic response relating to plastic straining only. The study focuses on two typical nuclear grade steels; ferritic SA508 Gr.3 Cl.1 and austenitic stainless steel AISI 316L. The effect of plastic strain on the thermoelastic response of both steels is investigated through the design and assessment of a calibration specimen used to determine the thermoelastic constant variation with plastic strain alongside with microstructural changes. It was found that the plastic strain has a stronger influence on the thermoelastic constant in SA508 than in AISI 316L. For uniform microstructures the influence of plastic strain on the thermoelastic response can be defined and, a larger influence of plastic strain on thermoelastic response was reported for coarse grains of austenite in AISI 316L and coarse grains of ferrite in SA508.

The second part of the work concerns development finite element (FE) models of weld mock-ups to demonstrate application of TSA-PSA. The modelling enabled the plastic strain experienced during welding to be predicted and adjustments made to the design prior to the mock-up manufacture. Once satisfied that the mock-ups were suitable for TSA, they were manufactured at TWI Ltd. TSA experimental work was conducted on each mock-up and the outcome was compared with the outputs from the calibrated FE models. The capability of TSA to identify plastic strain in welded components is assessed through the use of the weld mock-ups. The thesis makes a novel contribution to the development of TSA as a portable non-destructive, non-contact technique to assess WIP in components with the investigation of the influence of microstructural changes similar to that found in welds on the technique, as well as the design, manufacture and plastic strain predictions in weldments dedicated to the technique. The results indicate a stronger influence of the plastic strain on the thermoelastic constant in coarse-grained microstructure in both grades of steel.

Table of Contents

List of Tables

List of Figures

DECLARATION OF AUTHORSHIP

I, *Elise Camille Chevallier*

declare that this thesis and the work presented in it are my own and has been generated by me as the result of my own original research.

Assessment of welding induced plastic strain using the thermoelastic stress analysis technique

I confirm that:

1. This work was done wholly or mainly while in candidature for a research degree at this University;
2. Where any part of this thesis has previously been submitted for a degree or any other qualification at this University or any other institution, this has been clearly stated;
3. Where I have consulted the published work of others, this is always clearly attributed;
4. Where I have quoted from the work of others, the source is always given. With the exception of such quotations, this thesis is entirely my own work;
5. I have acknowledged all main sources of help;
6. Where the thesis is based on work done by myself jointly with others, I have made clear exactly what was done by others and what I have contributed myself;
7. Parts of this work have been published as:

Chevallier E.C., Blackwell S. and Dulieu-Barton J.M. Finite Element Modelling of a Series of Austenitic Stainless Steel 316 L Weldments to Inform Thermoelastic Stress Analysis Residual Stress Assessment. In: Quinn S., Balandraud X. (eds) Residual Stress, Thermomechanics & Infrared Imaging, Hybrid Techniques and Inverse Problems, Volume 9. Conference Proceedings of the Society for Experimental Mechanics Series. Springer, Cham (2017)

Signed: ....

Date: ....

Acknowledgements

First, I need to thank all my supervisors. At the university of Southampton, Janice Barton and at TWI Ltd Marcus Warwick and Nick O’Meara. Thank you for your advice, support, and patience through the years. I must also thank my former supervisors in TWI Ltd, Maartje, Ruth and Sabrina in a chronological order.

I would like to thank members of the RESIST project, for all the feedback and constructive comments.

In TWI, many people have helped me gathering information and understanding, I would like to them all for their input and in particular Philippe, Simon, Dan, Emily, Museok, Tyler, Damaso, John and Emma.

In Southampton, many people helped me through this project, and to start with, my PhD companions in the RESIST project, Geoff, Vishnu, Rachael. I also want to thank Andy for his availability and help he provided me during all my experiments in the TSRL lab as well as Sarah and Cedric for the fruitful discussion we had.

I must thank my friends and family for their invaluable and necessary support.
To my parents, to Lucie, Minh, Odilon,
to my grandparents Kaki, Philippe, Maman Françoise, to Papa Pierre,
to Marvin, Marion and Myke, to a bright future together.

Definitions and Abbreviations

AC-35 µm	Air Cooled 316L specimens
AR-27 µm	As Received specimens of AISI 316L material
AR	As Received specimens of SA508 material
CGHAZ	Coarse Grain Heat Affected Zone
CHD	Centre Hole Drilling
CPU	Central Processing Unit
EBSD	Electron Backscatter Diffraction
EDM	Electrical Discharge Machining
FE	Finite Element
Fer	Furnace Cooled SA508 Gr.3 Cl.1 specimens
FGHAZ	Fine Grain Heat Affected Zone
HAZ	Heat Affected Zone
GF	Gauge Factor
ICHAC	Inter Critical Heat Affected Zone
Mar	Water Quenched SA508 Gr.3 Cl.1 specimens
Mix	Air Cooled SA508 Gr.3 Cl.1 specimens
MMA	Manual Metal Arc
MBN	Magnetic Barkhausen Noise
PEMAG	Plastic strain magnitude
SEM	Scanning Electron Microscope
TC	Thermocouple
TIG	Tungsten Inert Gas
TSA	Thermoelastic Stress Analysis
TSA PSA	Thermoelastic Stress Analyis Plastic Strain Assessment
UK	United Kingdom
VF-106 µm	Furnace Cooled 316L specimens
XRD	X-Ray Diffraction

Notation

A_1, A_2	calibration constants
a	a width
$\bar{B}$	a calibration constant
B	a temperature gradient interpolation matrix
b	a depth
C	a concentration coefficient
C_0	the Stefan-Boltzmann constant
c_r, c_f	lengths
C	a constitutive matrix
C_P	a specific heat at constant pressure
d	a distance
d_0	a reference distance
e	an emissivity
f_f, f_r	scalar coefficients
I	an intensity
i, j, k	scalars indicating orthogonal directions
K	the thermoelastic constant of a material
K_0	the thermoelastic constant measured in a material free of plastic strain
$K_{0\%}$	the extrapolated thermoelastic constant value for a plastic strain free material
K	Kelvin
K^{TOTAL}	a stress intensity factor
K^P	a tress intensity factor from applied stress
K^S	a tress intensity factor from residual stress
$\overline{k_i}$	constants relative to the direction *i*
M_{C_P}	heat capacity matrix
M_κ	conductivity matrix
M_S	a stiffness matrix
n	a positive integer
P	an electric power
P_{min}	a load
P_{yield}	the load required to reach yielding
P_{net}	a fraction of the electric power

$\{p\}$	a body force tensor
p_1, p_2, p_3	directions orthogonal to each other
Q	a heat input
Q_{int}	heat flux per unit area flowing into the body
Q_{ext}	heat flux supplied externally to the body per unit volume
$\{Q_V\}$	heat flux over the volume tensor
$\{Q_S\}$	element surface heat flux tensor
q	a heat flux
q_{con}, q_{rad}	heat transfer, through convection and radiation respectively
R	a radial distance
$\{R_b\}$	body forces tensor
$\{R_s\}$	element surface force tensor
$\{R_c\}$	concentrated nodel load tensor
r	a radius
S	a surface area
T	a temperature
T_0	an initial temperature
T_{atm}	the atmosphere temperature
Tr	a surface load
t	time
$t_{8/5}$	the time required for a component to cool down from 800 °C to 500 °C
U	a voltage
u	a displacement
V	a volume
v_L^0	longitudinal velocity
v_T^0	transverse velocity
v_{ij}	the velocity of a wave travelling in direction *i* polarised in direction *j*
w	a width
w_1	a width
w_2	a width
x, y, z	spatial coordinates
α	coefficient of linear thermal expansión
β_c	a heat transfer coefficient
ε	a strain
ε^e	an elastic strain

ε^{p}	a plastic strain
$\dot{\varepsilon}^{pl}$	a plastic strain rate
$\dot{\bar{\varepsilon}}^{pl}$	a plastic strain rate integrated over a period of time
$\overline{\varepsilon^{pl}}$	an accumulated equivalent plastic strain
ε_{ij}^{pl}	plastic strain matrix components
η	an efficiency
θ, θ_{α}, θ_{β} ,θ_{γ}	angles
θ_0	a reference angle
κ	a thermal conductivity
λ	a wavelength
v	a welding speed
ρ	a density
σ	a stress
$\sigma_{i,j}$	stress matrix components
σ_1, σ_2	stresses in the principal directions
σ_Y	a yield stress
τ	a shear stress
φ	an angle
$\dot{x}$	a rate in *x*
$\bar{x}$	a virtual field
Δx	a change in *x*
{ }	a tensor
X^{DIC}	a quantity *X* measured usind digital image correlation
X^{FE}	a quantity *X* predicted using finite element analysis
X_{min}	the minimum value of the *X* series
X_{max}	the maximum value of the *X* series

Chapter 1: Introduction

1.1 Background and motivation

Residual stresses are the internal stresses that remain in a structure in absence of external forces. They occur as a result of dimensional incompatibility within the structure such as may be caused, for example, by local plastic strain, volumetric variation within the microstructure or by changes of dimensions due to differential heating and cooling. They can be classified by the length over which they equilibrate [1]. Type I residual stresses equilibrate over the length of the specimen, type II residual stress equilibrate typically over a number of grain dimensions and type III residual stresses balance within a grain [1].

Welding is one of the predominant causes of residual stresses and the type I residual stresses caused by welds influence the structural integrity of a welded component or structure. Welding Induced Plasticity (WIP) and Weld Residual Stresses (WRS) arise from misfit internal strains resulting from the heating and cooling of the weld when the molten material cools down and solidifies and the differential thermal expansion around the weld caused by severe and localised heat addition.

WIP and WRS promote creep degradation and stress corrosion cracking in service environments for susceptible materials in any aggressive environment, as well as leading to fabrication defects such solidification cracking and porosity [2]. Added to in service load, tensile residual stresses can reduce the in-service life of a welded component, which results in a higher stress intensity factor. The total stress intensity factor K^{TOTAL} depends on both primary (applied) and secondary (residual) stresses.

$$K^{TOTAL} = K^{P} + K^{S} \qquad 1.1)$$

The higher the stress intensity factor the closer to material is to failure. This is one of the main issues for reactor pressure vessels made from steels like ASTM SA508 Gr.3 Cl.1, which may suffer from radiation embrittlement. In cases where corrosion resistance is needed, AISI 316L and Inconel alloys are used. In a corrosive environment such as hydrolysed water, combined with a susceptible weld microstructure, stress corrosion cracking (SCC) will be accelerated by a higher value of K^{TOTAL}. Moreover, WIP has been shown to negatively affect weld integrity, since the associated accumulation of defects -dislocations- in the material will accelerate the nucleation of macro-scale defects that lead to component failure [3].

Existing methods for measuring the residual stress in a component are generalized into two categories: destructive and non-destructive methods. Destructive methods are generally relatively cheap and quick, but the component is left damaged or destroyed as material must be removed. When representative mock-ups of structures can be created, these techniques can be used and the component remains unharmed. In some cases, it is simpler or mandatory to assess the structural integrity of the component itself. This is where the need for non-destructive techniques (NDT) arises. NDT use physical phenomena such as ultrasound or diffraction to deduce the residual stress in a component. Diffraction techniques such as neutron and synchrotron diffraction cannot be used for on-site component. Portable X-ray diffraction devices exist but they are typically challenging to apply on weld components when large grains are present around the weld. The measurement becomes difficult where the crystalline structure of the welded metal is large [4] as a coarse grain size can reduce the number of crystals contributing to the diffraction peak such that the peaks become asymmetrical, resulting in error in the diffraction peak position and residual stress measured [4, 5].

Another important tool for predicting the plastic strain and residual stresses in components is finite element (FE) modelling. The welding process is simulated using a thermomechanical model and the residual stresses are calculated. In the literature, many models that predict residual stresses are reported. The technique can provide a prediction of the residual stress distribution in a weld, as long as the process is known. The accuracy of the results is also dependent on the quality of the model and input data and generally validation of the results against another technique is required. In some cases, the welding process and parameters, the material, calibration and validation material for the structure to inspect are not available, which makes residual stress prediction in the structure via FEA difficult.

In nuclear power plants, the structural integrity of safety critical pressure vessels and pipework is assessed by applying assessment methods, such as the R6 procedure [6] for structures containing defects. The R6 procedure provides simplified methods for assessing the integrity of defective structures based on elasto-plastic fracture mechanics. There are three levels of approach for characterising weld residual stress prescribed in R6. The first approach, Level 1, is a conservative assessment assuming a uniform distribution of a tensile residual stress of material yield stress magnitude. The Level 2 approach considers upper bound residual stress profiles for the class of weldment being considered. The third approach, Level 3, is more realistic as FE predictive analysis is coupled with actual residual stress measurements of residual stresses. Mock-up welds can be created and measured to provide as welded residual stress measurements which can then be used in integrity assessments or as validation for FE models.

There has been a considerable amount of work done in recent years allowing residual stress distributions to be evaluated experimentally and predicted with confidence using FE analysis (FEA) [7, 8]. WIP can be predicted using FEA, however, there is currently no standardised method to experimentally quantify WIP, hence the model predictions cannot be validated with confidence. Recently, efforts have been made to develop techniques for WIP measurements. Two existing experimental techniques to assess plastic strain are based on Electron Backscatter Diffraction (EBSD) and indentation. Both techniques require the component to be cut and polished to be observed under a microscope. Here arises the need for non-destructive plastic strain assessment methods that can be applied to laboratory mock-ups and in the future, on in-situ components.

1.2 RESIST project

Thermoelastic Stress Analysis (TSA) [9] is an experimentally-based technique which relies on the TSA equation:

$$\Delta T = -KT\ \Delta(\sigma_1 + \sigma_2) \qquad 1.2)$$

where, ΔT is the change in temperature, T is the temperature at the surface of the specimen, K is the thermoelastic constant and $\Delta(\sigma_1 + \sigma_2)$ is the change in the sum of the principal stresses. The TSA plastic strain assessment (TSA PSA) technique relies upon the variation of the thermoelastic constant K of the material, that occurs when a material has been subjected to plastic straining [10]. The thermoelastic constant, K, of a material is defined as

$$K = \frac{\alpha}{\rho C_p} \qquad (1.3)$$

where α is the coefficient of thermal expansion, ρ is the mass density and C_p the specific heat at constant pressure of the material. An infrared detector measures the temperature and the change in temperature of the component under a linear elastic cyclic loading.

The aim of the RESIST (Residual Stress and Structural Integrity Studies using Thermography) project was to develop a non-contact, non-destructive, full-field measurement and portable plastic strain assessment technique based on TSA. Since any change in K results in a change in the thermoelastic response, if the sum of the principal stresses in the component is known, K can be measured and compared to the thermoelastic constant with no plastic strain K_0. The change in K due to plastic strain is deduced and the plastic strain can be assessed. The RESIST project focuses on the investigation of the possibilities of obtaining the change in K and using this to obtain the amount of plastic strain inherent in the material. The method has been successfully applied to non-welded material [11], however, the next stage is to assess the feasibility of application on weldments. A series of 'weld mock-ups' with increasing complexity were designed to test the TSA PSA approach. FE simulations of the welded mock-ups were produced to compare against the experimental TSA results to provide a validation of the technique on weldments.

The results of the project will be useful for industries seeking to improve the safety and reduce the operating costs of structures by more accurately evaluating their integrity while using non-destructive methods that require portable equipment. Residual stress predictions in FE models of existing structures will be aided by TSA PSA, through measurements of the change in K as a result of plastic straining. The amount of plastic strain can be used to validate the plasticity models used in FE analyses, so the residual stress predictions can be used with confidence.

The knowledge of the integrity of a structure enables the remaining life to be predicted with greater accuracy which in turn means catastrophic failure can be avoided and inspection and maintenance schedules planned more effectively. To-date, TSA has been a laboratory based technique because cyclic loading is required to provide the necessary stress change. A key part of the RESIST project is to make the technique more portable and to establish a means of loading that does not involve a servo-hydraulic test machine. This is outside the scope of the work presented in the thesis but an important factor to consider in the overall RESIST project programme and its application in an industrial setting.

To develop a PSA technique based on TSA, an in-depth study over a wide range of topics is required. The RESIST project is funded by Innovate UK with a view to developing a fundamental understanding of the effect of welding induced plasticity on the thermoelastic response and to provide a means of applying the TSA technique on site. The work in the RESIST project is organised as presented in the diagram in Figure 1.1.**Error! Reference source not found.** The project is coordinated and managed by Enabling Process Technologies (EPT). The project partners are the University of Southampton (UoS), National Physical Laboratory (NPL), TWI Ltd (TWI), AMEC Foster Wheeler (AMECFW) and EdF Energy (EdF).

UoS is the scientific lead in the project and is responsible for the activities and supervision of a post-doctoral researcher, Rachael Tighe and three PhD students: Geoff Howell (PhD1), Vishnu Jaya Seelan (PhD2), and the author of this thesis (PhD3). NPL provides residual stress assessment of structures as well as establishing values of K of the plastically deformed material by characterisation of the three properties given in Equation (1.2). An essential part of the project is to mathematically model the effect of welding on the structure and identify the amount of plastic straining a component has experienced. To facilitate the evaluation of the effect of plastic straining on the thermoelastic response a series of ‘mock-up’ components were designed and modelled prior to manufacture. Thus, providing a means of verifying and evaluating the TSA PSA studies. TWI is responsible for the design and manufacture of the welded mock-ups and supports the RESIST project with knowledge of FE simulation of welding processes. EdF provides the access for on-site testing. AMECFW provides inputs regarding commercial exploitation of the techniques as well as advice on structural integrity assessment.

The researchers work in collaboration, as can be seen in Figure 1.1. The post-doctoral researcher focuses on the design and development of a methodology to apply TSA outside the laboratory. To this aim, a shaker device to apply cyclic loading was developed. PhD1 focused on the identification of areas of plastic straining from the TSA data and developed a technique for assessing the plastic strain. PhD2 works on the characterisation of welds using heat dissipation. PhD3 studied the influence of microstructural changes in welds on the assessment of the change in K with plastic strain and worked on the validation of the technique by designing and testing welded mock-ups, and predicting plastic strain distributions in the weldments using FE analysis.

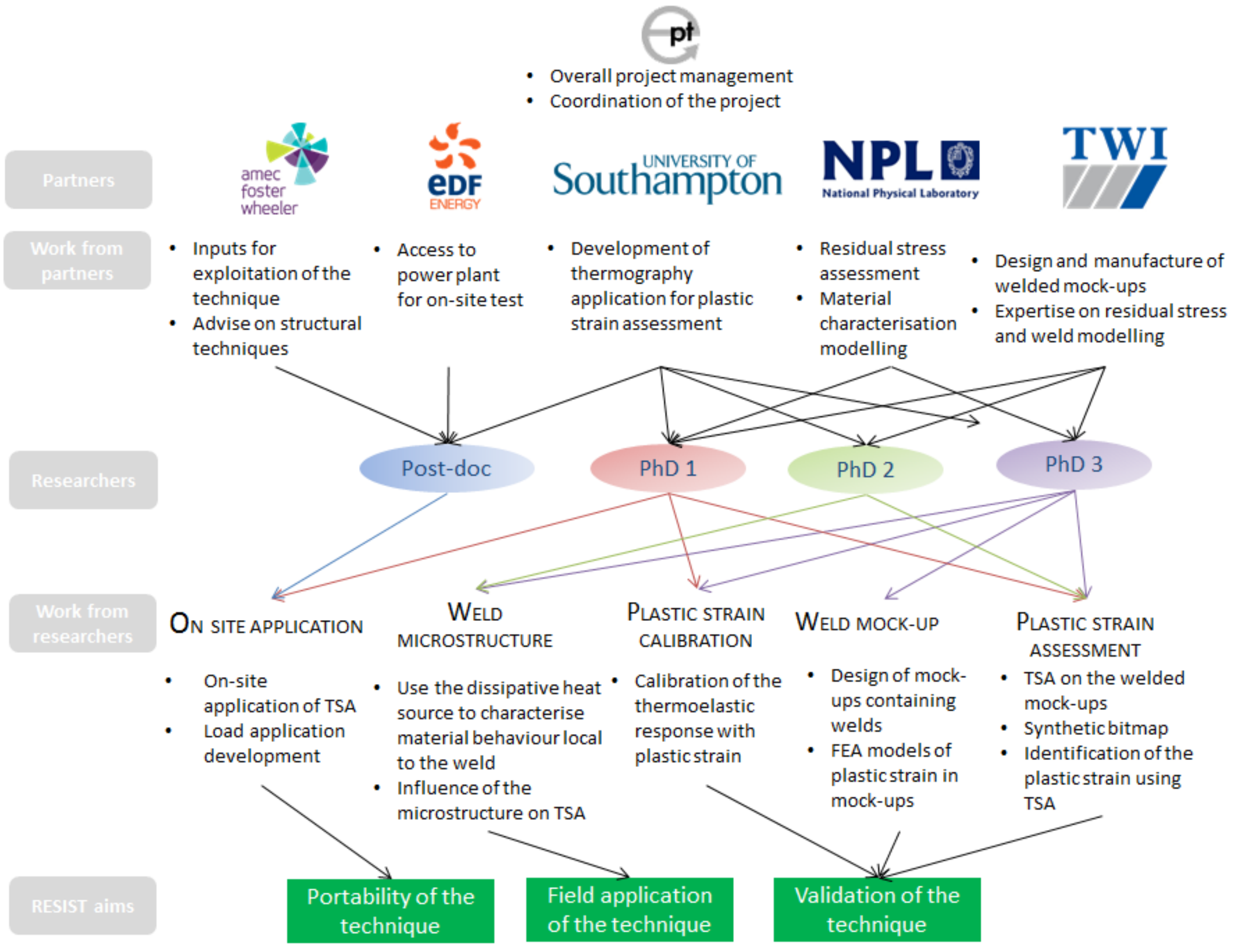

Figure 1.1: RESIST project organisation diagram

1.3 Aim and objectives

The aims of the PhD listed below are part of two main aims, which are, first, to study how microstructure alters the thermoelastic response with and without plastic strain for a range of weld microstructures and secondly, to design mock-ups that allow the thermoelastic response from specimens manufactured using different fusion welding procedures to be established. The design is implemented through FE modelling techniques that provide the plastic strain in the vicinity of the weld. The objectives of the PhD are:

A. Characterise the influence of welding induced microstructural changes on the thermoelastic response with and without plastic strain;

B. To develop weld mock-ups to demonstrate the capability of TSA to be used as a PSA technique on welds;

C. To develop FE models of each weld mock-up capable of predicting plastic strain;

D. To apply TSA PSA on mock-ups

E. To develop linear FE models capable of predicting the sum of the principal stresses in the mock-up when TSA was applied.

F. To demonstrate the capability of the TSA-PSA technique on welds to determine weld induced plastic strain.

1.4 Methodology

To study the influence of the weld microstructure on TSA readings, two materials commonly used in the nuclear industry were selected. Austenitic stainless steel AISI 316L is corrosion resistant, has good resistance to creep up to 600 °C and is used typically for pipework, pressure vessels and waste containers. As it is austenitic, solid state phase transformations (SSPT) will not drastically alter the properties of the steel during welding processes (as is the case for ferritic steels). Welding can induce grain growth and other microstructural changes such as precipitates and the creation of delta-ferrite. Ferritic ASTM SA508 Gr.3 Cl.1 is commonly used in pressure vessels due to its good weldability and good fracture toughness; SSPT occur during the welding of this grade of steel. Different SSPT occur in this material according to the cooling rate, which influences the diffusion of carbon in the atoms. SSPT are discussed in further detail in the next chapter. For both materials, thin strip specimens were designed and manufactured. Heat treatments were selected to replicate realistic welding thermal histories and resulted in microstructures characteristic of welds. The specimens were then evaluated using TSA and K was derived for each microstructural condition for both grades of steel. K values were then compared between microstructural conditions and reference values for each grade of steel. The specimens were then cut into specimens with tapered shapes and a gradient of plastic strain was induced so the variation of K with plastic strain could be determined and compared for the different microstructures.

To validate the TSA PSA technique, a series of weld mock-ups are designed using FE analysis. The geometry of the specimen and welding methods were investigated in order to induce enough plastic strain in the weld to observe with TSA PSA. The mock-ups were then manufactured. Thermocouples were used during welding process and centre hole drilling (CHD) residual stress measurements are made after welding. The FE models were created and calibrated by matching both the fusion line (taken from macrographs) and thermocouple data. Validation of the models against the experimental residual stress measurements was then performed. The residual stress and plastic strain are extracted from the models for comparison with the TSA PSA results.

1.5 Novelty

There are two contributions in this thesis, one in investigating the influence of microstructure on plasticity induced thermoelastic constant variations and the other in the design and manufacture of the mock-ups for the RESIST project i.e.:

the characterisation of grain growth influence on K in austenitic stainless steel 316L;

the characterisation of SSPT influence on K in ferritic steel SA508 Gr. 3 Cl.1;

The characterisation of grain size influence on the dependence of K on plastic strain in austenitic stainless steel 316L;

The characterisation of SSPT on the dependence of K on plastic strain in ferritic steel SA508 Gr. 3 Cl.1;

Design and manufacture of welded mock-ups suitable for demonstrating that TSA can detect changes in material properties including the effect of plastic straining;

FE modelling to predict the amount of plastic strain induced during welding for comparison with the TSA.

1.6 Structure of the report

In Chapter 2, a literature review of three subjects relevant to the PhD project is presented. These subjects are the structural integrity of welds in power plants, FE modelling of welds and plastic strain and its measurement techniques.

The influence of the microstructural changes due to welding on the thermoelastic response is presented in Chapter 3. The influence of grain growth and SSPT on the thermoelastic response is studied respectively for austenitic 316L and ferritic SA508 Gr.3 Cl.1 steels.

Chapter 4 describes the design and manufacture of a specimen that contains a gradient of plasticity. In Chapter 5 a description of the TSA of the specimen is provided and it is demonstrated that thermoelastic response dependent on the plastic strain.

In the two following chapters, Chapters 6 and 7, the design of two weld mock-ups to assess the capability of the TSA PSA technique are presented. In Chapter 6, mock-up A is presented. The design, manufacture, welding and cutting are detailed. The FE model is presented in three parts: the calibration of the thermal analysis, the validation of the mechanical analysis and the modelling of the cutting process, resulting in the FE model of

Mock-up A. Hardness measurements were obtained in the region of the weld. The predicted plastic strain, hardness and thermoelastic response of Mock-up A are compared.

In Chapter 7, Mock-up B, which is a single bead on a plate welded specimen, is presented. The area of weld induced plastic strain is predicted by modelling the welding process. The thermoelastic response of the specimen is obtained and compared with plastic strain predictions.

In Chapter 8, conclusions of the different parts of this report are recalled and a global conclusion on the work presented in this thesis is given, alongside recommendations for future work.

Chapter 2: A review of weld residual stress and plastic strain assessment

2.1 Structural integrity of welds

2.1.1 Weld microstructure

The heterogeneous heating and subsequent cooling a material experiences during welding can be detrimental to the life of a structure. At high temperatures, the material expands, when the material cools down, an incompatible strain is created and leaves residual stresses. When the weld solidifies, the metal shrinks and exerts a contraction force on the surrounding material. If the material cannot deform to account for this contraction because of a constraint, an incompatibility is created in [12].

In austenitic stainless steels, the thermal cycles are also responsible for the formation of carbides and the chromium depletion of zones adjacent to grain boundaries [13]. Typically, in austenitic stainless steels, the chromium concentration at the grain boundary will be reduced in certain parts of the heat affected zone (HAZ) and this region will be less passivated. Therefore, a crevice can form, with the crack walls remaining passive. Any applied stresses might open the crack which allows easier diffusion of solutes and hydrogen away from the crack tip and allowing the crack tip to corrode faster [14]. Stress corrosion cracking (SCC) is one of the major concerns regarding austenitic steel welds. The phenomenon requires three factors to be simultaneously present: a corrosive environment, a susceptible microstructure and a tensile stress intensity factor above a certain threshold. Preventing SCC is desirable and SCC can be avoided if the material can be changed for a less susceptible one at the design stage, or if the environment can be engineered to be less corrosive. However, the selection of a material for an application is often a compromise between its resistance to each failure mechanism associated with the application and its cost. One option to prevent SCC is the control of residual stress level.

In ferritic steel, complex microstructural changes occur as the metal is welded. The molten material is liquidised. It will solidify briefly as delta ferrite, then transform to austenite and finally alpha ferrite during cooling. According to the peak temperature, the hardenability of the alloy and the cooling rate, the microstructure of a welded region can comprise different phases with different material properties [15]. At temperatures where the austenite is stable, the carbon is dissolved, meaning the carbon atoms are in interstices among the iron atoms organised in a face centered cubic (fcc) crystal. When the metal cools down, austenite transforms into a body centered cubic (bcc) crystal. Reduced-sphere unit cells of fcc and bcc are represented in Figure 2.1 (a) and (b) respectively. If the cooling is slow enough, during the transformation, between 790°C and 725°C, carbon atoms escape from the lattice as they are not soluble in the alpha crystal (bcc) [16]. This transformation is reconstructive and the products of this transformation are allotriomorphic (grain boundary) ferrite, idiomorphic ferrite and pearlite [12]. The strain caused by this transformation is an isotropic volume change due to the difference in densities between parent and products [12]. If the austenite is rapidly cooled, carbon atoms cannot make an orderly escape from the iron lattice, which results in a distortion of the lattice [16]. The volume change is not isotropic and lead predominantly by a shear strain. The products from this type of transformation are Widmanstätten ferrite, acircular ferrite, bainite and martensite [12]. The transformations are dependent on chemical composition, and cooling rate. A continuous cooling transformation (CCT) diagram for SA508 Gr.3 Cl.1 (solid lines) is presented Figure 2.2.

In Figure 2.3, the fusion zone and HAZ extents are marked and microstructures at different distances from the fusion line are shown [12]. At 0.5 mm from the fusion line, the phases observed are bainite and martensite and this zone corresponds to the coarse grained HAZ (CGHAZ). The maximum temperature reached in this zone is between 1100°C and the melting temperature. At 1.8 mm from the fusion line, the phases observed are bainite, martensite and retained austenite. This zone corresponds to the fine grained HAZ (FGHAZ) where the maximum temperature reached in this zone lies between 790°C and 1100°C. At 3.4 mm from the fusion line, the phases observed are ferrite and austenite. This zone is called inter critical HAZ (ICHAZ) and the maximum temperature reached in this zone is between 670°C and 790°C [15]. In some steels, a concentration of an austenite stabilizer, such as carbon, can be found in the re-austenitised regions. When cooling, these locations transform into hard microstructures associated with poor toughness.

Ferritic steel may also be irradiated, in some environments. The material is subject to a change in the structure at the atomic level, which deteriorates the steel properties. Radiation embrittlement is of concern as fast fracture can occur as a result of reduced toughness.

It has been established that residual stresses in welds increase the risk of SCC in susceptible environments and materials. The fatigue life of a component can also be affected by residual stresses. For this reason, assessing residual stresses with accuracy is necessary to design against catastrophic failure. It is also required when assessing the acceptability of an existing flaw. The accurate determination of residual stresses is important to accurate assessment of the time left in case the structure needs repairing or replacing.

The two types of steel presented here have a different crystal structure (fcc and bcc). TSA is sensitive to the crystal structure since the three material properties; coefficient of thermal expansion, density and specific heat can vary with the crystal structure hence it is expected that the thermoelastic constant of an fcc structured steel differs from the thermoelastic constant of a bcc structured steel.

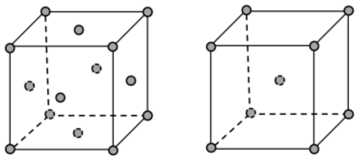

(a) fcc crystal structure (b) bcc crystal structure

Figure 2.1:Reduced-sphere unit cell representations of fcc (left) and bcc (right) crystal structures, adapted from [17]

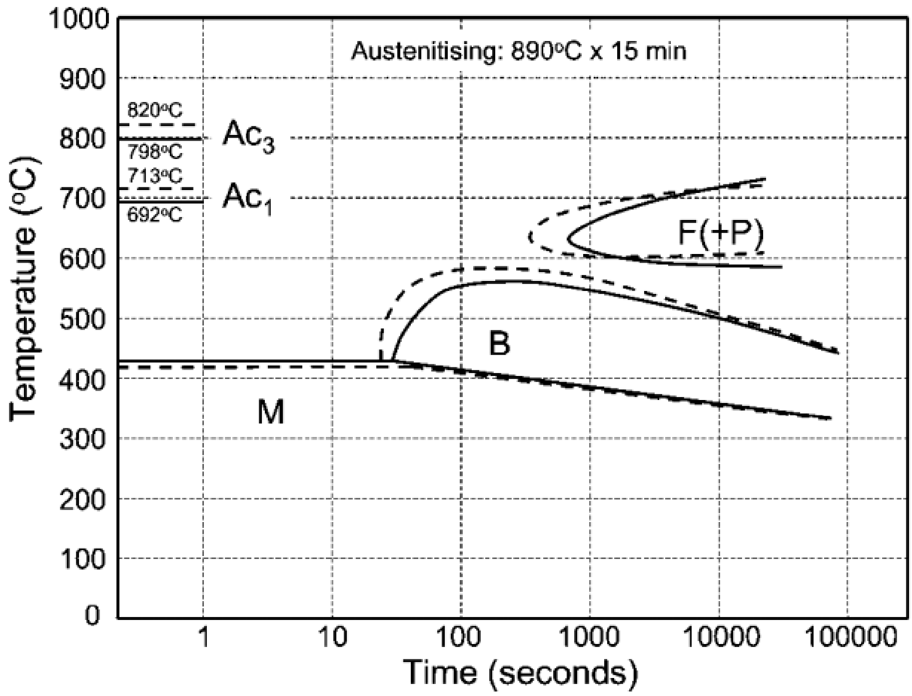

Figure 2.2: CCT diagram for SA508 Gr.3 Cl.1 ferritic steel (solid lines) [18]

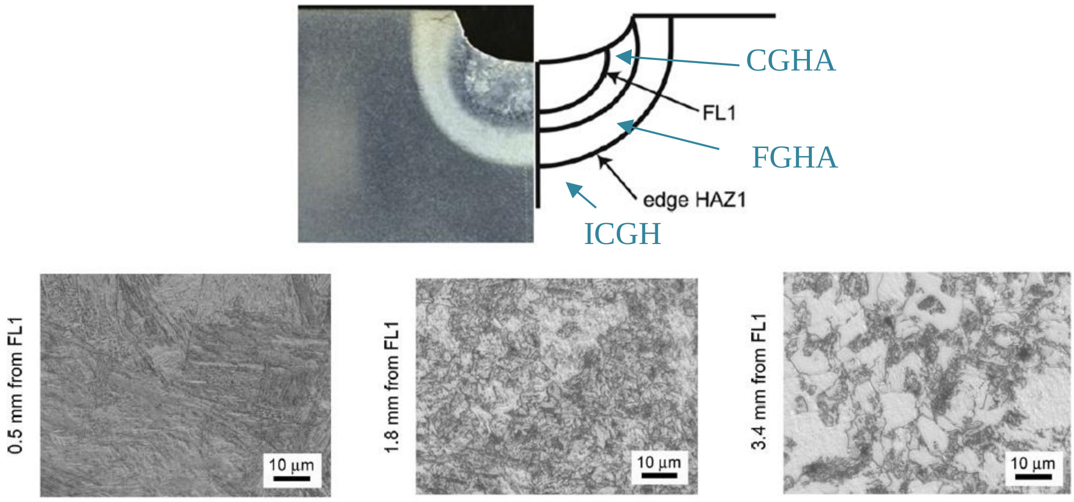

Figure 2.3 Optical macrograph (left) and schematic (right) of the macrostructure of a one-pass specimen (top) and micrographs showing microstructures at different distances from the fusion line (bottom) [15]

2.1.2 Structural integrity of welds in nuclear power plants

The structural integrity and life of a nuclear power plant is influenced by the structural integrity of its welds. Structural integrity of safety critical pressure vessels and pipework in nuclear power plant is assessed using the R5 procedure [19] for high temperature structures and R6 procedure [20] for structures containing defects. When assessing the structural integrity of a weld, the stress intensity factor for actual or postulated cracks is calculated using primary and secondary stresses. Primary stresses are the stresses induced by the loading applied in-service that can contribute to plastic collapse. Secondary stresses are those that cannot contribute to plastic collapse and residual stresses are considered as secondary stresses. Residual stresses are created during manufacturing, joining or during in service operation [21]. They are the stresses that remain in a component when no loading is applied. They can be classified by the length over which they equilibrate [1]. Type I residual stresses equilibrate over the length of the specimen, type II residual stress equilibrate typically over a number of grain dimensions and type III residual stresses balance within a grain [1]. In the R6 procedure, three levels of weld residual profiles for defect assessment can be adopted for an engineering critical assessment. In a Level 1 assessment, the residual stresses are assumed to be a uniform membrane stress of yield magnitude. In a Level 2 assessment, a typical bounding through-wall residual stress profiles based measurements [22] for the class of weld of interest is considered [21]. In a Level 3 assessment, a FE model of the weld can be used and the residual stress predictions compared with measurements on mock-ups. If the predictions and the measurements correspond well, the FE predictions are validated and used to assess the structural integrity of the structure. Level 3 residual stress assessment is the most accurate, but also the most time-consuming and expensive.

The FE method is not a standalone technique, and does not replace experiments. It is on the contrary, a complementary analysis tool that requires validation against experiment. In the following section some residual stress measurement techniques are described. The aim of this list is to present the techniques that the FE predictions of residual stresses can be compared to, for the purposes of validation. The list is not exhaustive, only the measurement techniques commonly used for the validation of austenitic steel weld residual stresses are discussed.

2.1.3 Residual stresses measurement techniques

The existing techniques to evaluate residual stress can be classified in two categories; destructive and non-destructive techniques. Destructive methods method measure the strain liberated when releasing any residual stress. Non-destructive techniques are based on physical phenomena such as diffraction, magnetism and ultrasound to deduce the lattice strain or a change in properties due to strains and residual stresses.

Destructive methods are generally relatively cheap and quick. However, the component is left damaged or destroyed as material has to be removed. Among destructive methods, some techniques can be considered as “semi-destructive” when the component can remain in service after performing the technique.

Hole drilling

Centre hole drilling is the most widely used semi-destructive technique for measuring near-surface residual stresses [23] as it is a relatively simple, quick, cheap and versatile technique [24]. The technique requires drilling a small cylindrical hole in the surface of the component, in the centre of a strain gauge rosette. A wide range of drill sizes (0.6 mm to 2.3 mm diameter) are available with 1.6 mm to 2.3 mm shanks [25]. The locally relieved surface strains are measured and the residual stress can be calculated from these strains using constitutive formulae of the material’s behaviour,

$$\sigma = (\sigma_{max} + \sigma_{min})A_1 + (\sigma_{max} - \sigma_{min})A_2 \, cos2\varphi \tag{2.1}$$

where A_1 and A_2 are hole drilling constants and φ is the angle from the x-axis to the direction of maximal principal stress, σ_{max}. The two calibration constants A_1 and A_2 depend on the geometry of the strain gauge used, the elastic properties of the material and the radius and depth of the hole. The gauges themselves have a physical size and the measure is an average strain rather than a point value, hence the coefficients A_1 and A_2 are obtained by integrating over the active gauge area. Hole drilling analysis assumes that the material is isotropic and linear elastic, that stresses do not vary significantly with depth and that variations of stress values do not exceed half the yield strength of the material [24]. The accuracy of the technique is reported to be about ± 50 MPa. The penetration of residual stresses measurement is about the magnitude of the hole drilled and the spatial resolution is 50 μm [26].

Hole drilling is the most standardised technique to measure residual stresses in weldments [23]. With incremental hole drilling technique, the depth of the hole is incrementally increased and through thickness residual stress can be obtained up to 0.2 times the ratio of hole depth to gauge circle diameter [27]. However, the use of strain gauge measurement offers an average stress measurement locally and the technique is difficult to apply in-situ as it is semi-destructive.

Deep hole drilling

The deep hole drilling technique is a semi-destructive technique that allows residual stress measurement in thick welded structures (up to 100 mm [10]) to be measured. Prior to drilling, blocks of steel are bonded to the structure on both sides. A reference hole is drilled through the wall and measured using an air probe system. A column of the material centred about the reference hole is then trepanned using the electro-discharge machining (EDM) technique. After trepanning, the reference hole is re-measured and the changes in diameter and column height are used to determine the residual stresses [28]. This technique was used by Smith et al. [28] to validate a FE models of thick welded structures (a 108 mm thick ferritic butt-welded plate and a butt-welded cylinder of 84 mm wall thickness) and good agreement was obtained. The DHD technique however requires a hole to be drilled through the thickness of the component. The component needs to be refilled or a mock-up needs to be created.

Contour technique

The component is cut transverse to the weld using a high precision method. The residual stresses in the exposed surfaces relax, and the resulting deformations are scanned, usually using a laser scanning or coordinate measurement machine [29]. The measurements are processed and a FE model is subsequently used to calculate the stress required for the deformed surfaces to become planar. This provides the residual stress distribution in the component before cutting. The contour method is fully-destructive and is used predominantly in laboratory studies [10]. Good practice guidelines were established in [30] to obtain weld residual stress measurement of high accuracy.

The technique was successfully used in [29] and [31] where results were used for validation of FE models. Smith et al. [32], used the contour and neutron diffraction techniques to assess the influence of hardening models on welding residual stresses in a Type 316 three-pass grove weld. Withers et al. [21] reported the contour method as a useful technique to validate the FE weld residual stress predictions as it can reach high resolution maps of stresses in the weld transverse direction. However, the stress map can be as large as the component only if a suitable EDM machine can be used to cut it.

In industries where access to part is difficult or when it would not be safe to damage a component, the need for non-destructive techniques arise. These are typically more expensive and the space and facilities required more complex than those of destructive techniques.

Diffraction techniques

Diffraction techniques utilise the crystal structure of a material and can therefore only be used on crystalline structures. The spacing d, between the atomic planes of a crystal lattice, is measured. A beam of known wavelength λ, is diffracted by a scattering angle 2θ, from its incident direction, according to Braggs' law:

$$2d\sin(\theta) = n\lambda \tag{2.2}$$

$$\varepsilon = \frac{\Delta d}{d_0} = \frac{d - d_0}{d_0} = -\cot(\theta\Delta\theta) \tag{2.3}$$

where d_0 or θ_0 needs to be measured in the material stress-free reference state. Three measurements of strains are made at each location to determine orthogonal stresses using Hooke's law.

The diffraction techniques used to measure lattice strains are well established methods and are often used as validation techniques for FE predictions, as in [31, 33-35]. The techniques, namely X-ray, neutron and synchrotron diffraction facilitate different depths of measurement. X-ray diffraction is typically a surface measurement technique as the strains are measured between 1 μm and 10 μm below the surface [21]. Neutron and synchrotron techniques typically measure strain up to a few centimeters [26] in the bulk of the specimen. Synchrotron measurements can be produced with a spatial resolution as small as 1 μm, whereas neutron diffraction measurements can reach 100 μm spatial resolution.

The techniques are dependent on the surface condition of the specimen to be tested [36]. The measurement becomes difficult when there are large grains in the weld metal [4] as coarse grains can reduce the number in crystals contributing to the diffraction peaks such that the peaks become asymmetrical. This results in random error in the diffraction peaks and in residual stress measurements [4, 5]. The technique can be used on actual structures because the equipment required can be miniaturized. XRD was used to measure residual stresses in ferritic steel weldments [4] and the results were in agreement with FE and neutron diffraction results. In [4] neutron diffraction measurements were in overall agreement with other data from measurements and predictions made using the inherent (or eigenstrain) strain technique, thermal elastic-plastic analysis, X-ray diffraction and the strain gauge method. It was outlined that it can be difficult to measure residual stress at a stress concentration point because the minimum volume to be measured depends on the neutron beam width.

Ultrasonic methods

The ultrasonic method is based on the variation in the velocity of ultrasonic waves in the material, called the acoustoelastic effect. The change in the wave gives a measure of the stress averaged along the wave path [26]. A calibration is required since acoustoelastic coefficients are required for the analysis. Different types of waves may be used, such as longitudinal waves, shear waves or Rayleigh waves, however, the critically refracted longitudinal wave method is the most commonly used. The stress can be calculated using the following equations

$$\frac{v_{pp} - v_L^0}{v_L^0} = \overline{k_1}\sigma_p + \overline{k_2}(\sigma_s + \sigma_w) \tag{2.4}$$

$$\frac{v_{p_1p_2} - v_T^0}{v_T^0} = \overline{k_3}\sigma_{p_1} + \overline{k_4}\sigma_{p_3} + \overline{k_5}\sigma_w \tag{2.5}$$

where v_L^0 and v_T^0 are the longitudinal and transverse velocities, v_{ij} is the velocity of a wave travelling in direction i polarised in direction j. When the wave propagates in a principal stress direction p_3 is orthogonal to p_1 and p_2 and the coefficients $\overline{k_i}$ are the appropriate constants [26].

Ultrasonic techniques have been used to measure residual stress [37], and allow greater penetration depth than diffraction techniques. The method is well suited to large industrial component inspection as the equipment is portable and tests are cheap to undertake [37].

However, rough, irregularly shaped, inhomogeneous, very small or extremely thin components can be difficult to inspect and changes in the ultrasonic velocity can be very small and hence, difficult to measure. The accuracy of the method relies on the calibration constants [10] and surface preparation is required [5].

As an illustrative example, ultrasound was used in [38] to measure residual stresses in stainless steel welded pipes. Results were compared with X-ray diffraction measurements and it was concluded that the ultrasound technique is quick and relatively low cost, however, the need for an unstrained reference, calibration and the influence of texture and structure effect were highlighted as main disadvantages of the technique.

2.2 Finite element prediction of weld residual stresses

2.2.1 Introduction

Since the early 1970s, the FE method has been used to simulate the welding process and predict residual stress fields [39],[40]. It was originally applied to power plant and aerospace components, where the safety aspects are of utmost importance. The computer capacities at that time only permitted simple calculations. With the advances in computing speed and capacity, FE modelling of welding is now commonly used to determine thermal cycles and weld residual stresses.

The analysis of welding processes involves several branches of physics and requires the coupling of various physical phenomena, as shown in Figure 2.4. The predominant couplings, in terms of influence are indicated with thicker arrows. Modelling the welding process while accounting for all the phenomena involved would be very challenging, and the most common tendency is to simulate different physical processes independently and then link them by making assumptions about their interactions [41]. A compromise between computational time and the accuracy of the models is required to make these assumptions, according to the outputs required from the analysis. A common approach consists of solving the thermal and mechanical problems sequentially. In the thermal analysis, the thermal fields are computed and used subsequently as a thermal loading in the mechanical analysis. This approach is frequently used in weld modelling and will be used in the work described in this thesis. In the following paragraph, the physics involved in the welding process is recalled and the common assumptions made to simplify the problem are enunciated.

The fluid dynamics from the melting and gradient in temperature of the material is captured by a heat input in the thermal analysis and as a soft solid in the mechanical part of the analysis. High conductivity can be prescribed to the weld region to mimic the convective heat transfer in the weld pool [42]. The thermal, mechanical and metallurgical problems are usually not solved all at once, as it would require solving a large system (due to coupled equations and the range of scales to be covered) and would require a large and costly computational effort. The heat generated during plastic deformation is negligible when compared to the heat produced during the welding. Therefore the stress and strain influence on metallurgy (referred as interaction 2b in Figure 2.4) are often neglected [43]. If the thermal analysis does not impact the metallurgy, and the microstructural changes do not affect the mechanical analysis (i.e. no SSPT), then, a “weakly”, i.e. “one-way” coupled analysis can be performed, which corresponds to highlighted interaction 3a in Figure 2.4 is included.

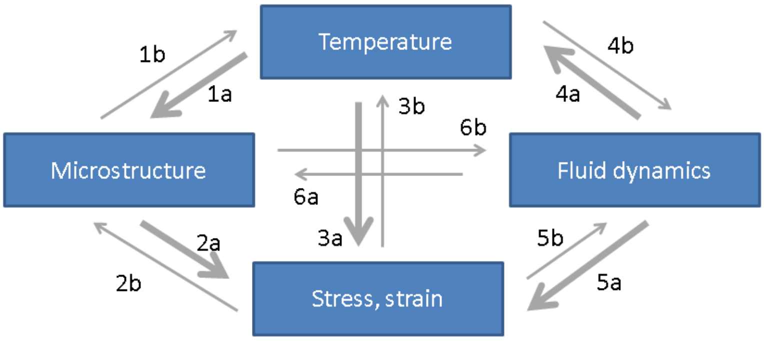

1a: Temperature affects the microstructure

1b: Latent heat released during phase transformation.

2a: Elastic and plastic deformation depend on microstructure.

2b: Stress and plastic strain (i.e. dislocations) cause microstructural transformation.

3a: Thermal stresses depend on the temperature fields through thermal expansion.

3b: Deformation heat due to strain affects temperatures and geometry.

4a: Temperature distribution in weld pool depends on convection.

4b: Temperature affects convection in weld pool.

5a: Flow in weld pool affects shape of solidified weld and hence weld bead stress concentrations.

5b: Weld pool shape depends on mechanical deformations.

6a: Convection/stirring changes metallurgical composition in weld metal.

6b: Convection in the weld pool depends on solidification state and growth mechanisms.

Figure 2.4: Physical phenomena involved in the welding process and their interactions [44]

2.2.2 Material characteristics

The steels of interest in this report are both used in the nuclear industry: austenitic steel AISI 316L and ferritic steel ASTM SA508 Gr.3 Cl.1. During the welding process, the temperature range experienced by the solid weld metal and the surrounding parent material varies from room temperature to fusion temperature. Therefore, material properties used in a welding analysis must be temperature dependent and the relationship is often non-linear.

Temperature dependent properties were reported by Bate et al. [45] for 316L, and by Hamelin et al. [46] for SA508. The data are presented in Appendix A.

The thermal properties required during a thermal FE analysis are:

- The specific heat, C_P, which is the amount of energy needed to modify the material temperature of a unit and is temperature dependent.
- The thermal conductivity, the capacity of a material to transport heat from one part to another within the body. This property plays an important role in welding simulations [47] since it is the main mechanism to transfer heat in the workpiece during welding. The conductivity can be artificially increased after the melting point, to account the convective stirring forces in the weld pool [42].
- The latent heat, which is the amount of energy necessary for a phase transformation to occur without temperature change,
- The heat transfer or film coefficient, which rule the surface heat convection in Newton’s law,
- The surface emissivity, the radiation depends on the surface condition.

The mechanical properties required during a mechanical FE analysis are:

- The coefficient of thermal expansion, α, measures the dimensional changes of the material. It can be assumed isotropic or anisotropic. It determines the thermal strain of the weldment and considers the changes in phases. In the case of austenitic steel 316L, no solid-state phase transformation occurs, so the coefficient of thermal expansion is only temperature dependent. In ferritic SA508, SSPT will occur in the workpiece, depending on temperature changes experienced. According to the phases produced, the material properties are different. The coefficient of thermal expansion value is similar between the phases martensite, bainite and ferrite but different for austenite [48].
- Elastic properties, which are used to relate stress and strain using Hooke’s law. Since the materials studied are isotropic, the elastic properties required are Young’s modulus and Poisson’s ratio.
- The yield strength. This temperature dependent property is extremely important in a weld model to calculate accurately the residual stress generated by the thermal load and constraints. Yield strength for the different phases that can appear after SSPT in SA508 were measured and reported by Hamelin et al. [46].

A constitutive model for the material plasticity has to be defined. This includes the yield criteria and the hardening model.

- Yield criteria:

Two yielding criteria are the Von Mises (or the distortion energy) criterion and Tresca (or maximum shear) criterion. Von Mises criterion stipulates that yielding is reached when the second invariant of the stress deviator exceeds a critical value. Whereas according to the Tresca criterion, yielding begins when the maximum shear stres reaches the value of the yield stress on the uniaxial tensile test, as represented in Equation (2.6).

$$\sigma_Y = \sqrt{\frac{1}{2}((\sigma_2 - \sigma_1)^2 + (\sigma_1 - \sigma_3)^2 + (\sigma_2 - \sigma_3)^2)} \tag{2.6}$$

$$\sigma_Y = 2\tau_{max} = \frac{\sigma_1 - \sigma_3}{2}, (\sigma_1 > \sigma_2 > \sigma_3) \tag{2.7}$$

where σ_Y is the yield stress, $\sigma_1, \sigma_2, \sigma_3$ represent the principal stresses and τ_{max} the maximal shear reached in the component.

- Hardening model:

If the material continues to deform in the same direction after reaching yielding, the stress increases with deformation, due to an increase in the resistance to plastic straining. This is called hardening. Hardening is modelled using the isotropic, kinematic and mixed hardening rules. The isotropic hardening model describes the expansion of the yield surface. Kinematic hardening accounts for the Bauschinger affect and modifies the yield strength of the material when the direction of flow changes. For uniaxial reverse loading: once loaded until yield in one direction (tensile), the material yield point upon reversed loading (compression) is shifted. The mixed hardening rule allows the yield surface to expand and translate at the same time. These work-hardening rules are depicted in Figure 2.5.

- Annealing temperature

High temperature annealing needs to be accounted for in welding simulations [7] as it influences the plastic strain prediction hence the residual stresses. A temperature above which the material loses all accumulated plastic strain is set. The associated stresses are relaxed due to the loss of hardening in the annealed region.

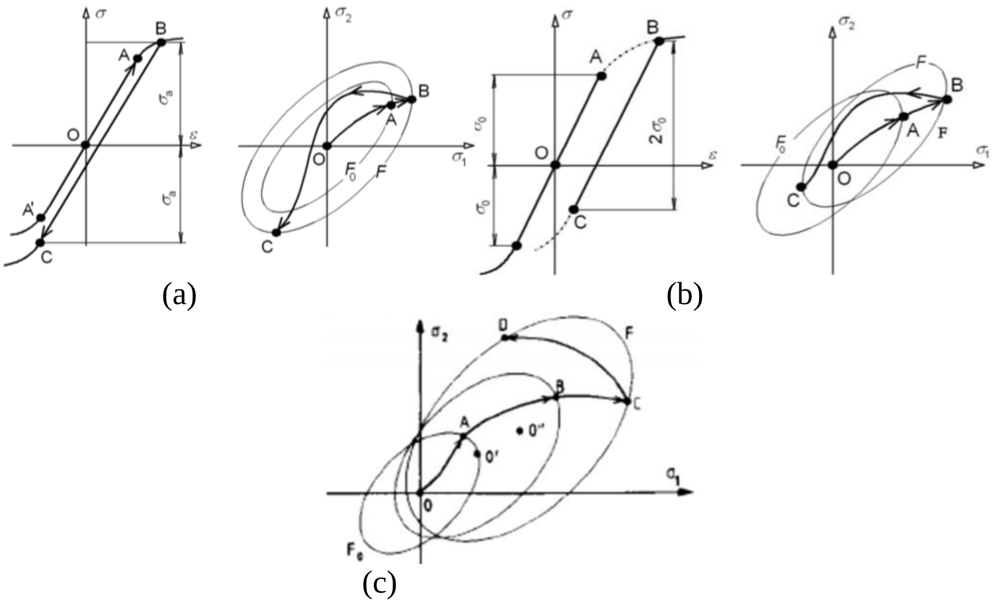

(a) (b)

(c)

Figure 2.5: Isotropic (a), kinematic (b) and mixed hardening rule (c) [49]

The thermo-mechanical analysis of welding process first requires a transient heat transfer analysis to calculate the welding temperature distributions. A moving heat source with a constant shape is often used to model the heat input provided to the work piece by the welding torch. The temperature distributions are then applied in a transient mechanical analysis. The thermal strains are computed and used to calculate the displacement, strain and stress fields. The governing equations and FE discretisation of the thermal and mechanical problems are outlined in the following sections, as well as the boundary conditions and the method to solve the equations.

2.2.3 Thermal fields prediction

During the welding process, the heat source heats and melts the metal. Then, the metal in the melted zone and heated region solidifies or cools down. The governing equation of the heat conduction added to the source term from the process is

$$\rho C_p \frac{\partial T}{\partial t} - \kappa \Delta T = \dot{Q}_V \tag{2.8}$$

where T is the temperature, ρ is the density of the material, C_p is the specific heat, κ is the heat conductivity and $\dot{Q}_V$ is the heat supplied externally into the body per unit volume from the welding process [44]. The power, P, of the welding torch is defined by

$$P = U \times I \tag{2.9}$$

where U is the voltage and I is the current used in the welding process.

Only a proportion of the electrical energy supplied to the welding torch is transferred to the weld. The rest is dissipated into the atmosphere through dissipation and convection. The proportion of power used to heat the weld metal, P_{net}, is defined using a welding process efficiency η such as

$$P_{net} = \eta P \tag{2.10}$$

The change in temperature with time needs to be defined to write the governing equations. For that, the heat input per unit weld length is defined as

$$\dot{Q_V} = \frac{\eta P}{\nu} = \frac{\eta UI}{\nu} \tag{2.11}$$

where ν is the travel speed of the heat source. The heat conduction is the heat flow through the material and the governing equation is Fourier law

$$q_c = -\kappa \nabla T \tag{2.12}$$

where q_c is the heat flux by unit time, κ is the thermal conductivity and T the metal temperature.

The heat also flows out or across the surface of the material. Two forms of heat flows are identified, the convection of the heat with air and radiation, when the heat is transmitted in form of light. The convection is governed by Newton's law, the heat transferred to the atmosphere is proportional to the product of the heat transfer coefficient and the difference between the metal temperature T and the atmosphere temperature T_{atm} as follows

$$q_{con} = \beta_c (T - T_{atm}) \tag{2.13}$$

where q_{con} is the heat transferred in the atmosphere per unit time and β_c is heat transfer coefficient.

The heat flow from the metal surface to the atmosphere is governed by Stefan-Boltzmann law, which stipulates that the amount of heat flowing into atmosphere through surface radiation is proportional to the difference between the fourth power of the temperature on the surface and that of the atmosphere:

$$q_{rad} = eC_0 \{T^4 - {T_{atm}}^4\} \tag{2.14}$$

where C_0 is the radiation constant for the black body, the Stefan-Boltzmann constant, $C_0 = 5.67 \times \text{J/mm}^2\text{sK}$, and e is the emissivity of the material.

The energy balance is then expressed in the form of an integral over the volume of the body, in its weak form obtained from the principle of virtual temperatures

$$\int_V \bar{T}(\rho C_p)T'dV + \int_V \bar{T}'\lambda T'dV = \int_S \bar{T}Q_{int}dS + \int_V \bar{T}Q_{ext}dV \tag{2.15}$$

where V is the volume of solid material, with surface area S, $\bar{T}$indicates that a virtual temperature distribution is being considered, Q_{int} is the heat flux per unit area, flowing into the body and Q_{ext} is the heat supplied externally into the body per unit volume.

The principle of virtual temperatures is applied to discretise the heat flux balance in terms of the nodal temperatures. This leads to an overall balance of the heat fluxes by the sum of element integrals. The temperature gradient in the element is calculated by appropriate differentiation of the shape functions and the constitutive law for the heat transfer is given by Fourier's law relating to the fluxes to the temperatures in terms of the constitutive conductivity matrix M_λ. The information of the temperature-gradient interpolation matrix and the constitutive relation is used in the equation of principle of virtual temperatures, Equation (2.16), where the integration over the structure is obtained as a sum of integration over the volume and areas of all finite elements. From this summation of element contributions, the full system of equilibrium equations, expressed in nodal fluxes, is obtained for all the nodal point temperature. This leads to the finite element equation system

$$M_{Cp}\{\dot{T}\} + M_\kappa\{T\} = \{Q_V\} + \{Q_S\} \tag{2.16}$$

where M_{Cp} is the heat capacity matrix, M_κ is the conductivity matrix of the system, $\{Q_V\}$, the heat flux over the volumes and $\{Q_S\}$ the element surface heat flux. The different contributions are obtained by appropriate integrations over the volumes and surfaces.

2.2.4 Mechanical fields prediction

The mechanical behaviour of a structure can be described with displacement, u, strain, ε, and stress field, σ. These quantities should satisfy the relations presented in the following. The strain and displacement fields are related through the strain displacement relation

$$\{\varepsilon^{total}\} \equiv \mathrm{B}\{u\} \tag{2.17}$$

where B is the temperature-gradient interpolation matrix for the thermal analysis. Stress and strain of an element are related by the law describing the material behaviour of the material

$$\{\sigma\} = \mathrm{C}\{\varepsilon^{total}\} \tag{2.18}$$

where C is the constitutive matrix, described by Hooke's law in the work presented in the report as the material studied are elastic-plastic, but other material models can be represented. The third equation is the force equilibrium equation

$$\{\sigma\}_{,j} + \{p\,\} = 0 \tag{2.19}$$

where $\{p\,\}$ is the body force tensor at any point within the volume. The equilibrium equations are re-written under their weak form using the principle of virtual work

$$\int_V \sigma_{ij}\delta\overline{\varepsilon_{ij}}dV = \int_V p_i\,\delta\overline{u_i} + \int_S Tr_i\delta\overline{u_i}dS \tag{2.20}$$

where $\delta\bar{\varepsilon}$ is the virtual strain, $\delta\bar{u}$ is a virtual displacement field and Tr is the surface traction at any point on *S*. The discretisation procedure is similar to that of the thermal analysis, the strain-displacement relation (2.21) and the constitutive relation (2.22) are integrated in the equilibrium equation and the principle of virtual work is applied. The contribution of each element volume and surface are added on the whole body and the system of equilibrium equations is obtained for the nodal point displacements. The general finite element equation of the system can be written as

$$M_S\{u\} = \{R_b\} + \{R_s\} + \{R_c\} \tag{2.21}$$

where M_S is the stiffness matrix of the system, $\{R_b\}$ the body forces over the volumes, $\{R_s\}$ the element surface forces and finally $\{R_c\}$ the concentrated nodal loads. The different contributions are obtained by appropriate integrations over the volumes and surfaces. Boundary conditions for residual stress prediction are very important, as it is the restrained part of the structure that is responsible for the creation of residual stress, as well as the non-uniform heating and cooling. Indeed, if the structure was heated and cooled uniformly throughout the whole geometry, free of displacement and rotation, then the material would expand during heating and shrink during cooling to come back to its original shape. Devices used to fix the structure in reality (e. g. tack welds, clamps) should be present in the FE model by setting displacements and rotations to the appropriate value. If no constraint is applied to the model, the displacement cannot be determined because the system of equation becomes singular. In three-dimensional problems, three translations and three rotations in the three directions should be restrained to prevent rigid body motion. Similarly, in two-dimensional problems, translations in the two directions of the plan and one direction around the axis normal to the plan must be fixed [39].

2.2.5 Assumptions and simplifications

2.2.5.1 Thermal heat source modelling

The heat input and heat losses are considered as boundary conditions of the model. The heat input can be represented in several manners. If the heating of the weld is quick, an instantaneous heating of the weld can be used. More often, the moving weld torch is represented by a transient heat source with constant geometry and velocity, providing the best accuracy. The existing techniques to model the heat source in FE modelling are surface and volumetric distributions.

The Gaussian surface heat distribution is a round shaped heat source normal to the surface. The flux distribution can be expressed as

$$q(r) = q(0)e^{-Cr^2} \tag{2.22}$$

where C is the concentration coefficient which determines the amplitude of the Gaussian distribution, and it is related to the actual heat source width. r is the radial distance from the centre heat source. $q(0)$ is the maximum heat flux at the centre of the source, and $q(r)$ is the surface heat flux at the radius r.

To calibrate the heat input with experimental values, the total heat input can be integrated over the surface of flux distribution and the concentration coefficient can be calculated using Equation (2.22) with a defined value of $q(0)$.

The double ellipsoid model proposed by Goldak et al. [50] is double ellipsoid heat flux which consists of two instantaneous heat input of a shape of a quarter of ellipsoid each (front and rear), as it can be seen in Figure 2.6. The front and rear quadrants power distribution are calculated using the following equations, respectively

$$q_f(x,y,z,t) = \frac{6\sqrt{3}f_f Q}{abc_f\pi\sqrt{\pi}} exp\left\{-3\left(\frac{x^2}{a^2}+\frac{y^2}{b^2}+\frac{(z+vt)^2}{c_f^2}\right)\right\} \tag{2.23}$$

$$q_r(x,y,z,t) = \frac{6\sqrt{3}f_r Q}{abc_r\pi\sqrt{\pi}} exp\left\{-3\left(\frac{x^2}{a^2}+\frac{y^2}{b^2}+\frac{(z+vt)^2}{c_r^2}\right)\right\} \tag{2.24}$$

where a and b are respectively the width and depth of the heat source, c_f and c_r the length of front and rear ellipsoidal, as depicted in Figure 2.6. These geometrical parameters can be defined from experimental measurements from the weld pool.

The quantities x, y, z are the local spatial coordinates, t is the time, v is the welding velocity, Q is the welding heat input power, ($Q = \eta UI$, where U and I are respectively the voltage and intensity of the current and η is the efficiency of the welding process).

The coefficients f_f and f_r denote the heat fractions on front and rear quadrants, respectively and f_f plus f_r equal two. These values are arbitrary and should be set according to the experimental conditions [51]. These parameters can also be selected to avoid discontinuities in the heat distribution between the front and rear ellipsoids, such as $f_f = \frac{2c_f}{c_f+c_r}$ and $f_r = \frac{2c_r}{c_f+c_r}$, as recommended by Lindgren in [41].

The use of this heat source model is recommended for good residual stress prediction in a single bead on plate model in [52]. In [45], the Goldak double-ellipsoid heat source model was used, and good agreement was found with thermocouples temperature predictions. Simpler heat-source models were designed and compared. In [53], an instantaneous heat source model was used to model a T-fillet joint. When compared with a moving heat source, the time required to run the transient heat source model was an order of magnitude higher. However, the simplified model tends to under-predict the residual stress and distortion.

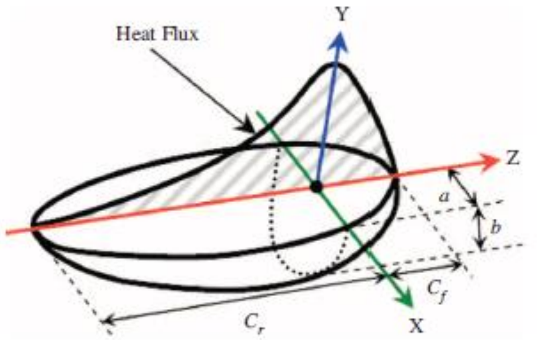

Figure 2.6: Double ellipsoid heat source configuration [50]

2.2.5.2 Weld material deposition

Different techniques exist to simulate the deposition of the filler metal in the weld bead. Among them, the element birth technique is the most used [54, 55]. It consists in creating the model with the welded material included, however, deactivating the weld material elements at the initial step. The appropriate elements are reactivated as the heat source passes, which ensures that extra, unrealistic stiffness is not present during the welding.

Another method, the quiet element technique, involves initially assigning the weld elements with very low stiffness and thermal conductivity properties so that they do not affect the rest of the model. According to the location of the heat source, the elements are assigned with their normal weld material properties. In another method, the element movement technique, the elements of the weld material are separate from the parent metal geometry. As the weld metal is deposited, the nodes of the weld and base metals are fused to form only one body [54]. The weld metal can also be modelled as part of the base geometry from the start of the welding step. The heat source melts the weld metal and parent material as it passes. This method is called the block dumping technique and is the easiest to implement.

The progressive adding of the weld material requires extra model set-up time and is more computationally expensive when predicting stresses, as well as more accurate [55] compared with the block dumping technique. In [55], the block dumping and element birth techniques were used to model the welding process of a single bead-on-plate specimen. Though the element birth technique was found to provide closer temperature predictions compared to thermocouple data -only graphic comparison is provided-, the computational cost of the element birth technique was significantly larger compared to that of the block dumping technique, for both thermal and mechanical predictions and the authors did not recommend to use the element birth technique in the mechanical analysis.

In Chapter 6 of this report, a bead on plate weld model is presented. The weld metal is modelled as already existing and being heated as the heat source moves along the welding direction, as recommended in [55]

2.2.5.3 Plasticity model

Austenitic 316L stainless steel is modelled in depth in this work; 316L behaviour is considered to be mixed isotropic-kinematic hardening.

Three models are discussed in literature: isotropic, kinematic and mixed isotropic-kinematic hardening. In [33], the three plasticity models were compared for the prediction of residual stresses, along with comparison to experimental residual stress values from neutron and synchrotron diffraction. The weld modelled in this comparison was a 316LN multi-pass slot weld using 316L filler material. It was found that isotropic hardening model over-predicts stresses, whereas kinematic hardening tended to under-predict them, and the mixed-hardening model lies in between and gives the most accurate stress predictions, in comparison with the experimental measurements. As a lack of material data can lead to a difficult calibration of a mixed-hardening model, it can be preferable to use an isotropic model as more conservative. However, the accumulated plastic strain was also predicted and it was found that the isotropic tends to under predict plastic strain and the kinematic hardening model over-predicts the quantity. This is only the case for multipass welds, where the material that does not reach annealing temperature will undergo thermal cyclic loading. This is where the hardening models differ, as the isotropic hardening model overestimates the elastic region whereas the kinematic hardening model underestimates it. This information is of primary importance for the relevance of the development of the TSA PSA technique, as a quantitative value of the accumulated plastic strain would allow the validation of the hardening model used, hence the validation of the residual stresses, when no residual stresses measurement can be obtained – for an on-site pipe for instance.

In [7], as well as testing the influence of the plasticity model on the residual stresses of the three-pass AISI 316L weld, the influence of the annealing temperature on WRS and weld plastic strain (WPS) was studied. The three hardening models mentioned above were tested, with three different annealing temperature models: a single annealing step of annealing temperature of 1050°C, a single annealing step of annealing temperature of 1300°C and a two-step annealing model, which consist in keeping the accumulated WPS constant between 1050°C and 1300°C. Above 1300°C, the accumulated WPS is reset to zero. It was found that the plasticity model used had more influence on the WRS than the WPS. This can be easily explained since a small change in the elastic strain will create a large change in the residual stress. The annealing model however, influences the WPS significantly more than the hardening model, and only influences the WRS if an isotropic hardening model is used in the modelling. In comparison with the neutron and synchrotron weld residual stresses, the combination of a mixed-hardening model with the two step annealing model showed the best results. However, it is recognised that material data to calibrate both mixed hardening model and two-step annealing model can be difficult to obtain, and it is recommended, if conservatism is sought, to use isotropic hardening model, in combination with a single step annealing model at melting temperature. In terms of relevance of the development of the TSA PSA, these results emphasize the importance of plastic strain assessment, in cases where material data cannot easily be obtained. As recommended, an isotropic model would have to be used. To reach more accurate – less conservative - WRS and WPS predictions, the annealing temperature model could be adjusted using TSA PSA measurements. Annealing temperatures would be tested and the predicted plastic strain would be compared with the TSA PSA plastic strains, validating the most accurate annealing temperature. As the WRS are sensitive to the annealing model when an isotropic hardening model is used, more accurate WRS predictions would be obtained.

2.2.6 Confidence in the models

2.2.6.1 Calibration of the thermal heat source

Calibration of the heat source is important in a weld model as the accuracy of the temperature fields calculation plays an important role over the stress calculation [56]. The thermal field must be calibrated against experiment, if possible, in order to ensure that an accurate thermal history will be provided to the mechanical analysis. In [52], recommendations are provided to obtain a calibrated simple bead on plate FE model via three steps. First, a Gaussian ellipsoidal heat source should be used, and for tungsten inert gas (TIG) welding process, with an efficiency of 0.75-0.8. The fusion boundary should correspond well between the experiment and the FE model, therefore, a macrograph of a cut of the weld, ideally at mid-length of the weld, is required. The fusion line of the FE model can be altered by changing geometrical parameters of the heat source model, and conductivity in the weld pool can be artificially increased, to model heat conduction in the molten zone [42]. The aim is to obtain a fusion zone close to that shown in the macrograph. Finally, thermocouples on the welded component provide temperature history at several locations, which can be compared to the FE model data. The three recommended positions for thermocouples [52] are

- on the weld face, at least 8 mm away from the edge of the weld bead,
- on the face not being welded, at about mid-length of the weld,
- in the plate, by drilling a hole in the centre of the plate, under the weld, at about mid-length of the weld again.

These positions were considered as the best positions to calibrate a FE model, as they allow the temperature to be recorded accurately, in opposition to thermocouples located at 4 mm away from the weld bead on the weld face, which were subject to arc shine, i.e. the heat reflected by the light of the arc has an impact on the temperature recorded. Thermocouples at these positions showed values up to 100°C higher than the predictions.

The weld model presented in this report is a double bead on plate, so no thermocouple can be placed under the weld bead by drilling a hole, and both faces are being welded, therefore, thermocouples located 10 mm and 15 mm away from the weld bead were used to calibrate the FE model. Nonetheless, several thermocouples were placed and used for the calibration.

2.2.6.2 Validation of stress predictions

The assessment of accurate, i.e. presumably lower residual stresses is of interest in industry as lower residual stress enables higher load carrying capacity and resistance of welds in the long term. It would not be practical to access the welded pipes in the reactor to obtain residual stress measurements, so FE modelling is preferred for this application. However, FE modelling of welds can be challenging, and when plausible results are obtained, confidence in the predicted stresses is not straightforward [28].

To gain confidence in the welding residual stress predictions, recommendations were made [31, 52]. Among the recommendations, the validation of the predictions against reliable residual stress measurements performed on a replica of the weld of interest (i.e. a mock-up) remains the essential step to validate the predictions. For this, suitable experiment residual stress and strain measurement techniques are required. Ideal techniques are full field, as both qualitative and quantitative comparison with FE model prediction can be performed. Another important feature of a good measurement technique for comparison with FE prediction is the spatial resolution of the technique [21]. The TSA technique has both characteristics, which highlights once more the potential of this technique to become a useful tool for validation of weld residual stress and strain predicted by FE modelling.

There has been considerable amount of work done so the magnitude and distribution of residual can be evaluated experimentally and predicted with confidence using finite element analysis (FEA) [46, 57]. WIP can be predicted using FEA, however, there is currently no standardised method to experimentally quantify WIP hence the model predictions could not be validated with confidence until recent development of WIP measurements.

2.3 **Plastic strain assessment**

2.3.1 Dislocation and plastic strain

A dislocation is a defect around which some of the atoms are misaligned [17]. Dislocations can be edge dislocation, screw dislocation or a combination of both. An edge dislocation is represented in Figure 2.7: an extra half plane of atoms terminates within the crystal, causing misalignment. The ability of a material to deform plastically depends on the ability of dislocation to move. For crystalline solids, plastic deformation is facilitated by a process called “slip”, which involves the motion of dislocations presented as a “caterpillar movement” along a preferred plane, called “slip plane”, as depicted in Figure 2.8 in the case of an edge dislocation. The portion of extra half-plane ultimately emerges from the surface of the crystal, forming an edge that is one atomic distance wide [17]. Slip bands can be observed under a high resolution transmission electron microscope, as the slip band etched more rapidly than the surrounding crystal as depicted in Figure 2.9.

The dislocation density is defined as the total dislocation length per unit volume. The number of dislocation increases dramatically during plastic deformation as new dislocations are created out of existing dislocations, defects, grain boundaries and surface irregularities [17]. With cold working, ductile metals become stronger when they are plastically deformed at temperature well below the melting point. The reason for strain hardening is that the dislocation density increases with plastic deformation. Dislocations hinder the movement of other dislocations hence strengthen the material. The measure of strain hardening is the percent of cold work (% CW) given by the relative reduction of the original area A_0 to the final value A_d:

$$\%\mathrm{CW} = 100 \times \frac{(A_0 - A_d)}{A_0} \tag{2.25}$$

The grain size also has an influence on the strength of the material. This is based on the fact that it is difficult for a dislocation to pass into another grain especially if it is very misaligned. Atomic disorder at the boundary causes discontinuity in slip planes hence grain boundaries hinder dislocation movement. The finer the grain size means more grain boundaries, which impede dislocation motion. Grain size d influences the yield strength according to the Hall-Petch equation:

$$\sigma_Y = \sigma_0 + \frac{k_y}{d^{1/2}} \tag{2.26}$$

where σ_Y is the yield strength of a material of grain size d, σ_0 the stress required in the material to start dislocation motion and k_y is the strengthening coefficient.

In welds, dislocations are introduced as a consequence of thermal stresses that result from rapid cooling and cause plastic deformation [17]. In the work described in the thesis, the plastic strain induced by uniaxial tensile loading is considered, as well as weld induced plastic strain. It was demonstrated in previous work [58] that it was possible to assess plastic strain levels using TSA PSA. It is assumed that the dislocation density influences the thermoelastic constant hence, the influence of the plastic strain depending on its origin is not considered in this work. Moreover, single-pass welds are under consideration. The difference between monotonic and cyclic plastic strain is not addressed in the present thesis.

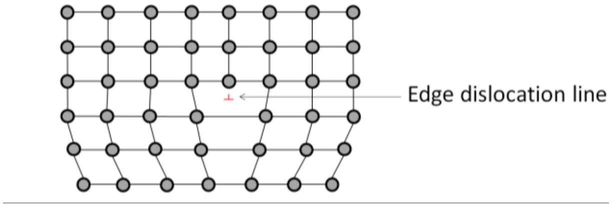

Figure 2.7: The atom positions around an edge dislocation; extra half-line of atoms represented in a plane. Adapted from [17].

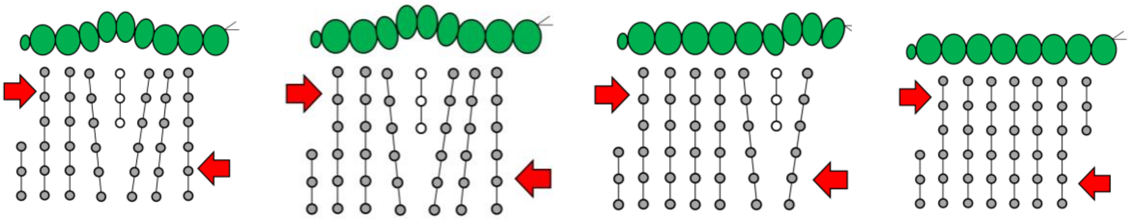

Figure 2.8: Representation of the analogy between caterpillar and dislocation motion. Adapted from [17].

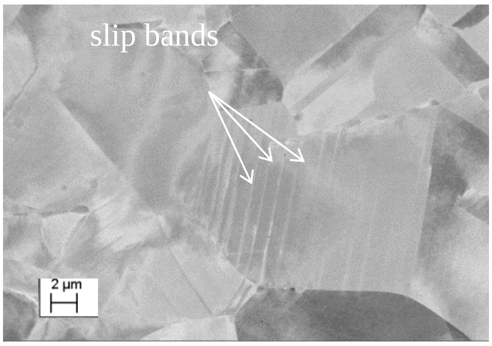

Figure 2.9: Slip bands in 316L stainless steel. Elise Chevallier and David Griffiths, TWI Ltd, 2014.

2.3.2 Techniques for assessing plastic straining in-situ

In Chapter 4, two techniques, DIC and strain gauges, are used to assess plastic strain in steel samples. The aim of this section is to present these techniques and explain how they work. It must be noted that it is not the aim to compare those two techniques with the plastic strain assessment technique being developed as DIC and strain gauge methods both require to be performed while the specimen is being deformed.

Strain gauges

The strain being applied to a specimen can be recorded using a strain gauge. The strain gauge's electrical resistance varies in proportion to the amount of strain in the component. In the work presented, bonded metallic rosette strain gauges are used and are presented herein. The metallic strain gauge consists of a metallic foil bonded to a thin backing which is attached directly to the test specimen. Therefore, the strain experienced by the test specimen is transferred directly to the strain gauge, which responds with a linear change in electrical resistance. A fundamental parameter of the strain gauge is its sensitivity to strain, expressed quantitatively as the gauge factor (GF). GF is the ratio of the fractional change in electrical resistance to the fractional change in length, or strain ε

$$GF = \frac{\Delta R/R}{\Delta L/L} = \frac{\Delta R/R}{\varepsilon} \qquad 2.27)$$

where R is the electrical resistance, L the length of the strain gauge.

To measure small changes in resistance, strain gauge configurations are based on the concept of a Wheatstone bridge. The general Wheatstone bridge, illustrated in Figure 2.10, is a network of four resistive arms with an excitation voltage, V_{EX}, that is applied across the bridge. The Wheatstone bridge is the electrical equivalent of two parallel voltage divider circuits. R_1 and R_2 compose one voltage divider circuit, and R_4 and R_3 compose the second voltage divider circuit. The output of a Wheatstone bridge, V_0, is measured between the middle nodes of the two voltage dividers.

$$V_0 = \left[\frac{R_3}{R_3 + R_4} - \frac{R_2}{R_1 + R_2}\right] * V_{EX} \qquad 2.28)$$

From this equation, it can be seen that when $R_1 / R_2 = R_4 / R_3$, the voltage output V_0 is zero and the bridge is balanced. Any change in resistance in any arm of the bridge results in a nonzero output voltage. The bridge is then unbalanced which produces a nonzero output voltage that is a function of strain.

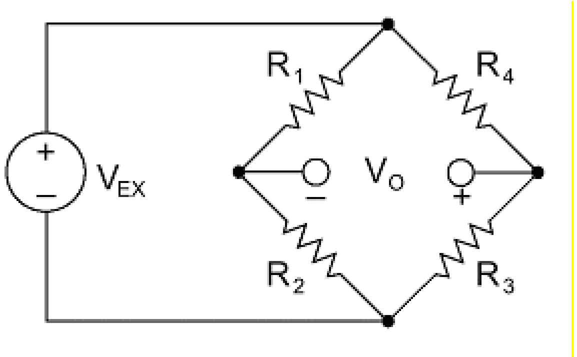

Figure 2.10: Strain gauges are configured in Wheatstone bridge circuits to detect small changes in resistance [59].

A wire strain gauge can effectively measure strain in only one direction. To determine the three independent components of plane strain, three linearly independent strain measures are needed, i.e., three strain gauges positioned in a rosette-like layout. A strain gauge rosette is attached on the surface with an angle θ_α from the *x*-axis. The rosette itself contains three strain gauges with the internal angles θ_β and θ_γ, as illustrated in Figure 2.11(a). The strain measured from these three strain gauges are ε_a, ε_b, and ε_c, respectively. The following coordinate transformation equation is used to convert the longitudinal strain from each strain gauge into strain expressed in the *x*-*y* coordinates,

$$\varepsilon_X = \frac{\varepsilon_x + \varepsilon_y}{2} + \frac{\varepsilon_x - \varepsilon_y}{2}\cos(2\theta) + \varepsilon_{xy}\sin(2\theta) \qquad (2.29)$$

where θ is the coordinate transformation angle, with positive counter clockwise direction. In the thesis, rectangular rosette strain gauges are used, i.e. $\theta_\alpha = 0^\circ$, $\theta_\beta = \theta_\gamma = 45^\circ$ as presented in Figure 2.11(b) Equation (2.29) is used to solve for the three unknowns, ε_x, ε_y, and ε_{xy} as follows

$$\begin{cases} \varepsilon_x = \varepsilon_a \\ \varepsilon_y = \varepsilon_c \\ \varepsilon_{xy} = \varepsilon_b - \dfrac{\varepsilon_a + \varepsilon_c}{2} \end{cases} \qquad 2.30)$$

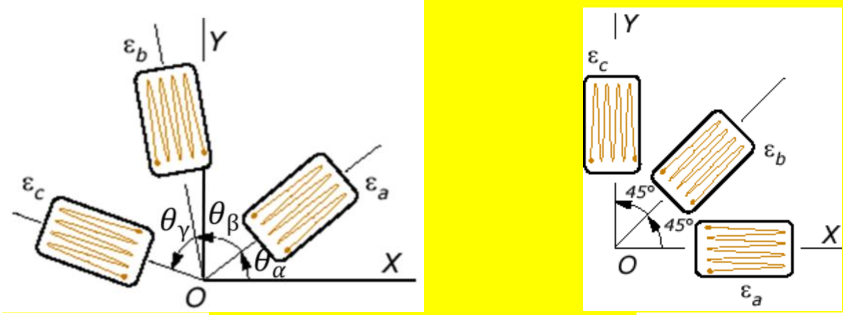

(a) (b)

Figure 2.11:(a) General rosette strain gauge layout and (b) 45° strain rosette aligned with the *x*-*y* axes, i.e., $\theta_\alpha = 0^\circ$, $\theta_\beta = \theta_\gamma = 45^\circ$ [60]

Digital Image Correlation

The Digital Image Correlation (DIC) technique has been developed over the past two decades into a full field, non-contact and portable measurement technique that has the capability to resolve in-plane strains -2D DIC- as well as out-of-plane deformation –stereo DIC- with sub-pixel accuracy. A typical set-up for stereo DIC is shown in Figure 2.12, it comprises:

i. Two high resolution CCD cameras mounted on an adjustable rail and a tripod
ii. A computer-camera interface to allow the cameras to be triggered at a user-defined rate
iii. A computer for controlling the DIC measurement procedure and processing the images to calculate deformation

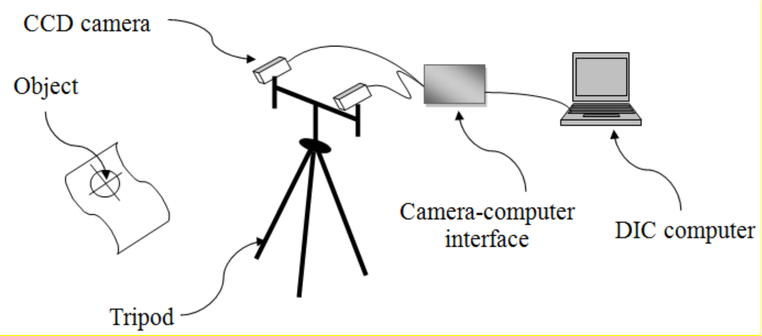

Figure 2.12: Diagram of a stereo DIC system set-up

The 2D-DIC technique is typically applied to images collected from a single camera positioned normal to the surface under investigation. A typical setup is shown in Figure 2.13.

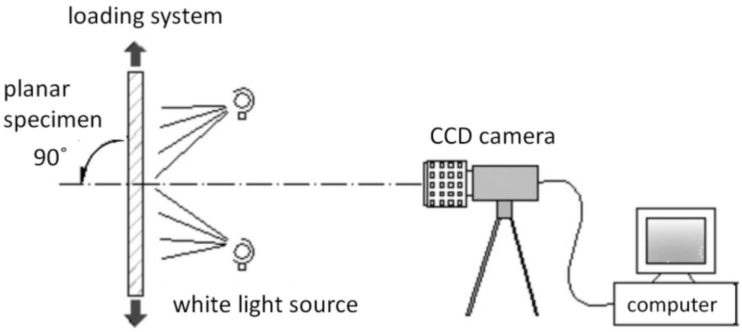

Figure 2.13: Schematic experimental setup for 2D DIC

The stages of the DIC deformation measurement process are given below and summarised by Figure 2.14.

Specimen preparation: DIC computes deformation by tracking random surface patterns. If the surface of a specimen does not contain adequate contrast then a speckle pattern needs to be applied. Some surfaces naturally possess such a surface pattern and no further surface preparation is required. The most common method for creating a speckle pattern and the method is to apply a light coat of acrylic spray paint.

Camera calibration: This stage is essential in stereo DIC because it determines the position and orientation of each camera with respect to the surface of the specimen and relates the pixel size of the object's image to the metric scale. The calibration procedure is performed by means of a calibration plate that contains a grid of dots with known sizes and distances. By considering multiple views of the calibration plate at different positions and orientations the software determines the required parameters. The calibration procedure for 2D strain measurements does not require a calibration plate. The important parameter in this case is the pixel/mm ratio which can be determined using an image of a ruler placed on the surface of the specimen.

Image acquisition: At least two images are needed to perform DIC measurements. These are typically referred to as the reference and deformed images. The former being the image taken when the specimen is subject to no load, the latter referring to the image recorded at a particular loading stage. In practice, various images are taken at different loading stages or at fixed times as a load is applied. The image acquisition rate is dependent on the application. The speed of the deformation process determines the optimal image acquisition frequency. The recent advances in the field of CCD camera imaging have led to the development of cameras that can be set to acquire images over a wide range of frequencies.

Displacement vector field computation: The acquired images are divided into sub-regions of user defined size; these are called subsets. The pattern contained in each subset is tracked to compute a displacement vector. This is achieved by applying a correlation function that searches for the best match between the subsets of the reference image pair and the deformed image pair. The resulting set of vectors from all the subsets is called the displacement vector field.

Full field strain data: In-plane strains are finally extracted by computing the gradient of the displacement vector field.

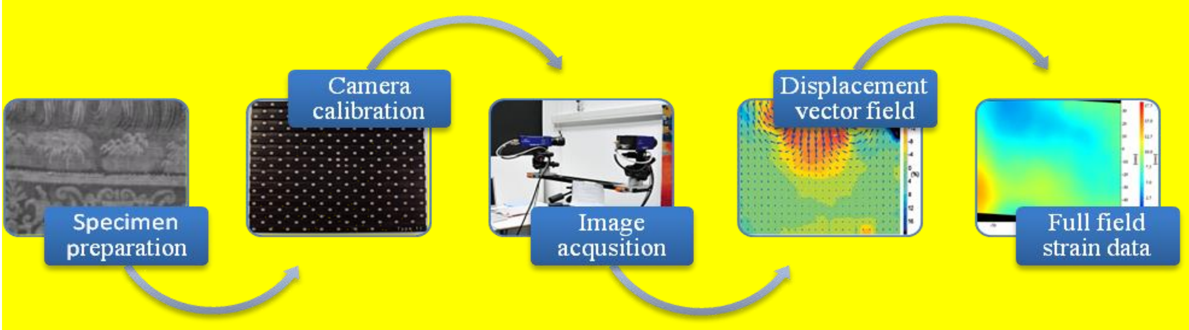

Figure 2.14: Block diagram for DIC deformation measurement stages

2.3.3 Weld plastic strain assessment techniques

Electron backscatter diffraction (EBSD)

EBSD is an SEM based electron-diffraction technique allowing automated mapping of crystal orientation. A beam of electrons is fired at a flat polished sample. Electrons that enter and back-scatter may escape the sample, at the Bragg angle. The electron that diffracts might collide into a phosphor screen, causing it to fluoresce. Kikuchi bands can be observed, which correspond to each of the lattice diffracting crystal plane. Plastic strain can be measured experimentally using EBSD with two techniques. The first technique is based on the principle that pattern quality of EBSD deteriorates with defects and dislocation density in material caused by plastic strain [61]. However, pattern quality depends on various factors so it cannot be solely linked to the plastic strain [62]. In the second technique developed by Kamaya [63], the crystal misorientation is measured using EBSD and correlated with the amount of plastic strain. Yoda et al. [64] used EBSD for damage evaluation in austenitic stainless steel in electrical power plants. A unique linear correlation was obtained between Kernel Average Misorientation (KAM) and plastic strain in both tension and compression. The technique has been successfully applied on non-welded structures where cold work introduced up to 14.4 % plastic strain [62]. Kamaya et al. showed in [65] that the technique was independent of some measurement conditions. In the study, A600 and SS304 were tested, the two material having different grain sizes. The plastic strain calibration obtained for both materials were similar which suggests that the technique is not influenced by the average grain size of the samples.

The technique was successfully applied on welds. Angeliu et al. [66] used Electron Backscatter Pattern technique (EBSP) to identify significant strains in the weld HAZ of boiling water reactor components made out of Type 304L stainless steel. Up to 10% plastic strain was assessed near the fusion line, with decreasing amount of plastic strain further away from the fusion line. Beaugrand et al. [67] used EBSD on transverse and longitudinal sections of a dissimilar joint, first, to capture the chemical composition profile as well as assess the distribution of local plastic strain around the dissimilar interface. The KAM technique was used and small plastic strain amounts were found in the “partially mixed zone”, immediately adjacent to the fusion boundary. Muránsky et al. [8] experimentally quantified welding induced plasticity (WIP) on the NeT-TG4 [57] specimen, a three-pass slot weld in a 316LN austenitic stainless steel plate using two different approaches, respectively based on indentation measured micro-hardness and EBSD measured crystal misorientation, that infer the level of plastic strain from empirical relationship acquired from material parent stress data. The two experimental techniques matched well, although some deviation in the coarse grain heat affected zone was reported. Discrepancy between EBSD and hardness WIP measurement is likely to be caused by poor grain statistics in the EBSD orientation maps. It was also mentioned that the calibration of plastic strain with KAM was performed on a 25 µm average grain size parent material. The calibration does not capture a potential change in microstructure in the weld metal or HAZ. The works mentioned outline new WIP measurement techniques that can be used as a second validation tool for FEA of weldments.

X-ray diffraction line broadening

Strains can be assessed using diffraction techniques. As it was mentioned in section 2.1.3., by using the Bragg equation, the change in lattice caused by the strain is identified. Micro-strain caused by dislocation causes broadening of the diffraction lines. Elastic deformation causes a shift in the position of the diffraction line. Plastically deformed materials may show both kind of strain giving rise to both line broadening and line shift. In [68], a three-pass slot weld specimen in austenitic stainless steel 316L was characterized using a focused high energy synchrotron radiation together with the spiral slit technique. A full map of residual strains was obtained to derive residual stresses. A novel data analysis approach was developed to overcome problems that usually arise from coarse grained specimens

Hardness

Hardness is defined as the resistance to indentation, and it is determined by measuring the permanent depth of the indentation. A fixed force and a given indenter are used, the indentation is obtained by measuring the depth or the area of the indentation. If a material has work-hardened, it will be require more load to deform, therefore the indent will be smaller for a constant load. The total deformation is measured, the elastic strain can be deduced if the elastic plastic properties of a material are known. The elastic strain is substracted form the total strain and the plastic strain is derived. Macro, micro and nano indentation can be performed, depending on the load that needs to be applied. Sample preparation is usually necessary with micro hardness test in order to provide a small enough specimen that can fit into the tester. Additionally, the sample preparation will need to remove any work hardening surface layer as well as making the specimen’s surface smooth to permit a regular indentation shape and good measurement, and to ensure the sample can be held perpendicular to the indenter.

In [7] a novel method to measure indirectly plastic strain from micro-hardness was developed. A tapered specimen of AISI 316L stainless steel was deformed in tension to introduce a known amount of plastic strain. Indentation was then performed and the hardness along the centreline of the specimen was used to create a calibration curve of micro-hardness against plastic strain. A three pass weld was then indented and the calibration was used to obtain the plastic strain in the weld. Results were compared with FE prediction of the accumulated plastic strain as well as EBSD [8]. It was found that the technique is accurate in the parent material but the technique fails to capture the change in microstructure from the weld and HAZ regions [7].

2.4 **Thermoelastic stress analysis**

2.4.1 Introduction

TSA is a full-field experimental stress analysis technique [58, 69] based on the measurement of a small temperature change (typically a few hundred mK) which arises from the elastic cyclic loading of a structure. In the case of a homogeneous isotropic material, that change can be related to the change of the sum of the principal stresses using the TSA equation

$$\frac{\Delta T}{T} = -\,K\Delta(\sigma_1 + \sigma_2) \tag{2.31}$$

where ΔT is the change in temperature, T the surface temperature in Kelvin, K the thermoelastic constant defined as $K = \frac{\alpha}{\rho C_p}$ where α, ρ and C_P are respectively the coefficient of thermal expansion, mass density and specific heat at constant pressure of the material. The derivation of this equation is fully detailed in the next paragraph. One of the main advantages of TSA is that it is non-destructive and little surface preparation is required [10]. In the case of metals, a thin layer of matt black paint is deposited on the specimen to be investigated, to improve emissivity conditions. As an elastic cyclic loading is required to use TSA, a means of applying this loading is required and this can be challenging in-situ, but options such as pneumatic shaker or magnetic shaker are being developed [70] which enable the technique to be portable. Finally, a sensitive infrared detector in the infrared camera detects the temperature and converts it into an electronic signal, which is then processed to produce a thermal image or video. TSA is a well-established stress analysis technique that has been reviewed [9, 69, 71-73] and used on applications such as defect assessment [74-79] and residual stress assessment [10, 72, 79-84], over a wide range of materials covering composites [74, 85-89] and metallic materials [82, 90] in marine [91]and aeronautics [92] and recently [70], power industry.

2.4.2 Physics behind the TSA equation

The derivation of the TSA equation can be derived from the first law of thermodynamics, as presented below. The whole derivation presented here is adapted from Greene et al. [73]. The first law of thermodynamics states that for a closed system undergoing a reversible process

$$dU = \Delta W + \Delta Q \tag{2.32}$$

where dU is an increase in the internal energy, ΔW is the work done by the system and ΔQ is the heat transferred from surroundings to the system. Equation (2.32) can be rewritten as

$$du = \Delta w + \Delta q \tag{2.33}$$

with lower case corresponding to quantities per unit volume.

Mechanical work done by external loading on the system is absorbed as strain energy stored within the deformed body. Based on a unit volume the work done can be expressed as the strain energy density.

$$dw = \sigma_{ij} d\varepsilon_{ij} \tag{2.34}$$

In thermodynamics, the entropy is defined per unit volume s as

$$dq = Tds \tag{2.35}$$

T being the absolute temperature in Kelvin. The quantity s is regarded as a thermodynamic parameter.

$$du = du(\varepsilon_{ij}, s) = \sigma_{ij} d\varepsilon_{ij} + Tds \tag{2.36}$$

Where ε_{ij} is another state variable which defines u in a process-independent manner. With elastic solids, one prefers a different set of state variables i.e. σ_{ij} and T which necessitates introducing Gibbs free energy as a thermodynamic potential. Gibbs free energy per unit volume g is defined as

$$g = u - Ts - \sigma_{ij}\varepsilon_{ij} \tag{2.37}$$

which upon differentiating becomes

$$dg = du - Tds - sdT - \sigma_{ij} d\varepsilon_{ij} - \varepsilon_{ij} d\sigma_{ij} \tag{2.38}$$

Using Equation (2.36), Equation (2.38) becomes

$$dg = -sdT - \varepsilon_{ij} d\sigma_{ij} \tag{2.39}$$

Equation (2.39) shows that Gibbs free energy g only depends on temperature and stress so it can be written

$$g = g(\sigma_{ij}, T) \tag{2.40}$$

whose differential form is

$$dg = \frac{\partial g}{\partial T} dT + \frac{\partial g}{\partial \sigma_{ij}} d\sigma_{ij} \tag{2.41}$$

and from Equation (2.39),

$$\frac{\partial g}{\partial T} = -s \tag{2.42}$$

and

$$\frac{\partial g}{\partial \sigma_{ij}} = -\varepsilon_{ij} \tag{2.43}$$

Since entropy is a thermodynamic property it can be described as a function of two independent state variables, in this cast stress and temperature hence

$$s = s(\sigma_{ij}, T) \tag{2.44}$$

$$ds = \frac{\partial s}{\partial T} dT + \frac{\partial s}{\partial \sigma_{ij}} d\sigma_{ij} \tag{2.45}$$

Combining Equation (2.42) in Equation (2.45)

$$-\left(\frac{\partial s}{\partial T} dT + \frac{\partial s}{\partial \sigma_{ij}} d\sigma_{ij}\right) = \frac{\partial^2 g}{\partial T^2} dT + \frac{\partial^2 g}{\partial T \partial \sigma_{ij}} d\sigma_{ij} \tag{2.46}$$

Using Equation (2.43) in Equation (2.45)

$$-ds = \frac{\partial^2 g}{\partial T^2} dT - \frac{\partial \varepsilon_{ij}}{\partial T} d\sigma_{ij} \tag{2.47}$$

In thermodynamics, the specific heat per unit mass at constant pressure or stress C_p

$$\rho C_p = \left(\frac{\partial q}{\partial T}\right)_\sigma \tag{2.48}$$

where ρ is the density, which is not constant as $\Delta\rho/\rho = -\varepsilon_{ij}$. By substituting Equation (2.35) into Equation (2.44) and (2.48)

$$\rho C_p = \left(\frac{\partial s}{\partial T}\right)_\sigma = T\left(\frac{\partial s(\sigma_{ij}, T)}{\partial T}\right)_\sigma \tag{2.49}$$

By partially differentiating Equation (2.42) with respect to T, i.e

$$\frac{\partial^2 g}{\partial T^2} = -\frac{\partial s}{\partial T} \tag{2.50}$$

and substituting Equation (2.50) into Equation (2.49)

$$\rho C_p = -T\frac{\partial^2 g}{\partial T^2} \tag{2.51}$$

Combining Equations (2.35), (2.46) and (2.51) gives

$$\frac{dq}{T} = \rho C_p \frac{dT}{T} + \frac{\partial \varepsilon_{ij}}{\partial T} d\sigma_{ij} \tag{2.52}$$

For an adiabatic process, $dq = 0$

$$\rho C_p \frac{dT}{T} = -\frac{\partial \varepsilon_{ij}}{\partial T} d\sigma_{ij} \tag{2.53}$$

For an isotropic material, as in the work presented in the thesis, the coefficient of linear expansion, α is defined as

$$\frac{\partial \varepsilon_{ij}}{\partial T} = \alpha \delta_{ij} \tag{2.54}$$

where δ_{ij} is Kronecker symbol, $\delta_{ij} = 1$ if $i = j$ and $\delta_{ij} = 0\ if\ i \neq j$.

Hence

$$\rho C_p \frac{dT}{T} = -\alpha \delta_{ij} d\sigma_{ij} - \alpha d\sigma_{kk} \tag{2.55}$$

Integrating Equation (2.55) over a period of time, from t_0 to t_1

$$\rho C_p \int_{t_0}^{t_1} \frac{dT}{T} = -\alpha \int_{t_0}^{t_1} d\sigma_{kk} \tag{2.56}$$

T_0 and T_1respective temperatures at t_0 and t_1

$$\rho C_p \ln\left(\frac{T_1}{T_0}\right) = -\alpha\left[(\sigma_{kk})_{t_1} - (\sigma_{kk})_{t_0}\right] \tag{2.57}$$

$$\rho C_p \ln\left(1 + \frac{\Delta T}{T_0}\right) = -\alpha \Delta\sigma_{kk}, \qquad \text{k=1,2,3} \tag{2.58}$$

$$= -\alpha(\Delta\sigma_1 + \Delta\sigma_2 + \Delta\sigma_3)$$

where σ_{kk} is the stress first invariant, σ_1, σ_2 and σ_3 are the principal stresses and ΔT the change in temperature associated with the stress change. Expanding the natural logarithm

$$\rho C_p \left[\frac{\Delta T}{T_0} - \frac{1}{2}\left(\frac{\Delta T}{T_0}\right)^2 + \frac{1}{3}\left(\frac{\Delta T}{T_0}\right)^3 - \cdots\right] = -\alpha \Delta\sigma_{kk}, \qquad \text{k=1,2,3} \tag{2.59}$$

During TSA, the change in temperature associated with the cyclic stress is very small – of the order of 100 mK – compared with the ambient temperature hence the higher order terms of the power series can be neglected, therefore

$$\rho C_p \frac{\Delta T}{T_0} = -\alpha \Delta\sigma_{kk}, \qquad \text{k=1,2,3} \tag{2.60}$$

and for plane stress isotropy, the following TSA equation can be written

$$\frac{\Delta T}{T_0} = -\frac{\alpha}{\rho C_p}(\Delta\sigma_1 + \Delta\sigma_2) \tag{2.61}$$

hence

$$\frac{\Delta T}{T_0} = -K(\Delta\sigma_1 + \Delta\sigma_2) \tag{2.62}$$

with K, the thermoelastic constant, defined as $K = \alpha/\rho C_p$.

2.4.3 Experimental considerations

Background infrared radiation

Infrared radiation is emitted by the component but also from the background and the surroundings bodies around the test. In practice there are two sources of radiation which must be minimised; the loading frame radiation as its frequency will be the same as the reference signal and the radiation of the component itself, reflected onto other surfaces such as lens or other optical devices. This effect is referred to as “narcissus” effect [73]. Both these effect can be effectively reduced in most experimental cases, and in the experimental work presented in the thesis, by shielding the experiment using black cloths, or material with low reflectivity in the infrared range

Specimen preparation

Any component subjected to a change in surface stress will exhibit a change in surface temperature. Infrared radiation will be emitted regardless of its surface condition. However, the magnitude of the infrared emission from the surface of the component is greatly increased if the surface has a high emissivity in the IR wavelength range. To reach the highest emissivity as possible, a thin layer of matt black paint is added on the surface. Substantial previous work has been carried out on a selection of paint for the purposes of IR thermography. In most TSA studies, RS matt black paint from RS components has been used and a detailed characterisation was carried out in [93] It has recently emerged that a change in the formula of RS matt black has occurred , reducing the adhesion to the surface of components and providing a significantly lower emissivity, which renders it unsuitable for quantitative TSA studies. To find a suitable replacement, a number of readily available alternative black paints were tested for surface finish and adhesion in [94] and the most suitable paint was identified as Electrolube EMBP400 matt black [70].

The sensitivity of TSA to surface preparation prior to painting was established in [70], where four levels of surface preparation were investigated. The first level involved a wire brush to remove debris whereas the remaining three levels firstly involved a wire brush and then 80, 120 and 180 grit SiC papers, respectively giving a progressively smoother finish. TSA was applied on the pipe and K was derived etermined for each surface finish. The first level of surface preparation provided results with a large standard deviation and more than 20% off compared to the literature value, whereas the three remaining levels provided results less than 6% off from each other and from the K value from the literature. From this experiment, it can be concluded abrasion is required to remove corrosion, however, the effort required to provide smoother finishes in Levels 3 and 4 did not provide any discernible difference with Level 2. Hence, the use of a wire brush and one type of SiC grit paper is recommended for TSA surface preparation.

Adiabatic conditions

TSA theory assumes adiabatic behaviour. It is therefore important to address what load frequency is acceptable for adiabatic material response. An adiabatic response requires that a balance be maintained between the thermal and mechanical energy. The minimum loading frequency to accomplish this can depend on the thermal conductivity and stress gradients in the structure. Most metals can be safely considered adiabatic for frequencies above 2Hz, but other factors such as the coating and system electronics might introduce concern below 10Hz. Higher loading frequencies usually can improve the detail in the data since heat transfer is minimized. Two potential issues arising from the frequency and paint thickness are addressed. Thermal lag is caused by the insulating effect of the paint coating. An increase in paint coating thickness will result in a smaller thermoelastic response at the paint surface than at the specimen surface. Thermal drag-on is a phenomenon related to both paint thickness and loading frequency. As the frequency increases, the wavelength decreases hence there is less input into the coating. The heat will not flow into the surface coating sufficiently quickly to maintain the temperature for accurate thermoelastic response to be recorded [10].

2.4.4 Data acquisition and processing

Lock-in technique for noise reduction

An infrared detector converts the incident radiant energy into electrical signals. The voltage output from a photon detector is proportional to the rate of incident photons. Planck’s law relates the emittance of a black body to the wavelength and the temperature of radiating body by

$$\phi_\lambda = \frac{2c}{\lambda^4}\left(\frac{1}{\exp(hc/\lambda kT) - 1}\right) \tag{2.63}$$

ϕ_λ is the spectral radiant photon emittance c the speed of light, λ the wavelength of light, h Planck’s constant, and k Boltzmann’s constant.

A lock-in analyser is employed as the signal-processing unit that extracts the thermoelastic information from the inherently noisy detector output signal. A lock-in analyser is presented Figure 2.15 as a series connected signal mixer and a low pass filter. The analogue instrument mixes a reference signal at the load frequency with the detector output to extract the actual thermoelastic response. The reference signal can originate from a function generator, load transducer, strain gauge, or any other source that is in phase with the loading frequency.

Mixing two signals of distinct frequencies f_1 and f_2 produces an output signal with frequency content of $f_1 + f_2$ and $f_1 - f_2$. The output signal from the photon detector will include the actual thermoelastic response at the reference frequency f_r and other broadband frequencies due to the inherent noise. Mixing the thermoelastic response with the reference frequency will cause the resultant output to be a direct current (DC) signal $(f_r - f_r = 0)$ and a signal at twice the original frequency $(f_r + f_r = 2f_r)$. Noise components are also mixed with the reference frequency, but their contribution to the DC signal is negligible. The low-pass filter of the lock-in analyser is used to recover the DC signal from the mixed output. The filter removes the portion of the signal above a cut-off frequency. Some detector noise that is close to the reference frequency will pass through the filter. The lock-in analyser then normalizes the DC signal from the reference signal amplitude to a value proportional to the actual measured thermoelastic output.

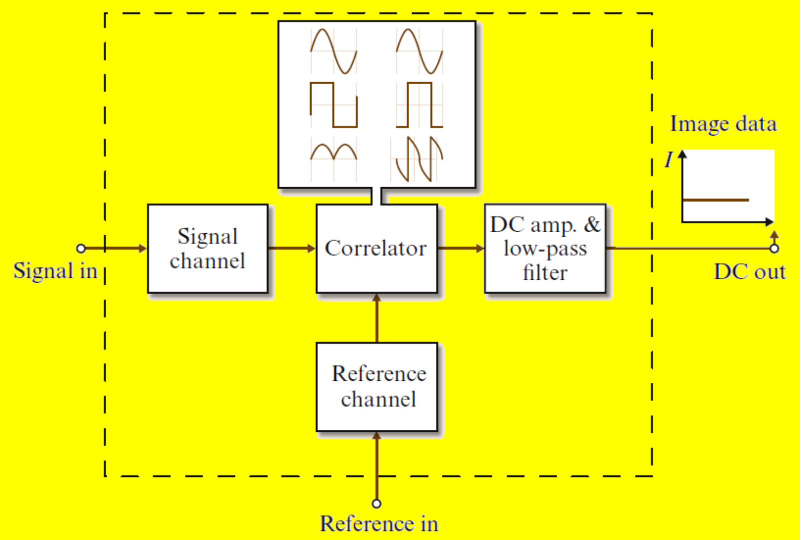

Figure 2.15: Schematic of simplified lock-in amplifier [73]

Phase and magnitude of the signal

Lock-in analysers used commonly in thermoelastic systems separate the detector output into two components: one in-phase and the other 90° out of phase with respect to the reference signal. The adiabatic structural response is expected to be in phase with the reference loading frequency. If heat conduction occurs in regions of high stress gradients, or if the loading frequency is insufficient for an adiabatic response, a phase shift from the reference frequency will occur and will be apparent as an out-of-phase detector signal. A quick confirmation of adiabatic response is to check for the absence of any out-of-phase detector signal.

Spatial resolution and gauge volume

In the work presented, a Cedip system is used which consists in a starring array devices is used. Starring array devices are similar to conventional CCD employed in video cameras. A planar imaging array is mounted behind a lens assembly. The field of view of lens-detector assembly depends on the optical magnification of the lens system, the stand-off distance between the lens and the component under observation and physical dimension of the detector array. In the work presented in the thesis, the pixel resolution is 320 x 256 with a pixel pitch of 30 µm. TSA is a surface technique, for adiabatic conditions the response is directly related to the surface stress and variation through the thickness cannot be picked up. For thin specimen, a plane stress condition is reached so the stress in the direction perpendicular to the surface can be neglected. More details on the system used can be found in Appendix C.

In the work present work, microstructural changes are considered. It should be noted that the spatial resolution is of the order of magnitude of a pixel hence microstructural changes will be averaged over an area of 1 mm². Grain size is typically a value averaged over a range of area hence TSA spatial resolution does not hinder grain size effects. However, if local microstructural changes were to be considered, i.e. vacancies, cavities, precipitates, twins and interstitial carbons, their effect would be averaged out over a pixel.

2.4.5 TSA as a plastic strain assessment technique

Mean stress effect

The mean stress effect is defined as temperature dependence of the elastic properties at room temperature. For the small changes in temperatures associated with the thermoelastic effect, *K*, the thermoelastic constant, is assumed to be a material constant that is independent of the stress field. However, *K* is a function of the coefficient of linear expansion, α that has been shown to be stress dependent as follows:

$$\left(\frac{\partial \alpha}{\partial \sigma}\right)_T = \frac{\partial}{\partial \sigma}\left[\left(\frac{\partial \varepsilon}{\partial T}\right)_\sigma\right]_T = \frac{\partial}{\partial T}\left[\left(\frac{\partial \varepsilon}{\partial \sigma}\right)_T\right]_\sigma \qquad 2.64)$$

Therefore if $= \left(\frac{\partial \sigma}{\partial \varepsilon}\right)_T$, differentiating by parts gives

$$\left(\frac{\partial \alpha}{\partial \sigma}\right)_T = -\frac{1}{E^2}\left(\frac{\partial E}{\partial T}\right)_\sigma \qquad (2.65)$$

Equation (2.65) shows that α will be stress dependent for materials whose elastic properties are sensitive to changes in temperature. This also implies that the thermoelastic response of such materials will be dependent on the mean stress of the applied stress cycle and cannot be assumed to be constant.

If the material's Young's modulus is high and the dE/dT term is small then the mean stress will have a negligible effect on the thermoelastic response. The practical significance of the mean stress effect for the materials given in Table 2.1 can be established by calculating the percentage of the material's yield stress, required to introduce an error of 5% by neglecting the mean stress dependence was examined. Calculations were carried out for 4340 steel, an aluminium alloy and a titanium alloy with values of 29%, 17%, and 5% and obtained respectively. In practical terms this analysis shows that, at least in the case of steels and aluminium, the mean stress effect will be effectively hidden within the ambient noise of the measurements (approximately 5%). The effect is shown to be significant in the case of the titanium alloys where a mean stress that is just 5% of the yield stress is required to introduce an error of 5% in the thermoelastic measurements. As for 316L stainless steel, dE/dT is considered negligible compared to $1/E^2$. Using Equation (2.65) α – hence K- is assumed constant with stress and the TSA equation for material with no mean stress effect can be used for 316L stainless steel.

Table 2.1: Material properties for three high strength alloys (adapted from [10])

Material	E (MPa)	dE/dT (MPa/K)	σ_y (MPa)
4340 steel	210×10^3	-56.7	304
Al-2024	72×10^3	-36.0	197
Ti-6Al-4V	120×10^3	-61.8	430
AISI 316L	193×10^3	≈ 0 [11]	250

Plastic strain influence on the thermoelastic constant

Rosenholtz et. al. [95] and Rosenfield et. al. [96], observed and studied the influence of plastic straining on the coefficient of thermal expansion and in [96] it was suggested that the effects of plastic straining arising from compressive loading are greater than plastic straining effects arising from a tensile loading. The origin of this phenomenon was not explained in [96] but is worth mentioning within the framework of the development of a PSA TSA based technique. In the present work, the focus is on tensile plastic strain as those are of concern in structural integrity. However, it would be interesting in further works to study the origin of the difference and quantify it.

Since the thermoelastic constant K of a material is a function of the coefficient of thermal expansion, the density and the specific heat, the plastic straining will influence K. Equation

(2.31) can be used in steels, it can be seen that, for a known stress state, a change in K can be measured using TSA. Quinn et. al. [11] performed TSA tests on steel specimens involving strain levels of 0%, 5%, 6% and 8% to assess the influence of plastic strain on K. A small but repeatable change in K was observed. In [58], a curved beam component was manufactured out of E1NA steel and plastic strain was assessed using TSA. A stress-free component of the same material and same shape was manufactured for reference. It was found that the thermoelastic response is different and larger in the areas of compression, which is consistent with results from [95] and [96].

Finally, in [10], the influence of compressive and tensile plastic strain was studied on three materials: two grades of aluminium, AA2024-T351 and AA7085-T7651 and stainless steel. Dogbone shaped specimens were manufactured to allow compression and tension without buckling or excessive deformation. Compressive and tensile loading were applied to the 316L specimens to obtain specimens with respectively -15%, -10%, -5%, 0%, 5%, 10% and 15% plastic strain. The results are plotted and presented in Figure 2.16 and it can be seen the thermoelastic constant increased with tensile plastic strain up to 6-8% and decreased with compressive plastic strain, as reported in [96]. It can be noted that in this graph, the normalised thermoelastic constant is used. This allows comparing measured thermoelastic constants at different levels of plastic strain to the thermoelastic constant measured for 0% plastic strain, i. e. K_0. The graph presented in Figure 2.16 is also used here to introduce two concepts: intercept and gradient of the linear interpolation. Those will be used in Chapter 5, to analyse results from different microstructures and compare them with the present literature. The blue line plotted on top of the values represents the linear interpolation of the data. In this case the intercept is 1 and the gradient is 0.0037. The intercept represents the ratio of the thermoelastic constant measured at 0% plastic strain compared to the theoretical value, and should equal 1. The gradient denotes the influence of plastic strain on the thermoelastic constant.

From the results from literature, the hypothesis that the dislocation density, related to the plastic strain level, is responsible for the change in thermoelastic constant. This hypothesis has not been validated experimentally or theoretically and will be commented in the present work.

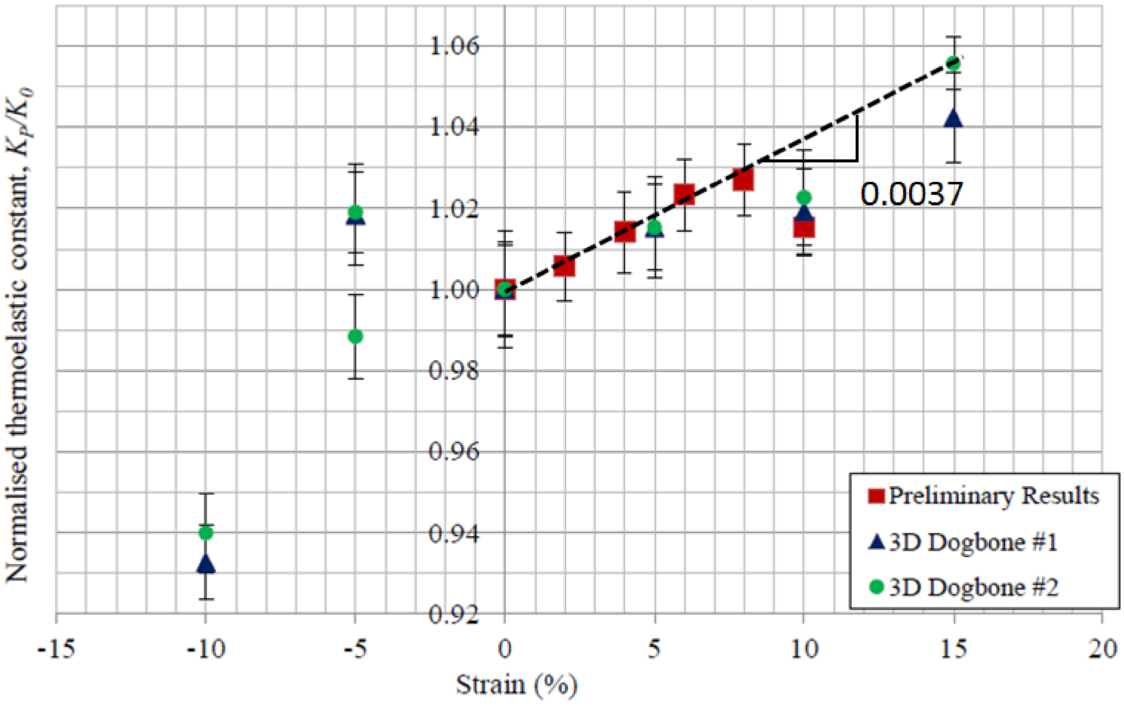

Figure 2.16 : Change in normalised thermoelastic constant K_p/K_0 with varying plastic strain (%) [10]

Physics behind TSA PSA

The influence of plastic strain on α, and thus K was observed experimentally in the works cited above. These works are at the origin of the TSA PSA technique development. The underlying physics the technique is based on can be understood from an atomic level, as explained below.

The thermal expansion strain is calculated as a function of temperature and can be expressed as:

$$\varepsilon^{th} = \frac{\Delta l}{l_0} = \alpha \, \Delta T \tag{2.66}$$

where Δl and l_0 represent the change in length and the initial length of a specimen respectively, induced by a change in temperature, ΔT. From an atomic perspective, thermal expansion is reflected by an increase in the average volume of a unit cell, which is a consequence of the minimisation of the potential energy presented in Figure 2.17.

The potential energy corresponds to the energy required to move two atoms to a different interatomic distance. An increase in temperature would cause the vibrational energy of the atoms to rise which leads to an increase in the average of the interatomic distance.

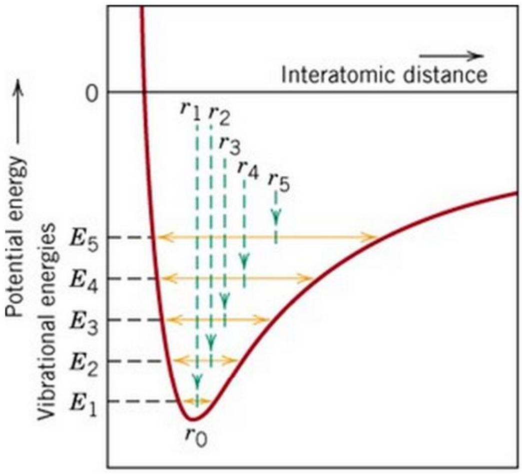

Figure 2.17: Plot of atomic energy versus interatomic distance demonstrating the increase in interatomic separation with temperature [17]

At dislocation edges, atoms are not bonded to the maximum number of nearest neighbours, as depicted in Figure 2.18 and therefore, the energy required to separate this atom from others is lower than for an atom bonded to the maximum number of nearest neighbours. Since the atomic bonding energy is lower at a dislocation, the vibrational energy is higher and so is the local value of α. Since K is directly linked to α, an increase in α would lead to an increase in K and a change in the thermoelastic response. This demonstrates why, in theory, the effect plastic deformation effects can change the thermoelastic response. It can be noted that, since boundaries act as dislocations, and hypothesis is that the dislocation density influences the thermoelastic constant was stated, fine grained components of the same material will have a larger K value compared to coarse grained specimens. It must be mentioned that it may be possible that other microstructural changes such as vacancies, cavities, precipitates, twins, interstitial carbon would also influence the thermoelastic response, but their influence is not examined in the present work, furthermore there is no literature discussing specifically these effects on the thermoelastic constant.

The technique has not yet been tested on weldments, and the aim of the RESIST project is to develop a methodology to assess the capability of the technique to quantify small amounts of welding induced plastic strain.

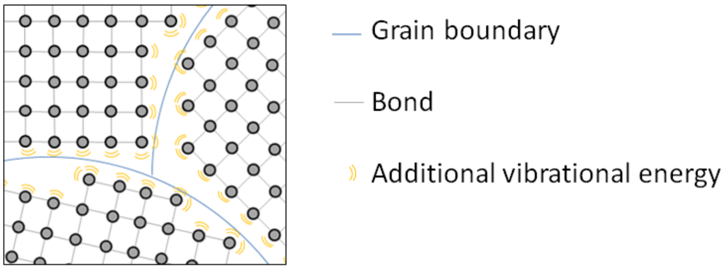

Figure 2.18: Schematic diagram of grain boundaries

2.5 **Summary**

Weld residual stresses are of primary importance in many area of industry, and in particular in the nuclear industry as they increase the risk of SCC in corrosive environment for susceptible materials and the brittle fracture of ferritic steel welded structures.

Residual stresses are typically hard to assess as they are not visible and cannot be measured directly, but through the derivation of another quantity, such as strain, lattice spacing, or ultrasonic properties. Moreover, in nuclear power plants, the structures containing residual stresses can only be accessed during an outage of the plant, and no destructive measurement can be performed. For these reasons, the FE technique is used to assess the structural integrity of welds in nuclear power plants.

FE modelling of welds is a challenging task, as the process combines different area of physics and many assumptions and simplifications need to be applied to the model to maintain reasonable computational times. Guidelines of reasonable assumptions can be found, such as plasticity model to use, geometry simplifications and heat source modelling. Calibration of the heat source and the validation of the model by comparing the predictions with measurements are essential to have confidence in the results provided by FE simulations.

The validation is usually performed by comparing the residual stresses predictions with residual stresses measurements. However, plastic strain also plays an important role in SCC, as well as fast fracture. Moreover, it has recently been demonstrated [7] that plastic strain can help validate the plasticity model, hence provide better – if less conservatism is sought – residual stress predictions.

TSA is a full field, non-destructive technique that can assess plastic strain in non-welded materials [58, 82]. If the technique can also assess plastic strain that arise from the welding process, a new, quick, non-destructive tool to gain confidence in the FE weld modelling prediction would become available.

Chapter 3: The influence of microstructural changes on the thermoelastic constant

3.1 Introduction

It has been proposed that the TSA PSA technique quantifies the plastic strain induced in a material through the measurement of the variation of the thermoelastic constant [11]. During welding, other microstructural changes can occur and may affect the thermoelastic response. Therefore, the combined influences of microstructural changes and plastic strain need to be decoupled if the plastic strain is to be measured by TSA PSA in welds. A material microstructure can be significantly transformed by the welding process. Microstructural changes can include grain growth, as shown in Figure 3.1, and SSPT in ferritic steels, e.g. SA508 Gr.3 Cl.1, as described in the previous chapter, section 2.1.

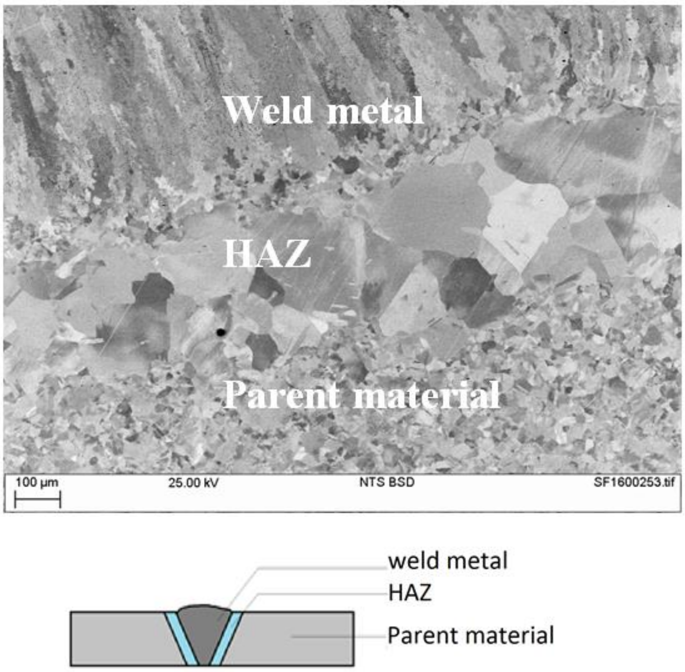

Figure 3.1: Microstructure in AISI 316L austenitic stainless steel bead-on-plate (top) and location of the areas in a butt-welded joint (bottom).

During the TSA PSA process, the thermoelastic constant of the welded joint is compared with the thermoelastic constant of the same material with known amount of plastic strain. If different microstructures or phases are contained within a welded joint, then the material properties C_p, ρ and α may vary within a region, which will result in a change in the thermoelastic response. Therefore it is necessary to establish the thermoelastic constant of the modified microstructure and/or each phase. If the influence of the microstructural changes on K is negligible in comparison to the change in K due to plastic straining, then the thermoelastic constant of the base material can be assumed and any changes in thermoelastic response in the vicinity of the weld can be associated with plastic strain. This response can then be calibrated to establish the amount of plastic straining experienced. If the microstructure has an influence on *K*, the dependence of *K* on plastic strain with grain size should be quantified to inform the application of the technique.

Grain size is of particular concern, as the technique is based on the increase of the coefficient of thermal expansion with energy associated with dislocation density [17]. Since grain boundaries and plastic strain are dislocations, they are both related to the dislocation density, it is expected that both grain size and plastic strain influence the coefficient of thermal expansion hence *K*.

To establish if changes in grain size or SSPT induced by the welding process have an effect on the thermoelastic response, it was necessary to design a series of experiments where specimens of known microstructure and phase were tested. It was decided to heat treat the specimens to obtain the required microstructure throughout the specimen. Firstly the dimensions of the specimens were defined by assessing the load required to provide a measurable stress induced temperature change for the TSA. CCT curves were used to establish the heat treatments necessary to obtain the required microstructure representative of the phases obtained in material after welding, such as weld region, HAZ and parent material in SA508. Micrographs were taken to confirm the microstructure. Finally TSA was performed on all the specimens and the thermoelastic constant was established.

3.2 Test specimen material and dimensions

The steels of interest in this report are both used in the nuclear industry: austenitic steel AISI 316L and ferritic steel ASTM SA508 Gr.3 Cl.1. The chemical composition of the AISI 316L sheet used was measured at TWI Ltd and is presented in Table 3.1.

Austenitic steels have good corrosion resistance in most environments and high service temperatures. Elements that promote the stabilisation of austenite, most notably nickel, are added to these steels in large quantities (generally over 8wt. %). Other austenite stabilisers are C, N and Cu. Series 3xx are based on the composition of iron, 6 to 20 % Ni and 18 to 30 % Cr. Type 316 substitutes approximately 2% Mo for a nearly equal amount of Cr to improve pitting corrosion resistance and the L grade, from low carbon grades (316L), has been widely used in applications where intergranular attack and stress corrosion cracking are a concern [97].

Ferritic steel specimens used in this report were taken from specimens of the NeT project [98], and the composition for this material is [15] presented in Table 3.2. ASTM SA508 Gr.3 Cl.1 is a low alloy steel and a key material in nuclear power plant components, such as pressure vessels, compressors and steam generators [99, 100] due to its high fracture toughness over the reactor operating transients [101].

C	**Si**	**Mn**	**P**	**S**	**Cr**	**Mo**	**Ni**	**Al**	**As**
0.020	0.49	0.92	0.032	<0.002	16.6	2.04	10.2	<0.01	<0.01
B	**Co**	**Cu**	**Nb**	**Pb**	**Sn**	**Ti**	**V**	**W**	**Ca**
0.002	0.20	0.45	0.02	<0.002	0.010	<0.005	0.08	0.05	<0.001

Table 3.1: Nominal chemical composition of the AISI 316L strip (and tapered) specimens (wt.%) (Fe=balance)

C	Si	Mn	Ni	Cr	Mo	V	Al	Cu	N
0.2	0.25	1.4	0.8	0.2	0.5	0.003	0.003	0.04	100 ppm

Table 3.2: Nominal chemical composition for SA508 Gr.3 Cl.1 steel (wt.%) [15] (Fe=balance)

The specimen dimensions were selected so that they fulfil the following conditions: Rectangular shape so that the specimens could be loaded in uniaxial tension to give a known uniform applied stress so that the thermoelastic constant can be established from the following expression:

$$K = -\frac{\Delta T}{T}\frac{1}{\Delta(\sigma_1+\sigma_2)} \tag{3.1}$$

where T is the surface temperature and $\Delta(\sigma_1+\sigma_2)$ denotes the change in the sum of the principal stresses. An infrared detector measures the temperature and change in temperature ΔT of the component under a linear elastic cyclic loading. The loading is uniaxial tension so the first principal stress is known, K can be derived and compared with reference values.The specimen microstructure should be uniform through the thickness;

1. The stress induced temperature change obtained from TSA should be above the noise threshold of the infrared detector used;
2. The maximum load applied to the specimen should correspond to a stress lower than the yield stress;
3. The specimen should fit in the servo-hydraulic tensile test machine and in the furnace.

A thickness of 2 mm was considered thin enough to limit the effect of conduction in the specimens so the heat treatment of the specimen does not produce large variation in microstructure through the thickness. Micrographs through the thickness of the specimen were taken to verify this aspect and are presented in Section 3.1. The servo-hydraulic tensile test machine grip can support area of 50 x 50 mm and the thickness can vary from 0 mm to 15.75 mm. The specimen's length was set to 200 mm to allow 50 mm at the top and bottom of the specimen to be gripped while providing sufficient area for imaging. The width of the specimen was set to 30 mm as the width of the specimen should be smaller than 50 mm and 30 mm allows sufficient surface area for imaging. Specimen dimensions were set to 200 x 30 x 2 mm in order to fulfil condition one, two and four.

Some preliminary calculations were required before applying the tensile elastic cyclic loading to the specimens, which involved conditions three and four. The noise equivalent temperature difference (NETD) of the Cedip Silver 480M system is 15.56 mK, and can be reduced to 4 mK with the lock-in technique for TSA [10]. Thermoelastic constants of $K_{316L} = 4.63 \times 10^{-12}\mathrm{Pa}^{-1}$ [10] and $K_{SA508} = 3.47 \times 10^{-12}\mathrm{Pa}^{-1}$ [46] for AISI 316L and SA508 respectively are used in the calculation. An error of 4 mK corresponds to an error of 2.88 MPa for AISI 316L and 3.81 MPa in SA508. Therefore a temperature change of 100 mK would reduce the NEDT to an error of 4% in the measurements. Since the loading is uniaxial, Equation **(3.1)** can be re-written as $\Delta T = KT_0\Delta\sigma_1$ and the requirement becomes $|KT\Delta\sigma_1| \geq 100$ mK.

From [10], $K_{316L} = 4.63 \times 10^{-12}\mathrm{Pa}^{-1}$ and T_0 can be estimated at 300 K. Therefore $|\Delta\sigma_1| \geq 72$ MPa. The cross-section area A of the specimen is 60 mm², so the minimum load amplitude to achieve a change in temperature of 100 mK is $\Delta P_{min} = 4.32$ kN. Condition four is fulfilled if $\Delta\sigma_1 < \sigma_Y$. The yield strength for AISI 316L and the different phases of SA508 are presented in Table 3.3. Since two materials are tested using the same specimen geometry, the minimum yield strength should not be reached. The maximum load that can be applied to the specimen before the material yields is $P_{yield} = 15$ kN based on a 250 MPa yield stress measured by Robinson in [10] for AISI 316L. Stress strain curves will be obtained and presented for each material and heat treatment in Chapter 4.

The elastic cyclic loading for TSA testing has a mean load of 7.5 kN and amplitude of 9 kN, which correspond to a change in the principal stress of 150 MPa. From the values of the cyclic loading, material parameter and ambient temperature, a change in temperature $|\Delta T| \geq 200\ \mathrm{mK}$ can be expected. The load is applied at a frequency of 10 Hz as advised in guidelines defined in [10], where frequencies between 5 Hz and 15 Hz are recommended for paint thicknesses between 15 µm and 25 µm (the specimens were painted according to the painting guidelines to obtain this range of paint thickness, but the paint thickness was not measured). It was shown by Robinson [10] that frequencies larger than 25 Hz can have an effect on the thermoelastic response. As the loading frequency increases, the spatial wavelength decreases, as a result there is less heat input into the coating, and the heat does not flow into the surface coating sufficiently quickly to maintain the temperature change for accurate thermoelastic measurements to be recorded [10].

For each material, four sets of three specimens were created. A 550 x 600 x 2 mm hot rolled sheet of AISI 316L was cut using water jet cutting into 200 x 30 x 2 mm specimens. Water jet cutting was selected to avoid any distortion in the specimens. No surface treatment was performed at this stage and this corresponds to the as received condition referred to as “AR”. Ferritic steel SA508 Gr.3 Cl.1 is hard to source as it is usually ordered in large quantities. It was therefore not possible to order a small quantity of virgin material to manufacture the strip specimens. Nonetheless, a welded specimen from the NeT project [46] was provided so that strip specimens of identical dimensions to those used with the AISI 316L stainless steel were EDM (Electro Discharge Machining) cut from the bulk material of the welded plate, 30 mm away from the weld to avoid the heat affected zone. The heat treatments performed. The EDM process was selected to minimize distortion when cutting the specimen. Sections through the thickness of the specimens were taken and observed near the surface to identify influence of the cutting on the local microstructure. These are presented in paragraph 3.4.

Material (phase)	316L (austenite)	SA508 (ferrite)	SA508 (bainite)	SA508 (martensite)
Yield strength (MPa)	250	418	420	863

Table 3.3: Yield strength values for 316L [10] and SA508 Gr.3 Cl.1 [46] at 25 °C

3.3 **Heat treatment**

The maximum temperature the furnace can reach is 1150 °C, and the cooling rates range from 0.1 °C/hr to natural cooling in the furnace, around 100 °C/hr. It is also possible to water quench in order to achieve higher cooling rates and harder microstructures in ferritic steels. The heat treatments selected here are compared to the thermal history of a weld in section 3.3.1 in Table 3.4 and in section 3.3.2, Table 3.5 respectively for AISI 316L and SA508. The heat treatments performed in the air furnace were performed at TWI Ltd by the author and Roger Barnett. The vacuum furnace heat treatments were performed at TWI Ltd by James Kern.

3.3.1 Austenitic steel

The heat treatments were selected to replicate three different weld microstructures. A set of three reference specimens was kept to represent the parent material. A second set of three specimens was soaked at annealing temperature for 2 minutes in an air furnace and then air cooled. The third set of three specimens was soaked at annealing temperature for 83 minutes in a vacuum and cooled at a rate of 100 °C/hr in the furnace to avoid oxidation layer to form. The heat treatments allow different recrystallization time, hence different average grain size. The cooling rate of 100 ^{o}C / hr is not realistic in a weld but can be experienced in the case of a stress relief or annealing heat treatment. The heat treatments used to produce the three different microstructures are summarised in Table 3.4. Thermocouples were attached to one specimen of each condition set and the thermal histories can be seen in Figure 3.2. During the heat treatment of the air cooled specimen (top of Figure 3.2), the specimen temperature rises up to the furnace temperature of 1150˚C. After 2 minutes at annealing temperature, the specimen is taken out of the furnace and the specimen temperature decreases abruptly. As for the furnace cooled specimen, the temperature increase is similar to that of the air cooled specimen, but cannot be seen on the graph. After about 4 000 s, the furnace is set to cool down at a rate of 100˚C/hr, which is the cooling rate that can be seen on the graph on the bottom of Figure 2.11.

Specimen type	**As Received (AR)**	**Air Cooled (AC)**	**Vacuum Furnace cooled (VF)**
Environment	-	Air	Vacuum
Soaking time at $T_{anneal} = 1050^{\circ}C$)	-	2 minutes	81 minutes
Cooling method	-	Air cooled	Furnace cooled
Cooling rate	-	-	100 ^{o}C / hr
Condition to be replicated	Parent material	HAZ	Heat treated material

Table 3.4: Heat treatments applied to the 316L specimens

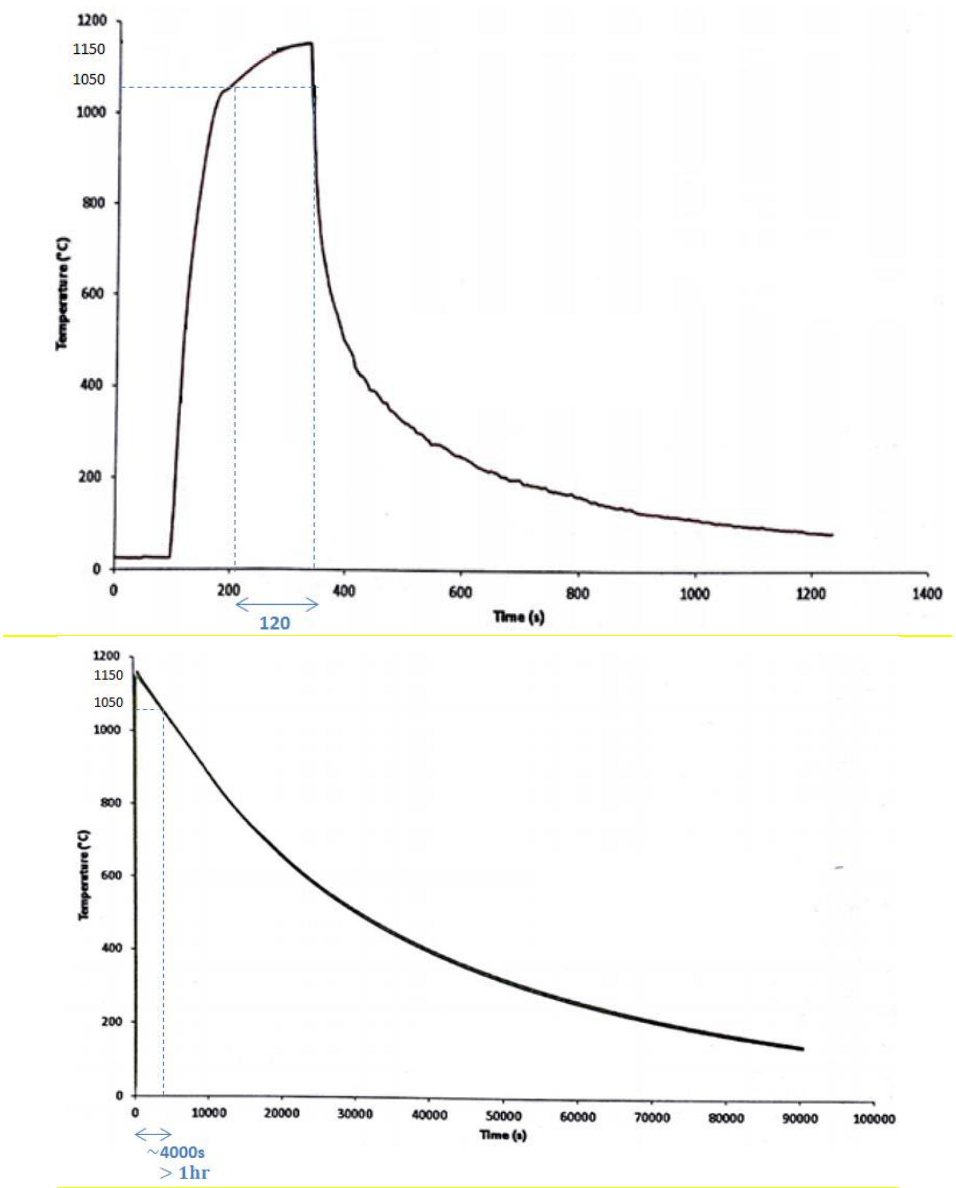

Figure 3.2: Thermal histories of AC (top) and VF (bottom) specimens

3.3.2 Ferritic steel

In SA508, mixtures of ferrite, retained austenite, martensite and bainite represent one aspect of microstructure variation that can be obtained after heat treatment at room temperature. A change in the coefficient of thermal expansion between different phases would produce a change in *K*. The coefficient of thermal expansion α varies significantly between austenite and other phases, such as martensite, ferrite etc. due to the change in atomic crystal structure as mentioned in 2.1.1. As an example, in SSPT simulations by O'Meara [102], the coefficient of thermal expansion at room temperature used are

$$\alpha_{austenite} = 2.42 \times 10^{-5}\,°C^{-1}$$

$$\alpha_{bainite} = \alpha_{ferrite} = \alpha_{martensite} = 1.49 \times 10^{-5}\,°C^{-1}$$

At room temperature, only small quantities of meta-stable austenite can be present in a ferritic steel as austenite transforms into other phases during cooling [15] , as can be seen in the CCT diagram presented in Figure 3.3 [18] hence the large discrepancy between coefficient of thermal expansion between austenite and other phases should not affect the overall change in *K* for this material. However, the phases have different material properties and any variation in *K* needs to be known to inform the application of TSA PSA in SA508. According to the CCT diagram, a heat treatment corresponding to the line numbered one would create mainly bainite, the heat treatment corresponding to line numbered two would create martensite and the heat treatment corresponding to the lined labelled three should create ferrite and carbides.

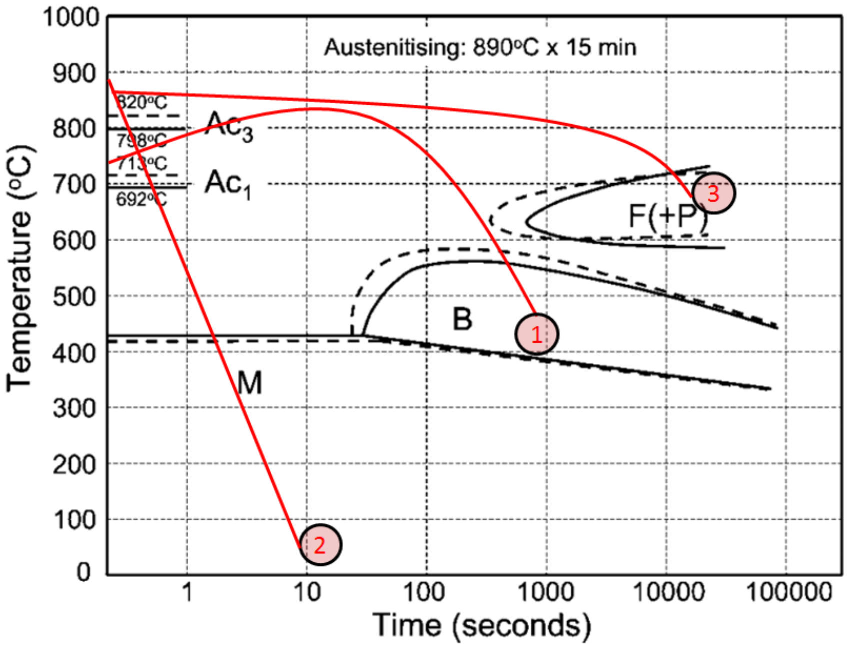

Figure 3.3: Curves of CCT for class 1 (solid lines) and class 2 (dotted lines) of grade 3 SA508 Gr.3 Cl.1 reactor pressure vessel [18]. In red, heat treatment selected.

To ensure different phases would be obtained from the selected heat treatment, simulations of phase proportions for a given thermal history were obtained from O'Meara [102]. The change in phase is modelled using the Li equation [103] for the diffusive transformation and is time dependent. The displacive martensite formation is modelled using the Koistinen-Marburger equation [104], which is only a function of temperature, the time is not taken into account as the transformation occurs almost instantaneously [105]. It should be mentioned that although bainite formation is considered as displacive [12] it is controlled by carbon diffusion and is therefore time dependent and modelled as such in [102]. The corresponding heat treatment, heating temperature, cooling rate and predictions of phase proportion are detailed in Table 3.5. Thermocouples were attached to one specimen of each condition set and the thermal histories can be seen in Figure 3.4. The lines representing the heat treatments presented in Figure 3.3 are approximation, however, the order of magnitude of the specimens at required temperatures can be observed in Figure 3.4: the plot at the top represents the temperature of the Mix specimen, which corresponds to the line labelled 1 in Figure 3.3.The temperature of the specimen is above 700˚C for 200 s and then cools down from 800˚C to 500˚C within 10 s and from 500˚C to 300˚C in approximately 100 s. According to Figure 3.3 the microstructure will contain bainite. The plot in the middle represents the temperature of the Mar specimen, which corresponds to the line labelled 2 in Figure 3.3. The temperature of the specimen is above 890˚C for 180 s and then cools down within 10 s which ensure the fully martensitic microstructure. The plot at the bottom represents the temperature of the Fer specimen, which corresponds to the line labelled 3 in Figure 3.3.The temperature of the specimen is above 890˚C which is the austenitising temperature for 10000 s which is significantly longer than 15 min, as required in Figure 3.3 and then cools down from 800˚C to 500˚C within 20 000 s and from 500˚C to 300˚C in 20 000 s. The long-time above austenitising temperature allows reaching the ferrite phase as seen in Figure 3.3.

Specimen type	**As Received (AR)**	**Mix of phases (Mix)**	**Ferrite and precipitates (Fer)**	**Martensite (Mar)**
Environment	-	Air	Vacuum	Air/Water
Heat soak temperature	-	800 ºC	1150 ºC	1150 ºC
Cooling method	-	Air cooled	Furnace cooled	Water quenched
Weld area reproduced	Parent material	CGHAZ	Parent material, ICHAZ	FGHAZ
Phases produced [102]	-	60% bainite, 30% martensite, 10% ferrite	100% ferrite	100% martensite

Table 3.5: Heat treatments applied to the SA508 specimens and produced phases

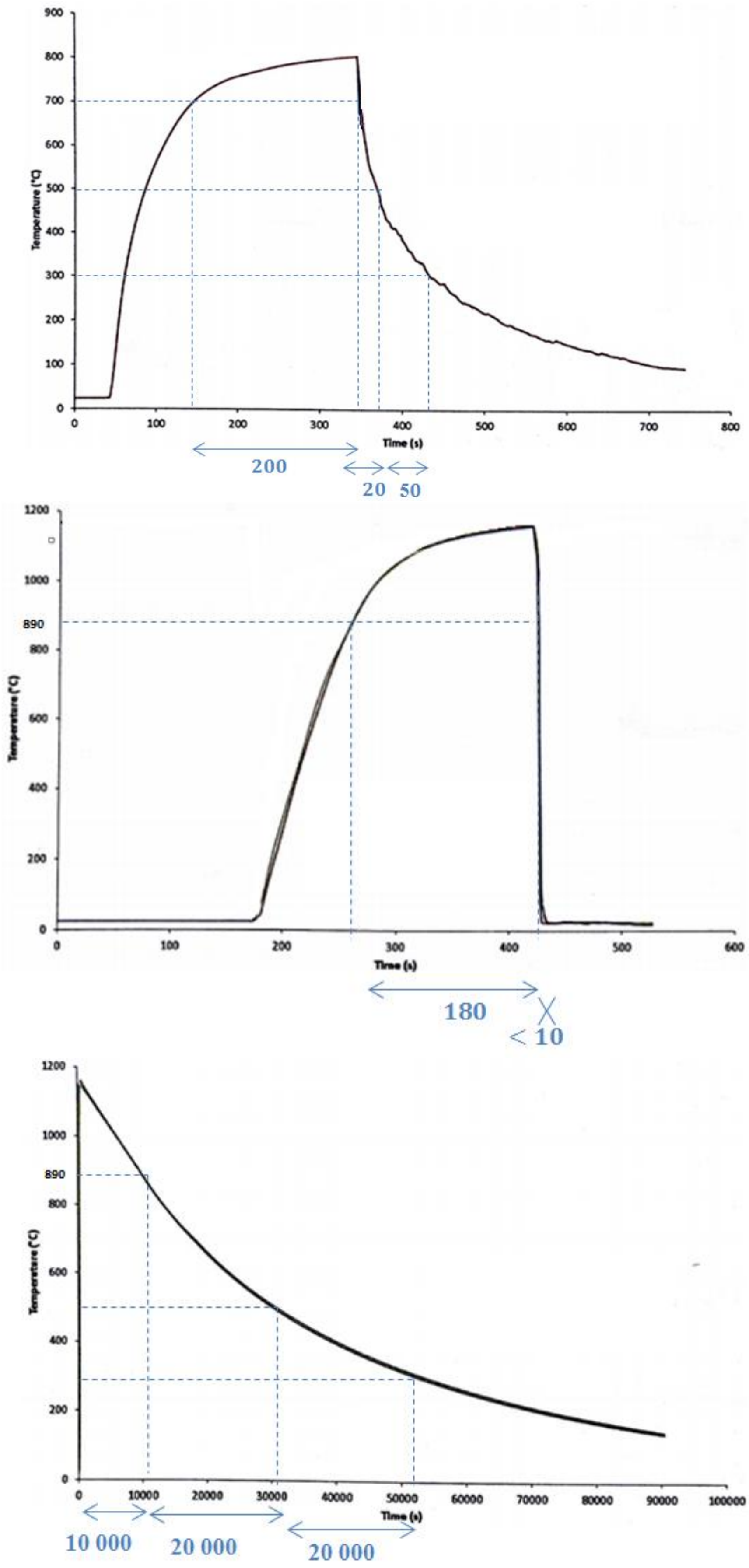

Figure 3.4: Thermal histories of Mix (top), Mar (middle) and Fer (bottom) specimens

3.4 **Microscopy**

Micrographs of the specimens were obtained to evaluate the difference in the microstructure between the different heat treatment conditions. A sample of the surface and a through thickness slice were extracted from a specimen of each set. The samples were prepared by Simon Ingram, material laboratory technician at TWI Ltd. The samples were grinded using SIAWAY grades 120, 320, 600, 1200 and 2500 sand paper and then polished using an active oxide OP-S silicon dioxide suspension (Struers) and mounted into a resin to enable observation using light microscopy. The images presented in this chapter were acquired by the author and a member of the metallography laboratory in TWI Ltd, Ashley Spencer, Simon Ingram and Diane Shaw.

3.4.1 Austenitic steel

The micrographs of the austenitic steel surface and through-thickness are presented in Figure 3.5 and Figure 3.6 respectively. The average grain size for the micrographs was calculated using the ASTM E112 – 13 three circles technique for grain size measurements [106] by Tom Adams, technician in the metallurgy laboratory in TWI Ltd. The results are presented in Table 3.6. The average grain size of the specimens refers to the average of the average length and average breadth measured in random samples of the surfaces. The average grain sizes of the AR, AC and VF specimens are respectively 27µm, 35 µm and 106 µm. It can be seen from the results that the heat treatments selected to replicate different weld microstructure did result in microstructures with different average grain sizes. Therefore, the TSA described in the following section established if the thermoelastic constant changes for different grain sizes. As the thermoelastic constant dependence on average grain size is of interest, the specimens AR, AC and VF are referred to as AR-27 µm, AC-35 µm and VF-106 µm respectively for ease of interpretation.

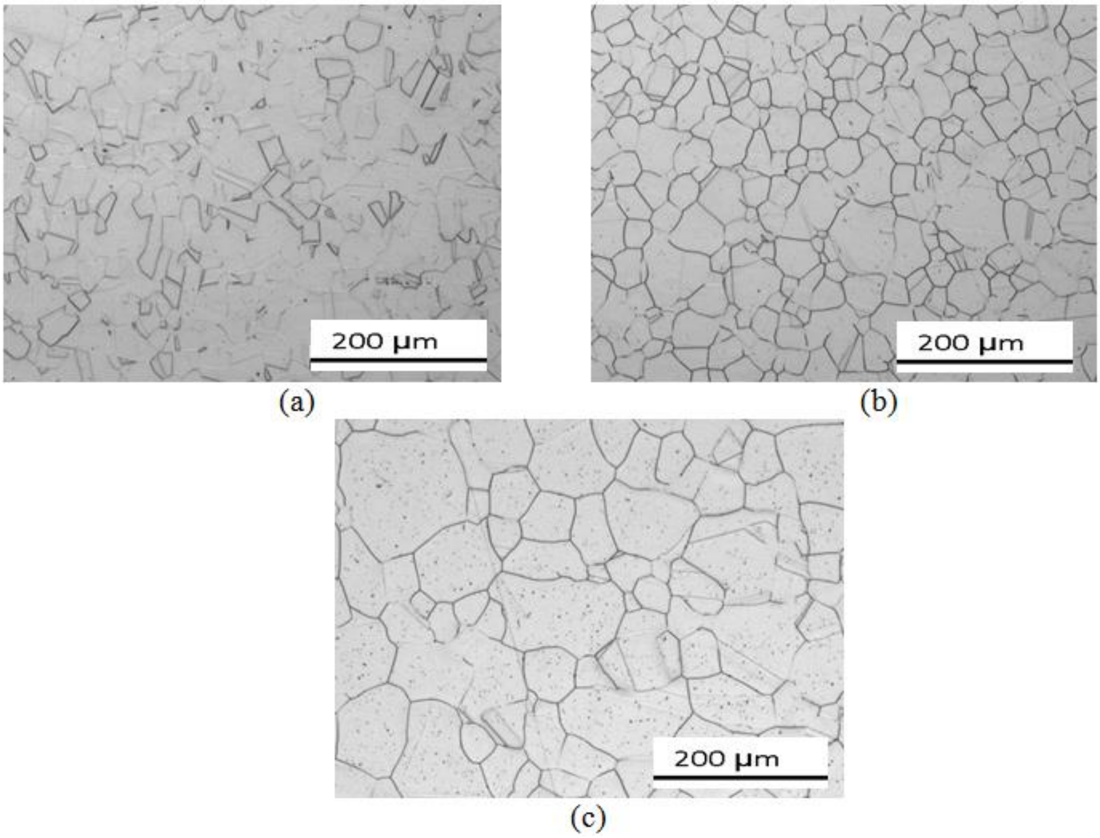

(a) (b) (c)

Figure 3.5: Micrographs of the surfaces of the AISI 316L AR-27 µm (a) , AC-35 µm (b) and VF-106 µm (c).

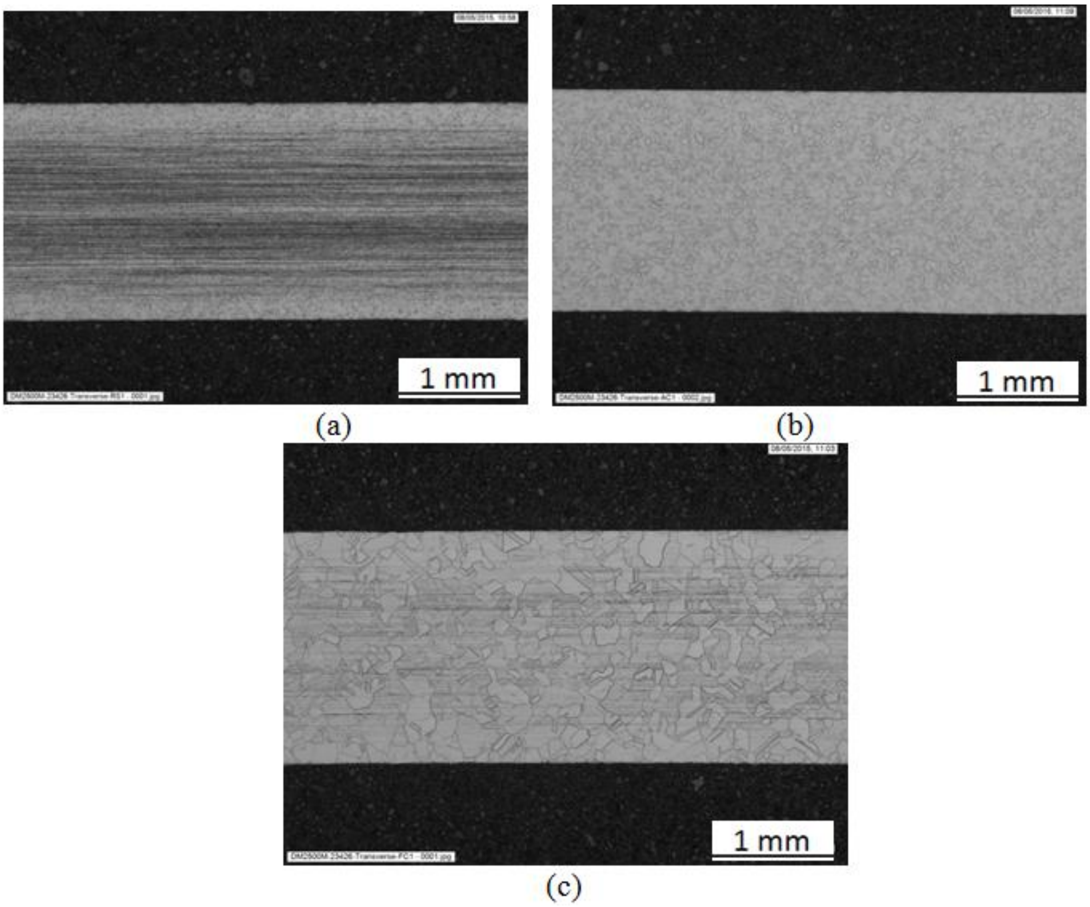

(a) (b) (c)

Figure 3.6: Through thickness micrographs of the AISI 316L AR-27 µm (a) , AC-35 µm (b) and VF-106 µm (c).

Specimen type	**AR**	**AC**	**FC**
Total (number of grains)	1117	4952	1310
Mean ASTM grain number	10.2	8.1	5.0
Standard deviation ASTM grain number	± 3.6	± 2.4	± 2.2
Max ASTM grain number	16.9	15.2	10.4
Min ASTM grain number	3.9	2.6	0.5
Mean (length/breadth/average), μm	33.9/20.2 27	45.8/25.2 35	133/78.7 106
Standard Deviation Mean (length/breadth/average), μm	± 39/22 11.78	± 37.5/25.9 31.7	± 96.4/60.8 78.6

Table 3.6: Average grain size of 316L microstructure resulting from respective heat treatment

3.4.2 Ferritic steel

The micrographs of the ferritic steel surfaces and through-thickness sections are presented in Figure 3.5 and Figure 3.6 respectively.

Once the heat treatments were applied to the SA508 specimens, the phases created in the specimens from each heat treatment were identified and compared with predictions. One specimen of each heat treatment group was used create samples to examine using light microscopy. It can be seen from the micrographs that the microstructures resulting from the three heat treatments are different and phase identification using micrographs reveals features of the expected phases, as identified in Figure 3.7 and Figure 3.8. Micrographs of AR and Mix specimens are clearly made of a mix of phases. The micrograph of Fer shows large grains of ferrite with some smaller regions containing precipitates and a micrograph of Mar specimens can be identified as containing martensite.

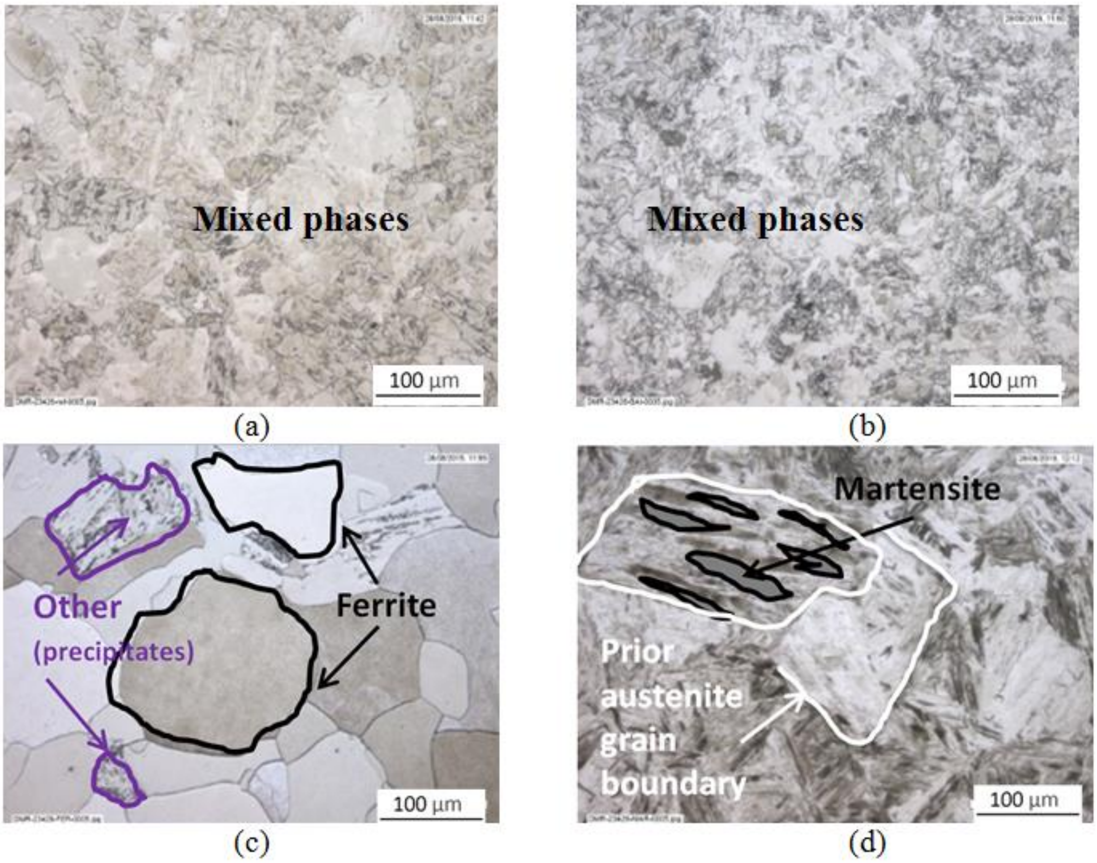

Figure 3.7: Micrograph of the surfaces of the SA508 AR (a) , Mix (b), Fer (c) and Mar (d).

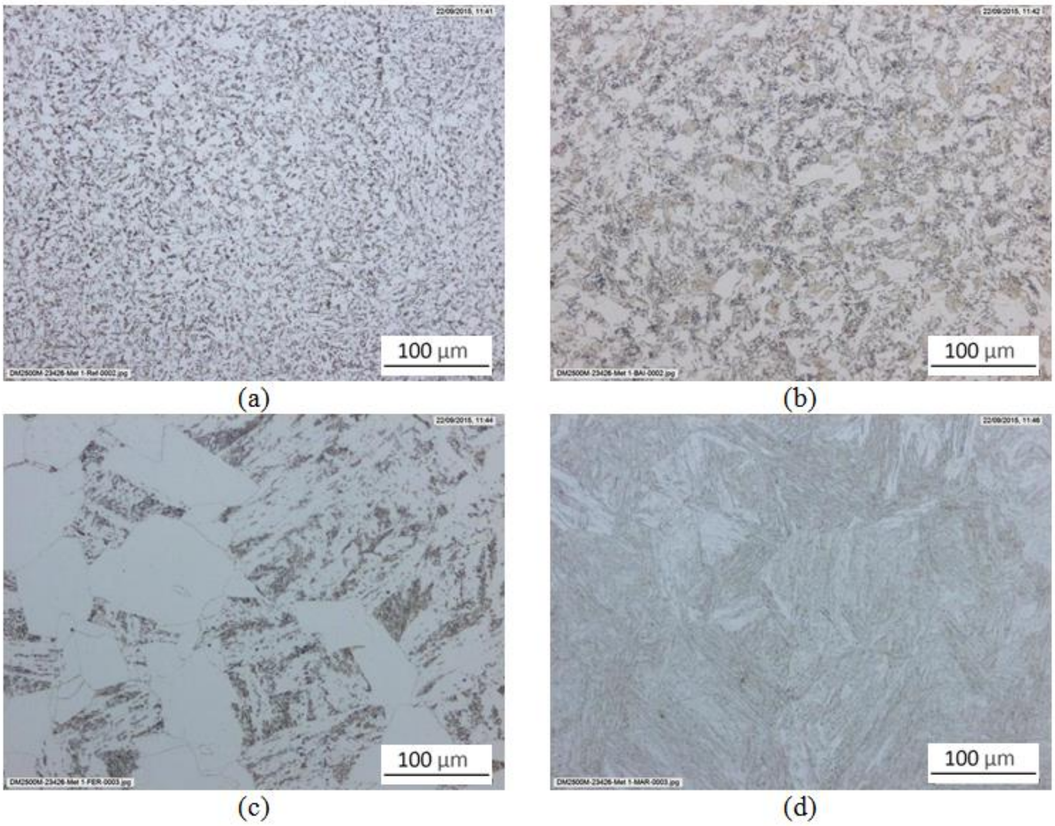

Figure 3.8:Through thickness micrograph of the of the SA508 AR (a) , Mix (b), Fer (c) and Mar (d).

The TSA imaged surfaces of the SA508 specimens correspond to the EDM surface. Hosseinzadeh et. al. have demonstrated that EDM is a source of compressive plastic straining along the cut [30] so lower values in the thermoelastic constant of the specimens which were not heat treated after EDM cutting are expected, since the heat treatment would relieve EDM induced plastic strain and residual stress. The recast layer from the EDM process was identified on the non-heat treated specimen, as shown in Figure 3.9.

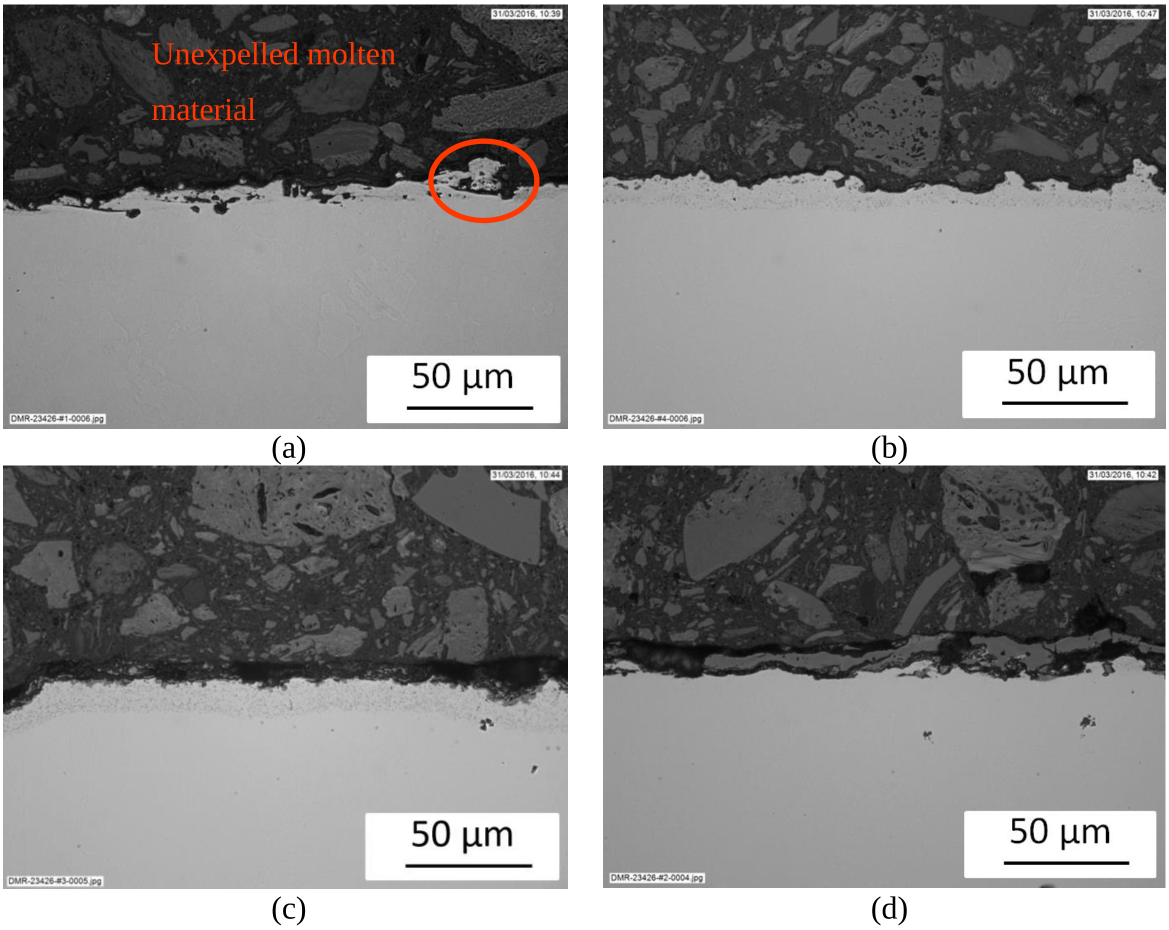

Figure 3.9: Identification of the recast layer of SA508 AR (a). In Mix (b), Fer (c) and Mar (d), the unexpelled molten material is removed.

3.5 **TSA results**

Specimens were abraded using 220 µm sand paper and cleaned with acetone. A thin layer of Electrolube high temperature matt black paint was applied to the specimens to ensure a uniform and high emissivity. The test specimens were mounted in a servo-hydraulic test machine. A tensile sinusoidal cyclic loading of 7.5 ± 4.5 kN was applied at a frequency of 10 Hz. A Cedip Silver 480M infrared camera was used to record temperatures. The detector records the infrared radiation from the surface of the specimen over a number of cycles for a user specified time and a given frame rate. In these tests, the videos were recorded for 3 s at a frame rate of 383 Hz and integration time of 1332 µs. The recorded data are processed and radiometric calibration files enable the thermoelastic signal to be directly processed into temperature data. Each pixel represents one of the elements in the detector array, and for each image of the video, each pixel contains a value that is proportional to the infrared radiation that was recorded over part of the cycle defined by the integration time. The temperature change is then calculated from a Fast Fourier Transform (FTT) based averaging procedure applied to the recorded images [10]. The average temperature and change in temperature were used to calculate the thermoelastic constant of each specimen using the TSA equation in the case of uniaxial loading. Both surfaces of each specimen were observed by turning the test specimen in the test machine and two specimens for each heat treatment were tested. The tests were done twice, one day apart. A total of eight thermoelastic constant values were derived for each microstructural condition.

3.5.1 Austenitic steel

The mean value and standard deviation were calculated and the results are summarised in Table 3.7 and plotted in Figure 3.10. The triangles represent the derived thermoelastic constants average value and the bar represents the standard deviation of the value. The box represent the reference interval of K value derived by Robinson [10]. All the mean derived values lay in the reference interval. The VF-106 µm provided on average a 0.4% smaller value than the finer grain size specimens. This tendency is consistent with the results expected in 3.1: the dislocation density of a coarse-grained material is lower than a fine-grained material, hence a smaller thermoelastic constant is expected in coarse-grained microstructures, compared to that of fine-grained microstructures.

Specimen set	**AR-27 µm**	**AC-35 µm**	**VF-106 µm**	**Robinson [10]**
Average value ($10^{-6}\mathrm{MPa}^{-1}$)	4.64	4.64	4.62	4.63
Standard deviation $10^{-6}\mathrm{MPa}^{-1}$)	0.05	0.03	0.04	0.04
Coefficient of variation	1.0%	0.6%	1.1%	0.8%

Table 3.7: Average value of thermoelastic constant for each 316L microstructure tested

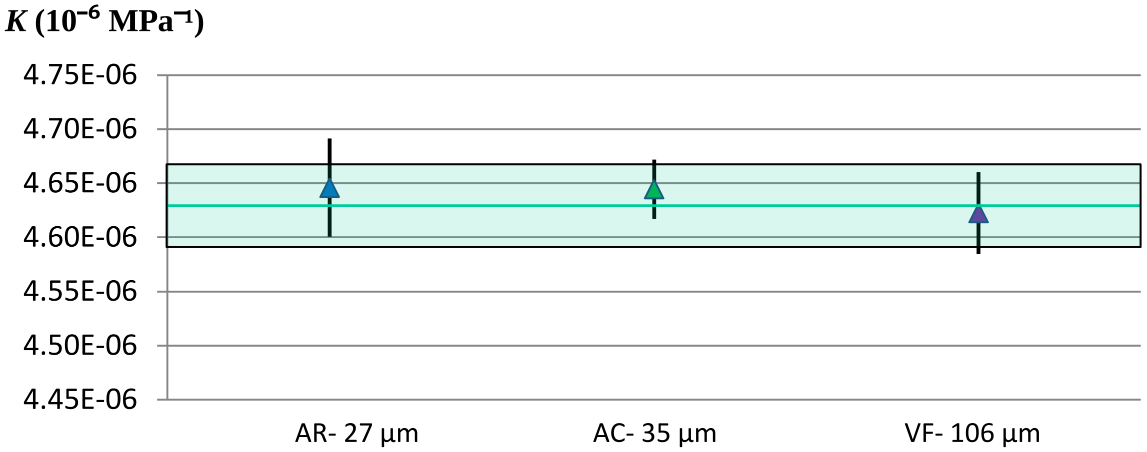

Figure 3.10: Average value of thermoelastic constant for 316L microstructure tested with standard deviation, and reference value from [10] represented with the green box.

3.5.2 Ferritic steel

The thermoelastic constant values for the different microstructures in the ferritic steel were measured. The average value of thermoelastic constant for SA508 specimens are presented in Table 3.8 and Figure 3.11.

Heat treatment	**AR**	**Mix**	**Mar**	**Fer**	**K value derived from [46]**
Average value ($\mathbf{10^{-12}Pa^{-1}}$)	3.36	3.47	3.42	3.53	3.47
Standard deviation ($\mathbf{10^{-12}Pa^{-1}}$)	0.07	0.05	0.05	0.05	N/A

Table 3.8: Average value of thermoelastic constant for each SA508 microstructure tested.

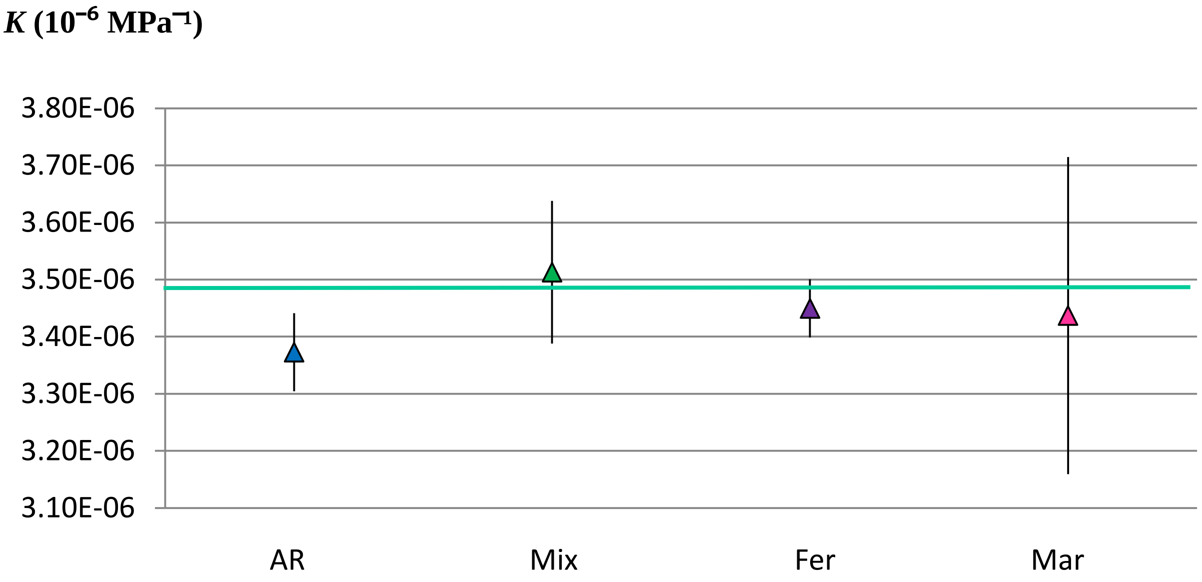

Figure 3.11: Average value of thermoelastic constant for each SA508 microstructure tested with standard deviation and reference value derived from literature values [46] and represented by the green line.

The AR specimens were manufactured from the parent material of a welded specimen and are potentially not free of plastic strain since the material used to manufacture the specimens is close to the heat affected zone of a multi-pass weld. The fabrication history of the original specimen can be found in (ADD REF) and the exact location the strip specimens were extracted from is presented in Figure 3.12 . Also, since these specimens were not heat treated, the residual stress and plastic strain induced by EDM were not relaxed. The recast layer was identified using scanning electron microscope (SEM) in section 3.4.2. This recast layer is known to contain plastic strain [107]. Plastic strain would modify the coefficient of thermal expansion, which could explain the slightly lower value in K of AR specimens.

The thermoelastic constant of a series of specimens from SA508 Gr.3 Cl.1 with different phase proportions was in the range of $3.36\ 10^{-12} Pa^{-1}$ to $3.53\ 10^{-12} Pa^{-1}$. The average thermoelastic constant of heat treated specimens differ by less than 5%. The reference value used here is derived from parent plate material properties (density, coefficient of thermal expansion and specific heat from [46]) using Equation (1.2). The measured thermoelastic constants of the different phases obtained differ by less than 4% with the thermoelastic constant from literature. However, since the dependence of the thermoelastic constant with plastic strain is not known, this does not allow any conclusions about the application of TSA PSA on this material to be drawn.

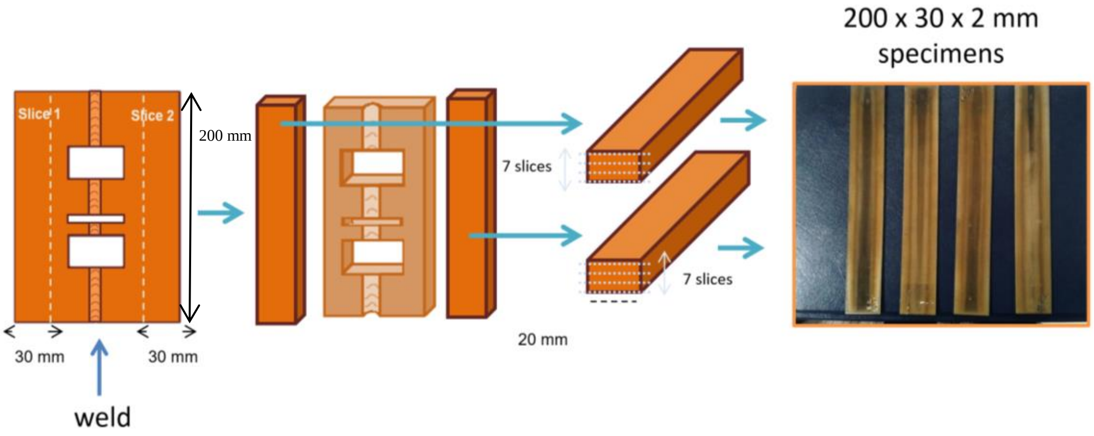

Figure 3.12: SA508 strip specimen extraction from a welded specimen.

3.6 Summary

The thermoelastic constant of a series of specimens produced from AISI 316L with different average grain sizes of 27 μm, 35 μm and 106 μm was in the range of $4.62\,10^{-12}\mathrm{Pa}^{-1}$ to $4.64\,10^{-12}\mathrm{Pa}^{-1}$. The largest K difference between heat treated specimens and reference value is reached by the FC specimens and represents 0.3% of the reference value for this material, which also corresponds to the standard deviation of the calculated reference value. According to [10], such a change would be interpreted as a 0.5% plastic strain. Therefore it is concluded that the thermoelastic constant of 316L is not influenced by different grain sizes, for the range of grain sizes tested. When examining a welded AISI 316L specimen, there will not be a change in the response caused by a change in the grain size of the parent metal, therefore any changes in the response can be attributed to the plastic straining experienced during the welding process. This finding assures that the proposed TSA PSA technique will not be influenced by the changes in the average grain size and indicates the feasibility of applying the technique to parent metal adjacent to weldments in components made from AISI 316L.

In the next chapter, plastic strains are induced in tapered specimens and in chapter 5 the thermoelastic response from each of the specimens are compared between microstructures. The dependence of thermoelastic constant on plastic strain is obtained for each microstructure studied in this chapter.

Chapter 4: Design of specimens with gradient in plastic strain

4.1 Introduction

The thermoelastic constants of 316L austenitic stainless steel specimens that had not been subjected to plastic strain were studied in Chapter 3. The results indicated that the grain size does not influence the thermoelastic constant significantly, i.e. within the threshold of precision given by Robinson [10]. To further investigate the effect of grain size on the thermoelastic constant and to determine the effect of plastic straining on the thermoelastic response a new specimen is designed that contains both plastic strain and different microstructures. If the thermoelastic constant does not change with grain size, then any change in response observed in specimens containing plastic strain is directly related to the plastic strain. If the thermoelastic constant varies with grain size, a dedicated relationship is required that includes the effect of the average grain size of the material and the plastic strain on the thermoelastic response.

The thermoelastic constants of plastic strain free samples of SA508 ferritic stainless steel with different material phase proportions (in Chapter 3) were found to be within 5% of each other. To inform on the influence of SSPT, the thermoelastic response of material with different phase proportions subject to plastic straining must be established. This is described here using the same specimen geometry as that for the 316L material. The purpose is to discern if there is a change in response that is greater than 5%, that can be attributed to the plastic straining.

A specimen is designed that includes a taper so that a varying gradient of plastic strain is introduced in the specimen by simple uniaxial loading. The design of the tapered specimen alongside the introduction of the plastic strain is described in the present chapter; the thermoelastic response from specimens with different grain sizes and phases is detailed in Chapter 5. A flowchart summarising all the steps of the work are presented in Figure 4.1. The specimens were manufactured from the strip specimens described in Chapter 3; full details of their design are described in section 4.3. The shape, inspired by [7], allows a range of plastic strain to be studied using only one specimen. It is essential that a known level of plastic strain is induced in the specimens, so firstly the amount of deformation that is required to generate the plastic strain is determined using FEA. A prerequisite for this is to define the stress-strain behaviour (particularly the yield and hardening characteristics) of the materials, which were determined using the strip specimens from chapter 3 and by taking data from the literature. The subsequent FEA is described in detail in section 4.3 where the final geometry of the deformed specimens is determined. The plastic strain induced in the tapered specimens is measured using DIC and strain gauges during loading; these experiments are described in section 4.4.

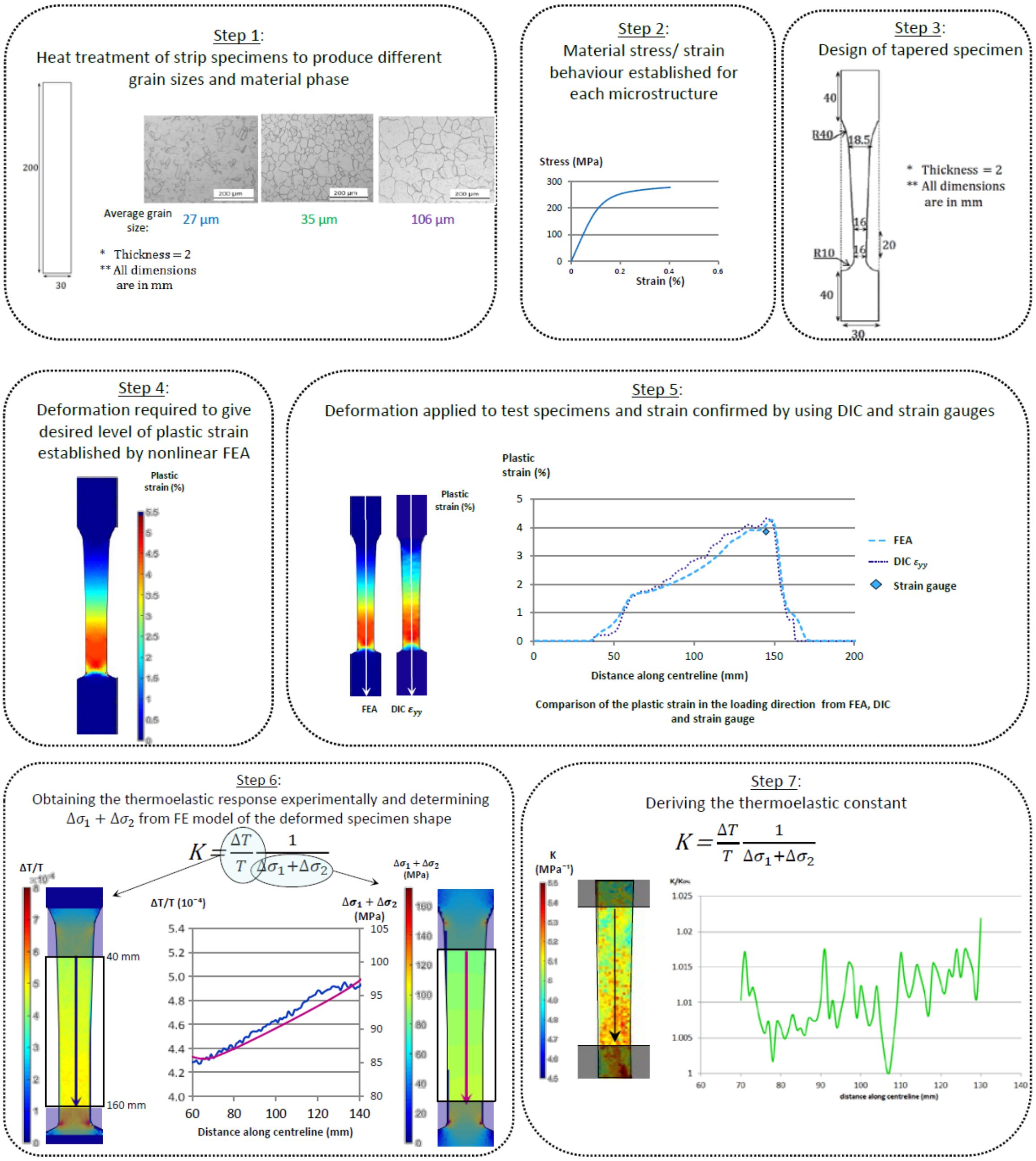

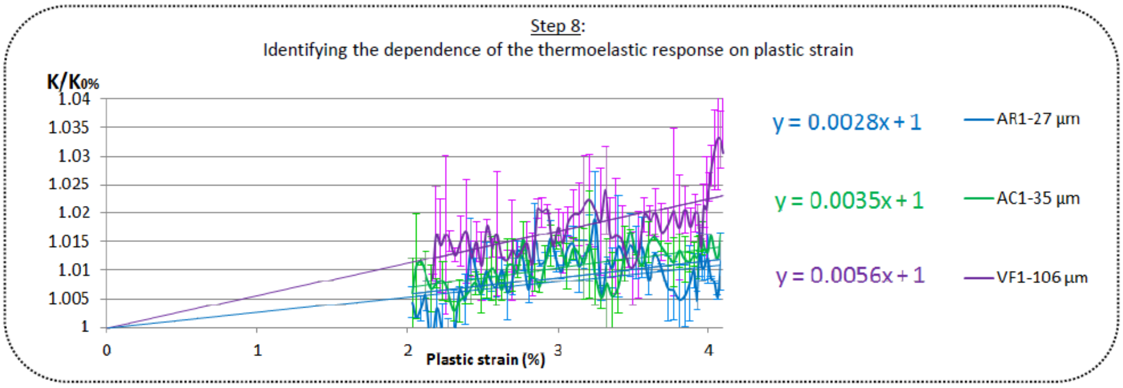

Figure 4.1: Steps involved to identify the dependence of the thermoelastic response on plastic strain.

4.2 Definition of the plastic strain of interest

The plastic strain derived from the TSA PSA technique is a scalar quantity and cannot be directional. For the purpose of this study, the accumulated equivalent plastic strain is used in comparison with the results from the TSA PSA technique.

In Abaqus, the accumulated equivalent plastic strain, PEEQ, also denoted $\bar{\varepsilon}^{pl}$, is defined as a scalar value equivalent to the Von Mises stress for plastic strains and is defined as:

$$\bar{\varepsilon}^{pl} = \int_0^t \dot{\bar{\varepsilon}}^{pl} \, dt \tag{4.1}$$

where $\dot{\bar{\varepsilon}}^{pl}$denotes the plastic strain rate defined as $\dot{\bar{\varepsilon}}^{pl} = \sqrt{\frac{2}{3}\dot{\varepsilon}^{pl} : \dot{\varepsilon}^{pl}}$ in Mises plasticity theory. Throughout the remainder of the thesis the terminology "plastic strain" will refer to this value.

4.3 Test specimen design

To produce a test specimen that contained different known amounts of plastic strain, it was decided to use a tapered specimen geometry inspired by the work of Muránsky et. al. [7], shown in the right hand sketch in Figure 4.2. The tapered shape allows a gradient of plastic strain to be introduced using uniaxial loading. The specimen used in the current work is shown in Figure 4.2. To maintain consistency it was decided that the strip specimens containing different microstructures and phases, described in Chapter 3, would be used. This meant that the taper had to fit to the existing strip specimens (shown to the left in Figure 4.2) and the tapered shape had to be such to the following criteria:

1. A known gradient of tensile plastic strain can be developed by a uniaxial tension loading,
2. The thermoelastic response of the specimen under elastic cyclic loading should be at least an order of magnitude greater than that of the detector threshold defined in 3.2.

To meet Criterion 1, the tensile loading must provide an amount of plasticity that is similar to that induced during welding (i.e. between 0% and 15%). The shape of the specimen must be symmetrical so the plastic strain is uniform across its width. The taper should be such that a distinct gradient of plastic strain occurs along the length of the specimen. A length of 40 mm at both top and bottom must be available to clamp in the test machine (as shown in the centre sketch of Figure 4.2). The dimensions w_1 and w_2 shown in Figure 4.2, with $w_1 > w_2$ must be defined using Criterion 2, i.e. the change in stress caused by the elastic cyclic loading in the region of interest, must create a change in temperature ten times larger than the noise detector threshold. In section 4.3.2, the possible values of w_1 and w_2 are discussed using calculation and a parametric study. To determine the final shape of the tapered specimen a FE model was produced, which also defined the applied displacement necessary to achieve the desired gradient of plastic strain.

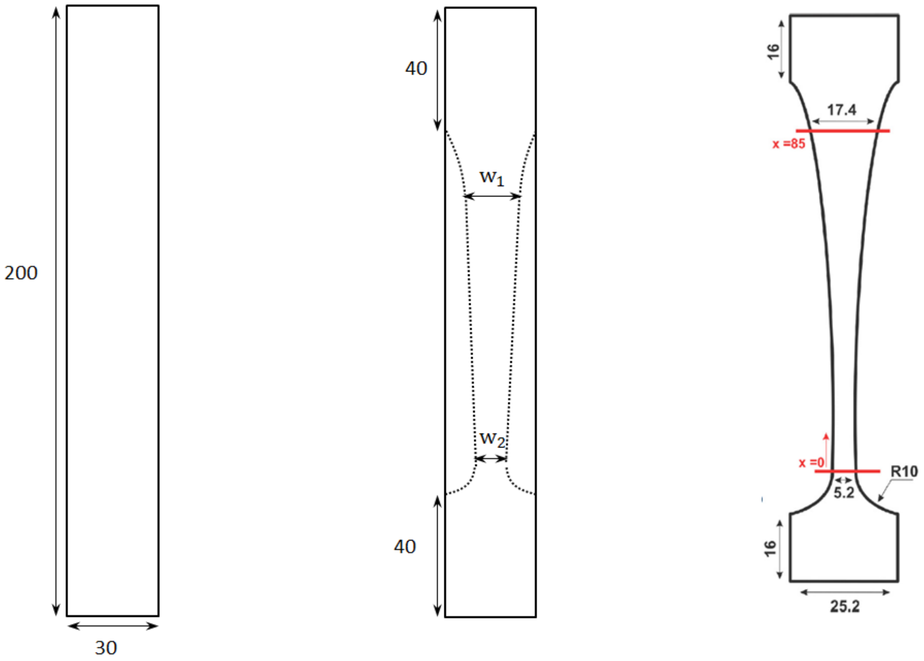

* Thickness of 2mm
** Dimensions are in mm

Figure 4.2: Initial shape and dimensions of the strip specimens (left), tapered shape with dimensions to be defined (middle) and tapered shape and dimensions from [7]. Dimensions are in mm. Drawing is not to scale.

4.3.1 Elastic and plastic material properties

As the different microstructures will have different yield stress, which is a parameter of paramount importance in the prediction of plastic strain, it was necessary to obtain experimentally the stress strain behaviour for each microstructure so that the 0.2% yield stresses could be incorporated in the plasticity model used. A strip specimen for each microstructure of the dimensions shown in Figure 4.2 was prepared with a three-gauge strain gauge rosette bonded to either side. The stress strain curves for the ASME SA508 and AISI 316L-106 µm were obtained experimental by the author whereas AISI 316L AR-

27 µm and AC-35 µm were obtained by PhD2, Vishnu Jaya Seelan, for the RESIST project (P. Jaya Seelan). The specimens were clamped in an Instron hydraulic tensile test machine and loaded with a tensile displacement at a rate of 0.5 mm/min. The stress strain curves for AISI 316L and SA508 specimens are presented in Figure 4.3 and Figure 4.4 respectively. The stress corresponding to 0.2% plastic strain is reported in Table 4.1 for both materials and Young's modulus is reported in Table 4.2.

It should be mentioned here that all the stress corresponding to the 0.2% plastic strain are greater than 200 MPa, which correspond to the stress applied on the strip specimens in Chapter 3. This ensures the loading applied during the TSA did not induce additional plastic strain. However the loading cannot be considered fully elastic for the VF-106 µm specimens.

It can be noticed in Figure 4.3 that the stress strain curves were obtained for strain up to 0.4%. The aim is to produce sufficient plastic strain in specimens containing different microstructures so the influence of weld induced plastic strain levels on the thermoelastic response can be studied. Hence an extrapolation of the data from Figure 4.3 and Figure 4.4 was performed using Ludwik's equation [108]:

$$\sigma = \sigma_0 + K_L \varepsilon^{n_L} \qquad 4.2)$$

where σ is the true stress, σ_0is the elastic limit, K_L is the strain hardening coefficient, ε is the true strain and n_L is the strain hardening exponent.

The parameters used to extrapolate the stress/strain curves are presented in Table 4.3 and Table 4.4 for AISI 316L and SA508 microstructures respectively.The extrapolated stress strain curves are presented in Figure 4.5 and Figure 4.6 for comparison with the experimental data respectively and the true AISI 316L and SA508 true stress/strain curves are presented in Figure 4.7 and Figure 4.8 respectively.

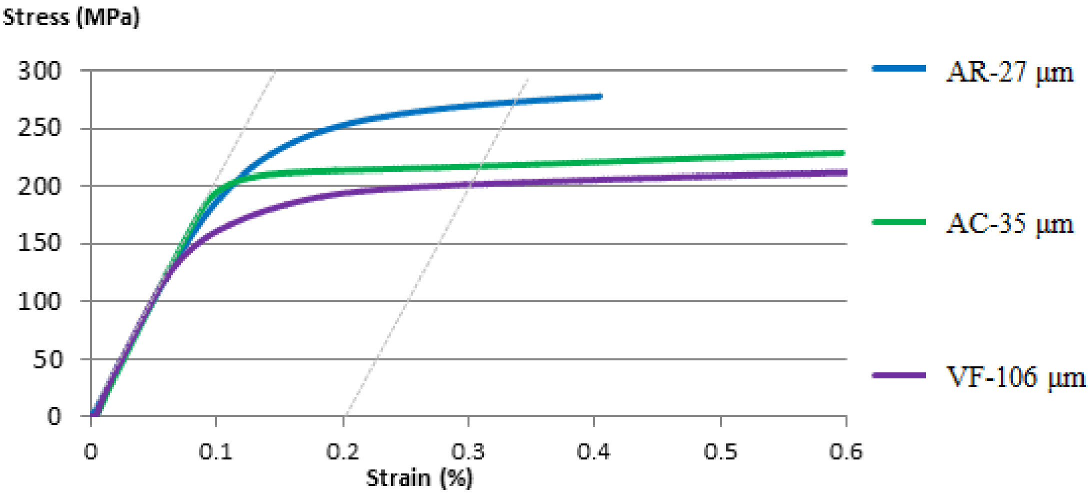

Figure 4.3: Stress strain curves of as received (blue), air cooled (green) and furnace cooled (purple) AISI 316L strip specimens.

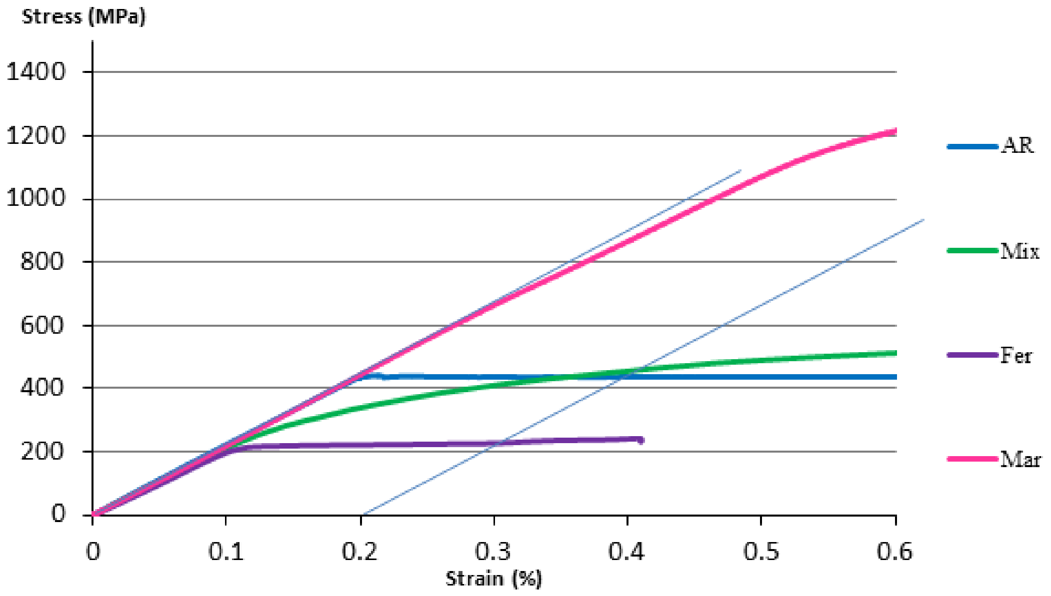

Figure 4.4: Stress strain curves of as received (blue), mixed phases (green), ferrite (purple) and martensite (pink) SA508 Gr.3 Cl.1 strip specimens.

AISI 316L	AR-27µm	AC-35µm	VF-106µm	
0.2% yield stress (MPa)	270	214	202	
SA508	**AR**	**Mix**	**Fer**	**Mar**
0.2% yield stress (MPa)	440	470	230	N/A

Table 4.1: 0.2% yield stress of each microstructure.

AISI 316L	AR-27µm	AC-35µm	VF-106µm	
Young's modulus (GPa)	206 ± 3	206 ± 3	206 ± 3	
SA508	**AR**	**Mix**	**Fer**	**Mar**
Young's modulus (GPa)	222 ± 3	212± 3	197 ± 3	217 ± 3

Table 4.2: Young's modulus of each microstructure.

AISI 316L	AR-27µm	AC-35µm	VF-106µm
σ_0 (MPa)	230	180	160
K_L	600	700	600
n_L	0.4	0.5	0.5

Table 4.3: Ludwik's equation parameters used in the extrapolation of stress/strain curves of AISI 316L microstructures.

SA508	AR	Mix	Fer	Mar
σ_0 (MPa)	400	400	235	1125
K_L	900	750	500	2500
n_L	0.6	0.3	0.5	0.6

Table 4.4: Ludwik's equation parameters used in the extrapolation of stress/strain curves of SA508 microstructures.

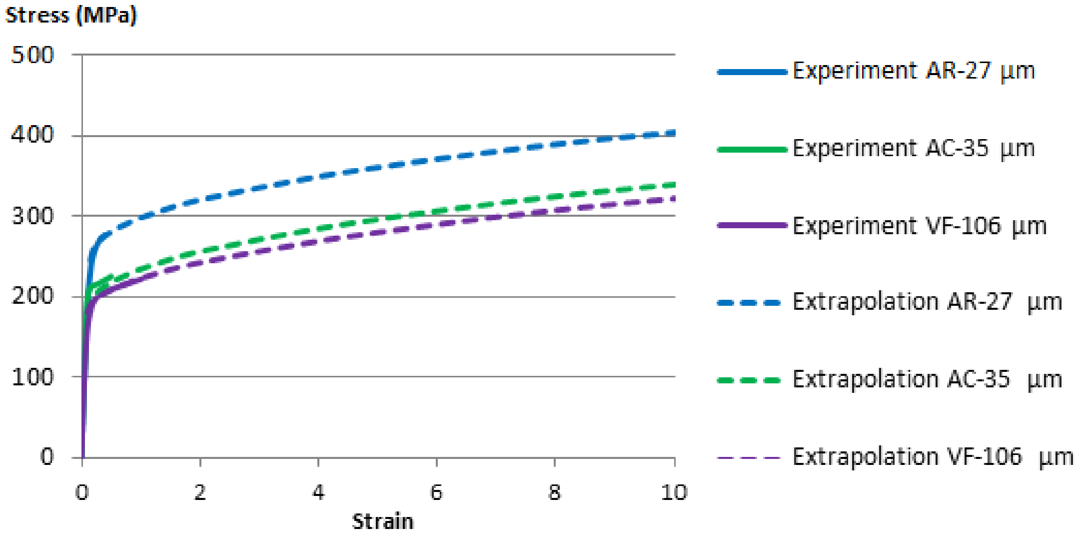

Figure 4.5: Extrapolated AISI 316L microstructures stress/strain curves

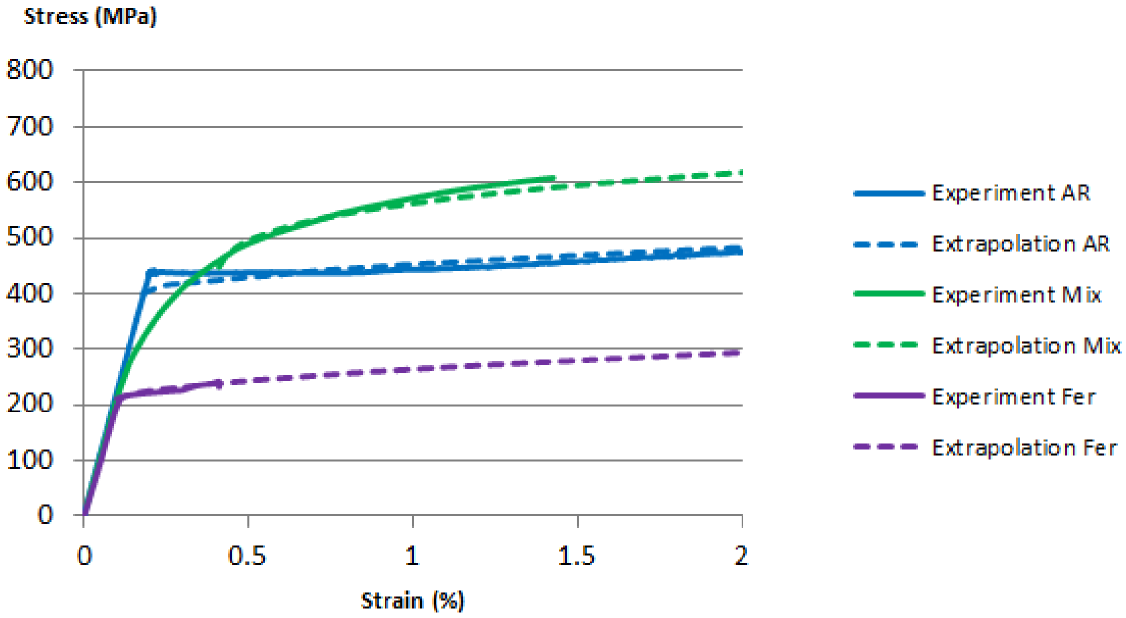

Figure 4.6: Extrapolated SA508 microstructures stress/strain curves

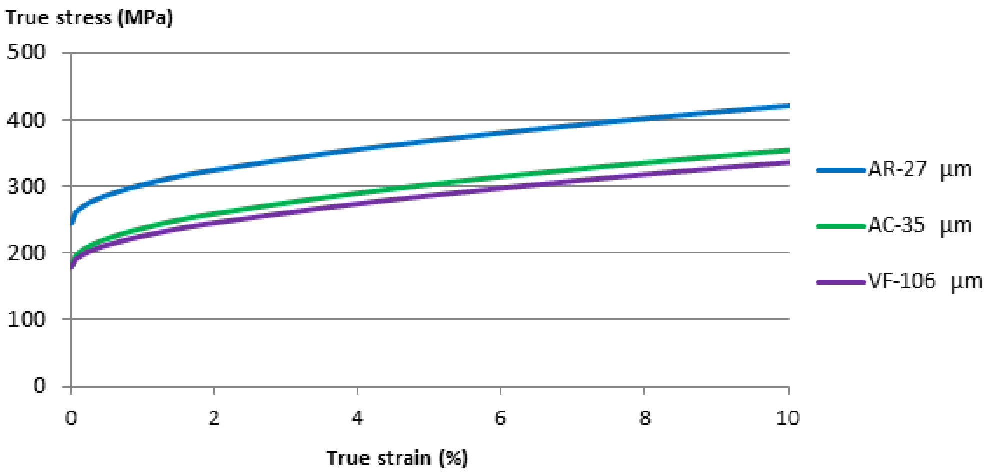

Figure 4.7: True stress strain curves of AISI 316L strip specimens.

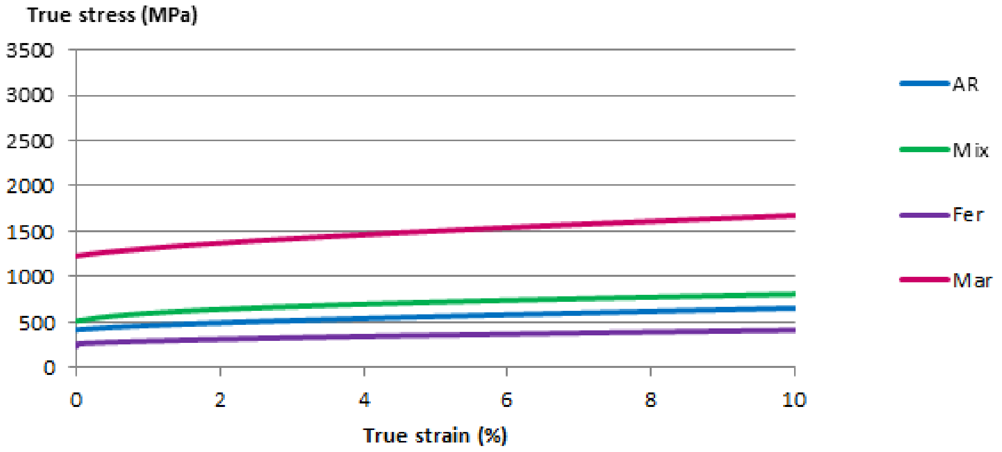

Figure 4.8: True stress strain curves of SA508 strip specimens.

In Figure 4.4 and Table 4.2 it can be noticed that the Young's modulus value varies from 197 GPa (Fer) to 222 GPa (AR) which is 12.5% larger than the Young's modulus of 199 GPa from [109]. As it was only possible to test one specimen of each type because of the restricted availability of the material it was decided to neglect these values and to use a Young's modulus of 199 GPa from [109] in all microstructure plastic strain prediction simulations for SA508. However, for the AR, Mix and Fer specimens the yield strength provided by the curves given in Figure 4.4 were used, as it was considered that the error in the measurement was from the strain gauge measurement and not from the test machine load cell which had been recently calibrated. Moreover this data compared well with those given in [109] and as the yield strength is very sensitive to heat treatment, it was considered appropriate to use the measured values. It should be noted that in Figure 4.4 the Mar specimen did not yield and therefore there was insufficient data to perform extrapolation using Ludwik's equation, so values from [48], combined with the assumed yield stress of Mar from strain gauge data were used to provide the extrapolation parameters.

4.3.2 FEA model

FEA is used to determine taper dimensions of the tapered specimens. Throughout the thesis, the FEA software Abaqus is used. The element type used in this model is C3D20R quadratic reduced integration 3D brick element and large displacement analysis was performed using NLGEOM in Abaqus step options.

The applied displacement necessary to develop the level of plastic strain required is determined from the FE models. Firstly some nominal dimensions are selected as the basis for the FEA these are given in Figure 4.9. This enabled a mesh sensitivity study on the two parameters of importance in the study:

1. The accumulated plastic strain prediction, PEEQ, after deformation.
2. The spatial variation in the sum of the principal stresses arising from the elastic cyclic load applied during TSA, referred as $\nabla(\Delta\sigma_1 + \Delta\sigma_2)$

Firstly the load application and boundary conditions and the displacement and load applied in the models must be established. The steps used in the model are presented in Figure 4.9. The top surface displacement is set to zero in all directions at all times. The modelling of the displacement is performed by applying a displacement to the bottom gripped surfaces of the specimen while the top gripped surfaces are kept free from displacement. The bottom and top gripped surfaces are depicted in Figure 4.10 and represent the area of the specimen in contact with the grips of the test machine during the experiment. The maximum and minimum load applied for the TSA are applied to a point, referred as “reference point”, which is kinematically coupled in all directions to the bottom gripped surfaces of the specimen.

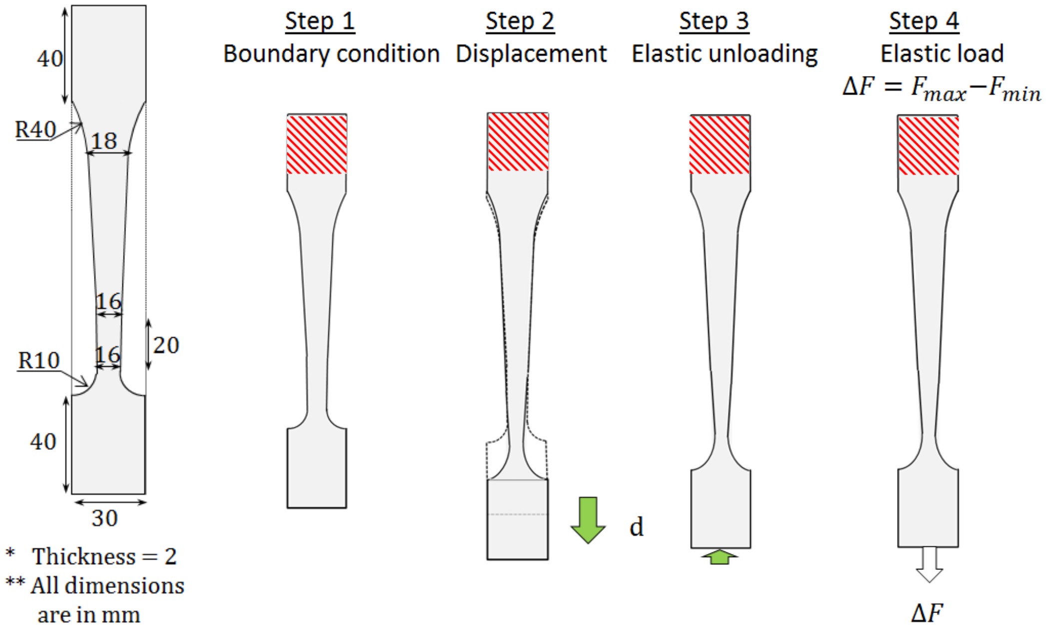

Figure 4.9: Nominal dimensions of the mesh sensitivity study specimens (left) and steps applied in the model (right)

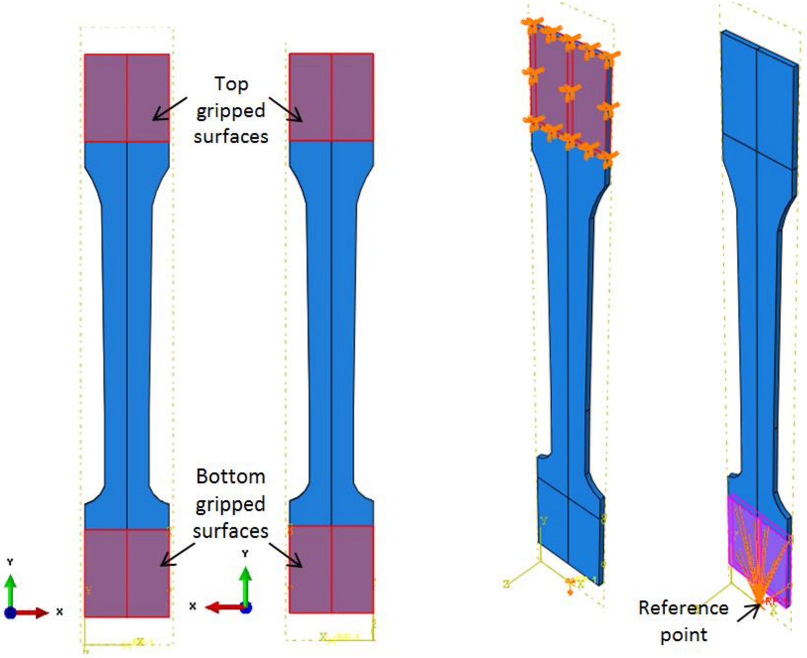

(a) (b) (c)

Figure 4.10: Top and bottom gripped surfaces (a), boundary condition of the top gripped surfaces (b. Displacement and load application to the bottom gripped surfaces via a reference point (c).

It should be noted that an error of 1.5% in $\nabla(\Delta\sigma_1 + \Delta\sigma_2)$ would mask the change in thermoelastic constant expected from the plastic strain. Therefore it is necessary to conduct a mesh sensitivity study to define the coarsest mesh possible with the required precision. Two mesh sensitivity studies were performed. The in plane element size and the through thickness size were considered. Mesh sizes of 3 mm, 2 mm, 1 mm and 0.6 mm were assigned to the model, with a constant number of three elements through the thickness, as depicted in Figure 4.11. The number of elements through the thickness of the specimen was increased from one to six elements, with an average element size of 3 mm on the surface of the specimen. The evolution of plastic strain values at 95 mm away from the top of the specimen as can be seen in Figure 4.12 and $\nabla(\Delta\sigma_1 + \sigma_2)$ with the mesh size and number of element through the thickness are presented in Figure 4.13 and Figure 4.14 respectively. The position 95 mm on the centreline was selected randomly, in the region of interest. For three elements or more through the thickness and for an in plane element size equal or smaller than 2 mm, the dependence of $\nabla(\Delta\sigma_1 + \Delta\sigma_2)$ on the mesh size is less than 0.1%, which is indicated by the transparent green box in Figures 4.9 and 4.10. The variation of PEEQ with the mesh sizes presented is smaller than 0.2% which is smaller than the accuracy requested for the study, 0.4% to obtain a variation in the gradient due to plastic strain less than 1%. It is concluded that the largest mesh that can provide the required accuracy has an average in plane element size of 2 mm with three elements through the thickness and hence is used for all the models in this chapter.

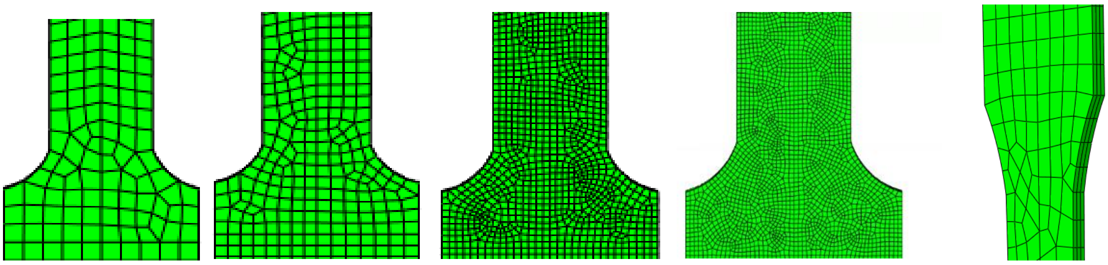

Figure 4.11: Meshes with element sizes of 3 mm, 2 mm, 1 mm and 0.6 mm (from left to right) with three elements through the thickness (right).

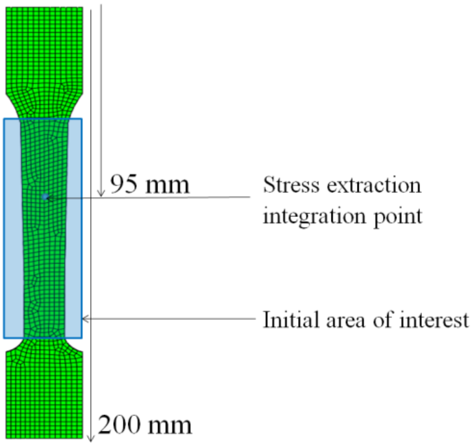

Figure 4.12: Location of the stress extraction for the mesh sensitivity study and initial region of interest.

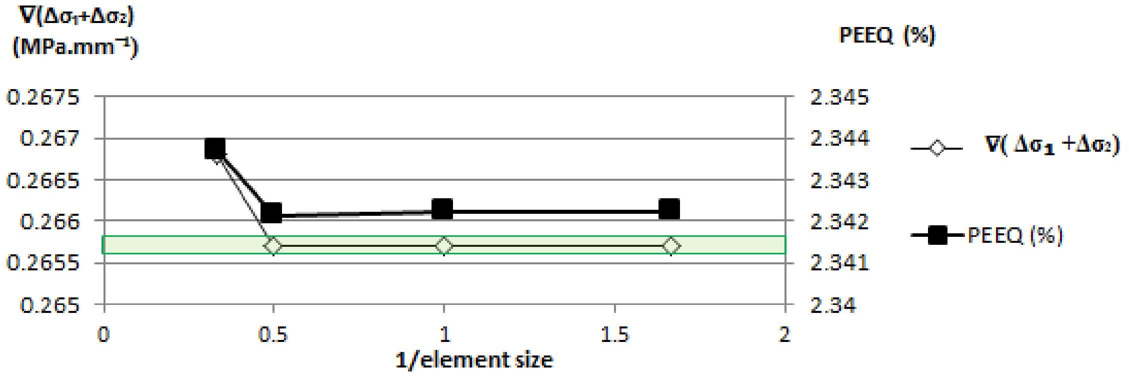

Figure 4.13: Variation of plastic strain and $\nabla(\Delta\sigma_1 + \Delta\sigma_2)$ 95 mm away from the top of the specimen for different in plane mesh sizes.

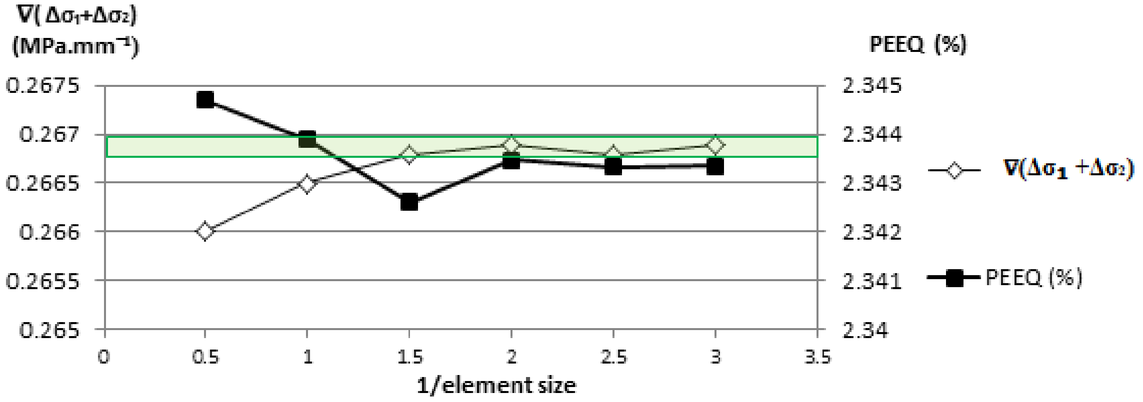

Figure 4.14: Variation of plastic strain and $\nabla(\Delta\sigma_1 + \Delta\sigma_2)$ 95 mm away from the top of the specimen for different mesh size through the thickness.

4.3.3 Test Specimen Dimensions, Manufacture and Deformation

The specimen geometry must be such that the yield point of the material is not exceeded during the cyclic loading necessary for the TSA. It is desirable that the load and specimen geometry produces a thermoelastic temperature of around 0.1 K to produce a large thermoelastic response and hence reduce the effect of noise. In Chapter 3 it was determined that a 0.1 K change in temperature corresponds to a stress change of 72 MPa. The maximum width of the specimen is 30 mm and the thickness is 2 mm so the minimum change load to achieve 0.1 K temperature change is 4.32 kN. During cyclic loading, a minimum load of 0.5 kN is applied to the specimen to avoid cycling close to zero and reduce possibilities of accidently applying compression which could lead to buckling of the specimen and render it unusable. Therefore the maximum cyclic load should be least 4.82 kN to provide a thermoelastic temperature change 0.1 K.

The specimen material should not yield, hence the smallest width of the specimen must be such that it is less than 202 MPa for the 316L material, i.e. the 0.2% yield stress for the furnace cooled material. A map of the accumulated plastic strain with a width of 18.5 mm is presented in Figure 4.15 at the maximum displacement applied (3 mm) and after elastic unloading using material properties of AR-27 µm AISI 316L. The plastic strain is identical, as unloading only affects the elastic strain, however, the length of the specimen is reduced by 0.2 mm after elastic unloading. By selecting a stress of 150 MPa this means $d_2 \geq 16$ mm. To select the width d_1, a FE model of the specimen was created and several widths were tested, assuming $d_2 = 16$ mm. Widths of 22 mm, 20 mm and 18 mm were tested on models and the accumulated plastic strain (PEEQ) gradient is presented in in Figure 4.16 , along the centreline of the specimens, as presented in Figure 4.17. A width between 18 mm and 20 mm allows the most of the specimen to be used for imaging. In this study, it is desirable that the plastic strain is not coupled with residual stress in the region of interest. The applied stresses and the residual stresses in x and y directions for the AR-27 µm AISI 316L specimen with a width of 18.5 mm are presented in Figure 4.18. It can be seen that the residual stress in the central part of the specimen are practically zero, as desired. This is further illustrated by the plots along the centre line of each specimen shown in Figure 4.19 and Figure 4.20. The region of interest where there is little residual stress is indicated in both Figures 4.19 and 4.20 and shown as the region of interest in the specimen in Figure 4.17. The shape with $\mathrm{w}_1 = 18.5$ mm provides the minimum residual stress level in the corresponding imaging area and was selected. The final specimen dimensions are given in Figure 4.21. The taper was stopped so that a 20 mm uniform width region was produced at the bottom of the specimen to allow the maximum plastic strain value to be imaged in an area free from residual stresses. This “flat” gradient corresponds to the plateau of plastic strain in Figure 4.16. The drawing shown in Figure 4.21 was adopted for all the test specimens regardless of material or heat treatment. The specimens were cut to the specified dimensions using EDM cutting with tolerance of 0.2 mm.

The plots presented in this section are plotted along the centreline. A comparison between the extraction of the data along the centreline and data averaged over 10 mm, 5 mm either side of the centreline was done for the accumulated plastic strain, as presented in Figure 4.22 and the change in the sum of the principal stresses, presented in Figure 4.23. The difference between the data extracted along the centreline and the averaged data are presented in Figure 4.24. It can be seen that the variation in plastic strain across the centreline causes a variation in the data less than 5% for the accumulated plastic strain, which is acceptable since this variation will cause a change in the final gradient (change in K due to plastic strain) which is less than the variation caused by the noise from experimental data. Hence it is considered the plastic strain extracted from the centreline is representative of the averaged plastic strain over 10 mm either side of the centreline. However, this simplification cannot be done for the change in the sum of the principal stresses since, as can be seen in Figure 4.24, the difference between the two dataset will cause a variation less than 1% in the region between 100 mm and 130 mm along the centreline. This order of magnitude could mask a change in thermoelastic constant due to plastic strain hence the data is averaged over 10 mm of the width in the analysis given in Chapter 5.

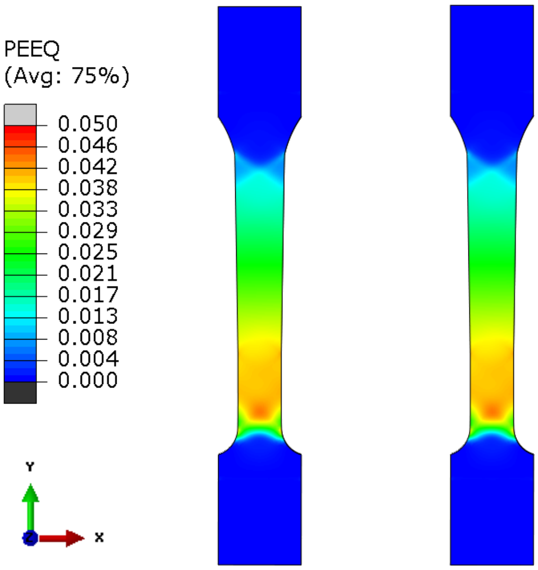

Figure 4.15: Accumulated plastic strain (%) in the specimen at the maximum displacement loading (left) and after elastic unloading (right) in the AR-27 µm AISI 316L specimen.

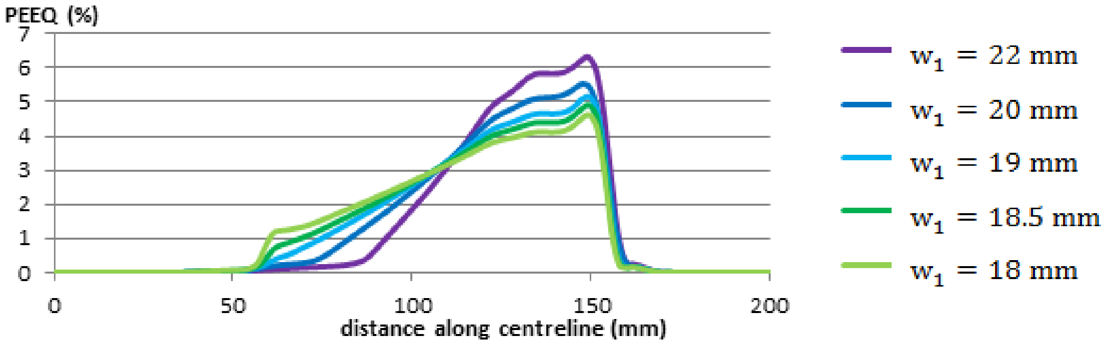

Figure 4.16: Gradient of accumulated plastic strain (PEEQ in Abaqus) with d_1 values for the AR AISI 316L specimen

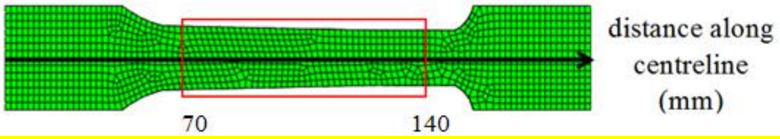

Figure 4.17: Centreline axis of data extraction (black arrow) and area of interest (red box).

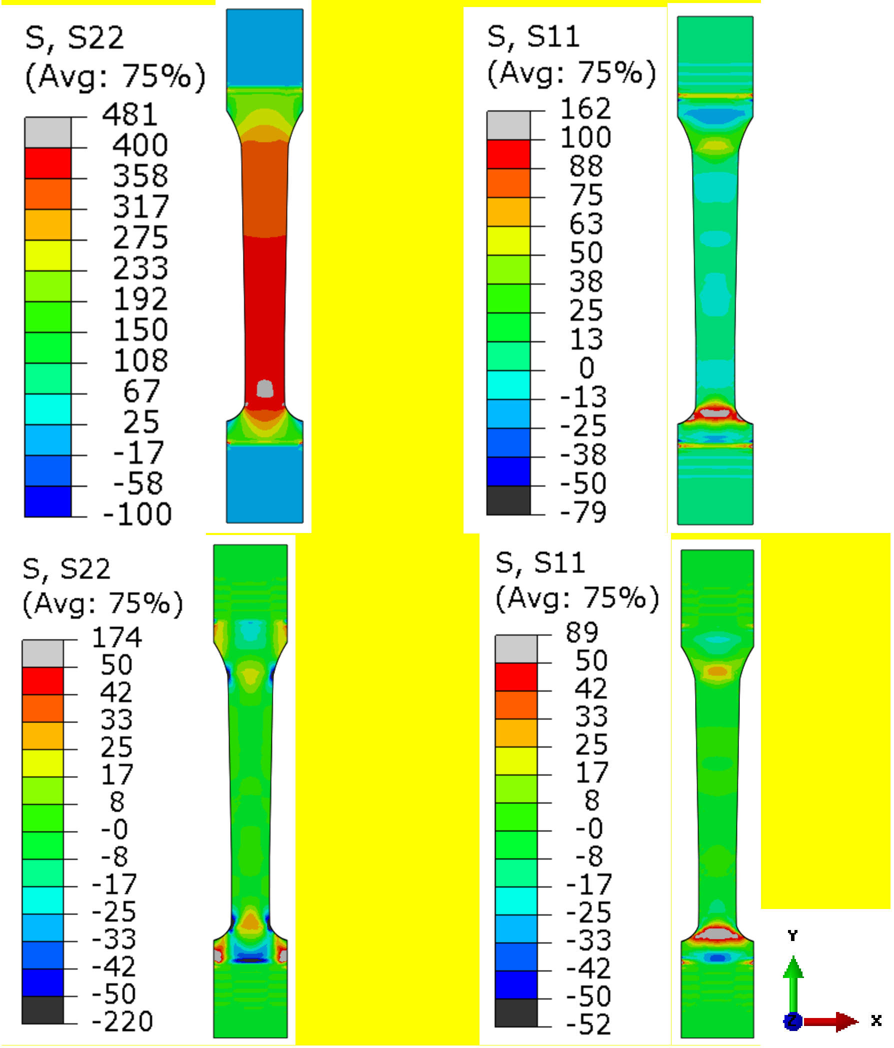

Figure 4.18: Stresses in the x –direction (S11) and y-direction (S22) at maximum displacement (top) and after elastic unloading (bottom) for the AR AISI 316L specimen

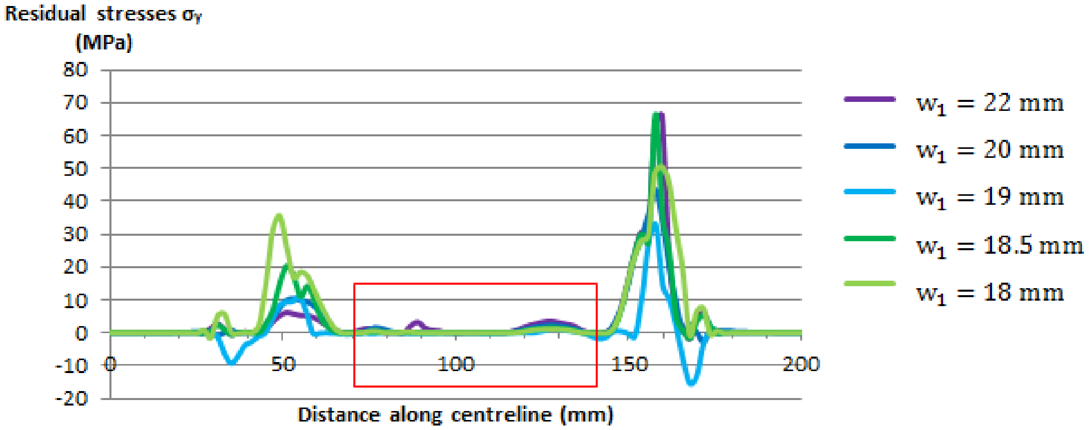

Figure 4.19: Residual stresses along the centreline in x direction of the specimen with w_1 values.

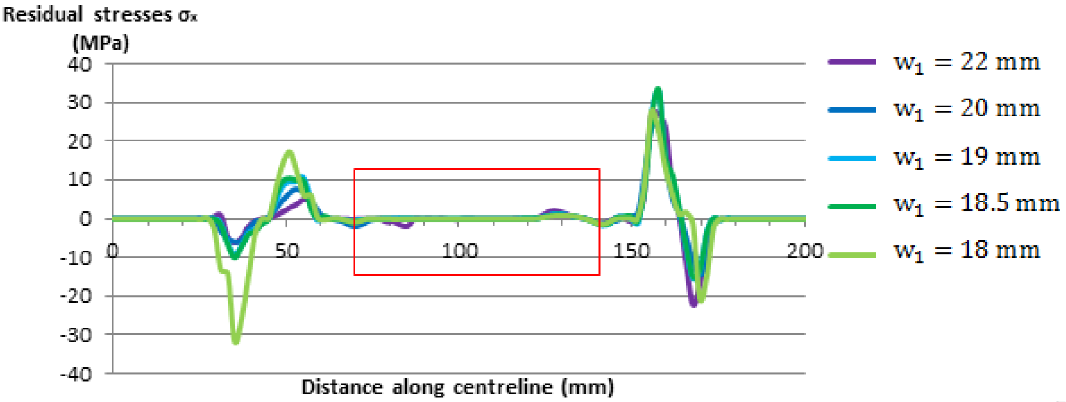

Figure 4.20: Residual stresses along the centreline in the y direction of the specimen with w_1 values.

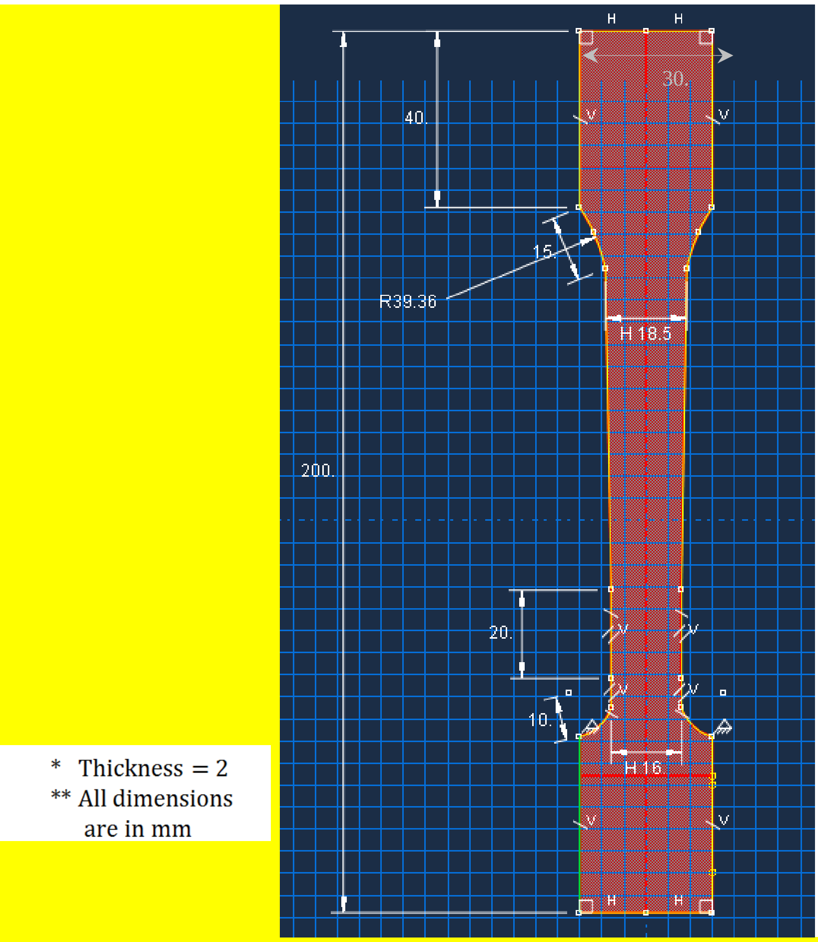

Figure 4.21: Final dimensions of the tapered specimens for a thickness of 2 mm.

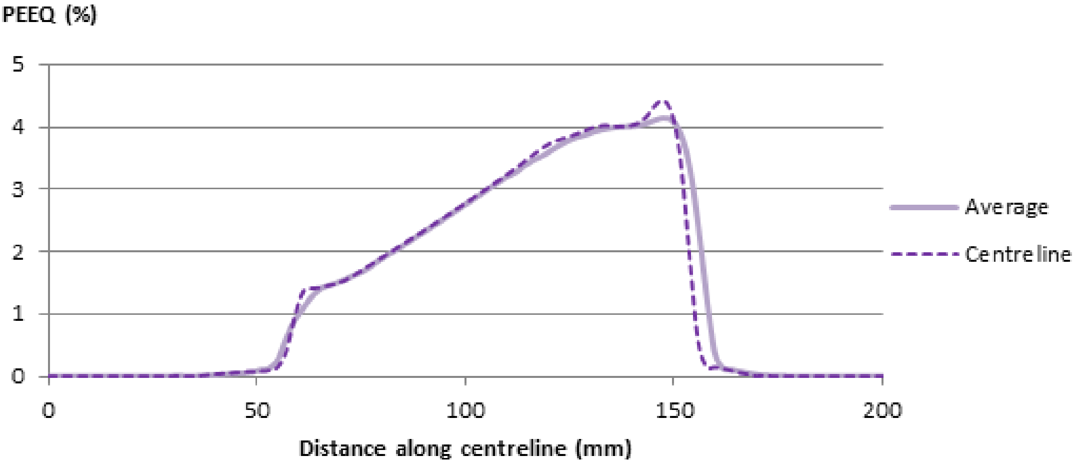

Figure 4.22: Comparison between the accumulated plastic strain (PEEQ) extracted along the centreline axis (labelled Centreline) et data averaged over 10 mm of the width, 5 mm either way from the centreline (labelled Average).

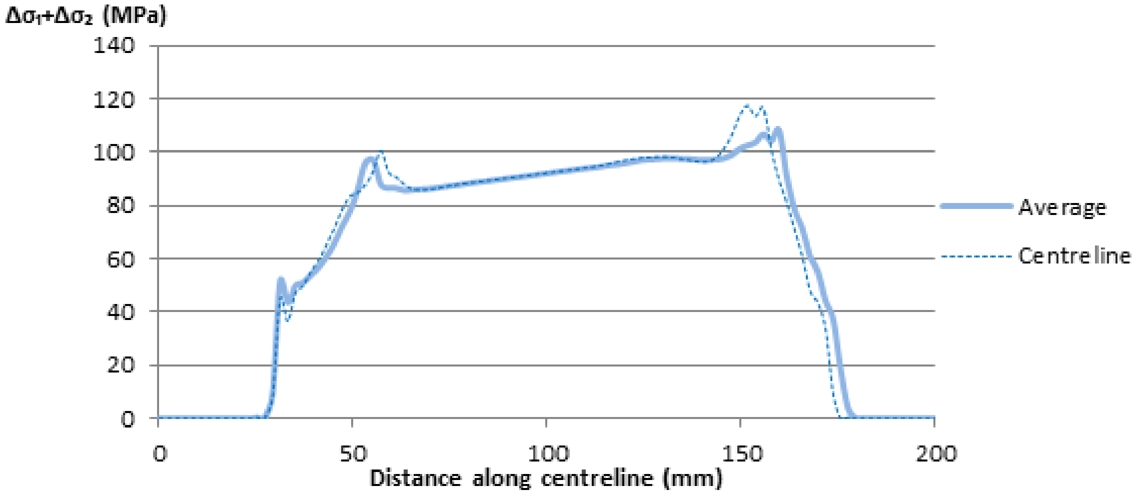

Figure 4.23: Comparison between the change in the sum of the principal stresses ($\Delta\sigma_1+\Delta\sigma_2$) extracted along the centreline axis (labelled Centreline) et data averaged over 10 mm of the width, 5 mm either way from the centreline (labelled Average).

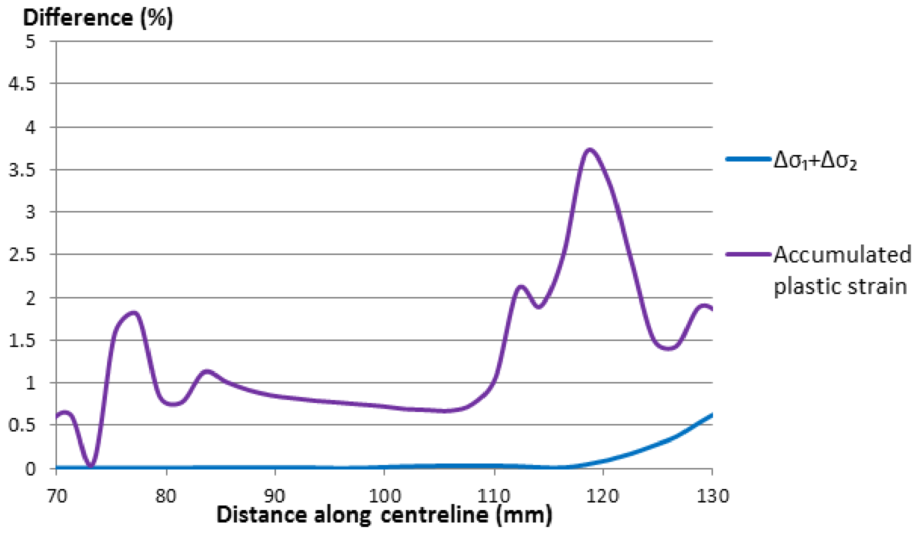

Figure 4.24: Difference between averaged data and data extracted along the centreline and data averaged over 10 mm, 5 mm either way from the centreline.

The strip specimens were EDM cut to create tapered specimens in the designed shape. As the material properties of the two materials are different, two separate cuts were performed. For both groups of AISI 316L and SA508 specimens, the specimens were piled up and cut all at once.

In total, six specimens were produced out of the AISI 316L strip specimens, two specimens of as received condition material (AR-27 µm), two specimens of the annealed for 2 minutes and air cooled specimens (AC-35µm) and two specimens out of the annealed for 81 minutes and vacuum furnace cooled material (VF-106 µm). Seven specimens were produced from the SA508 specimens: two specimens of as received condition (AR), two specimens heated to 800 °C for two minutes and air cooled (Mix), two specimens of heated to 1150 °C for two minutes and cooled at a rate of 100 °C/hr in a vacuum furnace (Fer) and one specimen heated to 1150 °C for two minutes and water quenched (Mar). A summary of the specimens used in this study are referred in Table 4.5.

The displacement required to obtain the desired plastic strain, as depicted in Figure 4.9 were derived and are presented for AISI 316L and SA508 specimens in Figure 4.26 and Figure 4.27 respectively and given in Table 4.5.

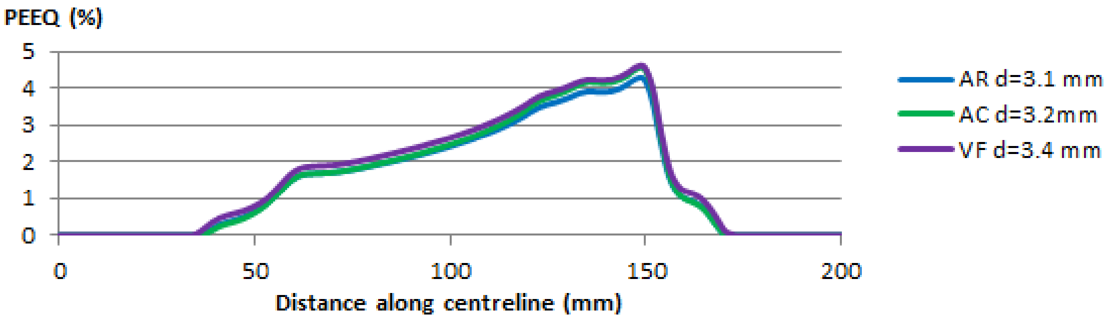

Figure 4.25: Plastic strain predictions in AISI 316L specimens and displacement applied.

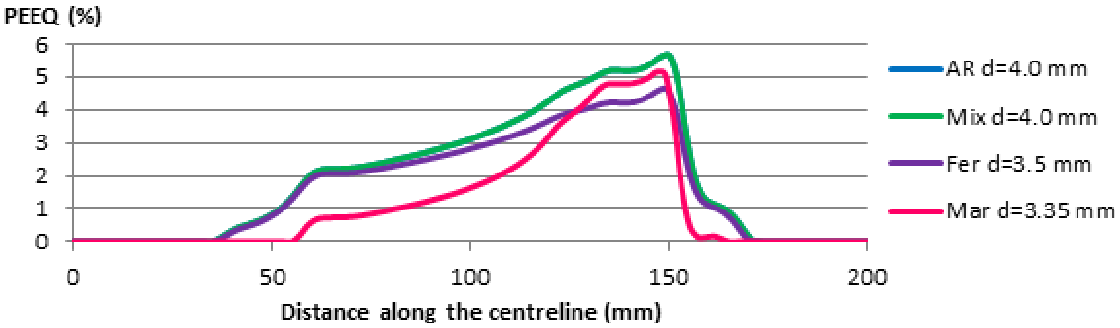

Figure 4.26: Plastic strain predictions in SA508 specimens and displacement applied.

AISI 316L	**AR1-27µm**	**AR2-27µm**	**AC1-35µm**	**AC2-35µm**	**VF1-106µm**	**VF2-106µm**	
Heat treatment	-		2 minutes at 1050 °C + air cooled		81 minutes at 1050 °C + vacuum furnace cooled		
Average grain size (µm)	27		35		106		
Displacement applied (mm)	3.0	3.1	3.1	3.3	3.3	3.4	
SA508	**AR1**	**AR2**	**Mix1**	**Mix2**	**Fer1**	**Fer2**	**Mar**
Heat treatment	-		2 minutes at 800 °C + air cooled		2 minutes at 1150°C + vacum furnace cooled at 100 °C/hr		2 minutes at 1150°C + water quenched
Phases	Mixed phases		60% bainite,		Ferrite + precipitates		Martensite

			30% martensite, 10% ferrite				
Displacement applied (mm)	4.64	4.0	4.0	4.0	3.25	3.15	3.35

Table 4.5: Specimens nomenclature, material, thermal history and microstructure.

4.4 Application and assessment of plastic straining in the tapered specimens

4.4.1 Experimental setup

The next step in the procedure is to apply the deformations established in the previous section and given in Table 4.5 to the tapered specimens. To confirm experimentally the amount of plastic strain each specimen had experienced, DIC and strain gauges were used during the deformation of the specimens. The plastic strain was obtained using the converged model for each specimen material and using the displacement given in Table 4.5 to compare with the experimental work.

DIC was used to obtain the strain on all specimens during the deformation process. A speckle pattern was applied with AMBERSIL RAL 9010 matt white paint and RS-764-3039 matt black spray paint. A representative speckle pattern applied on AR1-27 µm is presented in Figure 4.27. The speckle size varies in width from 0.2 mm to 2.0 mm with an average size of 0.4 mm and density of 2 speckles/mm² was measured. The specimen was deformed using an Instron hydraulic tensile test machine. Lengths of 30 mm at the top and at the bottom of the specimen were clamped into the grips of the test machine. The top grip remains in position while the bottom grip moves from the original position to the specified displacement at a rate of 0.5 mm/min. The images were recorded using an Imager E-lite 5M camera from LaVision with a Nikkon 54mm lens. Full details on the camera can be found in Appendix B. The results were processed with a subset size of 61 pixels x 61 pixels and step size of 20 pixels as is presented in Figure 4.27. The subset size is selected as small as possible to preserve accuracy and as large as necessary such that it allows convergence within 1% of the strain value, represented by the green box in Figure 4.28. In this study, a subset of 61 by 61 pixels is selected and is represented by the blue box in Figure 4.27.

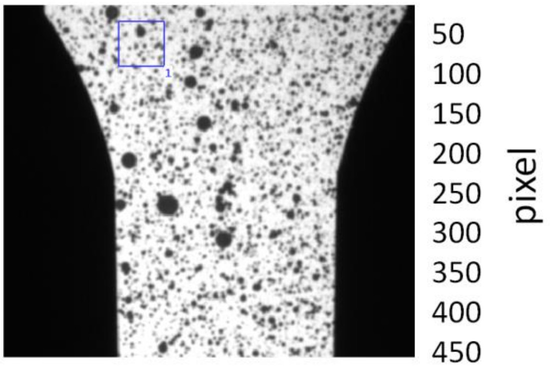

Figure 4.27: Representative speckle pattern applied on the tapered specimen with subset size of 61x61 pixels (blue box).

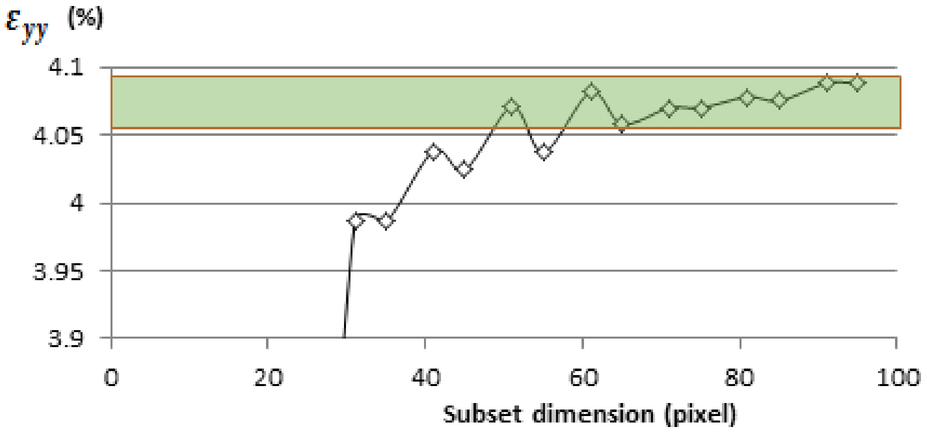

Figure 4.28: DIC strain ε_{yy} extracted at y=95 mm along the centreline of the specimen as a function of the subset size.

A strain gauge rosette was applied on the face of the specimen with no paint, allowing the strain to be recorded during the test using both DIC and strain gauge techniques. The position of the strain gauge rosette was identical for all specimens and is presented in Figure 4.29. The location of the strain gauge rosette was where the maximum strain was predicted, i.e. where the width is the smallest. The strain gauge was positioned on the specimens as presented in Figure 4.29, so that the three directions are different and as it can be seen in Figure 4.29, this caused the location of the measured strain to be 3 mm away from the centreline.

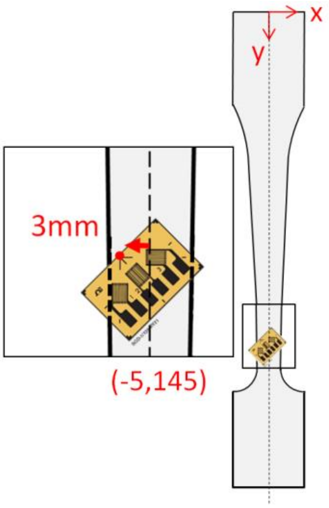

Figure 4.29: Strain gauge rosette measurement position

4.4.2 Comparison of the measured and predicted strains

A uniaxial tension load was applied to the specimens hence the accumulated plastic strain is reduced to the plastic strain in the principal direction ε_1^{pl} :

$$\bar{\varepsilon}^{pl} = \sqrt{\frac{2}{3}\varepsilon^{pl}:\varepsilon^{pl}} = \sqrt{\frac{2}{3}\left({\varepsilon_1^{pl}}^2 + {\varepsilon_2^{pl}}^2 + {\varepsilon_3^{pl}}^2\right)} \tag{4.3}$$

Due to the incompressibility of plastic strain [110],

$$\varepsilon_1^{pl} + \varepsilon_2^{pl} + \varepsilon_3^{pl} = 0 \tag{4.4}$$

$$\varepsilon_2^{pl} = \varepsilon_3^{pl} = -\frac{1}{2}\varepsilon_1^{pl} \tag{4.5}$$

$$\bar{\varepsilon}^{pl} = \varepsilon_1^{pl} \tag{4.6}$$

In the present tensile test, the strain measured with DIC is assumed equal to the plastic strain:

$$\varepsilon^{DIC} = \varepsilon^{total} = \varepsilon^{e} + \varepsilon^{p} \tag{4.7}$$

where ε^{total} is the total strain, which corresponds to the strain measured by DIC, ε^{e} denotes the elastic strain and ε^{p} is the plastic strain. The largest elastic strain can be assessed: in the experiments, the load applied to the specimen to obtain the desired plastic strain were all greater than 9 kN, the smallest surface area is larger than 30 mm² and Young’s modulus for the two types steel tested is of the order of 200 GPa. Hence

$$\varepsilon_{max}^{e} = \frac{\sigma_{max}}{E} \sim 1.5\ 10^{-6} \tag{4.8}$$

The plastic strain measured is of the order of magnitude of 0.01, hence $\varepsilon^{e} \ll \varepsilon^{p}$ and

$$\varepsilon^{DIC} \approx \varepsilon^{p} \tag{4.9}$$

This demonstrates the strain in the loading direction measured with DIC, ε_{yy} is a reasonable comparison with the accumulated plastic strain PEEQ, from the FE models in the region of interest, which does not include stress concentrations at either end of the specimen.

Figure 4.30 shows a comparison of the longitudinal strain obtained from the DIC and the predicted longitudinal strain from the FEA. Figure 4.30 also shows the position of the centre of the strain gauge rosette, which is located is 3 mm to one side of centreline (as shown in Figure 4.29), and at the longitudinal position of the maximum strain predicted by the FEA. The strain in the longitudinal direction obtained from the DIC and FEA along the centreline of the specimen, as well as the absolute value of the difference between the two, are plotted in Figure 4.31 for the AISI 316L microstructures and in Figure 4.32 for the SA508 microstructures. It should be noted that there were two specimens of each material and although it was planned to apply identical displacements to each specimen during the test the displacements varied, as presented in Table 4.5; hence two FE models corresponding to the actual applied displacement were produced and are shown in Figure 4.31 and Figure 4.32 with the exception of the SA508 mix (Figure 4.32b).

DIC measurements and FE predictions of the longitudinal plastic strain in AISI 316L specimens are presented in Figure 4.31 a b and c for the AR-27 µm, AC-35 µm and VF-1-106 µm respectively, along with the absolute difference between the two data sets. It is clear that the DIC and FEA are in very good agreement for with a variation of less than 0.25% plastic strain. In VF2-106 µm specimen, the difference is smaller than 0.25% up to 100 mm along the centreline and less than 0.5% plastic strain from 100 mm to 130 mm. The DIC data are missing for AC2-35 µm AISI 316L specimen as the light varied throughout the deformation and the images could not be processed.

Table 4.6 provides a comparison between the longitudinal strain given by the strain gauge rosette, the DIC and the FEA for the AR-27 µm and VF-106 µm specimens. Unfortunately the strain gauges detached for the AC material. The difference is smaller than 3%. This result suggests any variation between DIC and FEA arise from the extrapolation of the stress strain curves used in the finite element modelling. It is concluded FE model over predicts plastic strain in VF-106 µm up to 0.5% plastic strain.

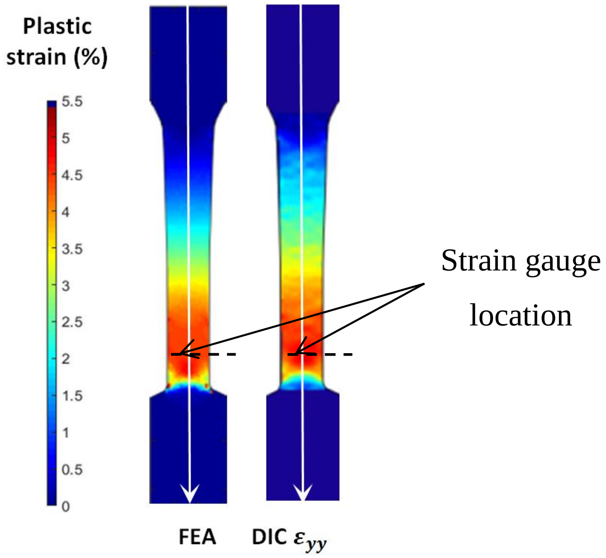

Figure 4.30: Contour plot of the DIC measurements (right) and FEA plastic strain prediction (left) for AISI 316L AR2-27 μm specimen, along with data extraction lines and strain gauge location (black dotted line).

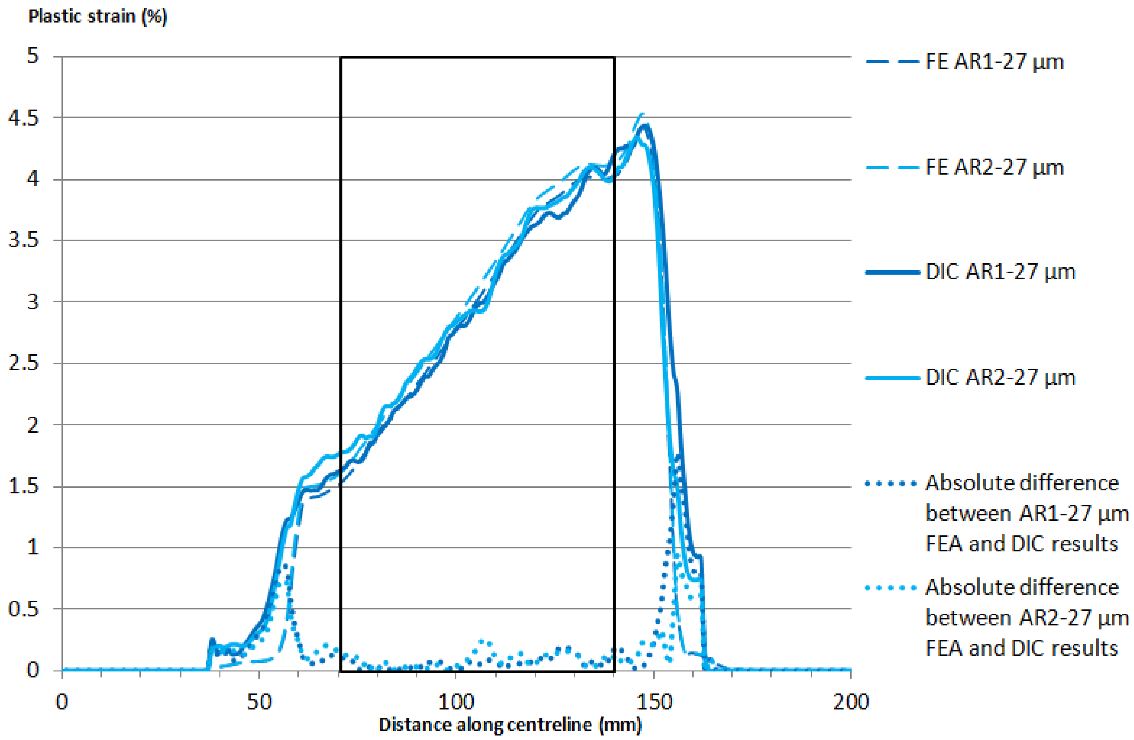

(a)

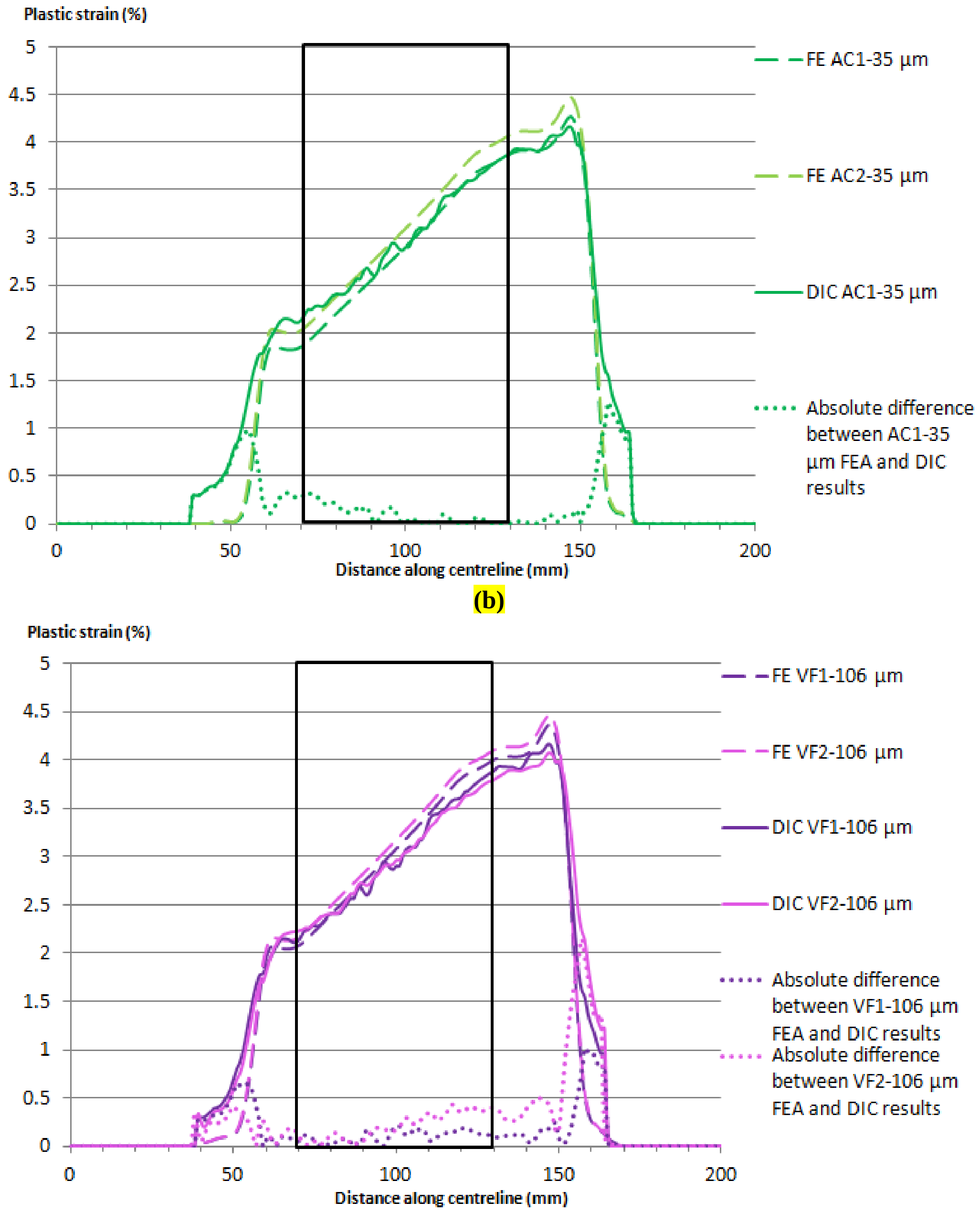

(b)

(c)

Figure 4.31: Comparison of the predicted accumulated plastic strain (FE) with the strain in the loading direction ε_{yy} from DIC (DIC) in AISI 316L AR-27 µm (a), AC-35 µm (b) and VF-106 µm (c) specimens.

Longitudinal strain (%)	**AR2**	**VF2**
Strain gauge rosette (%)	3.98	3.65
DIC	3.88	3.67
FE	4.03	4.20

Table 4.6: Comparison of FE, DIC and strain gauge results.

Figure 4.32 a to d plots the longitudinal plastic strain derived from the DIC and that predicted by the FEA along the centre line of each specimen for each material condition. It can be seen that the difference between FEA and DIC is significantly higher for SA508 microstructures compared to that of AISI 316L. Since DIC data differed from each other for two specimens of the same microstructure (i.e. AR1 and AR2) the origin of the difference is more likely to arise from the DIC than from the FE model. A reasonably uniform difference of less than 1% plastic strain is observed between DIC and FEA over the region of interest of AR1, AR2 Mix1 and Fer2. Mix2, Fer1 and Mar show good agreement between DIC and FEA results, with less than 0.25% absolute value of the plastic strain difference in the region of interest, apart from a difference up to 0.5% plastic strain in the interval from 120 mm to 130 mm along the centreline in Mix2 and Fer1 specimens and between 70 mm and 90 mm in Mar specimen. In Figure 4.32 d for the Mar specimen it can be seen that there is a departure in the DIC data which could be attributed to poor lighting or speckle.

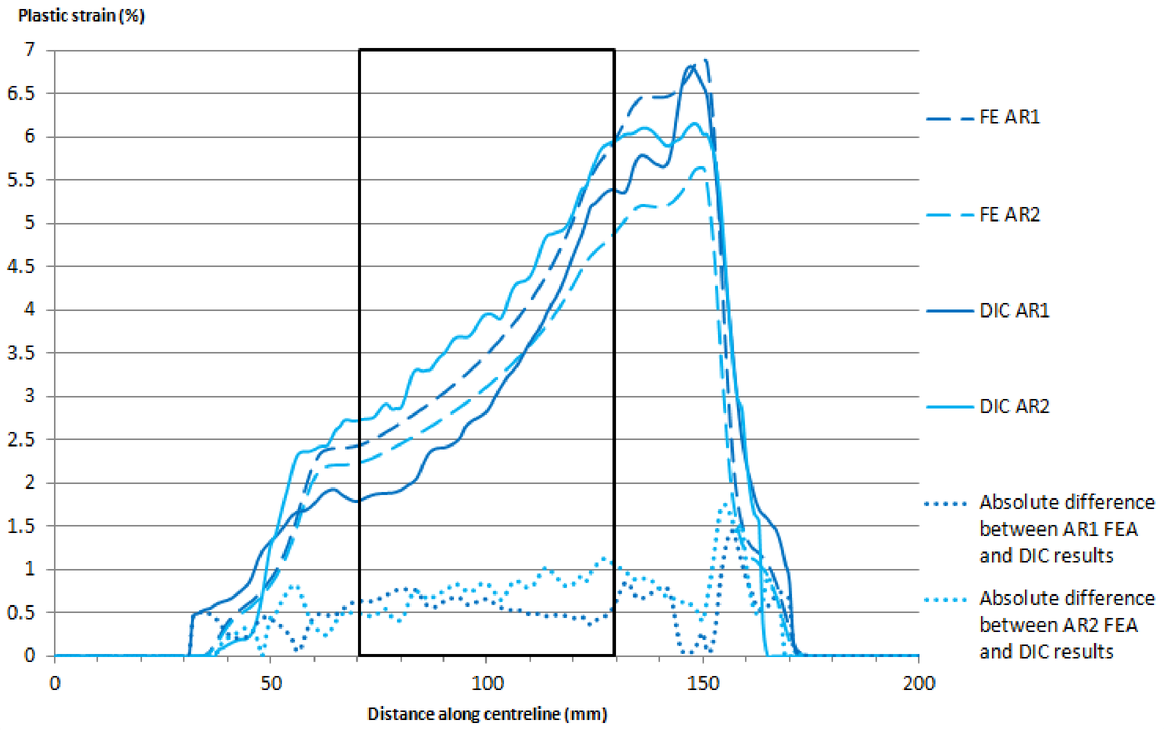

(a)

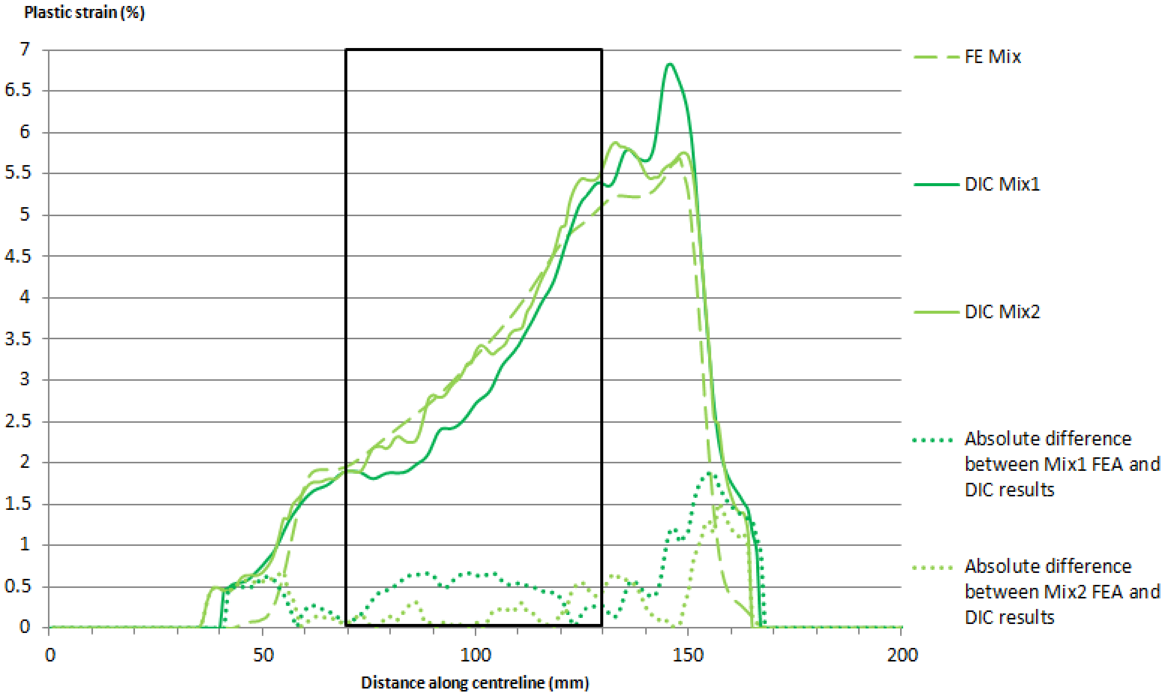
Plastic strain (%)
7
6.5
6
5.5
5
4.5
4
3.5
3
2.5
2
1.5
1
0.5
0
0
50
100
150
200
Distance along centreline (mm)
FE Mix
DIC Mix1
DIC Mix2
Absolute difference between Mix1 FEA and DIC results
Absolute difference between Mix2 FEA and DIC results

(b)

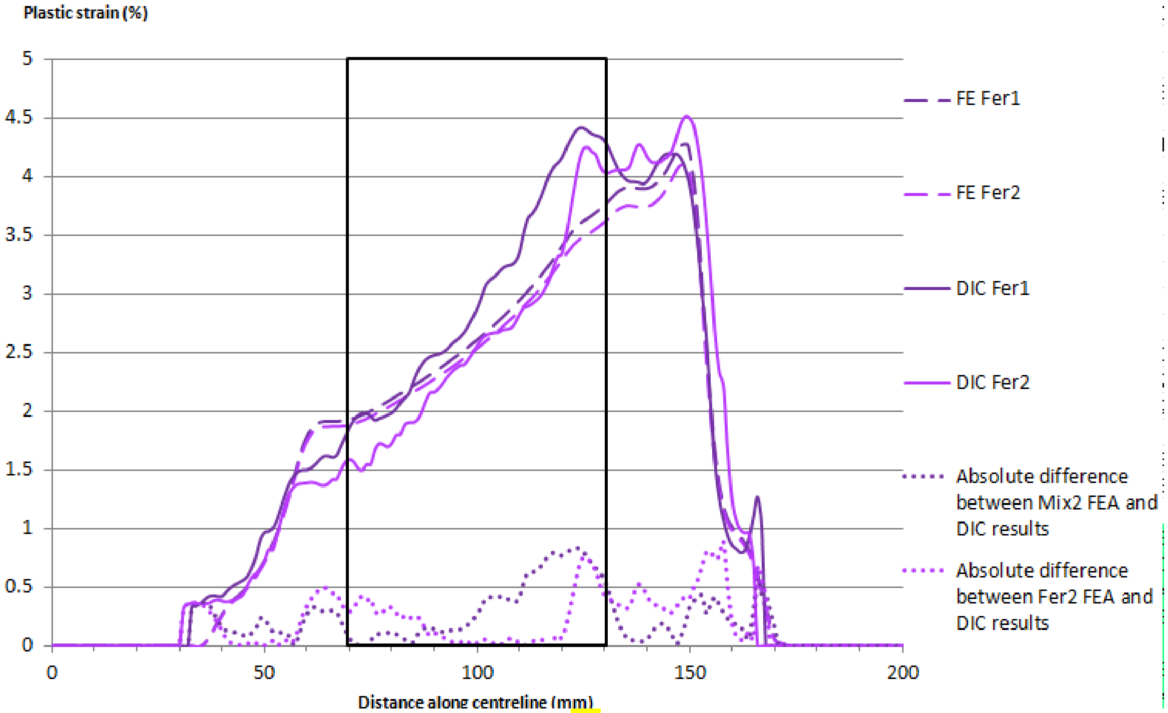
Plastic strain (%)
5
4.5
4
3.5
3
2.5
2
1.5
1
0.5
0
0
50
100
150
200
Distance along centreline (mm)
FE Fer1
FE Fer2
DIC Fer1
DIC Fer2
Absolute difference between Mix2 FEA and DIC results
Absolute difference between Fer2 FEA and DIC results

(c)

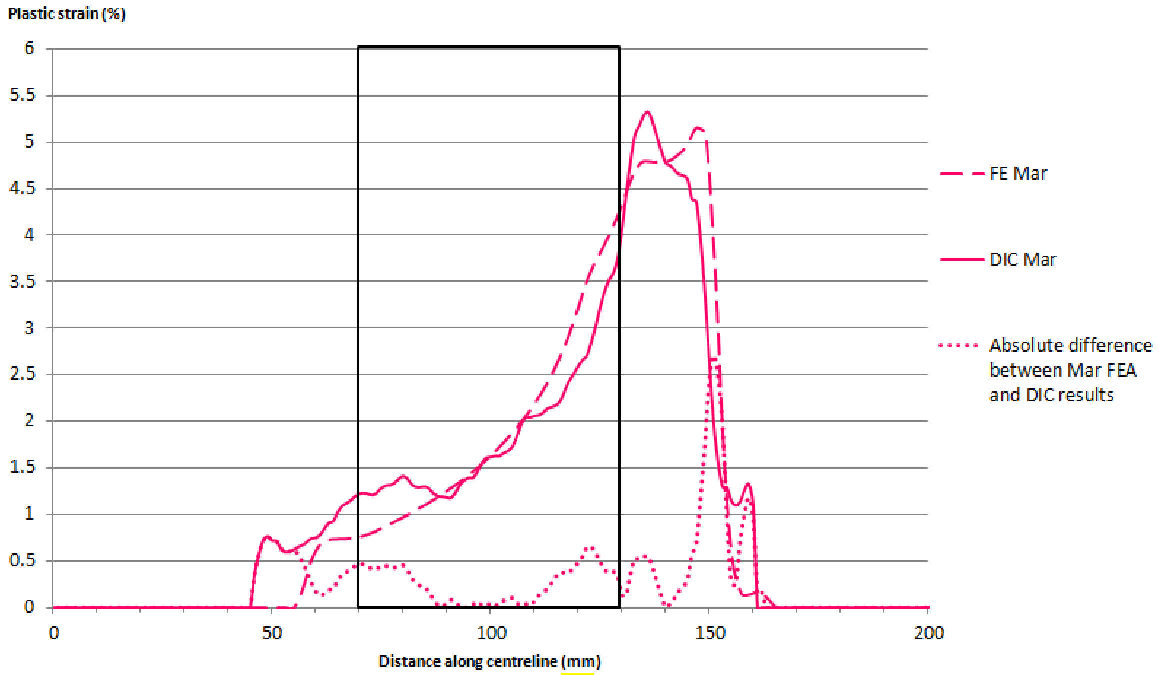

(d)

Figure 4.32: Comparison of the predicted accumulated plastic strain (FE) with the strain in the loading direction ε_{yy} from DIC (DIC) in SA508 AR (a), Mix (b), Fer (c) and Mar (d) specimens.

Longitudinal strain (%)	**AR1**	**AR2**	**Mix1**	**Mix2**	**Fer2**	**Mar**
Strain gauge rosette (%)	5.00	5.00	6.00	4.60	3.17	4.10
DIC	5.28	4.99	6.05	5.00	3.65	4.54
Difference in % between DIC and strain gauge measurements	5.30%	0.2%	0.8%	8%	13.15%	9.7%
FE	5.85	4.90	5.10	5.10	3.60	4.57
Difference in % between FEA predictions and strain gauge measurements	14.5%	2%	17%	9.8%	11.9%	10.3%

Table 4.7: Comparison of FE, DIC and strain gauge results for SA508 specimens.

Table 4.7 provides a comparison between the longitudinal strain given by the strain gauge rosette, the DIC and the FEA for SA508 specimens with the exception of Fer1 as the strain gauge detached before the end of the test. The agreement of Mix2, Fer2 and Mar is of the order of 10% with both FEA and DIC results, which indicates satisfactory agreement between the techniques and the plastic strain predictions from the FEA model are validated by both DIC and strain gauge experiments. The strain gauge data of AR1 and Mix1 however compares better with the DIC measurements than with the FEA data which suggests the discrepancy between FEA and DIC data is caused by a physical phenomenon which would not have been captured by the model. Since the FE model plastic strain predictions and change in the sum of the principal stresses are intended to be used in Chapter 5, AR1 and Mix 1 specimens are discarded from the study.

4.5 Summary

In this section, the absolute value of the difference between DIC and FEA results was calculated along the centreline, in the area of interest.

- The correlation between the two techniques was found to be better for the AISI316L specimens. The larger deviation in the SA508 specimens plastic strain predictions could arise from the DIC tests.
- The values of plastic strain assessed using the FE models in this chapter will be used in Chapter 5. Areas where the plastic strain may be less reliable were identified on each specimen. Specimens for which the DIC data and strain gauge measurements do not validate the FEA predictions are discarded from the study, as the model is used in both plastic strain assessment and thermoelastic constant derivation.

Chapter 5: Identifying the dependence of the thermoelastic response on plastic strain

5.1 Introduction

The thermoelastic constants of 316L austenitic stainless steel specimens that had not been subjected to plastic strain were studied in Chapter 3. The results indicated that the grain size does not influence the thermoelastic constant significantly, i.e. within the threshold of precision given by Robinson [10]. The thermoelastic constants of samples of SA508 ferritic stainless steel with different material phase proportions samples that had not been subject to plastic straining were derived in Chapter 3 and found to be within 6% of each other. To inform on the influence of SSPT, the thermoelastic response of material with different phase proportions subject to plastic straining must be established.

In Chapter 4 a specimen that includes a taper so that a known gradient of plastic strain is introduced in the specimen by simple uniaxial loading was designed. So that identical microstructures could be maintained, the specimens were manufactured from the strip specimens described in Chapter 3. The plastic strain induced in the tapered specimens was measured using DIC and strain gauges during loading and predicted using FEA.

The purpose of the present chapter is to assess the dependence of *K*, for the microstructures studied in Chapter 3, on plastic strain. The thermoelastic response is obtained by performing TSA on the tapered specimens, and is presented in section 5.2. The change in the sum of the principal stresses due to the elastic loading applied to the specimens during the TSA tests must be known to derive the thermoelastic constant. This quantity is predicted using FEA in section 5.3 and the confidence in the predictions is discussed. In section 5.4, the relationship between the thermoelastic constant and plastic strain is presented for different grain sizes in AISI 316L and for different phase proportions in SA508. The results are discussed and conclusions from the study are drawn. Finally, in section 5.5, a summary of Chapters 3, 4 and 5 conclusions on the overall influence of the microstructure on the dependence of thermoelastic response to plastic strain is presented.

5.2 Specimen preparation and experimental work

The polishing and abrasion history of the specimens from strip to deformed tapered specimens is depicted in Figure 5.1. In Chapter 3 the thermoelastic constant, K_0, is derived for the strip specimens for each microstructure. Prior to testing, all of the strip specimens were abraded with sand paper and cleaned with acetone before a thin layer of Electrolube matt black paint was applied. After this work was completed approximately 18 months passed before making the tapered specimens, which were cut from the strip specimens, as described in Chapter 4. Prior to the EDM cutting, the original paint was removed and then paint applied to make a speckle pattern to facilitate the DIC described in Chapter 4. After the tapered specimens were deformed and the plastic strain was induced (see Chapter 4), the speckle pattern was removed by cleaning with acetone and a thin layer (30.55 μm on average with a coefficient of variation of 10.65%) of Electrolube matt black paint was applied; it should be noted that the specimens were not abraded in case of modifying the plastic strain developed by the applied loading described in Chapter 4.

The test specimens were mounted in a servo-hydraulic test machine. A tensile sinusoidal cyclic loading of 2.5 ± 1.5 kN was applied at a frequency of 10 Hz. This loading was selected to create a change in temperature larger than 50 mK while ensuring the loading remains elastic in the region of interest. A Cedip Silver 480M infrared camera was used to record temperatures. The detector recorded the infrared radiation from the surface of the specimen for 3 s at a frame rate of 383 Hz and integration time of 1332 μs. The IR camera was found to be out of calibration and measuring consistently 4 °C less than the actual temperature which produces a reduction of the thermoelastic response of 1.4% and is corrected for in all of the data presented in the thesis.

The results showed that the thermoelastic response was around 20% higher when compared to the results in Chapter 3 from the strip specimens (from which the tapered specimens were made). This was consistent for both materials and all microstructures. Therefore it was decided to abrade the specimens as it was considered that an oxide layer may have developed on the specimens which modified the thermoelastic constant. The specimens were abraded with sand paper of grit average particle diameter of 220 μm and the tests were performed again. The thermoelastic response was found to be on average 6 % higher for AISI 316L and 5.7% higher for SA508 specimens compared to the results in Chapter 3. A comparison of ΔT from the abraded samples and non-abraded samples can be seen in Figure 5.2 for AISI 316L and Figure 5.3 for SA508. In the remaining parts of the thesis, the analysis presented is based on the ΔT values from the abraded specimen.

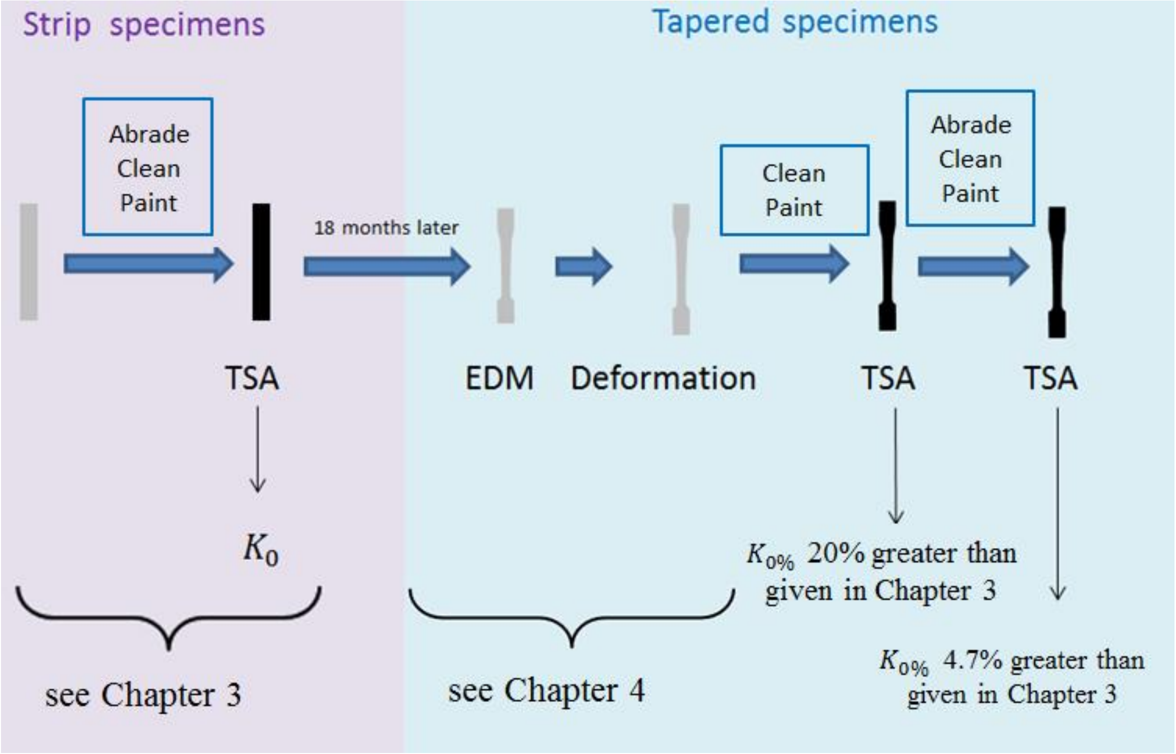

Figure 5.1: Specimen production and preparation.

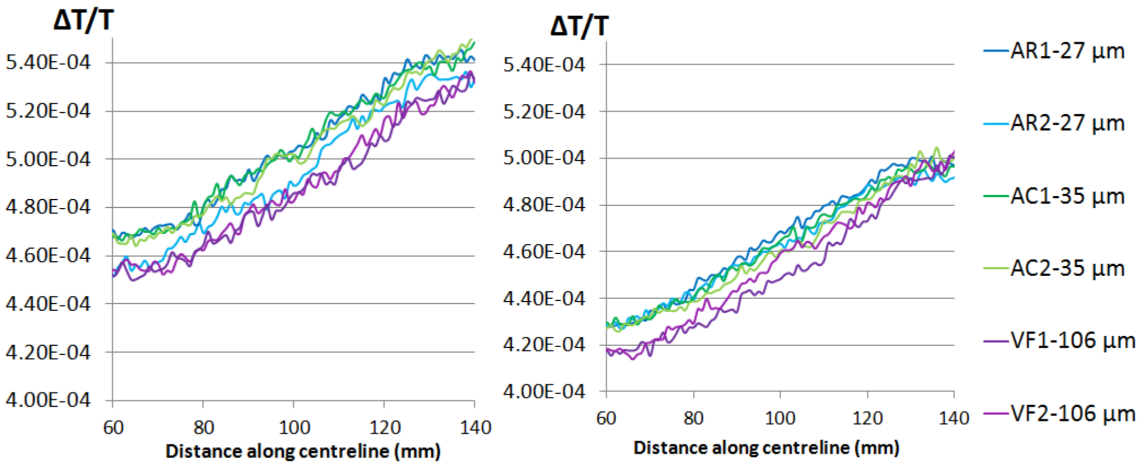

(a) (b)

Figure 5.2: Thermoelastic responses of the non-abraded (a) and abraded (b) AISI 316L specimens.

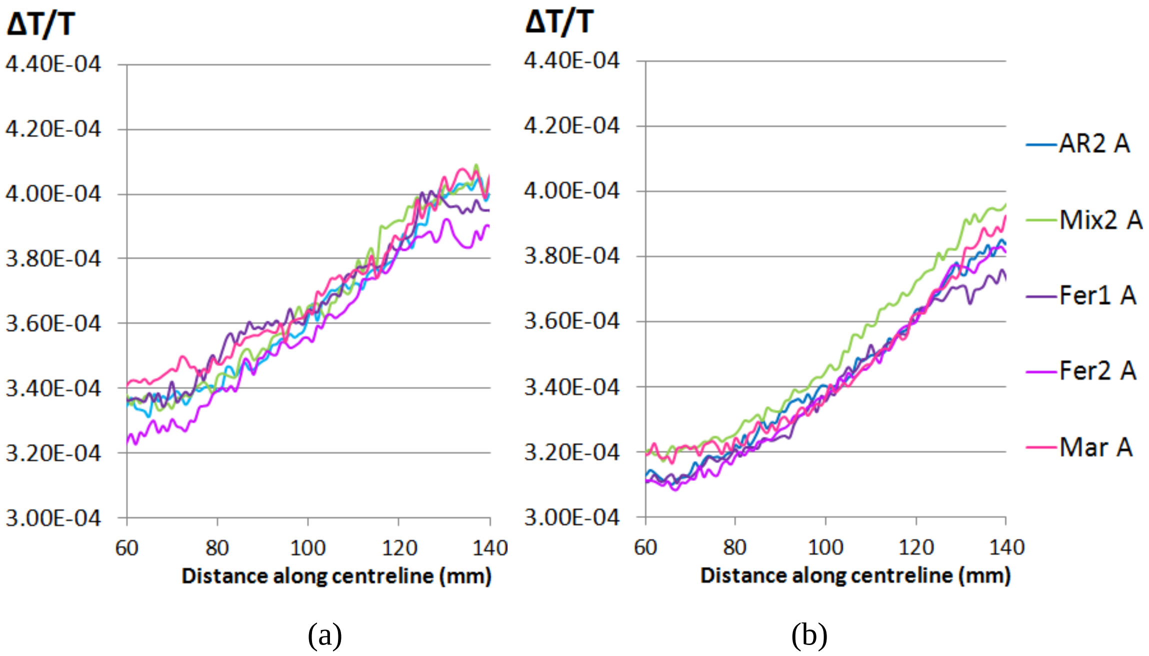

Figure 5.3: Thermoelastic responses of the non-abraded (a) and abraded (b) SA508 specimens.

5.3 FE model of the tapered test specimens

To derive *K* from the thermoelastic data presented in the previous section it is necessary to establish the change in the sum of the principal stresses, $\Delta\sigma_1+\Delta\sigma_2$, resulting from the load applied to each specimen. This is not straightforward because of the difference in material condition as each specimen was subjected to different displacement to achieve the desired level of plastic deformation, as described in Chapter 4. A further complication is that the initial geometry of the tapered specimens differed from tenth of millimetres from the designed shape due to inaccuracies in the manufacturing process. Therefore the final geometry of the all the tapered specimens is different. The difference is small; a few millimetres in length and a few tenths of a millimetre thinner in the width and thickness. As the change in thermoelastic constant expected from plastic strain is of the order of magnitude of 1.5%, even small changes in geometry could mask the effect of plastic strain. An error in the estimation of $\Delta\sigma_1+\Delta\sigma_2$ of 1.5%, is generated by a change in the cross-sectional area of 1.25 % hence differences in the width and thickness of specimens of the order of one tenth of a millimetre are important and are present in the tapered specimen. Therefore two approaches have been taken to obtain the final deformed shape of the tapered specimens and are used to establish $\Delta\sigma_1+\Delta\sigma_2$ for each specimen in an attempt to bound the influence of the geometry; these are described below:

Case 1: Linear elastic models of the deformed specimens were created using quadratic C3D20R element in ABAQUS. The geometry of each deformed specimens was measured using an electronic calliper tool of 0.01 mm precision. The dimensions of the AISI 316L specimens are presented in Table 5.1 and in Table 5.2 for SA508 specimens. The change in the sum of the principal stresses, $\Delta\sigma_1+\Delta\sigma_2$, experienced by each specimen, was determined by applying a static load, ΔF, equivalent to the load range applied to the specimens during the collection of the thermoelastic data. The top surface displacement is set to zero in all directions to represent the clamping boundary condition. The difference in elastic load applied for the TSA is applied to a point, referred as “reference point”, which is kinematically coupled in all directions to the bottom gripped surfaces of the specimen, as depicted in Figure 5.4.

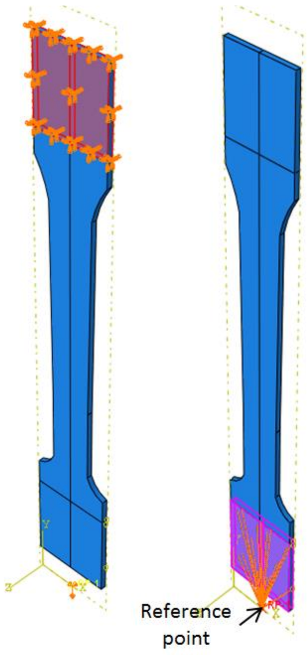

Figure 5.4: Boundary conditions and load application applied to the linear elastic FE model.

AISI 316L	AR1-27µm	AR2-27µm	AC1-35µm	AC2-35µm	VF1-106µm	VF2-106µm	Average	Standard deviation
40	29.58	29.65	29.45	29.43	29.61	29.63	29.56	0.09
53	18.46	18.49	18.43	18.50	18.62	18.63	18.52	0.08
130	15.54	15.49	15.54	15.64	15.58	15.52	15.55	0.05
155	15.57	15.57	15.62	15.64	15.58	15.58	15.59	0.02
165	29.56	29.44	29.37	29.56	29.62	29.57	29.52	0.08
thickness	1.99	1.94	1.96	1.97	1.99	1.96	1.97	0.016

Table 5.1: **Average measured widths and thickness of the AISI 316L specimens after deformation.**

SA508	AR1	AR2	Mix1	Mix2	Fer1	Fer2	Mar	Average	Standard deviation
40	30.30	30.28	30.06	30.91	30.21	30.16	30.14	30.29	0.26
53	18.47	18.52	18.46	18.41	18.54	18.50	18.50	18.48	0.04
130	15.40	15.46	15.4	15.45	15.68	15.55	15.48	15.49	0.08
155	15.52	15.51	15.51	15.48	15.71	15.61	15.62	15.56	0.07
165	29.36	29.33	29.28	29.25	29.34	29.29	29.33	29.31	0.03
thickness	2.06	2.10	1.99	2.05	1.99	2.07	1.99	2.03	0.04

Table 5.2: **Average measured widths and thickness of the SA508 specimens after deformation.**

Case 2: Instead of measuring, the geometry the elastic-plastic FEA of the deformation described in Chapter 4 was used to establish the final deformed shape of the each specimen. A displacement was applied to each specimen model and relaxed, then ΔF was applied in the same way as Case 1 to obtain $\Delta\sigma_1+\Delta\sigma_2$. Due to the presence of residual stresses in the model, as depicted in Figure 5.5, the analysis was restricted to the area where the residual stress was lower than 0.2 MPa. It should be noted that the residual stress only has an effect on the model; it has been shown that the thermoelastic response of steel is not dependent on the mean or residual stress [10]. Therefore it should be possible to simply subtract the effect of the residual stress from the predicted $\Delta\sigma_1+\Delta\sigma_2$ from the model but this is a cumbersome procedure so only data from the central portion of the specimens was used as indicated in Figure 5.5.

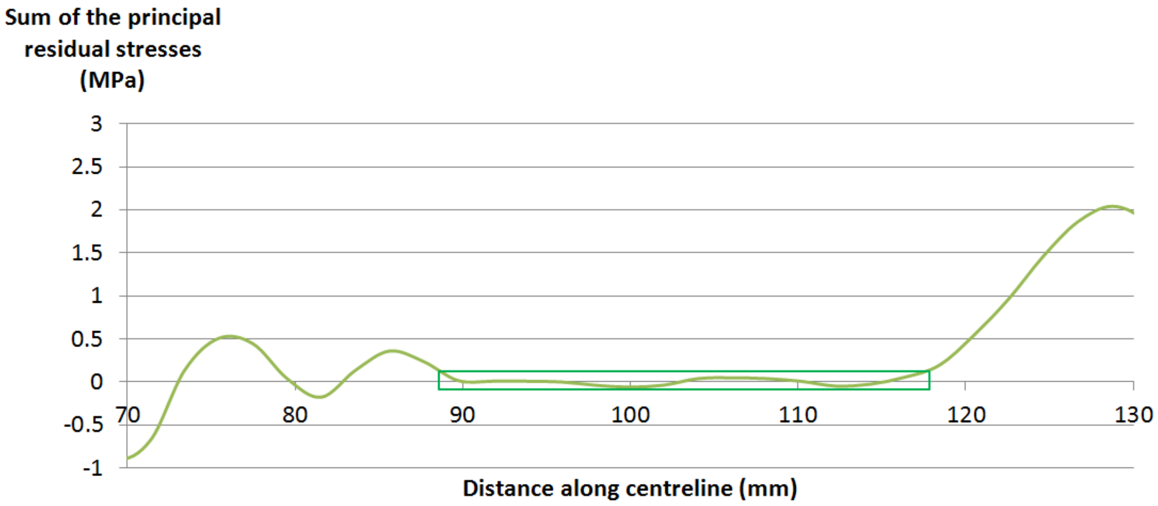

Figure 5.5: Sum of the principal residual stresses after deformation in AR1-27µm and extent of usable data in Case 2.

The change in the sum of the principal stresses along the centreline of each specimen is shown in Figure 5.6 for the AISI 316L specimens and in Figure 5.7 for the SA508 specimens. Case 1 is shown with the dotted line and Case 2 is shown with the full lines and it can be seen that there is a difference of a few MPa between each cases for each material type. There is a much greater deviation in the Case 1 results as these take account of the actual initial shape of the specimens; in Chapter 4 it is explained that there were some manufacturing inaccuracies which resulted in the shape of each specimen not being identical to the originally designed shape. In Case 2, there is a much smaller deviation as the models did not account for the initial difference in shape. In all cases errors in the prediction of the stress experienced in the specimens will cause a discrepancy in the calculation of *K* that may be of the same order of magnitude of that caused by the plastic straining. It is clear from Figure 5.6 and Figure 5.7 that using the Case 2 approach over predicts the stresses by an amount that will influence the calculation of *K*. It is also clear that both the Case 1 and Case 2 data sets provide approximately the same gradient in the $\Delta\sigma_1+\Delta\sigma_2$ with respect to specimen position. Thus, indicating that the slight anomalies in the shapes have little influence on the rate of change in stress along the centreline of the tapered specimen and justifying neglecting the actual deformed shapes from the predications of plastic strain in Chapter 4. Hence in the further analysis presented in the chapter the stresses to determine *K* are the ones derived from Case 1.

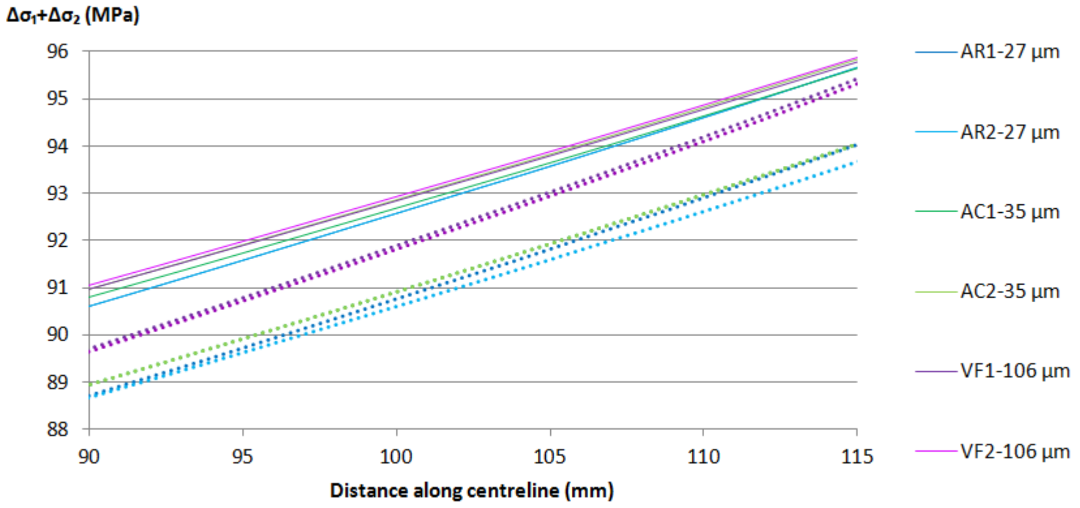

Figure 5.6: Change in the sum of the principal stresses predictions for AISI 316L specimens with Case 1 (dotted lines) and Case 2 (full lines) FE models.

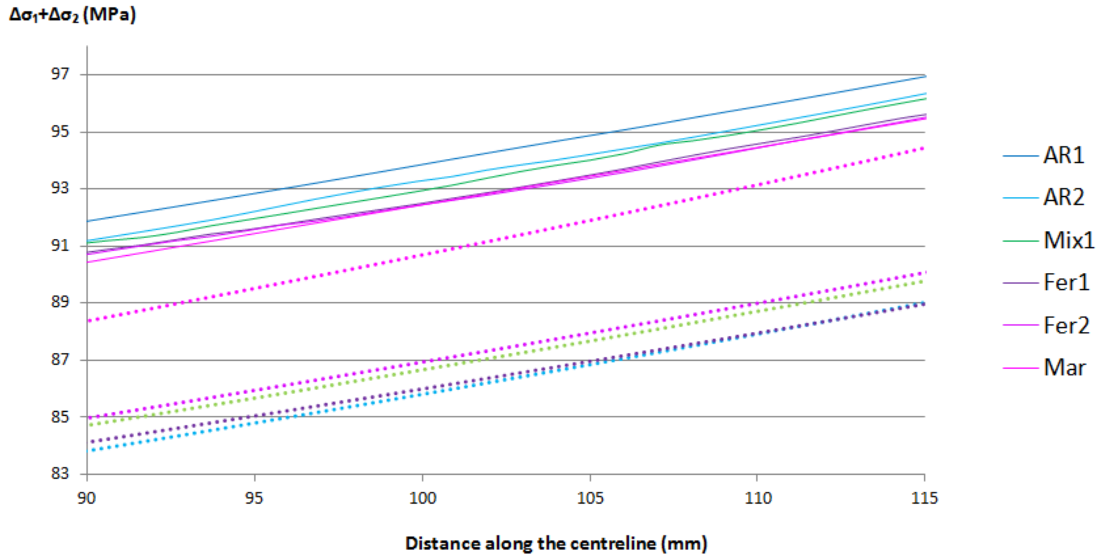

Figure 5.7: Change in the sum of the principal stresses predictions for SA508 specimens with Case 1 (dotted lines) and Case 2 (full lines) FE models

5.4 Derivation of the thermoelastic constant

To derive the thermoelastic constant, K, full field maps of the thermoelastic response $\Delta T/T$ and the sum of the principal stresses $\Delta\sigma_1+\Delta\sigma_2$, derived from Case 1, were imported in MATLAB and combined to give full field maps of K. In Figure 5.8 full field maps are presented for all AISI 316L (left) and SA508 (right) specimens.

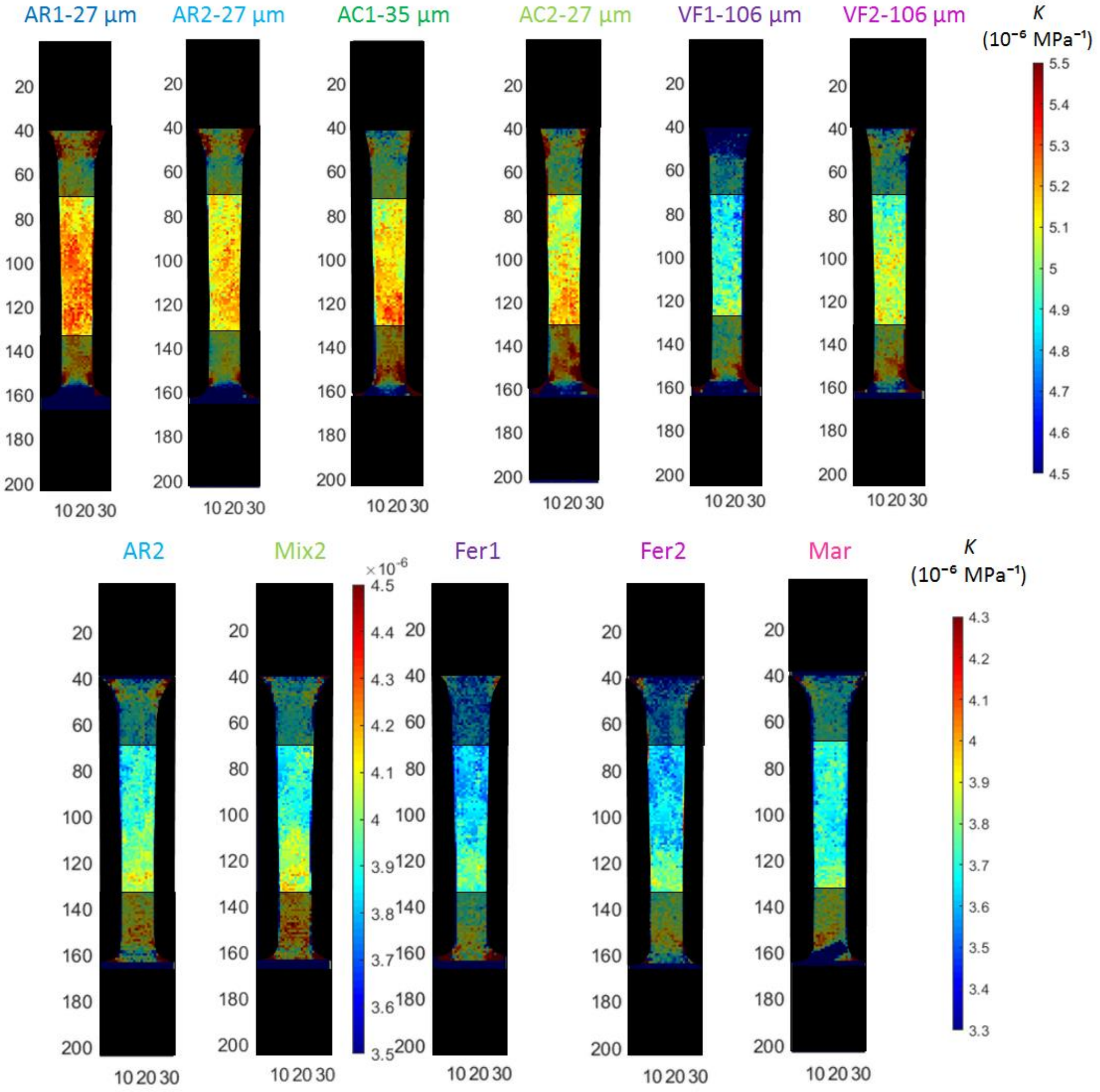

Figure 5.8: Full field plots of K values of 316L specimens (top) and SA508 specimens (bottom) .

The thermoelastic constants were derived using the $\Delta\sigma_1 + \Delta\sigma_2$ values from Case 1 and normalised against the extrapolated $K_{0\%}$ value for a clearer presentation of the influence of plastic strain. The extrapolated $K_{0\%}$ values are reported in Table 5.4 and Table 5.6 for AISI 316L and SA508 respectively. The values are plotted against the FEA plastic strain predictions established in Chapter 4 in Figure 5.9 for the different conditions of the 316L stainless steel and in Figure 5.12 for SA508 microstructures. A linear interpolation is made for each data set and specified in the legend of each figure.

The gradients of the linear interpolations of K against plastic strain for the different AISI 316L microstructures are presented in Figure 5.10 and the values are reported in Table 5.3. It can be noticed that the gradients of the linear interpolations of the coarser grained specimens are larger than those of smaller grained specimens. These results indicate a larger influence of the plastic strain on coarser grained microstructures. From the gradient values reported in Table 5.3, it can be noticed that the gradient values of the fined-grained microstructures (0.0028 for AR-27 μm and 0.0034 for AC-35 μm) are significantly smaller compared to the gradient of the coarser grained microstructure (0.0056 for the VF-106 μm). This is consistent with results from Robinson [10], and is not surprising since the material used in [10] was not heat treated to the annealing temperature and hence a microstructure similar to the as received material is expected.

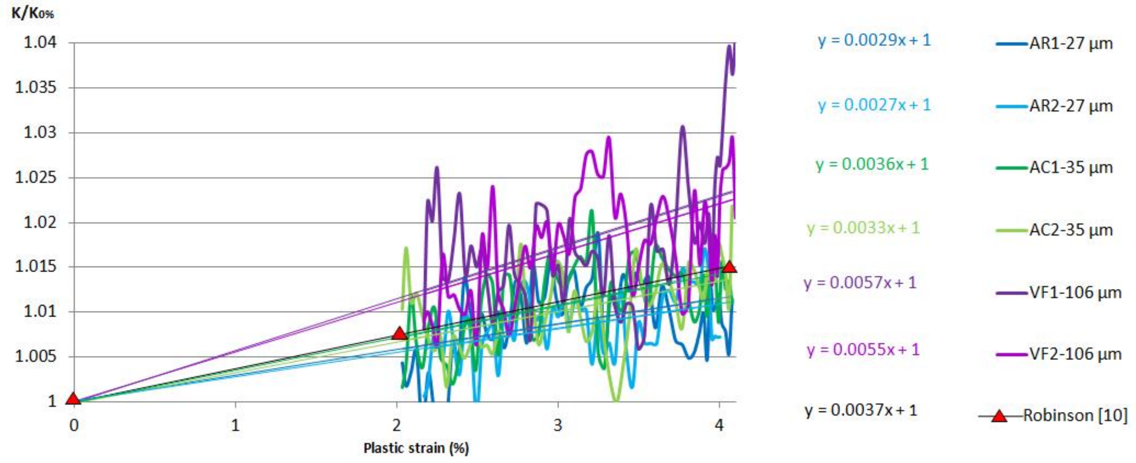

Figure 5.9: Normalised thermoelastic constant variation with plastic strain in AISI 316L microstructures derived with Case 1 and respective linear interpolation equations.

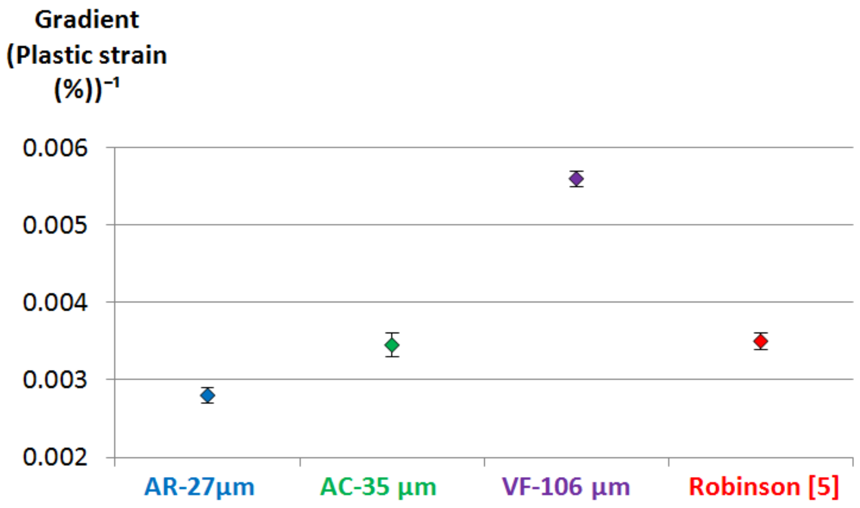

Figure 5.10: Linear interpolation gradients normalised against the extrapolated $K_{0\%}$ of AISI 316L specimens and gradient derived from Robinson [10]

AISI 316L	AR – 27μm	AC – 35 μm	VF – 106 μm	Robinson [10]
Average	0.0028	0.0034	0.0056	0.0037
Standard deviation	0.0001	0.00015	0.0001	0.00011

Table 5.3: Average of the linear interpolation gradients (in % plastic strain) of the thermoelastic constant of AISI 316L specimens against plastic strain for both specimens of each microstructure and standard deviation.

The extrapolated values of the thermoelastic constant at 0% plastic strain are presented in Figure 5.11. The data indicate that $K_{0\%}$ values are larger for finer grained specimens. It should be noticed that this result contradicts the results from Chapter 3. The $K_{0\%}$ values were averaged and compared with the thermoelastic constant calculated in Chapter 3 in Table 5.4. Increases of 8% and 7% were observed in AR-27 μm and AC-35 μm $K_{0\%}$ values, whereas a lower increase of 3% was observed for VF-106 μm. One possible explanation of this variation could be the time that has passed between the two sets of experiments, potentially leading to chemical reactions related to ageing. It can be noticed that the variation in K values for material free of plastic strain also indicates a dependence on grain size, the results suggest the chemical reaction leading to higher values of K would be more significant for finer grains compared to coarse grains. The difference in $K_{0\%}$ values compared to those derived in Chapter 3 is unexpected. However, it can be pointed out that the $K_{0\%}$values derived here comply with expectations from the introduction chapter i.e. if K is influenced by plastic strain it is likely that the dislocation density influences K. In fine grained microstructures it is likely that dislocation density is larger than that of the coarse grained microstructure hence a larger K value might be expected as observed here.

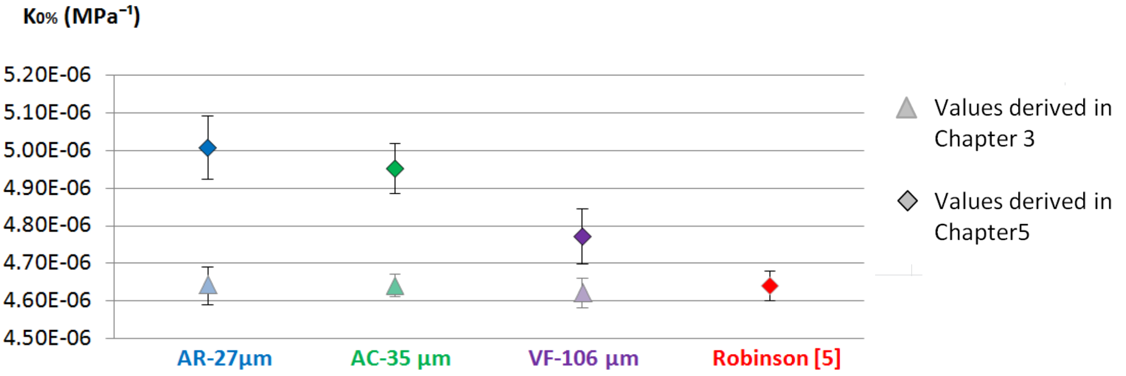

Figure 5.11: Extrapolated thermoelastic constant at 0% plastic strain of AISI 316L specimens and thermoelastic constant at 0% plastic strain from Robinson [10].

AISI 316L	AR – 27μm	AC – 35 μm	VF – 106 μm
K_0 measured in Chapter 3 (10^{-6} MPa^{-1})	4.64	4.64	4.62
$K_{0\%}$, intercept (10^{-6} MPa^{-1})	5.01	4.95	4.77
Difference	8%	7%	3%

Table 5.4: **Thermoelastic constant with no plastic strain measured in Chapter 3 compared with the intercept of the calibration curves and deviation for AISI 316L specimens.**

Unlike the comparison for 316L microstructures, it would not be appropriate to discuss the results for SA508 specimens based on grain size. For instance, two dimensions are required to characterise a martensite lathe, which is typically between a few hundred nano-meters and a couple of microns in width and up to a few hundred microns in length. Hence the different microstructures are discriminated on their relative dislocation density. Martensite forms by a shear mechanism, it induces a significant strain fields around it and this can lead to dislocation rich regions of soft material around the martensite. Since the transformation is diffusionless, pre-existing dislocations are likely to be retained. Hence it is assumed the Mar specimens contained dislocations before the plastic straining. The AR specimens were extracted from a bulk of material which may contain dislocations prior to plastic straining from manufacturing processes. The Fer specimens were heated up to annealing temperature and significant grain growth was observed in Chapter 3. It is assumed the Fer specimens were free of dislocation before plastic straining. The Mix specimens were heated up to 800°C, which allowed a certain amount of stresses and plastic strains to be relaxed. Hence the dislocation density is likely to be greater than that of Fer and lower than that of AR and Mar specimens.

In Figure 5.13 it can be noticed that the gradient of the linear interpolation of specimens of lower dislocation densities are larger than that of higher dislocation densities. This result can also be seen in Table 5.5 as the average value of Fer specimens is of 0.031, which is larger than that of Mix (0.025), which is also larger than those of AR (0.013) and Mar (0.012). The coefficient of variation is reported in Table 5.5 only for the Fer specimens as only one specimen of AR, Mix and Mar was retained in the study. However, it can be seen as with the 316L specimens, there is a clear indication of a larger influence of the plastic strain on microstructures with lower dislocation densities. Moreover, a coarsed-grained microstructure means a lower dislocation density compared to a fined-grained microstructure. Hence the indication of a larger influence of the plastic strain on the thermoelastic constant for microstructures with lower dislocation density is supported by the results from both SA508 and 316L steels.

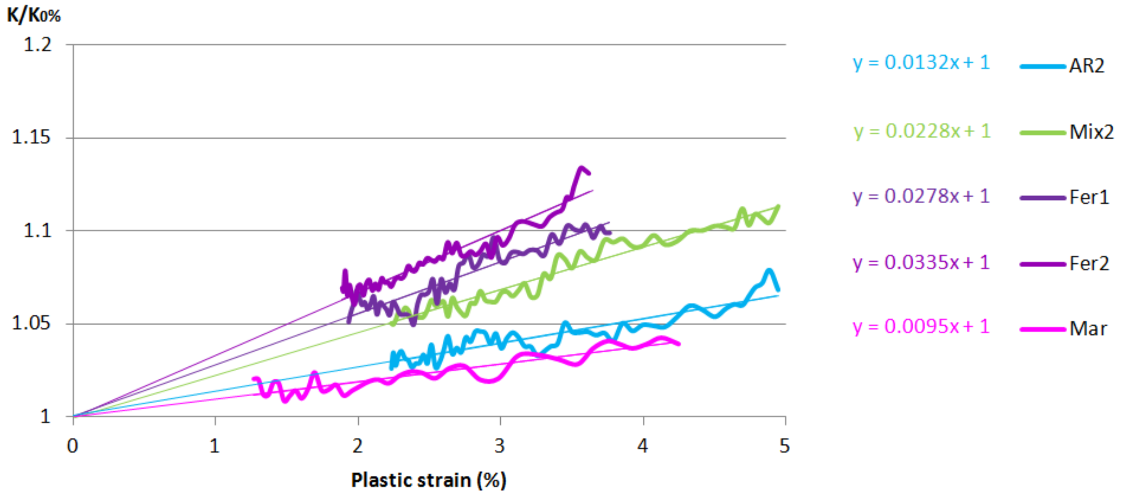

Figure 5.12: Normalised thermoelastic constant variation with plastic strain in SA508 microstructures derived with Case 1 and respective linear interpolation equation.

Figure 5.13: Linear interpolation gradient normalised against the extrapolated 0% plastic strain thermoelastic constant of SA508 specimens.

SA508	AR	Mix	Fer	Mar
Average	0.013	0.025	0.031	0.012
Standard deviation	N/A	N/A	0.001	N/A

Table 5.5: Average of the linear interpolation gradient (all in per % plastic strain) of the thermoelastic constant of SA508 specimens against plastic strain derived using Case 1, Case 2, for both specimen of each microstructure and coefficient of variation

The extrapolated values of the thermoelastic constant at 0% plastic strain are presented in Figure 5.14. Compared to the $K_{0\%}$ values derived in Chapter 3, some differences are noticed, with smaller K values for microstructures with fewer dislocations ($3.57\ 10^{-6}\ \mathrm{MPa}^{-1}$ for Fer specimens compared to $3.65\ 10^{-6} MPa^{-1}$, $3.67\ 10^{-6} MPa^{-1}$ and $3.67\ 10^{-6} MPa^{-1}$ for AR, Mix and Mar specimens.

An influence of the microstructure on both gradient and intercept has been observed. From the results presented, the thermoelastic constant of a material with low dislocation density would be more sensitive to a variation in plastic strain compared to a high dislocation density microstructure.

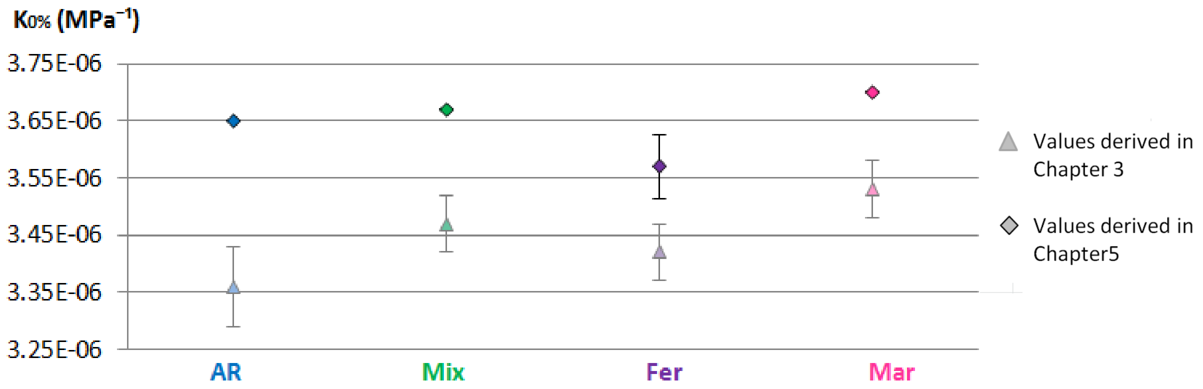

Figure 5.14: Extrapolated thermoelastic constant at 0% plastic strain of SA508 specimens.

SA508	AR	Mix	Fer	Mar
K_0 measured in Chapter 3 (10^{-6} MPa^{-1})	3.36	3.47	3.42	3.53
$K_{0\%}$, intercept (10^{-6} MPa^{-1})	3.65	3.67	3.57	3.67
Coefficient of variation (%)	12%	5%	4%	2%

Table 5.6: **Thermoelastic constant with no plastic strain measured in Chapter 3 compared with the intercept of the calibration curves and deviation for SA508 specimens.**

5.5 Summary

The thermoelastic response from the tapered test specimens (described in Chapter 4) that had been plastic strained was obtained and the results were described in the present chapter. The dependence of the thermoelastic constant on plastic strain was determined. The results showed that the thermoelastic constant is dependent on plastic strain and that the level of the dependence is influenced by the dislocation density in both AISI 316L and in SA508. The results confirm an increase in K for tensile plastic strain which for AISI 316L is in agreement with [10]. It was shown for both material types, fewer dislocations make the material more sensitive to changes in plastic strain. Furthermore, the $K_{0\%}$ values for microstructures with large dislocation densities are greater than those with fewer dislocations**.**

It may be concluded that materials with lower dislocation density will have a lower thermoelastic constant but a greater sensitivity to plastic strain. If a there is a significant change in average grain size, e. g. a ratio of 10, or in phase, with presence of martensite and large grains of ferrite in the region of interest, the thermoelastic constant may vary with both microstructure and plastic strain and the variations may be of the same order of magnitude. Thus when attempting to deduce the WIP from changes in thermoelastic constant a consideration of the material microstructural changes as a result of welding is necessary.

An important consideration when applying TSA has been identified. A variation of 20% on average over the thermoelastic responses of all the specimens was observed as a result of the condition of the specimen surface. The thermoelastic response from the oxide layer that had formed over a period of 18 months was shown to have significant influence increasing the response. When the layer was removed the response reduced to the level observed in new specimens. However, a larger K_0 value was still obtained than that measured in Chapter 3 for the as received and air cooled material compared to vacuum furnace cooled material. The origin of the variation was not clarified. A potential explanation could lie in the occurrence of a chemical reaction between the paint and the surface of the specimens, as the specimens were left with paint on for eighteen month before being cleaned with acetone. The origin of the change was not clear. It is however suggested that the ageing/chemical reaction is itself influenced by the grain size and the depth of influence of this reaction would have to be significant enough not to be removed by the abrasion performed during the sample preparation.

Chapter 6: Defining the thermoelastic response from a welded component: Mock-up A

6.1 **Introduction**

It has been shown that the thermoelastic response is influenced by plastic strain experienced by a component [10]. The observation that the plastic strain can change the thermoelastic response has only be verified for components that have been directly mechanically deformed, and not caused by heating and cooling as experienced in a welding process. One of the aims in the current PhD project is to assess the feasibility of applying TSA to welded components to assess the plastic strain.

The first step in the process is to design a welded component that contains a sufficient amount of plastic strain to produce a detectable change in the thermoelastic response. It was therefore decided to adopt an approach used in industry and create a 'mock-up'. Mock-ups are used in industry for the validation of FE models, when it is not possible to obtain measurements from the actual structure (e.g. in the nuclear industry). The structure or a part of the structure is manufactured, at the same dimension or at a different scale and measurements are performed on the mock-up, e.g. to give information to calibrate and validate the FE model. Once the FE model is validated, it can be used to predict distortion, stresses, fatigue resistance etc.

The aim of the work described in this chapter is to define a procedure to assess the potential of using TSA for plastic strain assessment using mock-ups. The proposed procedure is given in Figure 6.1. In the current PhD the focus is on predicting the plastic strains by modelling the welding process. The thermoelastic response, $\frac{\Delta T}{T}_{TSA}$, of the mock-up was obtained by Geoff Howell in a parallel PhD project [94], the different activities of the present PhD and that of [94] are shown in Figure 6.1. An FE model of loaded mock-up was also produced in [94] to derive the thermoelastic response of the mock-up (neglecting the effects of welding) and termed this FE model as a "synthetic bitmap" of thermoelastic data. The response calculated from the synthetic bitmap $\frac{\Delta T}{T}_{FE}$ was subtracted from the experimental thermoelastic response to identify regions where the weld induced plastic strain changes the thermoelastic response. In the present chapter the regions identified where plastic strain may exist [94] are compared with the predicted plastic strains predicted using the FE model of Mock-up A described in this chapter.

The idea behind Mock-up A was to create a simple weld specimen where the plastic strain and residual stress are known. The creation of such a mock-up requires a design step to take into account all requirements concerning manufacturing of the weld and the mock-up as well as the TSA testing, which are described in the chapter. Design and manufacturing of the mock-up are presented. A FE model of the welded plate is created, calibrated and validated against experimental measurements. Manufacturing and FE modelling results of the mock-up up are discussed and features of a new mock-up, Mock-up B, are suggested, based on conclusions drawn from Mock-up A.

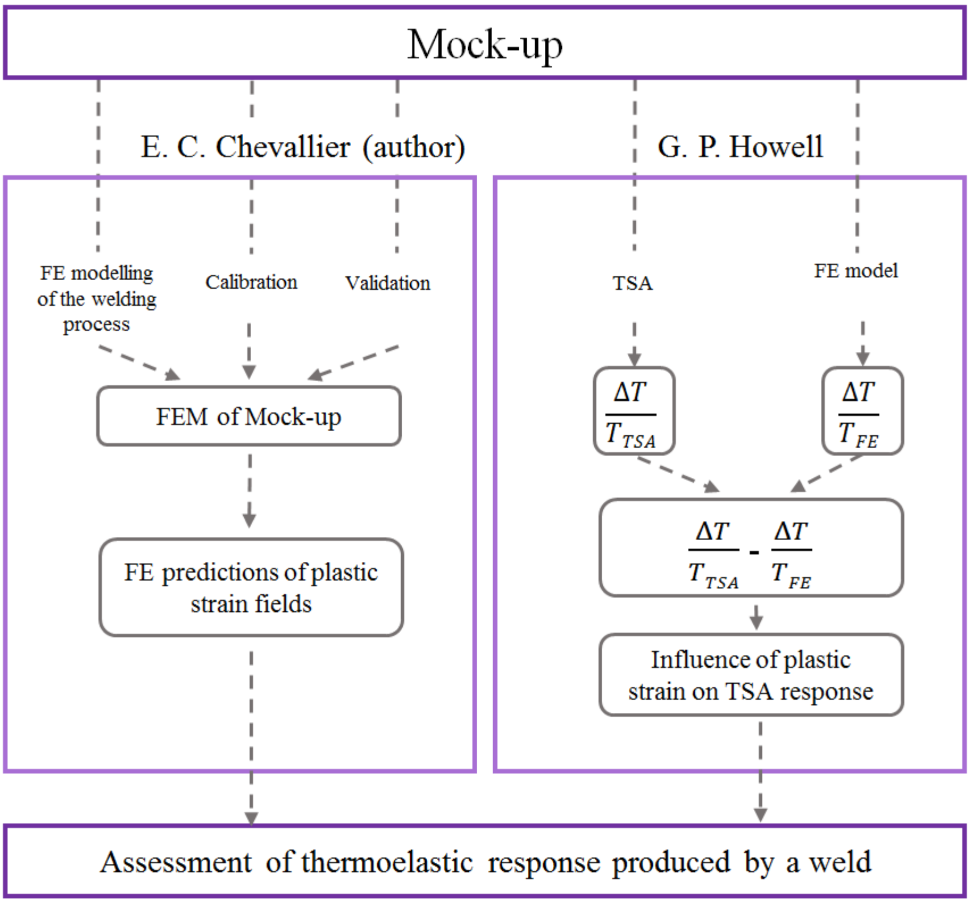

Figure 6.1: Procedure to compare the plastic strain prediction from FE model of the mock-up with TSA PSA results.

6.2 Realisation of the mock-up

Figure 6.2 shows the geometry and dimensions of Mock-up A. It is a strip of material with a welded section at the centre. It is essentially a slice through a weld, where the weld penetration in the base material can be imaged. The proposed imaged region is shown in green on Figure 6.2 which is a zoom-in on the weld. To apply TSA it is necessary to load the component, it is proposed to apply a tension load to Mock-up A as shown in Figure 6.2. For the TSA it is desirable that the applied stress field through the thickness of the specimen is uniform. To this end it was decided that the specimen should be as thin as possible, at around 7 mm. The other dimensions of the specimen were decided upon to facilitate loading, i.e. 40 mm gripping length and also to give a region of interest that resulted in a good resolution for TSA and without the need for higher magnification. It should be noted that the mock-up specimen should not contain distortion because of the welding process hence the specimen is symmetrical with a weld on both edges.

To realise the mock-up specimen it was decided to produce the specimen from a large plate, with a weldment on either side at the centre as shown in Figure 6.3, known as a double bead-on-plate. Here only filler metal is added on top and bottom of the plate, removing the added complexity of joining two metal pieces but replicating realistic temperature fields that cause plastic straining in an actual weld. To minimise distortion the welds on each side of the plate were produced simultaneously and then the specimen was cut as shown in Figure 6.3. The difficulty here is to ensure there is no distortion caused by residual stress release during the cutting.

The bead-on-plate specimen was AISI 316L stainless steel and the deposited weldment material is 308 stainless steel. The chemical composition of the parent plate was obtained at TWI Ltd and is presented in Table 6.1. The dimensions of the plate are 321 x 270 x 15 mm as presented in Figure 6.3. The welding process is manual metal arc (MMA) welding with a heat input of 2310 W at a welding speed of 3.7 mm/s. Figure 6.4 shows the two welders welding simultaneously both sides of the plate.

To monitor the temperatures developed in the welding process eight thermocouples were attached on both sides of the plate as shown in Figure 6.5. The thermocouples were placed away from the middle of the plate, i.e. the location of mock-ups, so as not to impede the cutting. After complete cooling of the plate, residual stress measurements were calculated from centre hole drilling (CHD) measurements. The positions of the CHD are presented in Figure 6.6 and were taken on both sides of the plate. Again, the locations of the CHD, which is a semi-destructive technique, were chosen away from where the mock-ups are cut. When the welds were fully cooled, a 6 mm slice transverse to the weld was cut 20 mm away from the start of the weld. The process used was electro discharge machining (EDM). This slice was used to create a macrograph of the bead, presented in Figure 6.7, and later used for the calibration of the thermal model. Three 7 mm slices were cut further away in the plate, as presented in Figure 6.8. These specimens were evaluated as shown in Figure 6.1 in [94]. The mock-ups did not contain any distortion resulting from the cutting.

C	**Si**	**Mn**	**P**	**S**	**Cr**	**Mo**	**Ni**	**Al**	**As**
0.020	0.4	1.21	0.034	0.003	16.6	1.97	9.9	<0.01	<0.01
B	**Co**	**Cu**	**Nb**	**Pb**	**Sn**	**Ti**	**V**	**W**	**Ca**
0.001	0.17	0.41	0.01	<0.002	0.011	0.012	0.07	<0.05	<0.01

Table 6.1: Nominal chemical composition of the parent plate of Mock-up A (wt.%) (Fe=balance)

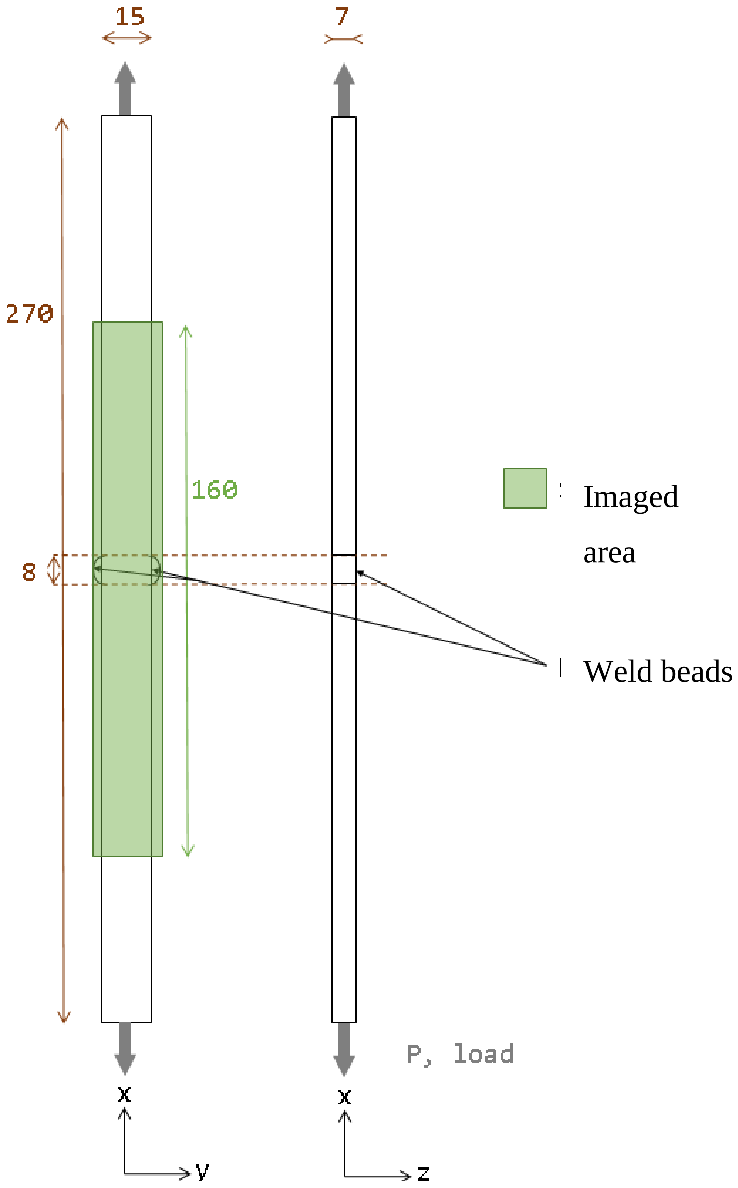

Figure 6.2: Mock-up A dimensions (in mm), loading and scanned area (green).

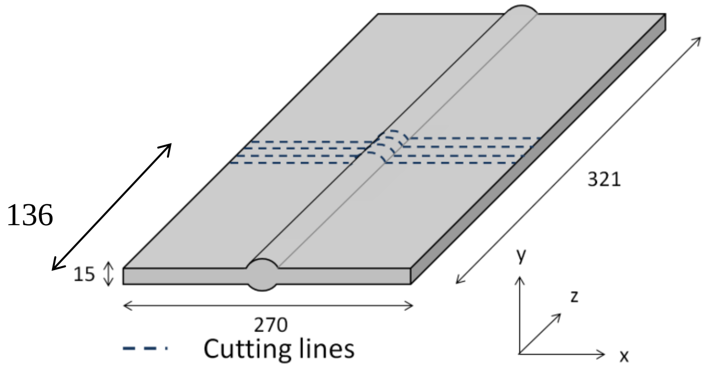

Figure 6.3: Double bead-on-plate dimensions (in mm) and cutting lines. Drawing is not to scale.

Figure 6.4: MMA welding simultaneously on each side of the plate

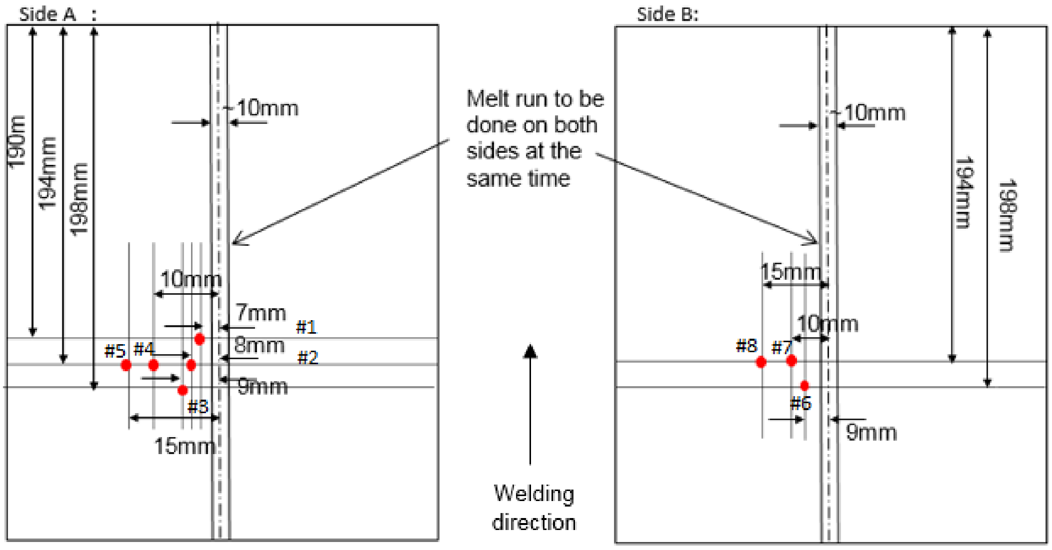

Figure 6.5: Location of thermocouples

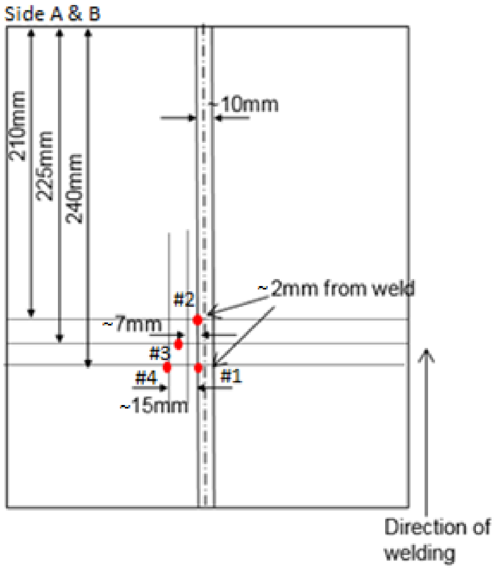

Figure 6.6: CHD locations

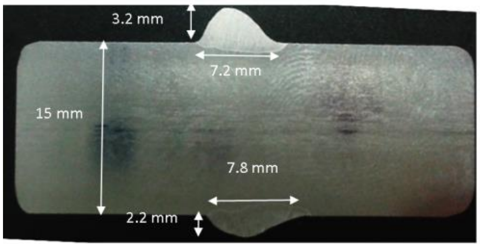

Figure 6.7: Macrograph of the two beads

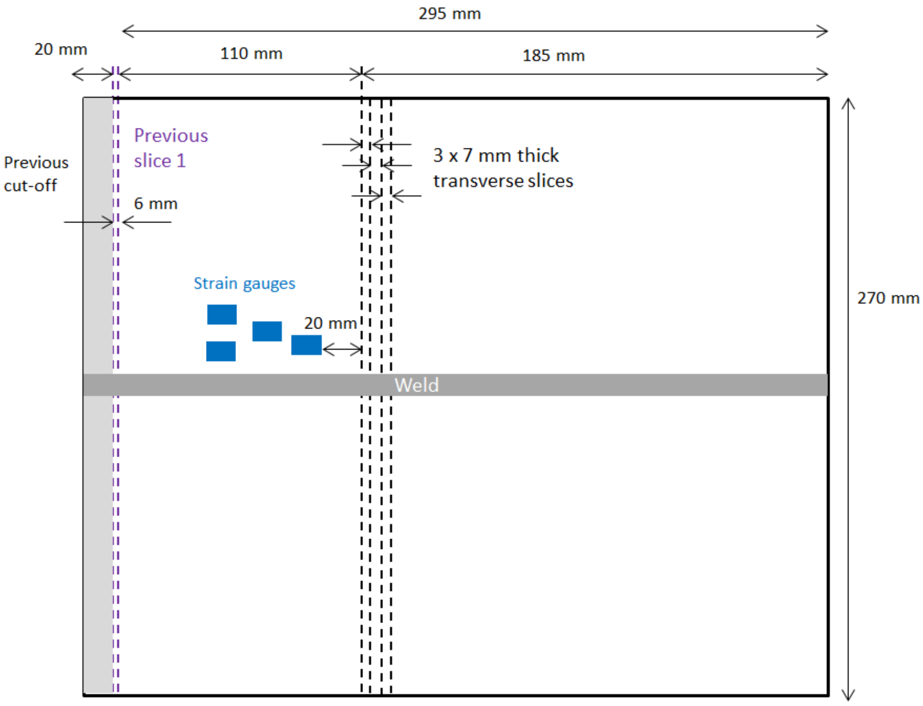

Figure 6.8: EDM cut of the plate

6.3 Microscopy analysis

In this chapter, the plastic strain predicted using FEA, hardness and TSA PSA is compared along the centreline of Mock-up A, depicted in Figure 6.9. To investigate the microstructure along the centre line, one of the Mock-up A slices was cut and mounted so the microstructure along the line was obtained and is shown in Figure 6.10 to Figure 6.13 as depicted in Figure 6.9. The micrographs are presented in Figure 6.10 to Figure 6.16. For all the micrographs presented in the chapter, the samples were prepared by Simon Ingram, material laboratory technician at TWI Ltd which were ground using SIAWAY grades 120, 320, 600, 1200 and 2500 sand paper and then polished using a monocrystalline suspension diamond from MetPrep of 3 µm, 1 µm and 0.25 µm. Struers OP-U polishing product was used as a final manual finishing step as the samples were initially prepared for EBSD. The micrographs images were then captured by the author and Dr David Griffiths, from TWI Ltd using the acquisition settings given in Table 6.2.

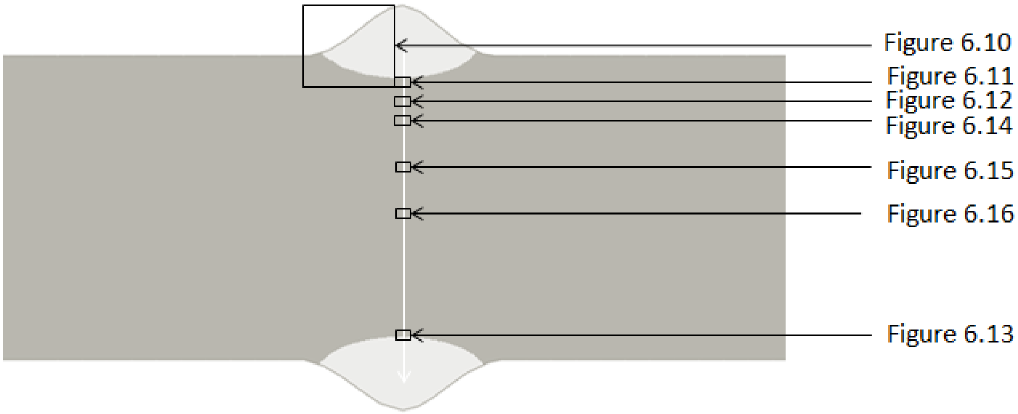

Figure 6.9: **Location of the micrographs presented in Figures 6.10 to 6.15.**

Accelerating Voltage	25.00 kV
Specimen Tilt (degrees)	70.00 °
Hit Rate	99.70 %
Speed of Acquisition	10.04 Hz

Table 6.2: Image acquisition settings

From Figure 6.10, it can be seen that the weld contains elongated grains. In the HAZ, just under the weld, an area of large grains has formed as can be seen in Figure 6.11. A gradient in grain size can be observed, the larger grains are several hundreds of microns of length and breadth and the finer grains are that of parent metal, of several tens of microns as it can be seen in Figure 6.12. The opposite weld was also imaged, and the presence of large grains is also noted. On one of the large grains, several slip bands can be observed, denoting the presence of plastic strain in the HAZ region.

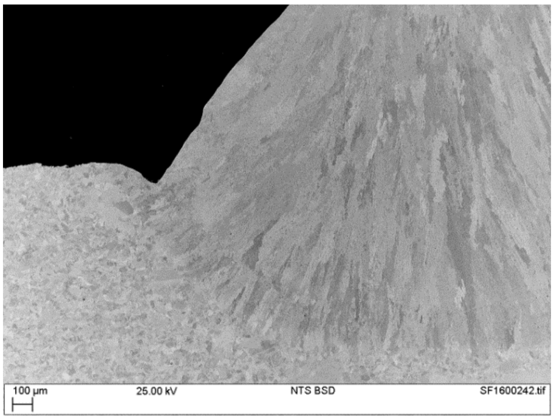

Figure 6.10: Elongated grains in the weld region.

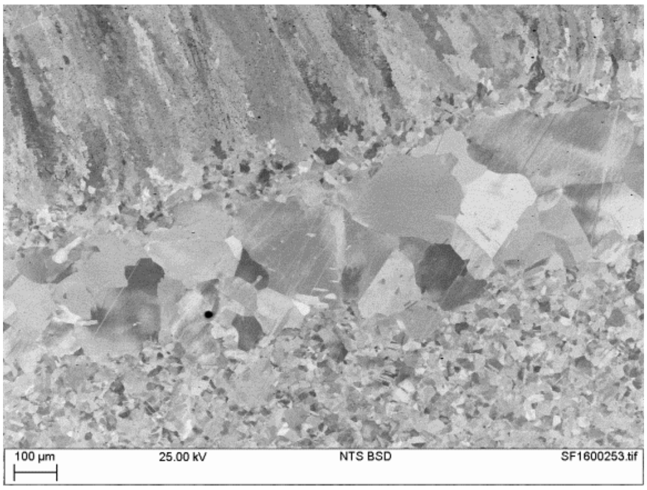

Figure 6.11: HAZ grain growth.

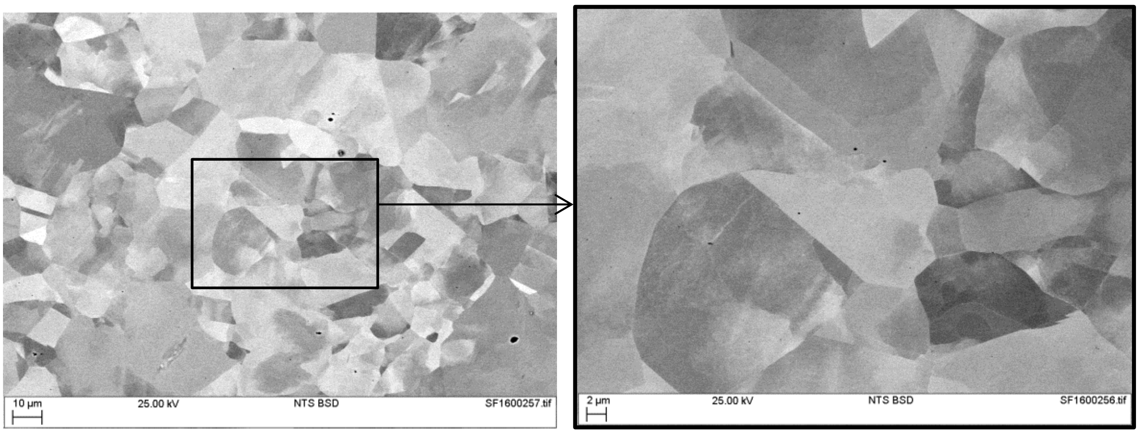

Figure 6.12: Parent material under HAZ.

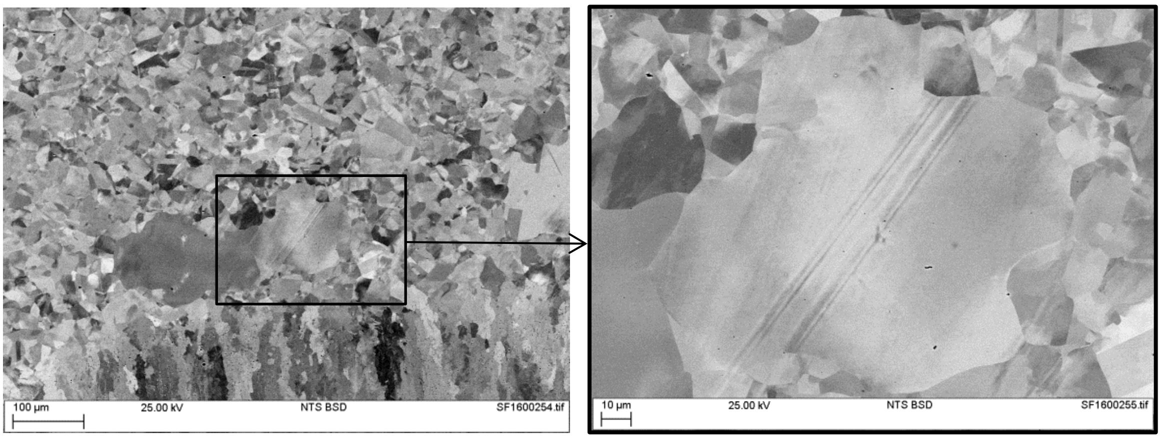

Figure 6.13: Grain growth under weld bead and slip bands.

Along the centreline, further under the weld and HAZ, grains where no plastic strain was expected were analysed. The grains at 20 mm, 45 mm and 75 mm under the weld bead can be compared in Figure 6.14, Figure 6.15 and Figure 6.16 respectively. The grains at 20 mm and 45 mm under the weld bead have a uniform microstructure of grains of tens of microns in size. In the centre of the specimen, a significant number of slip bands is observed. This plastic strain is likely to have arisen during the cold rolling process when the plate was manufactured. The microstructural information is crucial to understand any deviation between the plastic strain derived from the experimental techniques and FE predictions.

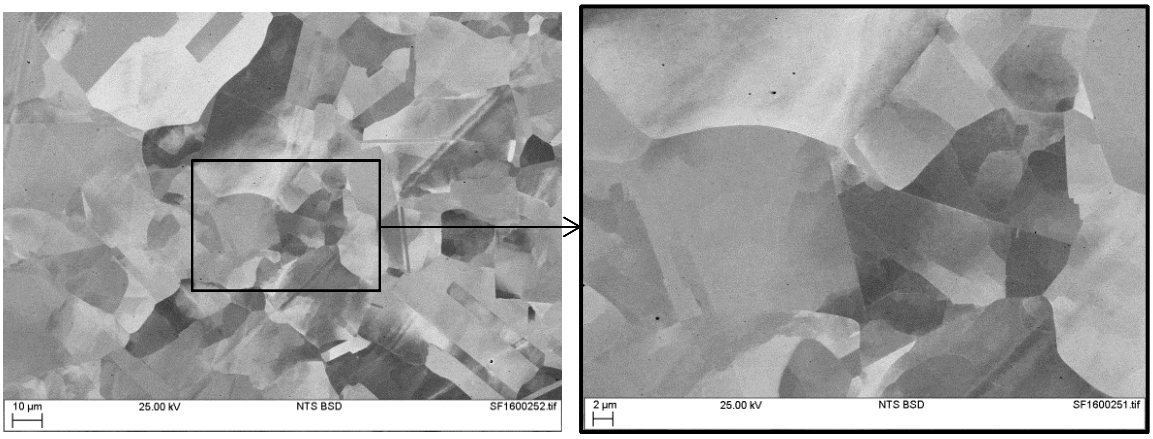

Figure 6.14: Grains in parent plate, 20 mm under the weld bead.

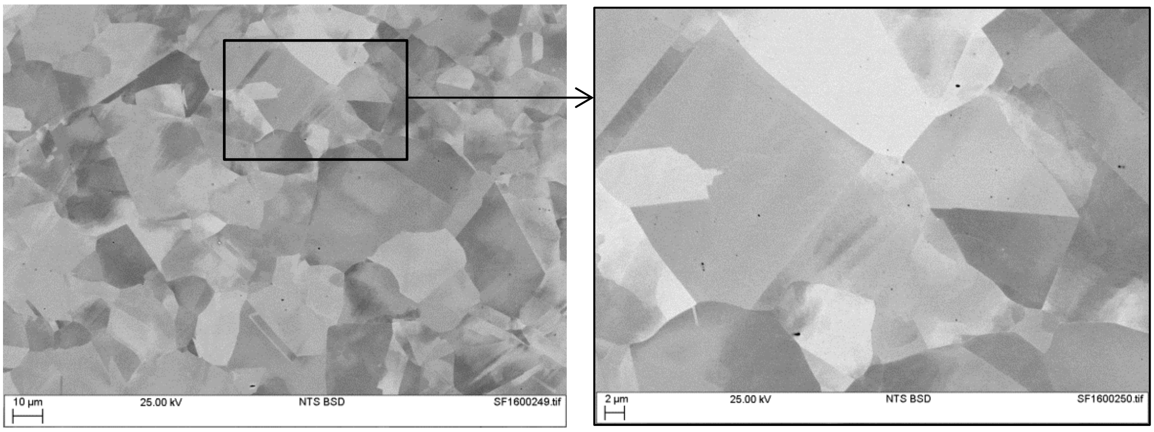

Figure 6.15: Grains in parent plate, 45 mm under the weld bead.

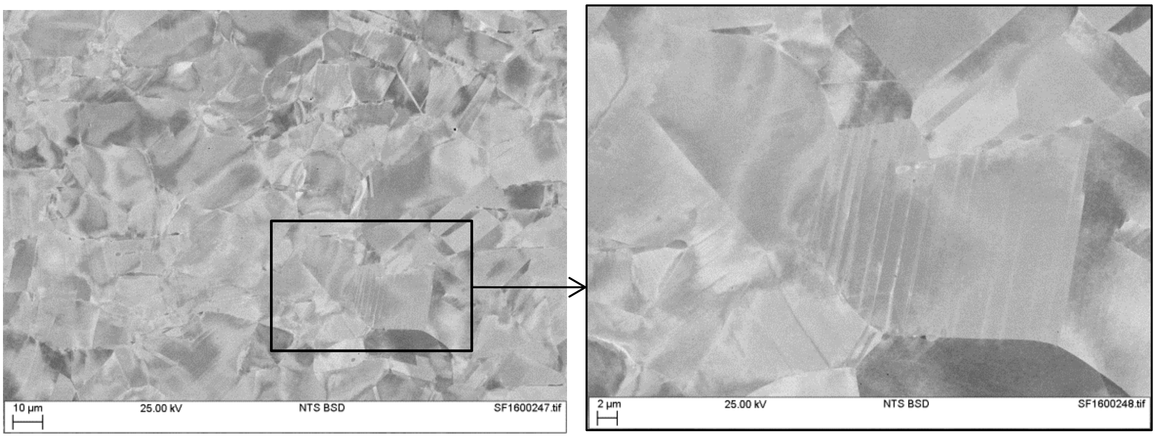

Figure 6.16: Grains in parent plate, 70 mm under the weld bead.

6.4 FE analysis prediction of the temperature fields in the welded plate

The FE analysis software Abaqus 6.14-3 was used to create the model of Mock-up A. In this section, the geometry, mesh and calibration of the thermal model are presented.

6.4.1 Geometry and mesh of the model

The dimensions of the plate depicted in Figure 6.3 were used to create the geometry of the bead-on-plate model. The bead thickness and width varied along the weld, due to the manual aspect of the welding process. Nonetheless, for simplicity of the modelling, the bead shape was considered constant, and the shape is presented Figure 6.17. Thermal and mechanical material properties from [45] were assigned to the parent and deposited material in the model. The temperature dependent properties are presented in Figure 6.18 to 6.22 and the values can be found as tables in Appendix A. The plasticity of the material is modelled using an isotropic hardening model [31]. These material properties have been used in several studies [31, 45] and provided good residual stress predictions, compared to neutron diffraction residual stress values.

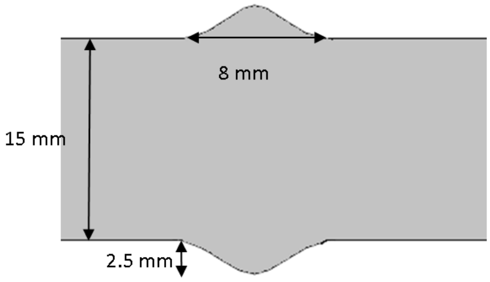

Figure 6.17: Geometry and dimensions of the beads in the FE model

For the thermal analysis, it is recommended [39] that the mesh size in the weld should be smaller than a quarter of the molten area to allow penetration and bead shape to be predicted accurately. In the model, the weld zone width is 8 mm, therefore brick elements of 1x1 mm^2 were used to map the weld and heat affected zone, as can be seen in Figure 6.23. Along the length of the weld, the elements are extruded along 5 mm, which is smaller than the heat source length. The mesh is fine around the weld and heat affected zone as the temperature and stress gradients are large in these area. The mesh is coarser in the regions where no temperature or stress gradient is present, as presented in Figure 6.23. To calculate the temperature fields, the elements are linear heat transfer dedicated elements, referred as DC3D8 in Abaqus.

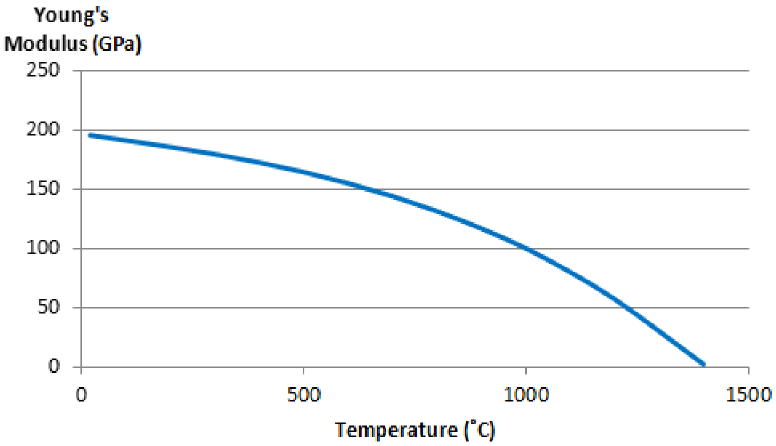

Figure 6.18: Young’s modulus variation with temperature. Data from [45]

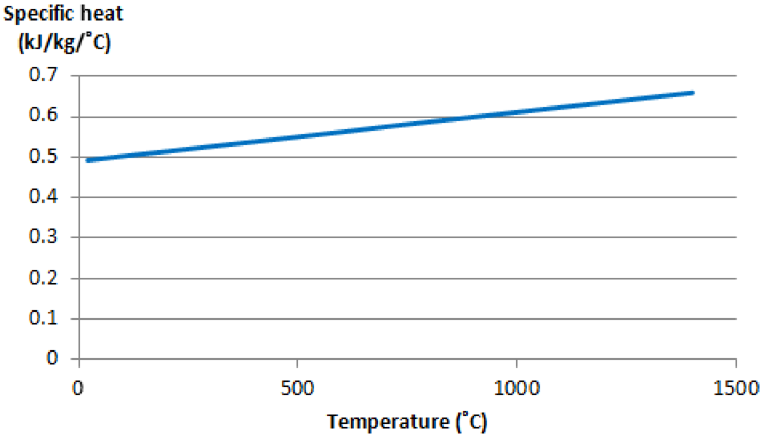

Figure 6.19: Specific heat variation with temperature. Data from [45].

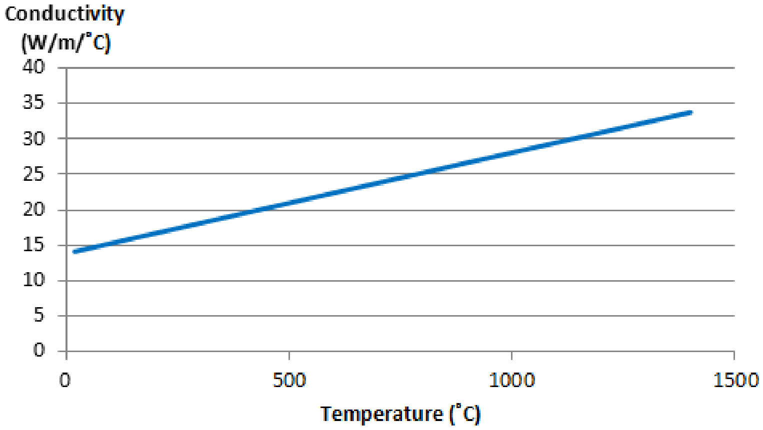

Figure 6.20: Conductivity variation with temperature. Data from [45].

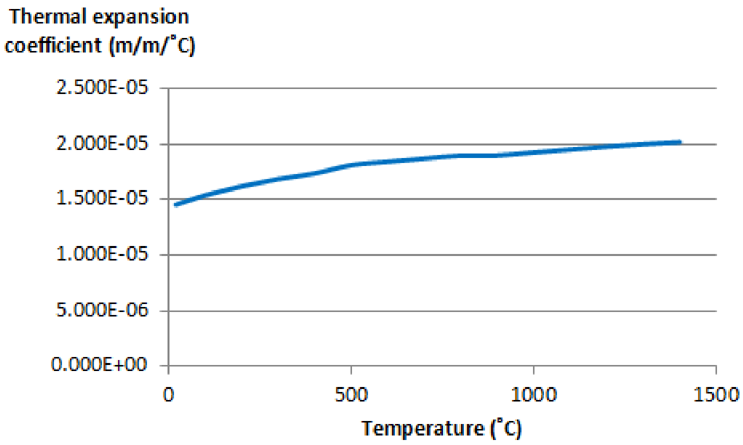

Figure 6.21: Thermal expansion coefficient variation with temperature. Data from [45].

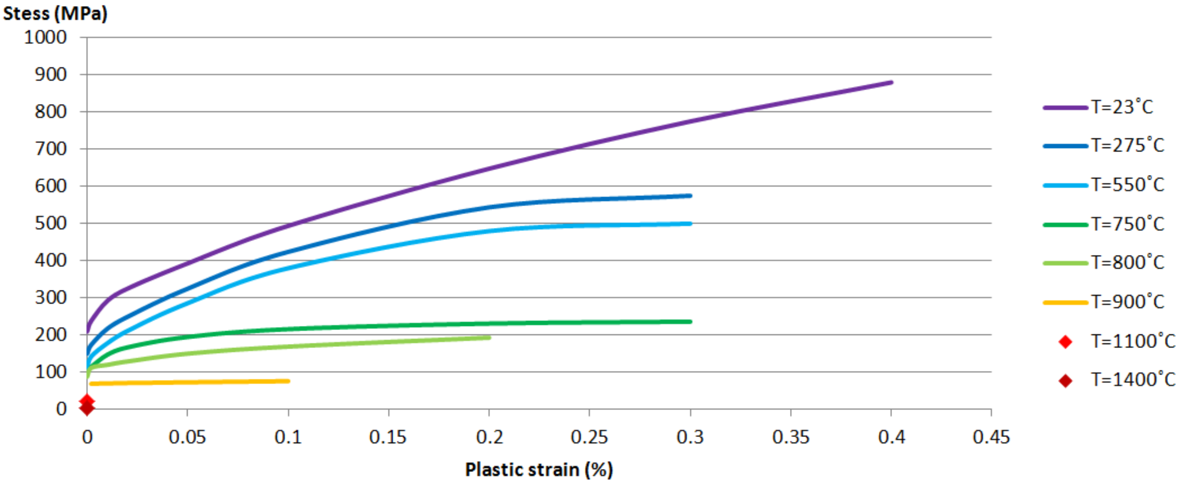

Figure 6.22: Stress-strain curve variation with temperature. Data from [45].

6.4.2 Calculation of temperature fields

To model the heat source, a double ellipsoidal moving heat source model, developed by Goldak [50], was used to simulate the deposition of the double bead-on-plate, as recommended in the 316L bead-on-plate modelling in [52]. The parameters used for the heat input, efficiency and geometrical parameters of the double ellipsoid are presented in Table 6.3 and refer to Figure 2.6 As mentioned in Chapter 2, values of 0.6 and 1.4 are recommended for parameters f_f and f_r [41]. The heat input, Q was derived from the voltage and current used during the welding process. The average welding speed was derived the length of the plate and the measured time of the welding process. Values of efficiency η between 0.75 and 0.85 were tested iteratively along with geometrical coefficients a, b, c_f and c_r of the order of magnitude of the torch size and the bead sizes. The set of values that gave the best match between the thermocouple data and fusion zone were selected as described in the next paragraph.

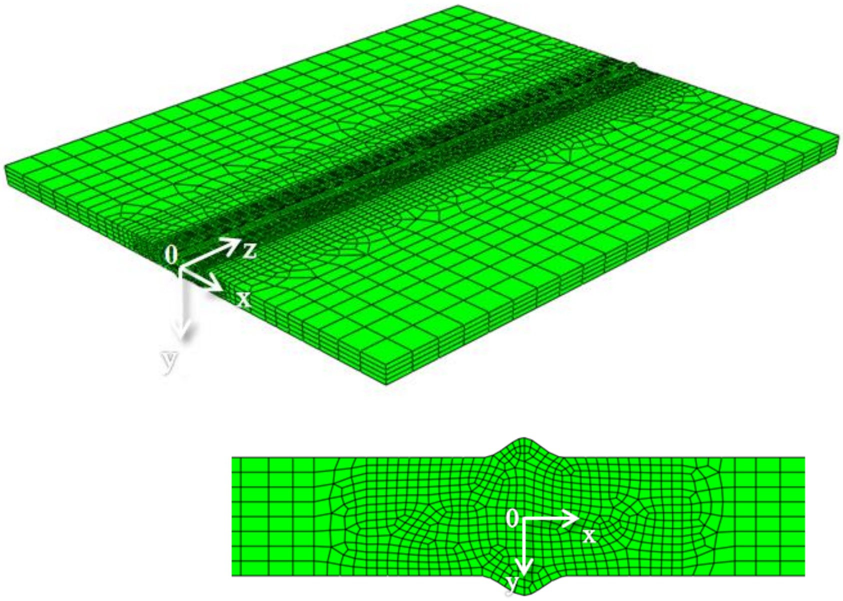

Figure 6.23: Mesh of the thermal model (top) and transverse to the weld view (bottom)

$\boldsymbol{a}$ (mm)	$\boldsymbol{b}$ $(\boldsymbol{mm})$	$\boldsymbol{c_f}$ (mm)	$\boldsymbol{c_r}$ (mm)	$\boldsymbol{v}$ (mm/s)	$\boldsymbol{Q}$ (W)	η	$\boldsymbol{f_f}$	$\boldsymbol{f_r}$
2	2	2	2	3.7	2300	0.8	0.6	1.4

Table 6.3: Experimental parameters used in Goldak heat source model

6.4.3 Calibration of the heat source

To calibrate the thermal model, the FE predicted temperature distribution should match that of the welded plate. During the welding process, the plate temperature was recorded by thermocouples at locations defined in Figure 6.5. Following guidelines from [52], thermocouples 4, 5, 7 and 8 can be used for good calibration as the others are too close to the weld and may be influenced by other parameters than temperature coming from the conduction of the heat input in the plate such as arc shine [52]. Thermocouples (TC) 4 and 5 were compared with the temperature node corresponding to the nearest position in terms of distance away from weld bead in Figure 6.24. Temperature measurements from TC 4 and TC 5 were compared with the temperature histories of the modelled plate at nodes located at 10 mm and 15 away from the weld bead respectively. The efficiency of the welding process was set to 0.8 so the peak temperature of the predictions matched that of the measurements.

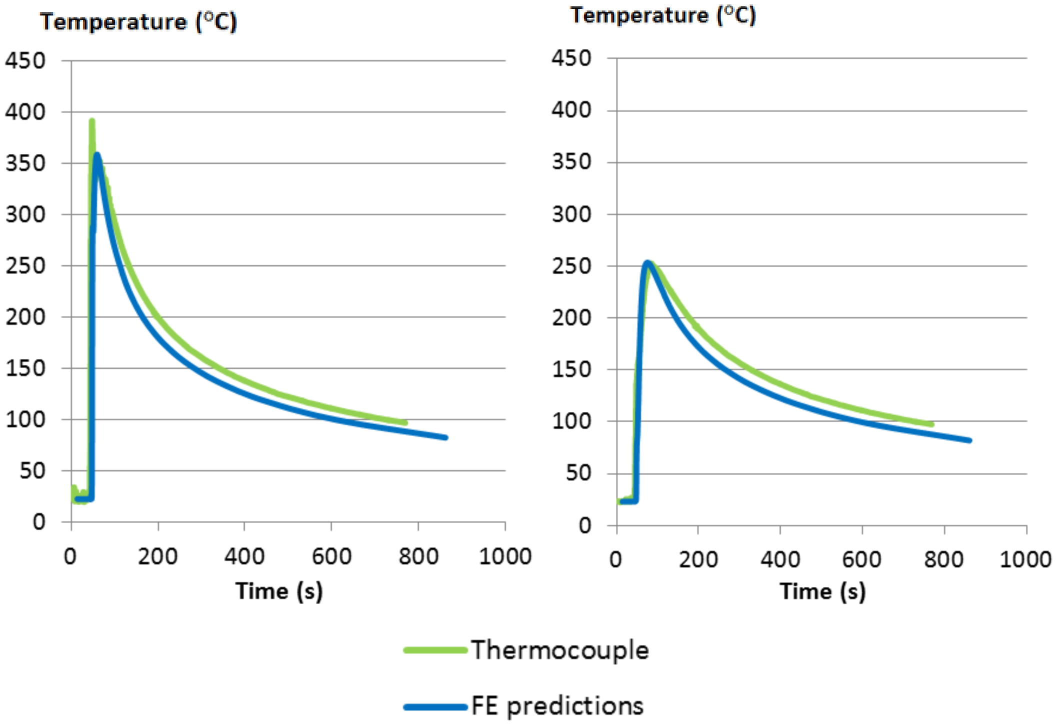

Figure 6.24: Comparison between temperature experienced at 10 mm (top) and 15 mm (bottom) away from weld bead experimentally (green) and from FE prediction (blue)

The fusion line, which corresponds to the separation between the molten zone and heat affected zone, is compared between the FE model and the macrograph in Figure 6.25. To evaluate the match in the two, several parameters such as the area, the perimeter, the width and the penetration of the weld pool in the plate can be compared. As the welds on both sides of the plate were welded using the same parameters, an average of the data mentioned below is reported in Table 6.4, alongside data for the FE predicted weld area and the results are compared. Apart from the penetration, the deviation in the features is below 10% which guaranties reasonable prediction of the weld area. The penetration variation of 23% represents 0.23 mm and is considered acceptable in comparison with the resolution of TSA (0.13 mm) and hardness measurements (0.5 mm).

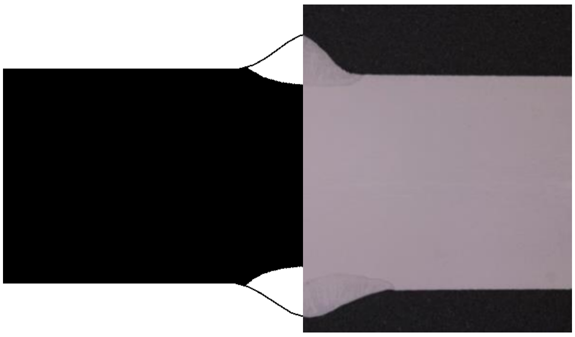

Figure 6.25: Comparison of the fusion line from the FE thermal model (left) and the fusion area identifiable from macrograph (right).

	Top weld Macrograph	**Bottom weld Macrograph**	**Average weld Macrograph**	**Weld FE model**	**Deviation (%)**
Area (mm²)	18.32	16.15	**17.23**	18.44	7.02
Perimeter (mm)	19.83	20.52	**20.17**	18.99	5.85
Width (mm)	8.10	9.5	**8.8**	8.37	4.89
Penetration (mm)	0.85	1.16	**1.00**	1.23	23

Table 6.4: Comparison of area, perimeter, width and penetration of welds from macrograph against FE predicted weld area.

6.5 FEA prediction of the residual stress and plastic strain in the welded plate

6.5.1 Calculation of displacement, strain and stress fields from the temperature fields

The mesh is formed of 3D brick elements, referred as C3D20R in Abaqus. The boundary conditions used in the heat transfer step consist in modelling the tack welds of the experiment. These are modelled by fixing the nodes on the red lines of the bottom of the plate depicted in Figure 6.26. The same boundary conditions are kept for the cooling of the plate.

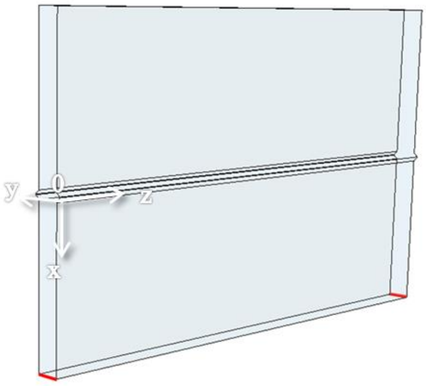

Figure 6.26: Tack welds boundary condition modelling by prescribing displacement at the nodes on the red lines.

6.5.2 Stress predictions

The stresses in the direction transverse to the weld and longitudinal to the weld are presented in Figure 6.27. As expected, longitudinal tensile stresses are obtained along the bead, with compressive stresses elsewhere, to maintain equilibrium of the structure.

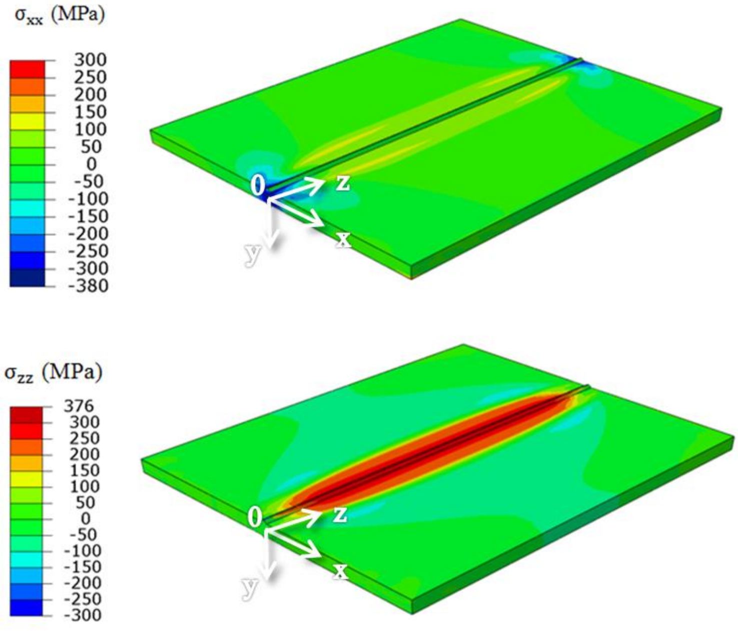

Figure 6.27: Stress field in the direction transverse to the weld (σ_{xx}) and longitudinal to the weld (σ_{zz}) after cooling of the plate

To validate the stress predictions, the centre hole drilling measurements presented in Table 6.5 and Table 6.6 were compared with results from the mechanical analysis. The hole drilling and the measurements were performed by technicians at TWI by abrasive machining. The stress measurements from the centre hole drilling value correspond to the relaxation of a hole of 2 mm diameter. The procedure to calculate stress values from measured micro strain relaxation around the hole is explained in [111]. Values of the stress at the centre hole drilling position were extracted from the model at both top surface and at the node 2 mm deeper in the plate. The stress fields are symmetric from both sides of the (Oxz) plane, due to symmetric nature of the heat source model and boundary conditions. Therefore, only the top surface values of the FE model were compared with CHD measurements values which were taken from both sides A and B of the plate, almost symmetrically. The distance of each CHD measurement from the weld bead is specified in Table 6.5 and Table 6.6. The paths which the values were extracted from are depicted in Figure 6.28.

Gauge	**Distance from weld edge (mm)**	**Stress in the direction transverse to the weld (MPa)**	**Stress in the weld longitudinal direction (MPa)**
1A	2	100	579
2A	2	48	529
3A	7.5	68	356
4A	17.5	-63	21

Table 6.5: Residual stress calculation from CHD on face 1

Gauge	**Distance from weld edge (mm)**	**Stress in the direction transverse to the weld (MPa)**	**Stress in the weld longitudinal direction (MPa)**
1B	2	111	474
2B	2	109	430
3B	8.5	73	337
4B	15	-35	14

Table 6.6: Residual stress calculation from CHD on face 2

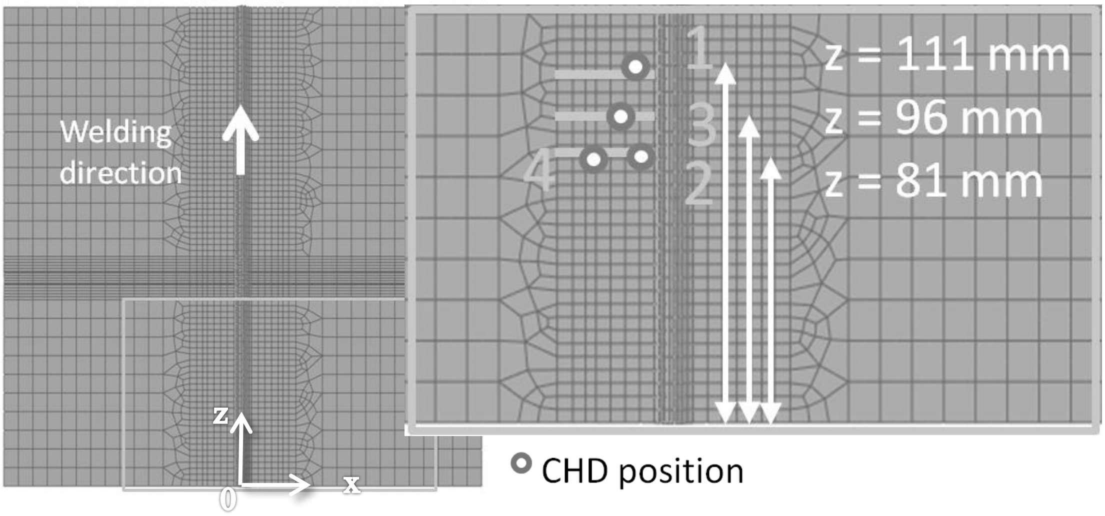

Figure 6.28: Paths positions of extracted values

In Figure 6.30, the stresses in the (Ox) and (Oz) direction are extracted along the paths at z = 81 mm, z = 96 mm and z = 111. CHD measurements are plotted on the same graph for comparison and error bars of ± 30 MPa appear on the graph around the CHD measurement values. It can be seen that the symmetric CHD measurements (i.e. CHD 2A and 2B) values are consistent with their respective symmetric value considering the ±30 MPa error.

Near the weld bead, the transverse stresses measured using CHD correspond well to the FEA predictions. Also, high tensile longitudinal residual stresses are measured with the CHD and predicted by the FE model. However the difference between CHD measurements and FEA predictions represents 67% of the predicted stresses and 191% of the yield stress. A possible explanation for these high values is potential work hardening of the material during cold rolling the plate manufacturing process which was not considered in the modelling work.

At 7 mm away from the weld bead edge, CHD values and FE predictions show good agreement for the transverse residual stresses. The longitudinal residual stresses measured using CHD are consistently larger than those predicted by the FE model. The discrepancy of the longitudinal residual stresses can either be attributed to work hardening or to the errors in CHD residual stress calculation in regions of stresses higher than 70% of the yield magnitude, which is the case here as stresses are larger than 147 MPa.

At 15 to 17 mm away from the weld bead edge, a decrease in both tensile and longitudinal residual stresses is observed from the predicted and measured residual stresses. However, compressive residual stresses were measured with CHD whereas FE predicted tensile residual stresses. It can be seen in Figure 6.29 that compressive residual stresses are predicted by the FE model, further away from the weld bead, at 20 mm or deeper in the plate, 5 mm under the top of the plate thus a shift in the data -which potential causes are discussed later in the paragraph- could explain the discrepancy. However, no compressive transverse residual stresses are expected along the path in the FE model. As presented in Figure 6.27, tensile transverse residual stresses are expected in the middle of the plate with compressive residual stresses at the start and end points to make the balance. The compressive transverse residual stresses measured by the CHD are unexpected at this location in the plate. The fact that one of the welders wire ended before reaching the end of the plate (forcing the welder to stop the torch while getting a new wire) might have caused this start/stop effect to produce compressive residual stresses.

It should be noted that validation against CHD values can be challenging for three reasons. The first reason is that if the stress/strain relationship is non-linear, as it is the case after yielding, the calculated residual stress will be in error [27] which tend to increase when the stress-strain curve becomes flatter, approaching the idealized perfectly plastic behaviour [112]. When the measured residual stress is close to the yield stress of the tested material, the stress concentration caused by the presence of the hole may induce localised yielding. It is therefore necessary to establish a threshold level of residual stress below which yielding is negligible [112-114] and it was found that errors are negligible when the residual stress is less than 70% of the proportional limit of the material [27]. When the initial residual stress is equal to the proportional limit, errors of 10% to 30% and greater [27] have been observed.

The second reason is that large stress gradients are present in the heat affected zone, where the CHD values were measured. Gradients exist both through the thickness and along the path transverse to the weld, which make the comparison not fully relevant, as CHD measurements should be done on specimen where the residual stresses are constant through the depth of the drilled hole [23].

The third reason for scatter in the comparison can be the weld bead geometry. The process used to deposit the filler metal on both sides of the plate was manual arc welding. The manual part aspect of the process necessarily implies irregularities in the weld, as well as the non-uniform welding speed, and the difference in weld speed between the two welders.

Some CHD values were taken 2 mm away from where the weld bead was expected to be, but given the actual geometry of the bead, presented in Figure 6.31, the weld bead could in reality be closer or further away which would disturb the residual stress field. The weld bead geometry is not reported here for each CHD measurement as it is believed the discrepancy between CHD and FEA data is due to a combination of the three causes mentioned and cannot be explained solely by the slight shift of the weld bead.

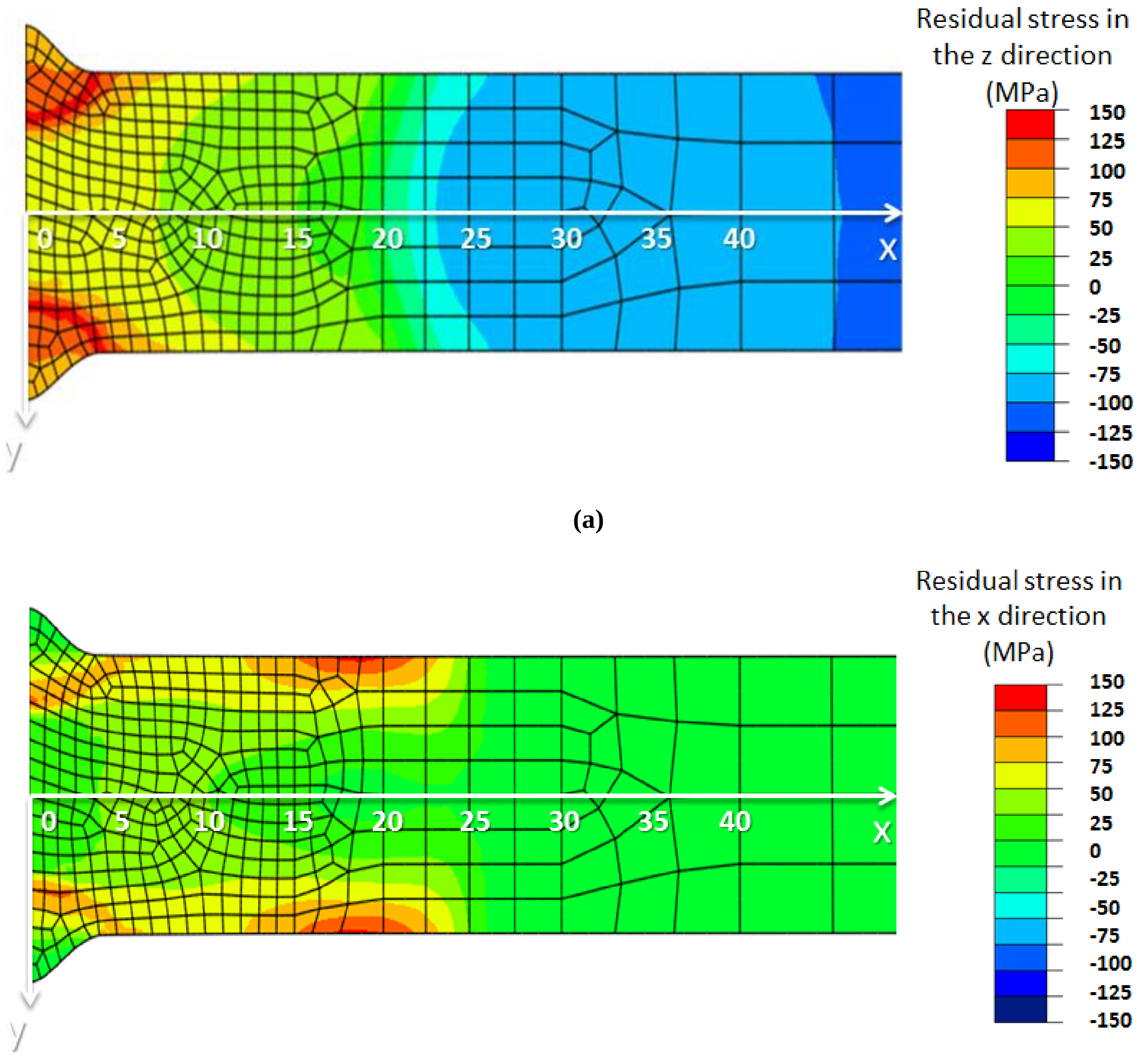

(a)

(b)

Figure 6.29: Through weld residual stress cross section in the z- direction (a) and in the x-direction (b) at z=81 mm.

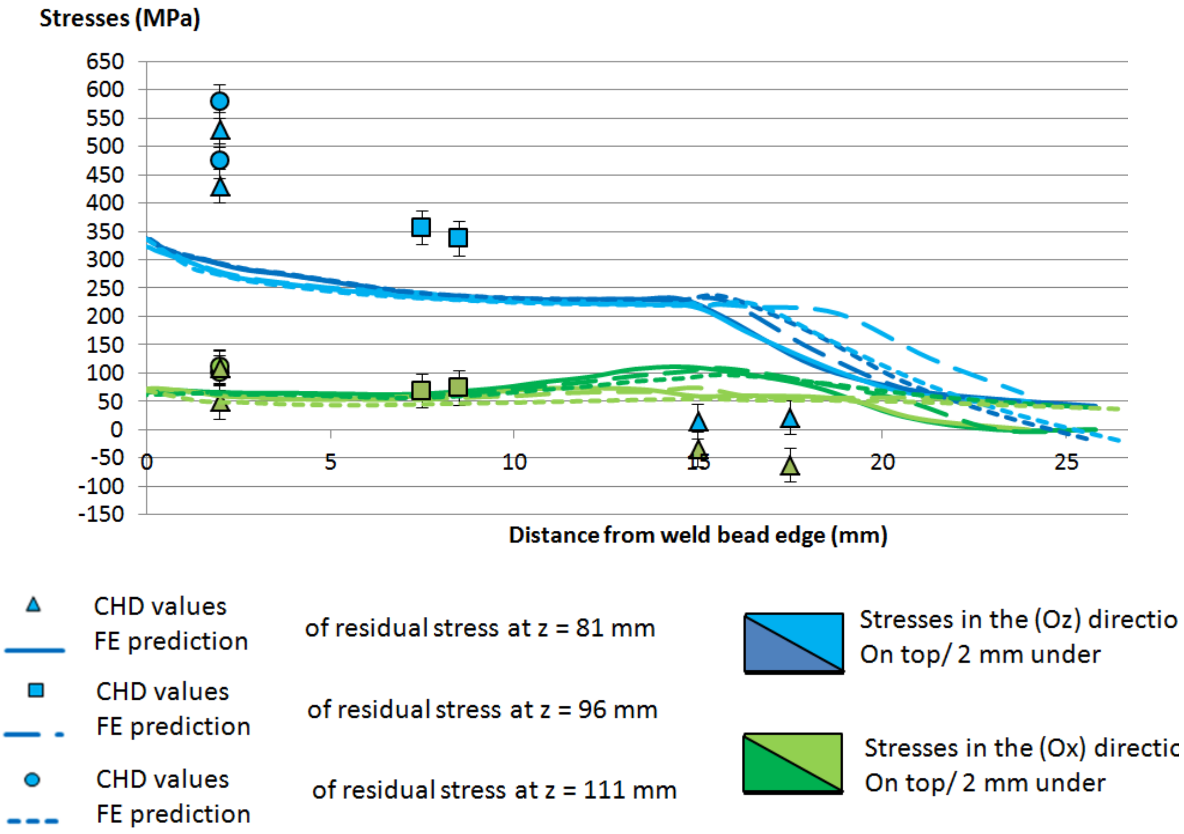

Figure 6.30: Comparison of CHD values with FE prediction of stresses in the x direction (green colours) and z direction (blue colours) along paths z = 81 mm, z =96 mm, z = 111 mm at the top and 2mm under the surface.

Figure 6.31: Bead-on-plate after welding

6.6 **Plastic strain assessment**

6.6.1 Finite element modelling predictions

The equivalent plastic strain, referred to as PEEQ in Abaqus was predicted in the whole plate. As Mock-up A is a slice cut from the middle of the plate, the plastic strains were extracted from the corresponding centreline plane at mid length of the plate. The equivalent plastic strain predicted in the area of interest is presented in Figure 6.32. The line of data extraction is represented and will be used for comparison with the TSA PSA technique as well as hardness measurements.

In Figure 6.32, it can be seen the maximum plastic strain builds up beneath the area corresponding to the weld. Along the weld through thickness centreline, maximum values of 5% plastic strain are predicted next to the region where the annealing temperature was reached and the plastic strain relaxed. The limit of the areas reaching melting temperature (1400 °C) and annealing temperature (1050 °C) are plotted next to equivalent plastic strain predictions in Figure 6.32. The FEA accumulated equivalent plastic strain predictions in the annealing temperature region reaches about 1.5% plastic strain.

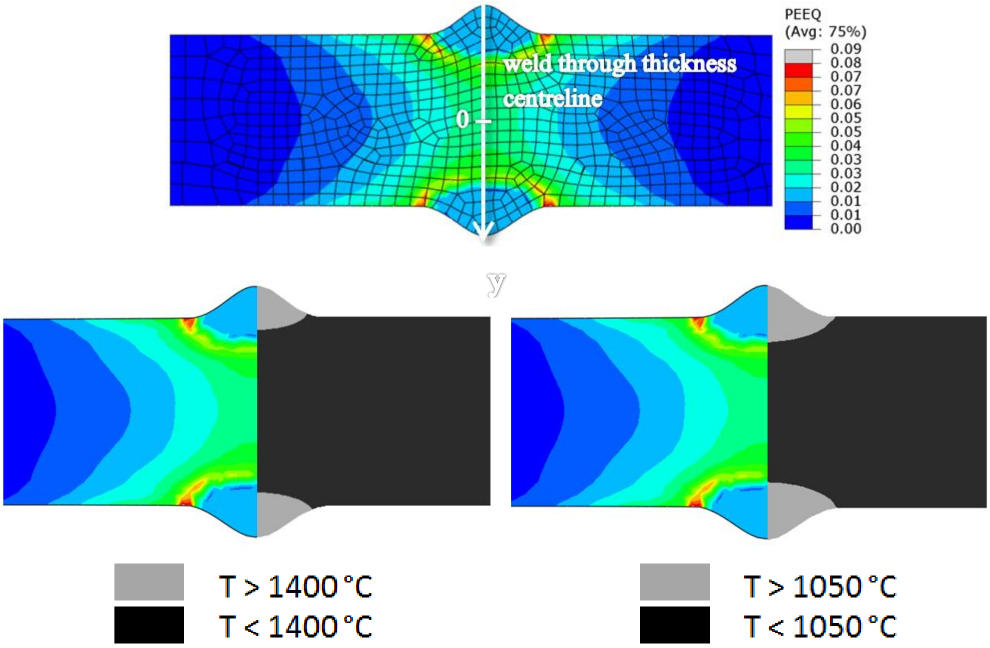

Figure 6.32: Line selected for preliminary comparison (top). Comparison of the melting temperature region (left) and anneal temperature region (right)

6.6.2 Comparison of Mock-up A with TSA PSA results

TSA was performed on one of the slices that compose Mock-up A by Howell [94] and the thermoelastic response of Mock-up A, $(\frac{\Delta T}{T})_{TSA}$ was obtained [94]. To identify any regions containing plastic strain the synthetic bitmap of Mock-up A was created to provide $(\frac{\Delta T}{T})_{FE}$. As the thermoelastic constant varies practically linearly with an increase in plastic strain as reported in Chapter 5, $(\frac{\Delta T}{T})_{TSA}$- $(\frac{\Delta T}{T})_{FE}$ is referred to as the "plastic strain thermoelastic response" is proportional to the amount of plastic strain in the slice, and can therefore be compared with the plastic strain prediction from the FE model described in this chapter, by normalising both results against the value in the centre of the plate. The comparison is presented in Figure 6.33. The plastic strain thermoelastic response of the weld beads was not taken into account for simplicity of data processing.

The plastic strain thermoelastic response reaches minimum value at the centre and increases towards the weld beads. This tendency matches that of the plastic strain predicted by the FEA in the region from -4 mm to 4 mm. However, the peaks of plastic strain predicted by the FE model are not observed in the plastic strain thermoelastic response and an increase in plastic strain thermoelastic response is observed in the regions near the weld bead. This increase may be due to the weld microstructure, or to the material properties change, as the weld bead was created using 308 filler metal. A drop in plastic strain thermoelastic response can be observed in the region from 6 mm to 7 mm. This region corresponds to the area beneath the weld bead where coarser grains were reported in section 6.3, which would be consistent with results from Chapter 5 as coarser grained microstructure may exhibit a lower thermoelastic constant. However this result is only observed on one side of the sample and a symmetrically similar decrease in the thermoelastic response might be expected, although because of the welding the plate is not completely symmetrical. An increase in the plastic strain thermoelastic response is observed between 3 mm and 5 mm which does not correspond to the FE predicted plastic strain.

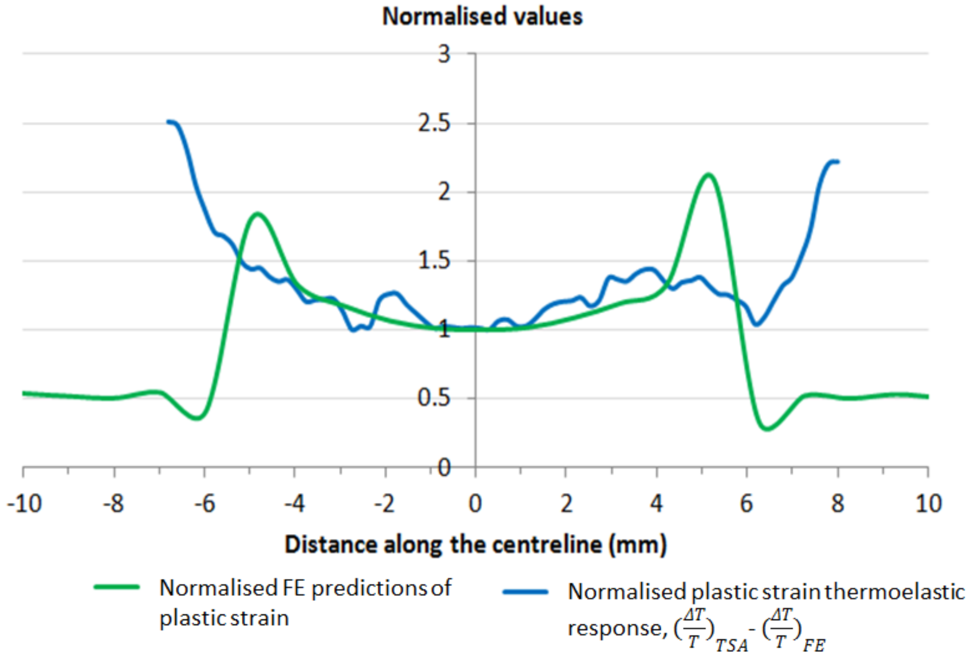

Figure 6.33: Comparison of the normalised plastic strain thermoelastic response $(\frac{\Delta T}{T})_{TSA}$- $(\frac{\Delta T}{T})_{FE}$ with normalised FE plastic strain predictions

6.6.3 Hardness measurements

To confirm the amount of plastic strain in mock-up A, micro-hardness indentation measurements were performed by Damaso de Bono from TWI, Middlesbrough. An indent load of 30 gf was used in a nano indenter NanoTest Platform 3 by Micro Materials Ltd with a diamond Berkovich tip. The measurements were taken under continuous stiffness mode. The depth of the indent was measured and the hardness was derived along three lines at the centre of the weld, along the centreline, 0.5 mm apart from each other. On each line, indents are 0.5 mm apart, as presented in Figure 6.34. The hardness results on the three lines were averaged and are presented in Figure 6.35. The average hardness values were then normalised against the value at the centre of the plate and for comparison with normalised FEA and plastic strain thermoelastic response in Figure 6.36.

In Figure 6.35 it can be noted that the minimum hardness values are obtained at -6 mm and 7 mm along the centreline axis. These locations correspond to the HAZ, where large grains were identified in section 6.3. The yield strength of the large grains would be significantly lower compared to that of parent material and explains the lower hardness values [7]. The plastic strain maxima predicted by the FEA are not captured by the hardness measurement. This is likely to be caused by the variation in grain size in that area. A small increase similar in trend and magnitude to that reported from the plastic strain thermoelastic response was noticed between 3 mm and 5 mm, as it can be seen in Figure 6.36. This could suggests some phenomenon, not taken into account in the FE model, caused similar increase in both plastic strain thermoelastic response and the hardness measurements. More importantly, in Figure 6.36, it can be seen that where the plastic strain thermoelastic response increases coincides directly with a decrease in the hardness.

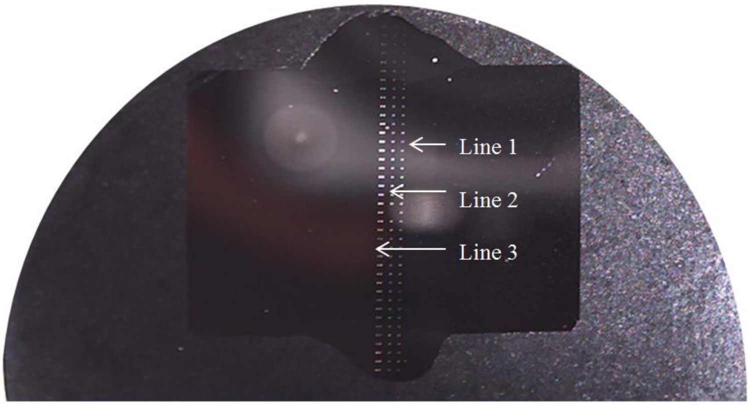

Figure 6.34: Location of the indents.

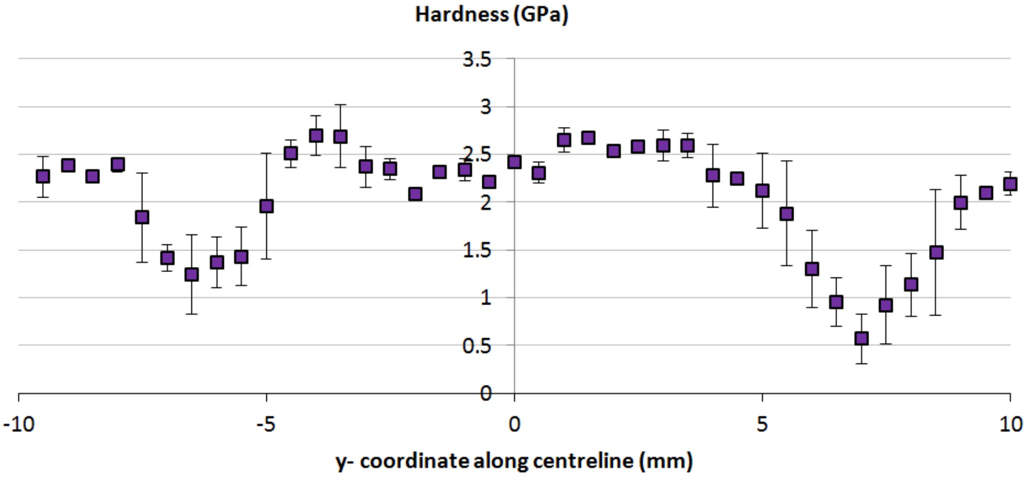

Figure 6.35: Hardness and standard deviation along the centreline of the weld

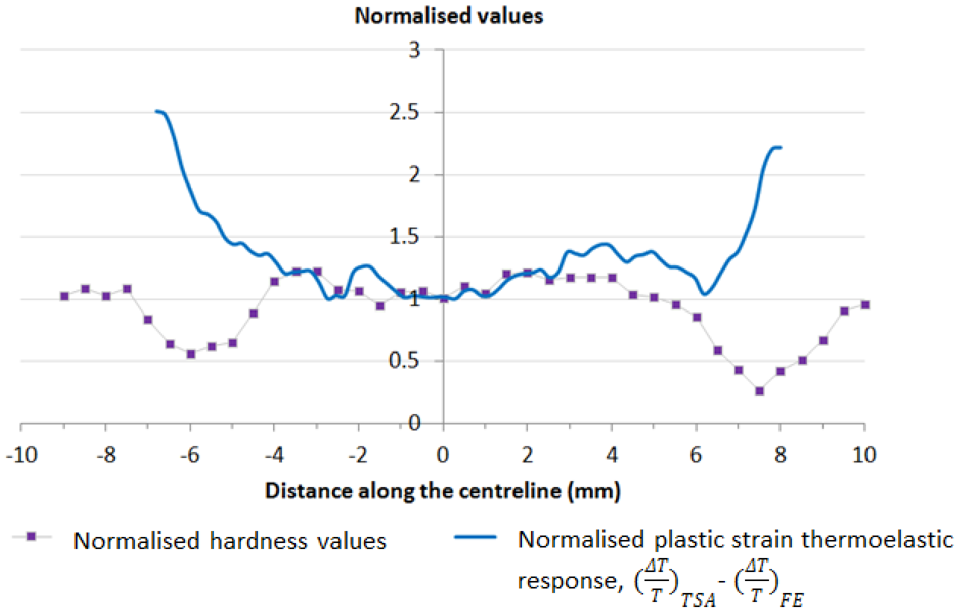

Figure 6.36: Comparison of the normalised plastic strain thermoelastic response $(\frac{\Delta T}{T})_{TSA}$ - $(\frac{\Delta T}{T})_{FE}$ with normalised hardness measurements

6.7 **Summary**

6.7.1 Summary and conclusions

In this chapter, Mock-up A, the first weldment designed for TSA testing was presented. It was welded on both sides simultaneously and subsequently cut to create three seven millimetre thick slices in the direction transverse to the weld so the weld could be imaged with TSA. A FE model of the welded plate was created. The temperature fields were calculated and calibrated against two thermocouples measurements of the welding process. The fusion line of the model was compared and matched with that of the weld. The displacements, strain and stress fields were calculated, based on the thermal fields. A total of eight locations of centre hole drilling measurements were compared with the predicted residual stresses and the results were satisfactory for half of them. The equivalent plastic strain was extracted along the centreline of the specimen for comparison with the thermoelastic response of the weld as well as hardness measurements.

The microstructure was analysed from top to centre of the centreline and a variation in microstructure was observed: large elongated grains are observed in the weld region. In the HAZ, beneath the top weld, very large grains of hundreds of microns of length and breadth could be observed. The microstructure of the parent material could be observed between the HAZ and the centre of the plate. A high density of slip bands was observed in the centre, which indicates plastic straining in this region. As the cold rolling process of the plate was not modelled, it is likely that this process is the cause for the creation in plastic strain which would not be predicted in the FE model.

The thermoelastic response from Mock-up A was compared to the FE predictions of plastic strain. A slight increase of the thermoelastic response from the centreline to the weld bead was observed, which is consistent with the FE predictions. However, the plastic strain peaks from the FEA did not coincide with the increase in the thermoelastic response. This may be due to the material change, or weld microstructure and demonstrates the sensitivity of TSA PSA to features other than plastic strain. To investigate this further the hardness of Mock-up A was measured along the centreline and compared with FEA and TSA results. The hardness did not capture the plastic strain peaks predicted by FEA due to the large gradient in grain size in the HAZ. However, a decrease in the hardness measurement coincides almost exactly with an increase in the plastic strain thermoelastic response.

6.7.2 Further work

During the manufacture, a number of unknowns were encountered, which jeopardized the confidence in the accuracy of the modelling, and therefore plastic strain fields, which are fundamental in the case of this first step. The manufacturing and modelling challenges encountered are listed and were taken on board to create a simpler weldment, Mock-up B, which is presented in the next chapter.

Non-uniform bead

The manual aspect of the welding process involved many unknowns which cannot be taken into account in the modelling, such as welders speed compared to each other, non-uniform speed of each welder independently, weld trajectory not straight, weld beads not uniform, one welder ran out of filler metal during welding process.

Modelling the cutting process

In the model of Mock-up A, the EDM cutting was not modelled. However this process can have an effect on the plastic strain, as reported in [115]. The surface imaged in TSA coincides with the EDM cut surface and cannot be properly modelled.

To avoid problems encountered during manufacturing of Mock-up A, Mock-up B is an autogenous weld, so no filler metal is involved in the modelling.

To circumvent the problems encountered in the FE model of the cutting of mock-up A, the geometry of mock-up B is designed so no cutting is required. The whole mock-up will fit in the servo-hydraulic tensile test machine.

Cold rolling plastic strain

In the middle of the plate, a number of slip bands were identified. These are likely to have formed during the cold rolling of the plate while being manufactured. In Mock-up B, the plate to be welded will be cut to dimensions and heat treated to anneal former existing plastic strain. This will ensure all plastic strain created in Mock-up B will arise from the welding process and can be predicted using FEA.

Chapter 7: Defining the thermoelastic response of an autogenous edge weld: Mock-up B

7.1 Introduction

The aim of the work described in this chapter is to improve on Mock-up A by accounting for all the uncertainties that have been revealed in the work described in the previous chapter. The aim is as in chapter 6 to create a simple welded specimen where the plastic strains are known. Here it is ensured that all the necessary weld parameters are known, so that the plastic strain can be predicted accurately with FE modelling. The mock-up is also designed to be cyclically loaded in a servo-hydraulic test machine with the weld positioned to be imaged with the infrared camera.

7.2 Realisation of the mock-up

For Mock-up A one of the major difficulties was the uncertainties produced by the EDM cutting of the mock-up from the large bead-on-plate specimen; particularly in predicting the residual stress relaxation during the cutting. Therefore it was decided that for Mock-up B there should be no cutting. A further consideration was controlling the shape and size of the weld bead in Mock-up A so Mock-up B contain an autogenous weld, where filler material is not used and hence it is not necessary to include the filler metal in the model. The dimensions of Mock-up B are presented in Figure 7.1 and the weld was created using the TIG welding process so that autogenous edge weld specimen comprises AISI 316L stainless steel. The chemical composition of the parent plate used to manufacture Mock-up B was tested in TWI Ltd and is presented in Table 7.1. The dimensions of Mock-up B are such so that it fits in directly in the servo-hydraulic test machine grips. The grip requires at least 40 mm of material to clamp with a thickness up to 15.75 mm. The thickness of the plate from which the mock-up was manufactured is 10 mm. The length of the specimen is 180 mm to allow sufficient material to grip.

Before welding, the plate was stress relieved at the annealing temperature (1050 °C) for 30 minutes. The welding process used is Tungsten Inert Gas (TIG) welding with a current of 200 A and voltage of 12 V, resulting in a heat input of 2400 W. The welding speed is 2.0 mm/s. During the welding, the plate was not constrained that is it was free to distort so that the boundary conditions do not influence the plastic strain field. To monitor the temperatures developed in the welding process eight thermocouples were attached on one side of the plate as shown in Figure 7.2. The results are presented in Figure 7.3 and will be used in section 7.3 to calibrate the FE model heat source. A macrograph of a replica of the weld was obtained, as presented in Figure 7.4 and will also be used for the heat source calibration.

Figure 7.1: Geometry and dimensions of Mock-up B. All dimensions are in mm.

C	**Si**	**Mn**	**P**	**S**	**Cr**	**Mo**	**Ni**	**Al**	**As**
0.019	0.35	1.36	0.030	0.002	16.5	2.00	9.9	<0.01	<0.01
B	**Co**	**Cu**	**Nb**	**Pb**	**Sn**	**Ti**	**V**	**W**	**Ca**
0.001	0.17	0.29	0.02	<0.002	0.008	0.006	0.08	<0.05	0.001

Table 7.1: Nominal chemical composition of Mock-up B (wt.%) (Fe=balance)

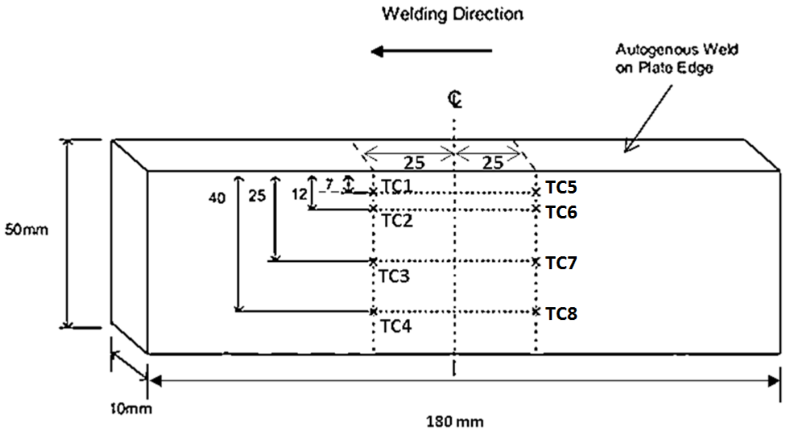

Figure 7.2: Thermocouples positions

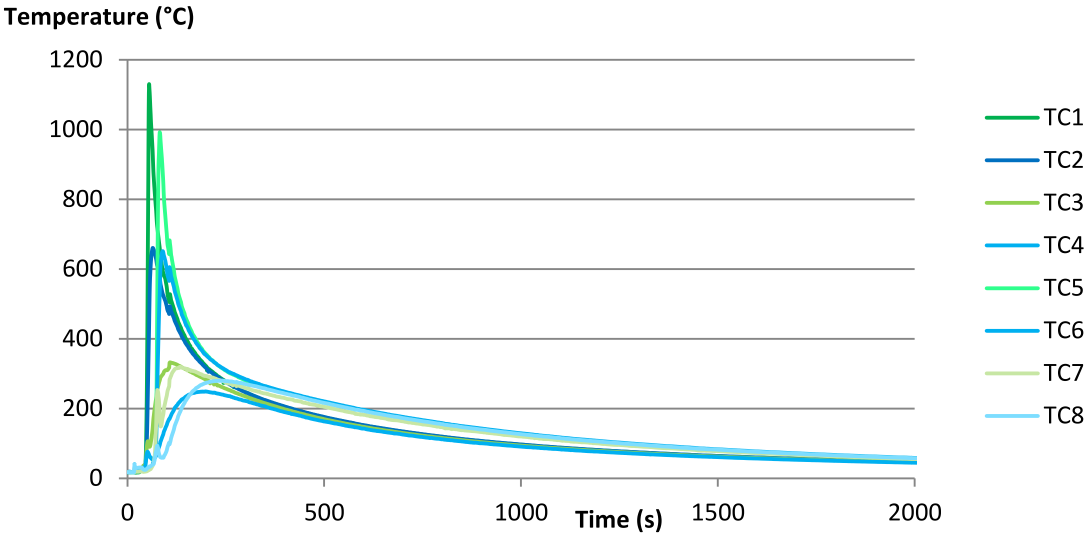

Figure 7.3: Thermocouples measurements

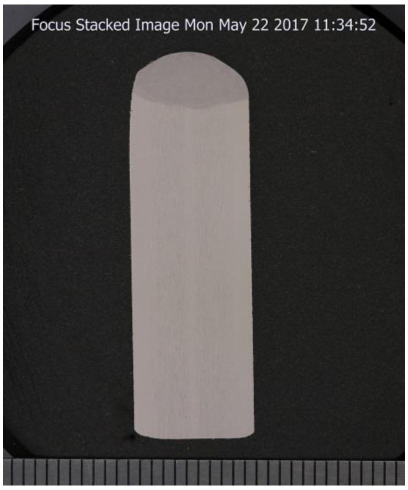

Figure 7.4: Macrograph of the fusion zone

7.3 FE analysis prediction of the temperature fields

7.3.1 Geometry and mesh

The dimensions of the plate depicted in Figure 7.1 were used to create the geometry of the edge weld FE model. Properties from [45] were used to model the thermal and mechanical properties of the parent material. The material properties used for the model are presented in Appendix A. The elastic-plastic behaviour is modelled using an isotropic hardening model as described in Chapter 6.

For the thermal analysis, it is recommended [39] that the mesh size in the weld should be smaller than a quarter of the molten area to allow the penetration and bead shape to be predicted accurately. In the model, the weld zone width is 10 mm, therefore brick elements of 0.5 mm² (1 mm in the x direction and 0.5 mm in the y direction) were used to map the weld and heat affected zone, as can be seen in Figure 7.5. Along the length of the weld, the elements were extruded to 5 mm, which is smaller than the heat source length 5 (6 mm). The mesh is fine around the weld and the heat affected zone as the temperature and stress gradients are large in these area. The mesh is coarser in the regions where no temperature or stress gradient is present, as presented in 7.5. To calculate the temperature fields, the elements are linear heat transfer dedicated elements, referred as DC3D8 in Abaqus.

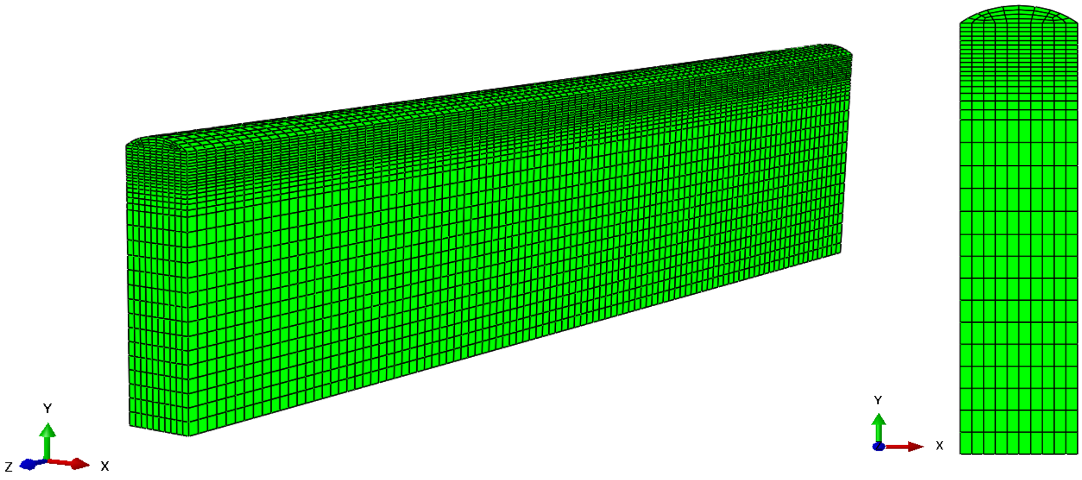

Figure 7.5: Mesh of the whole model (left) and transverse view of the weld bead region (right).

7.3.2 FE predictions of the temperature fields

To model the heat source, the double ellipsoidal moving heat source model, developed by Goldak [50], was used to simulate the autogenous weld. The parameters used for the heat input, efficiency and geometrical parameters of the double ellipsoid are presented in Table 7.2 and are defined in Figure 2.6.

The predictions of temperature fields were compared to the temperatures recorded in the plate during manufacturing using thermocouples as shown in Figure 7.6. The difference in temperature between the FE predictions difference and the thermocouples measurement does not exceed 10%, apart from the thermocouple TC4. Further away from the weld bead, the peak temperature predicted from the FE model exceeds the measurements by 50 °C, which is a difference of around 20%.

The fusion line, which corresponds to the separation between the molten zone and heat affected zone, is compared to the FE models and the macrograph in Figure 7.7. To evaluate the match in the two, several parameters such as the area, the perimeter and the penetration of the weld pool in the plate are compared in Table 7.2. It can be seen from Table 7.3 that the predicted fusion area is 35% higher than the measured one. This is due to the penetration prediction being 20% higher than the measured weld penetration, which represent less than 2 mm difference. This difference is acceptable for two reasons. First, in this chapter the plastic strain predictions are used to define the area of plastic strain to locate where the expected change in thermoelastic constant will occur. Hence the region of interest and the accuracy of its definition are known, and the discrepancy can be considered in the study. Secondly, when a lower penetration was obtained in the model, the match in thermocouples predictions with measurements was reduced. As the macro was obtained from a replica of the weld and the thermocouples were obtained from Mock-up B itself, the match with the thermocouples readings and the temperature predicted by the model was considered to be more important.

a (mm)	b (mm)	c_f (mm)	c_r (mm)	v (mm/s)	Q (W)	η	f_f	f_r
3	3	3	3	2.0	2400	0.8	0.6	1.4

Table 7.2: Experimental parameters used in Goldak heat source model

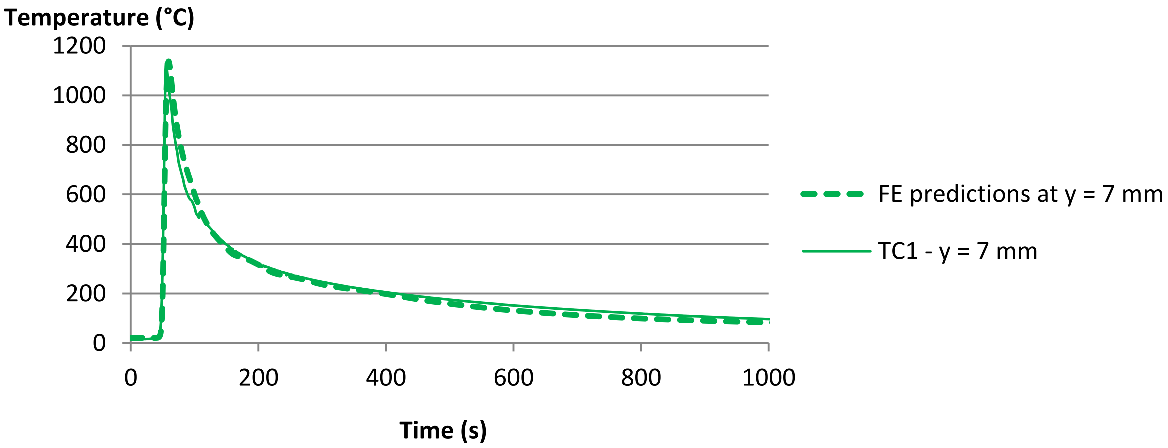

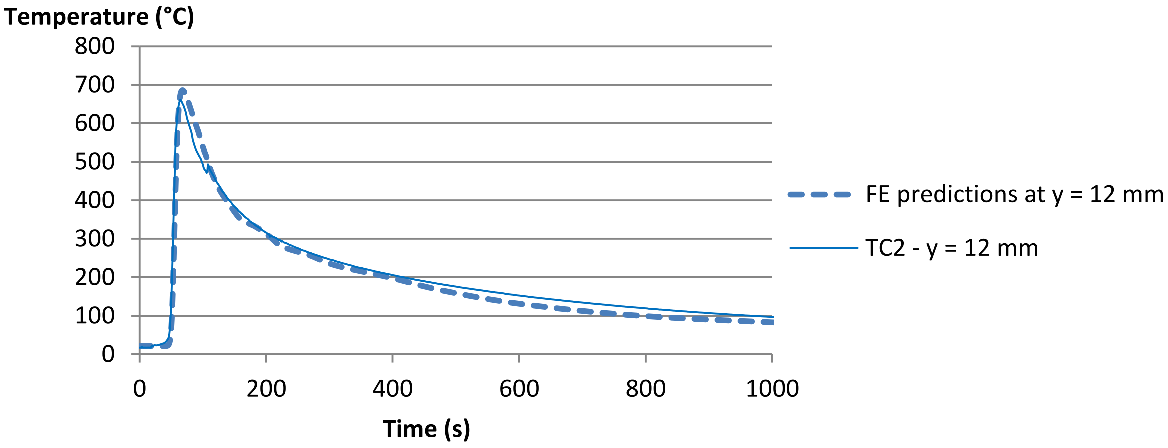

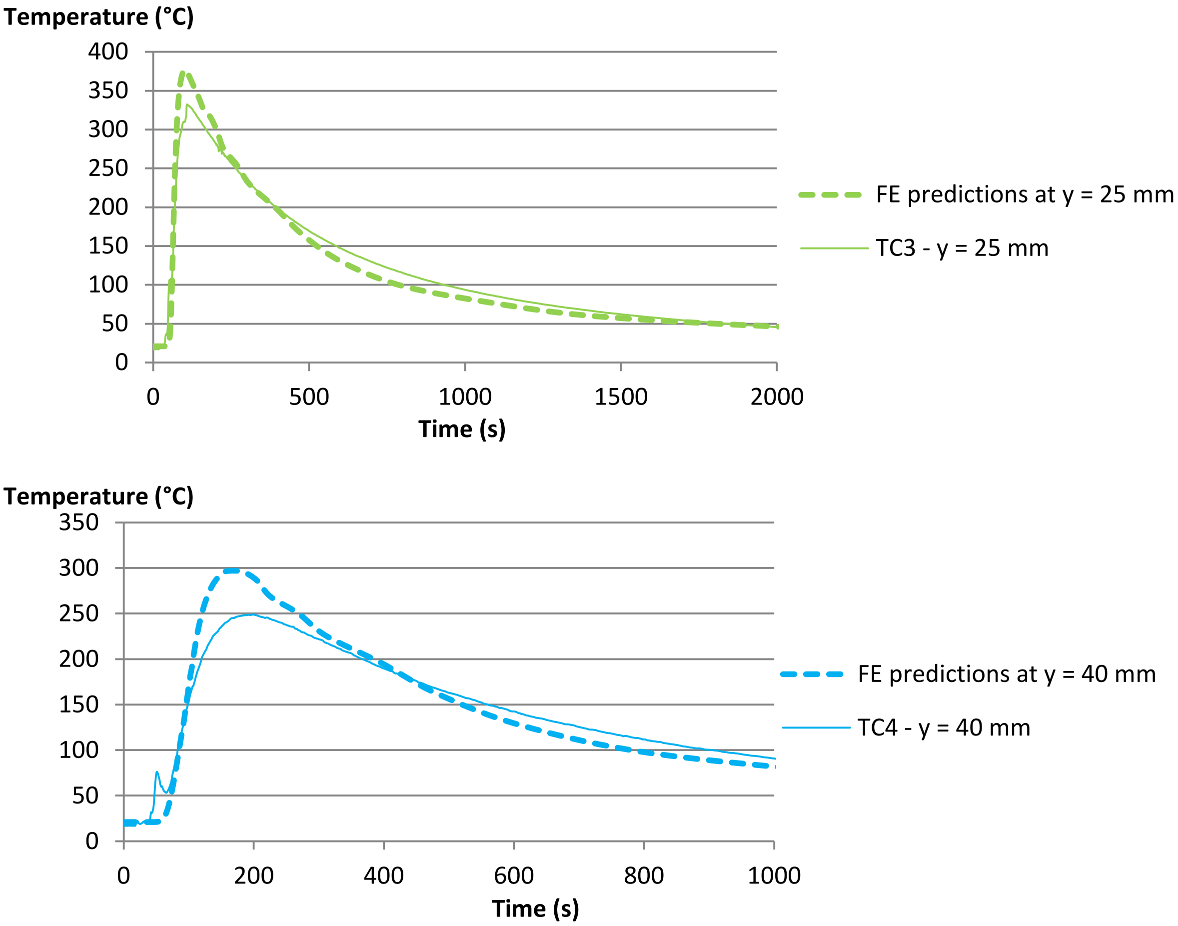

Figure 7.6: Comparison of temperature FE predictions and thermocouple data

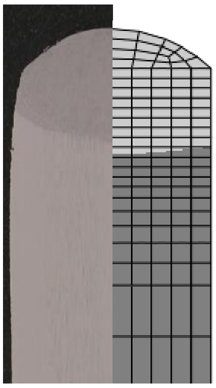

Figure 7.7: Comparison of the fusion line from the FE thermal model (left) and the fusion area from macrograph (right).

	Macrograph	FE model	Deviation (%)
Area (mm²)	33.85	57.915	35
Perimeter (mm)	23.40	30.239	15
Penetration (mm)	4.68	6.55	20

Table 7.3: **Comparison of area, perimeter, width and penetration of welds from macrograph against FE predicted weld area.**

7.4 FE analysis prediction of the plastic strain

7.4.1 Boundary conditions

As the movement of the plate was not constrained during the welding and cooling, boundary conditions in the model restrained the plate to move but allowed deformation. The directions of the restrained displacement are presented in Figure 7.8.

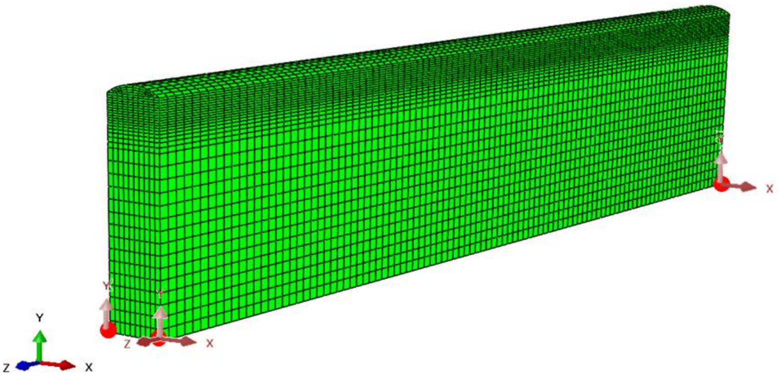

Figure 7.8: Prescribed displacement boundary conditions applied in the mechanical analysis.

7.4.2 Distortion

After the plate had cooled any distortion that had occurred because of the welding process was evaluated by measuring the parameter d shown in Figure 7.9. The displacement field in the y direction is presented in Figure 7.10 and the measured and predicted d values are presented in Table 7.4. The measurements were performed with a ruler and graph paper hence are accurate to 0.1 mm. The distortion predictions are validated by the measurement, which also provides a form of validation of the weld model. The distorted geometry must be considered when evaluating the stresses induced in the plate for the TSA.

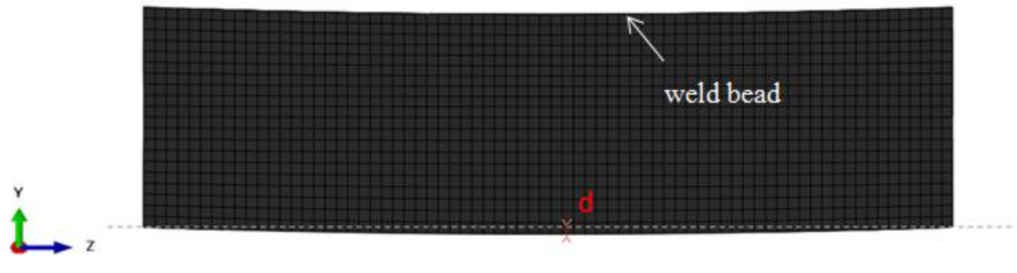

Figure 7.9: Distortion after welding

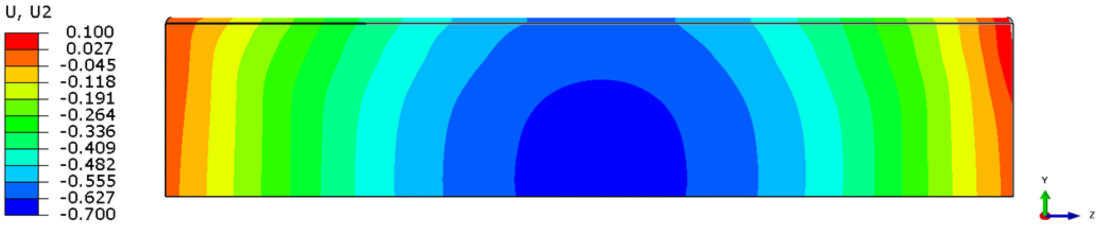

Figure 7.10: FEA predictions of displacement in the y direction

	d (mm)
FEA predictions	0.7
Measurements	0.6 ± 0.1

Table 7.4: Measured and predicted distortion of the plate

7.4.3 Plastic strains

The plastic strain fields were predicted in the plate as depicted in Figure 7.11 and plotted along the line shown in Figure 7.11 in Figure 7.12. It can be seen from Figure 7.12 that the welding induced plastic strain region occurs in a region about 17 mm from the weld into the material. This region is indicated by a vertical dotted line for comparison with the thermoelastic response as described in section 7.5.

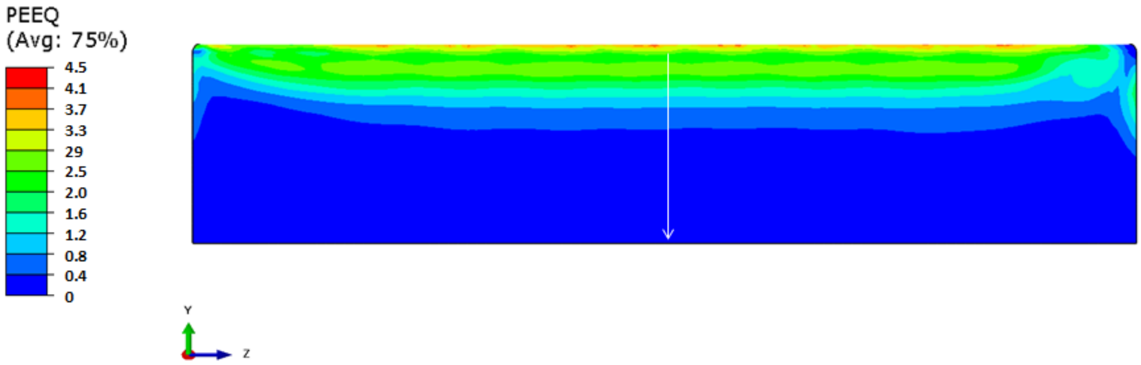

Figure 7.11: FE predictions of the equivalent plastic strain (PEEQ).

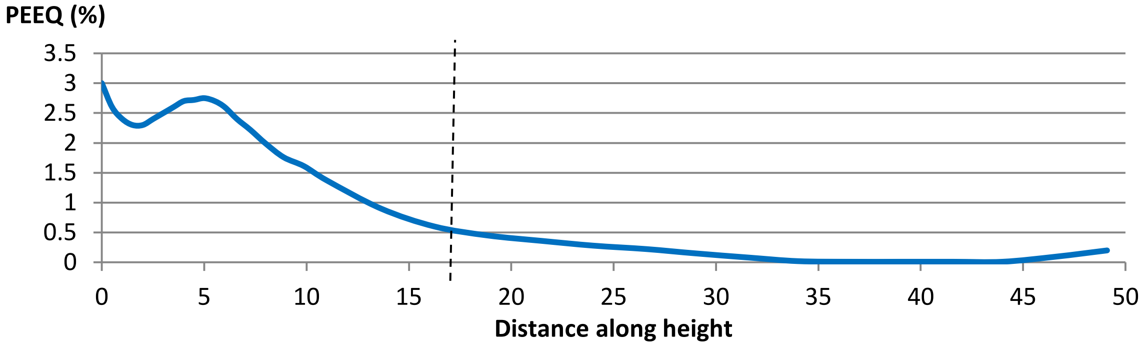

Figure 7.12: Equivalent plastic strain (PEEQ) predictions along the height.

7.5 Thermoelastic stress analysis

A servo-hydraulic tensile test machine was used to apply a cyclic load of 20 kN ± 15 kN at a frequency of 10 Hz. The thermoelastic response was captured using the FLIR photon detector photon detector.

7.5.1 FEA prediction of the stress state in mock-up B

The stresses induced in the welded plate were calculated using a linear elastic model. The model was created to replicate the deformed shape after welding induced distortion. The shape presented in Figure 7.9, was used, using length, width and thickness of Figure 7.1. A mesh sensitivity study was performed. Here the change in the sum of the principal stresses correspond to 50 MPa, hence a change in 0.5 MPa would mask the thermoelastic response produced by plastic strain, hence the mesh influence on the model should be less than 0.05 MPa, which is the case for all the mesh sizes tested as it can be seen in Figure 7.13, meaning the influence of the mesh can be neglected.

To predict $\Delta\sigma_1+\Delta\sigma_2$ caused by the cyclic loading, maximum and minimum loads are applied to a point, referred as "reference point". This point is kinematically coupled to the bottom gripped surfaces of the specimen such that the load is transferred. The reference point is located on the axial symmetry line of the simulated specimen to avoid the application of moments. To model the grip action on the specimen, the top surfaces at the front and back of the specimens are prevented from displacement. In Figure 7.14, the load and boundary conditions are shown as applied to the front of the specimen.

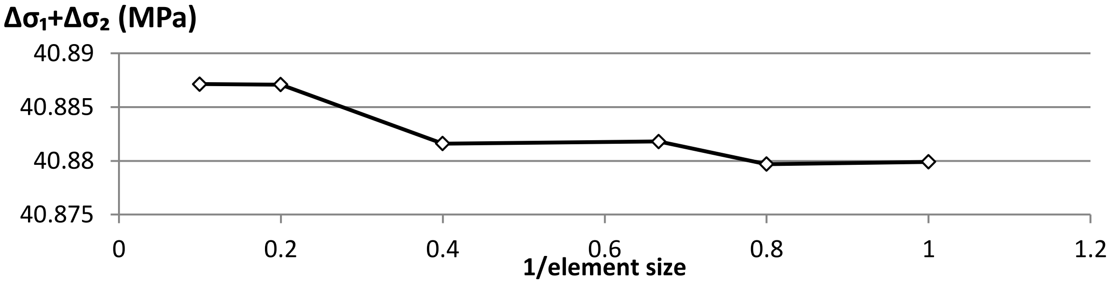

Figure 7.13: Influence pf the element size on $\Delta\sigma_1+\Delta\sigma_2$ determined in the centre of Mock-up B

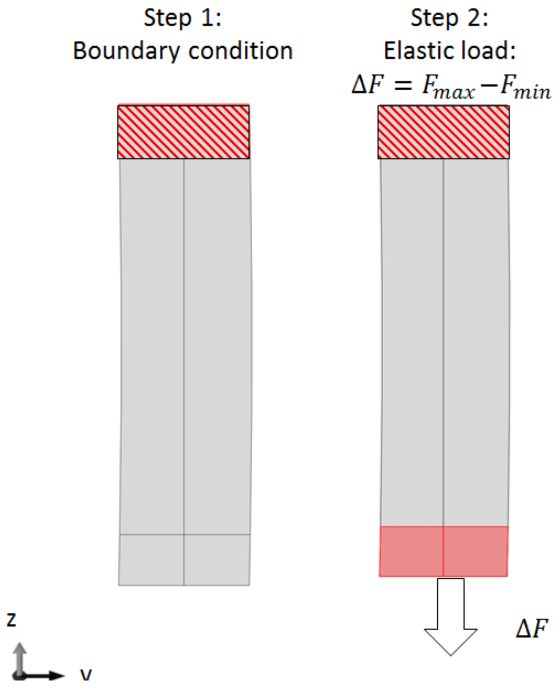

Figure 7.14: Boundary condition (Step 1) and load application (Step2) applied to the front surfaces.

7.5.2 Geometry sensitivity study

As mentioned in section 7.4, after welding, the plate had deformed and the deformation can be represented by d, as presented in Figure 7.9. FEA prediction of d is 0.7 mm and the deformation was measured as 0.6 mm ±0.25 mm. The influence of the distortion was studied, by varying d in the model in 0.1 mm increments, from 0 mm to 1 mm. The predicted change in the sum of the principal stresses according to *d* is presented in Figure 7.15. A change in d of 0.1 mm produces a change of 1 MPa in the gradient in $\Delta\sigma_1+\Delta\sigma_2$ across the width of the specimen. Such a change is sufficient to mask any change in the thermoelastic response arising from the level of plastic strain predicted by the model. However, the gradient of $\Delta\sigma_1+\Delta\sigma_2$ along the height of the specimen is constant for a set d value. This information ensures any change in gradient of the thermoelastic response cannot be attributed to errors on measured distortion of mock-up B.

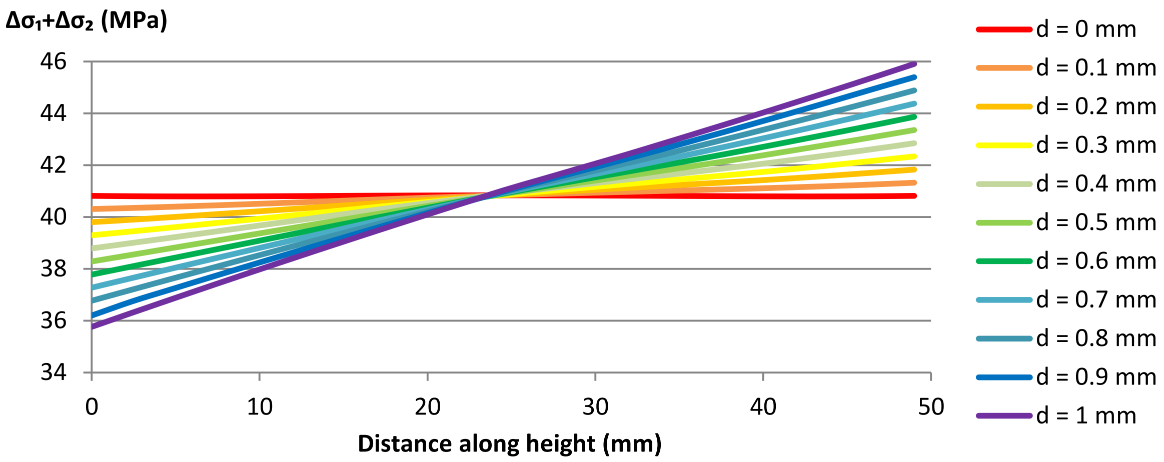

Figure 7.15: The influence of distortion on $\Delta\sigma_1+\Delta\sigma_2$ at mid-length (the weld cap is at the origin).

7.5.3 Results

The thermoelastic response, phase and photograph of mock-up B are presented in **Error! eference source not found.**. The black dotted lines define the weld bead (left) and the thermally affected zone, which coincides with the plastic strain region (right). The thermoelastic response and phase were averaged along the length of the area of interest and plotted along the height of the specimen in Figure 7.16, along with the plastic strain predictions. In the region of the weld bead, the geometry is not uniform, leading to a change in phase, but also a change in stresses as the thickness is not constant, which reduces the thermoelastic response. From both surface plot and graph, it can be seen that the region of plastic strain corresponds with a region of lower average phase. A change in phase can denotes heat conduction occurring in regions of high stress gradients, or that the loading frequency is insufficient for adiabatic response. The welded side of the specimen was thicker due to welding. This creates a gradient in stress in the specimen that can be seen in the thermoelastic response of the specimen in Figure 7.16. Modelling such a variation in thickness to the level of accuracy required can be challenging to reach, especially in the case of complex geometry where stress concentration would be ignored or emphasised due to uncertainties in geometry measurements. Moreover the geometry of the weld bead is not uniform hence the transition in the weld bead area can be difficult to model accurately.

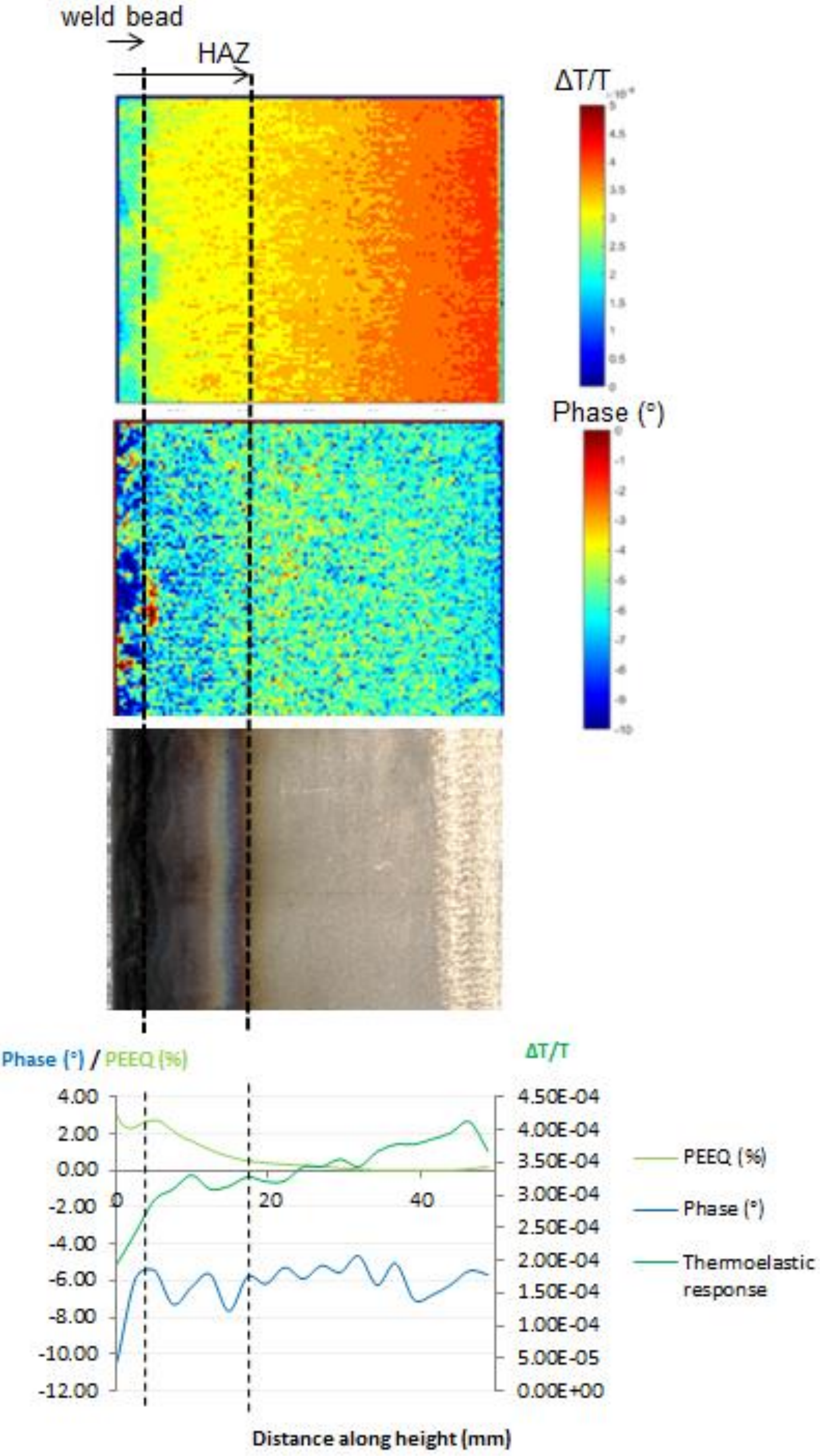

Figure 7.16: Plastic strain predictions (PEEQ), thermoelastic response *ΔT/T* and phase and average over the length of the area interest along the height of the specimen.

7.6 Summary

A second weld mock-up, Mock-up B, was designed to improve on Mock-up A. The Mock-up was designed so that the weld region and heat affected zone was visible on the surface and the specimen could be fitted in the test machine, without cutting. The welding process was simulated using FEA and the plastic strains were predicted. TSA was conducted on Mock-up B and it was shown that both the response and the phase of the response varied in the region corresponding to the plastic strain. The stress state was simulated using a linear FE model, and it was found that the distortion of the specimen during welding had a significant influence on the stress gradient, which emphasises on the need to model the distorted geometry when assessing stress levels for TSA analysis.

The plastic strain region corresponded well with a change in the phase data. As no change in the stress is expected in this region, the change in phase could be caused by features of the HAZ region.

In conclusion, an influence of the plastic strain on the phase of the thermoelastic response was observed. However, to quantify the level of plastic strain, means of assessing the geometry in an accurate manner to simulate the linear stress state in the component is required.

Chapter 8: Summary, conclusions and future work

8.1 Introduction

The aims of the PhD were to assess the influence of microstructure on the influence of plastic strain on the thermoelastic response and to design mock-ups that allow the thermoelastic response from welded specimen to be investigated. The work undertaken can be divided into four topics:

- the study of the influence of weld microstructure on the thermoelastic response;
- the study of the influence of plastic strain on the thermoelastic constant of materials containing different microstructure;
- FE modelling of the welding process to predict welding induced plastic strains;
- assessment of the capability of TSA PSA to characterise weld induced plasticity.

A brief summary followed by the conclusions, as well as future work are presented in the subsequent sections.

8.2 Microstructure influence on the thermoelastic response

To study the influence of the weld microstructure on TSA readings, two materials commonly used in the nuclear industry were selected: austenitic steel AISI 316L and ferritic SA508 Gr.3 Cl.1. For both materials, thin strip specimens were designed and manufactured. Heat treatments were selected to replicate realistic thermal history and resulting microstructure in a weld. TSA was applied on the specimens and the thermoelastic constant was derived for each material and microstructure. Values were then compared between microstructures and to the reference value.

The thermoelastic constant of a series of specimens produced from AISI 316L with different grain sizes varying from 27 μm to 106 μm were found to be 0.22% away from the reference value for this material, which is in within the standard deviation reported for the reference value. According to [10], such a change would be interpreted as less than 0.5% plastic strain. Therefore it is concluded that the thermoelastic constant of an AISI 316L specimens that has not been subjected to plastic strain is not influenced by different grain sizes produced during welding.

The thermoelastic constant of a series of specimens from SA508 with different phase proportions (mix of ferrite, bainite and martensite, pure ferrite, pure martensite) was in the range of $3.36\ 10^{-12}\mathrm{Pa}^{-1}$ to $3.53\ 10^{-12}\mathrm{Pa}^{-1}$. The average thermoelastic constant of heat treated specimens differ by less than 5%. This variation could be interpreted as the influence of plastic strain on thermoelastic constant hence knowledge of the metallurgic phases present in a component is required before applying TSA PSA. To further investigate the effect of weld microstructures on the thermoelastic constant and to determine the effect of plastic straining on the thermoelastic response a new specimen was designed that contains both plastic strain and different microstructures.

8.3 Influence of microstructure on the dependence of thermoelastic constant on plastic strain

A tapered test specimen was designed so that the influence of plastic strain could be studied alongside microstructure. Plastic strain was induced in the specimens with a uniaxial tensile loading and assessed using three independent methods, FE analysis, DIC and strain gauges mounted on each specimen. The plastic strain induced in the specimens varied from 2% to 4% in the AISI 316L specimens and from 1% to 6% plastic strain in the SA508 specimens.

The thermoelastic response was obtained and the change in the sum of the principal stresses was predicted using FEA, allowing the thermoelastic constant to be derived. The dependence of the thermoelastic constant on plastic strain was obtained for each microstructure studied. The extrapolated thermoelastic constant of the plastic strain free material, $K_{0\%}$ was used to normalise the data and a linear interpolation of the normalised thermoelastic constant with plastic strain was performed. The results show that the dependence of the thermoelastic constant with plastic strain is influenced by the microstructure, i.e. grain size in AISI 316L and phase proportions in SA508.

The results showed that the thermoelastic constant is dependent on plastic strain and that the level of the dependence is influenced by the dislocation density in both AISI 316L and in SA508. The results confirm an increase in K for tensile plastic strain which for AISI 316L is in agreement with [10]. It was shown for both material types, fewer dislocations make the material more sensitive to changes in plastic strain. Furthermore, the $K_{0\%}$ values for microstructures with large dislocation densities are greater than those with fewer dislocations.

It may be concluded that materials with lower dislocation density will have a lower thermoelastic constant but a greater sensitivity to plastic strain. If a there is a significant change in average grain size, e. g. a ratio of 10, or in phase, with presence of martensite and large grains of ferrite in the region of interest, the thermoelastic constant may vary with both microstructure and plastic strain and the variations may be of the same order of magnitude. Thus when attempting to deduce the WIP from changes in thermoelastic constant a consideration of the material microstructural changes as a result of welding is necessary.

8.4 Plastic strain assessment in a welded component: Mock-up A

Mock-up A is a 7 mm transverse slice extracted from the centre of a double weld bead on plate specimen, transverse to the weld. A FE model of the welded plate was created. The temperature fields were calculated and calibrated against two thermocouples measurements of the welding process. The fusion line of the model was compared and matched with that of the actual weld. The displacements, strain and stress fields were calculated, based on the thermal fields. A total of eight centre hole drilling measurements were compared with the predicted residual stresses and the results judged satisfactory, considering the gradient and large stresses present in the measurement area.

The predicted equivalent plastic strain was extracted along the centreline of the specimen for comparison with the thermoelastic response of the weld as well as hardness measurements and microstructure analysis. It was observed that the minimum of the derived thermoelastic response due to plastic strain was observed in the middle, similarly to the minimum of predicted plastic strain. However, TSA PSA did not capture the peaks in plastic strain predicted by the FE model.

A small increase in both hardness and change in thermoelastic response was observed between 3 mm and 5 mm on the centreline. As this change is consistent between the two techniques, it may have been caused by plastic strain induced during material manufacturing process, which was not included in the FE model. The microstructure of the parent material could be observed between the HAZ and the centre of the plate. A high density of slip bands was observed in the centre, which indicates plastic straining in this region. As the cold rolling process of the plate was not modelled, it is possible that this process caused the plastic strain which would not be included the FE model. More importantly, it could be seen that the plastic strain thermoelastic response increase coincides directly with a decrease in the hardness.

Uncertainties in Mock-up A

The results and uncertainties that have been revealed in the design of Mock-up A were used to enhance the design of a new mock-up especially created for TSA testing. In Mock-up A, two manufacturing processes, other than welding were identified as potential sources of plastic strain creation.

- The AISI 316L plate used to create Mock-up A had been cold rolled. This process is known to induce plastic strain. However, the amount and location of cold rolling induced plastic strain are unknown. The material was not stress relieved prior to welding and hence artefacts from the rolling process would still exist in the material, away from the welded region.
- After welding, Mock-up A slices were cut using EDM. EDM cutting is a complex technique involving melting of the material and produces plastic strain approaching the EDM cut surface which is imaged in TSA. EDM induced plasticity could not be properly modelled as no simple technique exists to model the plastic strain induced by EDM cutting.

8.5 Design, modelling and TSA of an autogenous edge weld: Mock-up B

A second weld mock-up, Mock-up B, was designed to improve on Mock-up A. The Mock-up was designed so that the weld region and heat affected zone was visible on the side surface and so that the mock-up could be fitted in the test machine, without cutting. The welding process was simulated using FEA and the plastic strains were predicted. TSA was conducted on Mock-up B and the following remarks were found:

- The plastic strain region corresponded well with a change in the phase of the thermoelastic response. As no change in the stress is expected in this region, the change in phase could be caused by features of the HAZ region. This result is promising regarding the capability of the technique to identify potential regions of residual stresses and plastic strain.
- The stress state was simulated using a linear FE model, and it was found that the distortion of the specimen during welding has a significant influence on the stress gradient, which highlights the need to know very accurately the geometry of the component under investigation.

8.6 Implication of the results on the application of the TSA PSA technique

The sensitivity of the TSA to plastic strain was assessed. An increase in the thermoelastic constant was observed with tensile plastic strain, which confirms the findings from [10]. The precision of the technique relies on the precision with which the discussed relationship is obtained, which involves both the accurate assessment of plastic strain, and the precision of the derivation of the thermoelastic constant. The variation in measurements was quantified in the experimental work and its influence on the relationship between the thermoelastic response and the plastic strain was assessed.

The phase of the thermoelastic constant also showed sensitivity to plastic strain region indicating the phase could be used along with the thermoelastic response to assess plastic strain using TSA PSA.

The accuracy of the technique to determine the deformed shape of the tapered specimens which is used to establish the stress in the specimen during TSA is of paramount importance. The specimen geometry should be established with an error that would modify the response significantly less than that expected from a change in plastic strain. The level of accuracy required can be challenging to reach especially in the case of complex geometry where stress concentration would be ignored or emphasised due to uncertainties in geometry measurements.

A deviation of 20% of the thermoelastic response was observed before and after abrasion of the samples This discrepancy is significantly greater than the plastic strain influence on thermoelastic constant and underlines the need of a uniform surface preparation before applying TSA PSA.

An increase of 5% which is believed to arise from chemistry and ageing was observed in K_0. If the thermoelastic constant of the same piece of material free of plastic strain can be assessed, the variation in thermoelastic constant due to plastic strain could be observed, assuming the changes in K produced by ageing and chemistry are uniform. However, if it is not the case, or if deriving K_0 is not possible, the increase in K of 5% would mitigate any variation in thermoelastic constant due to plastic strain.

8.8 Future work

The potential of TSA PSA as a new portable, non-destructive, full-field surface plastic strain assessment technique was assessed. Further information is required to develop confidence in the influence of plastic strain on the thermoelastic response as suggested below.

- In both AISI 316L and SA508 steels, an increase in the thermoelastic constant measured in Chapter 3 was observed in the tapered specimens examined in Chapter 5. The origin of the variation was not clarified. A potential explanation could lie in the occurrence of a chemical reaction between the paint and the surface of the specimens, as the specimens were left with paint on for eighteen month before being cleaned with acetone. This would demonstrate influence of abrasion, paint, chemistry and time effects on the thermoelastic constant. Further work should be carried out to identify the origin of the change and analyse its sensitivity to grain size.
- In Chapter 6, an increase in both hardness measurements and thermoelastic response provided by Howell [94] were observed in a parent material region. The microstructure of the specimen in this region will be analysed to find the origin of this increase. If the increase is confirmed to have been caused by plastic strain, the thermoelastic response obtained in Mock-up A will assess the capability of the technique to capture plastic strain in a welded component, regardless of the grain size in the material and it could be then noted that the technique is sensitive to plastic strain caused by other processes than welding, such as during manufacture. The processes used during manufacture are not always known hence cannot be modelled. Therefore the technique will overcome this lack of information which can be a great asset for structural integrity on plants. The slip bands observed in the middle of the plate are likely arising from the cold roll process. However, this can only be confirmed by examining the middle of the plate in a region away from the weld.

The applicability of the technique on site has been investigated by Tighe et. al. [70]. Portable loading and TSA equipment were developed and applied on site. The thermoelastic response was obtained. However, to apply TSA PSA on-site, the stress caused by the loading in the component must be known.

- Defining the geometry of the component was found to be critical in order to accurately predict TSA stresses.
- As for the feasibility of application of TSA on-site, the next mock-up should contain welds in pipes of interest to industry.

As an overall conclusion, the influence of plastic strain on the thermoelastic response reported in Chapters 5, 6 and 7 indicates potential of the TSA PSA technique. The influence of microstructure on the thermoelastic constant was assessed in Chapter 5 for two nuclear grade steels, AISI 316L and SA508 and it was found that SA508 material is more sensitive to plastic strain than AISI 316L. Moreover, a coarse microstructure was reported to produce a larger influence of plastic strain on the thermoelastic constant in both types of steel. TSA PSA technique sensitivity on surface preparation and component geometry assessment are of paramount importance. The thermoelastic response of Mock-up A [94] and Mock-up B weldments were analysed and weak correlation between the region of plastic straining and thermoelastic response was found.

Appendix A Material properties used in the weld FEA

Mock-up A: 316L [45] and [116]

Poisson's ratio	Latent heat (°C)	Density (kg/m^{-3})	Film coefficient [116] (10^{-6} W/mm^2/°C)	Radiation emissivity [116]
0.294	1400	7966	5.0	0.5

Table A.1.: Poisson's ratio, latent heat and density parameters for 316L [45] and [116]

Material properties /Temperature (°C)	Specific heat (kJ/kg/°C)	Conductivity (W/m/°C)	Linear thermal expansion coefficient (10^{-6} mm/mm/°C)	Young's modulus (GPa)
20	0.492	14.12	14.56	195.6
100	0.502	15.26	15.39	191.2
200	0.514	16.69	16.21	185.7
300	0.526	18.11	16.86	179.6
400	0.538	19.54	17.37	172.6
500	0.550	20.96	17.78	164.5
600	0.562	22.38	18.12	155.0
700	0.575	23.81	18.43	144.1
800	0.587	25.23	18.72	131.4
900	0.599	26.66	18.99	116.8
1000	0.611	28.08	19.27	100.0
1100	0.623	29.50	19.53	80.0
1200	0.635	30.93	19.79	57.0
1300	0.647	32.35	20.02	30.0
1400	0.659	33.78	20.21	2.0

Table A.2.: Temperature dependent properties for 316L characterisation [45]

Plastic strain (%)	0	0.2	1	2	5	10
Temperature (°C)	True stress (MPa)					
23	210	238	292	325	393	294
275	150	173.7	217	249	325	424
550	112	142.3	178	211	286	380
750	95	114.7	147	167	195	216
800	88	112	120	129	150	169
900	69	70	71	73	76	81
1100	22.4	23.4[i]	24.4[i]	25.4[i]	26.4 [i]	27.4 [i]
1400	2.7	3.7[i]	4.7[i]	5.7[i]	6.7 [i]	7.7 [i]

Table A.3.: Temperature and plastic strain dependent true stress for 316L [45].

[i] Data extrapolated for finite element analysis

Appendix B DIC camera properties

Imager *E-lite* 5M is a high sensitivity, high resolution digital camera, equipped with an interline transfer chip with progressive scan readout. The camera comes with a fast Gigabit Ethernet interface for distances up to 100 m. In combination with its small and lightweight design, the camera is ideal for flexible and portable use.

General System Specifications
A/D-converter 12 bit
Interface Gigabit Ethernet, max. 100 m
Lens mount: C-mount, adapter to F-mount included
Number of pixels 2448 x 2050 pixels

Pixel size 3.45 x 3.45 µm²
Active area 8.5 x 7.1 mm²
Spectral range 400 – 850 nm
Dynamic range 8.5 bit
Readout noise 16 e-
Frame rate 10 frames/s
Binning yes
Windowing yes
Dimensions (WxHxL) 86.7 x 44 x 29 mm³

Weight 220 g
DaVis Software
Operation system Windows XP
Data acquisition user programmable
Command Language ‚C‘ syntax for system and user functions

Appendix C TSA equipment

Cedip Silver 480M

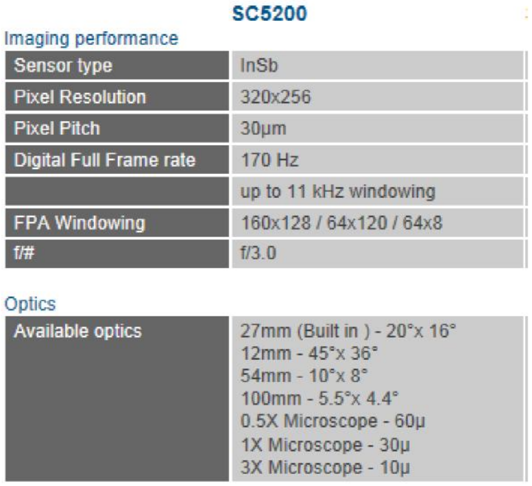

SC5200

Imaging performance

Sensor type	InSb
Pixel Resolution	320x256
Pixel Pitch	30µm
Digital Full Frame rate	170 Hz
	up to 11 kHz windowing
FPA Windowing	160x128 / 64x120 / 64x8
f/#	f/3.0

Optics

Available optics	27mm (Built in) - 20°x 16° 12mm - 45°x 36° 54mm - 10°x 8° 100mm - 5.5°x 4.4° 0.5X Microscope - 60µ 1X Microscope - 30µ 3X Microscope - 10µ

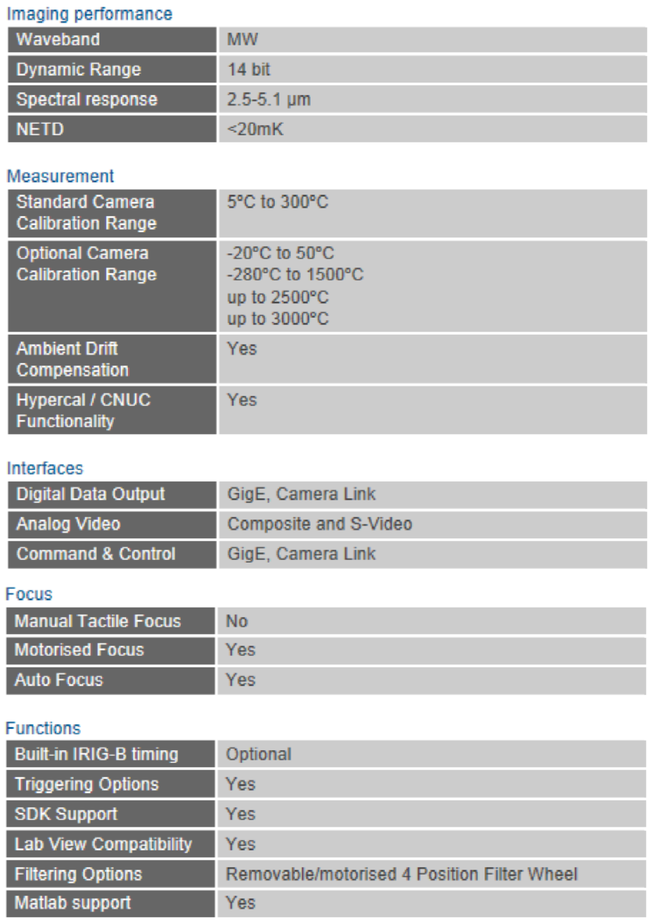

Imaging performance

Waveband	MW
Dynamic Range	14 bit
Spectral response	2.5-5.1 µm
NETD	<20mK

Measurement

Standard Camera Calibration Range	5°C to 300°C
Optional Camera Calibration Range	-20°C to 50°C -280°C to 1500°C up to 2500°C up to 3000°C
Ambient Drift Compensation	Yes
Hypercal / CNUC Functionality	Yes

Interfaces

Digital Data Output	GigE, Camera Link
Analog Video	Composite and S-Video
Command & Control	GigE, Camera Link

Focus

Manual Tactile Focus	No
Motorised Focus	Yes
Auto Focus	Yes

Functions

Built-in IRIG-B timing	Optional
Triggering Options	Yes
SDK Support	Yes
Lab View Compatibility	Yes
Filtering Options	Removable/motorised 4 Position Filter Wheel
Matlab support	Yes

References

1. P.J. Withers, and H.K.D.H. Bhadeshia, *Residual stress. Part 2 - Nature and origins.* Material Science and Technology, 2001. **17**(4): p. 366-375.
2. M. Consoni, C. F. Wee and C. Schneider. *Manufacturing of welding joints with realistic defects*. in *50th Annual Conference of the British Intitute of Non-Destructive testing*. 2011. Telford, UK.
3. A. Sáez-Maderuelo, L. Castro and G. de Diego, *Plastic strain characterization in austenitic stainless steels and nickel alloys by electron backscatter diffraction.* Journal of Nuclear Materials, 2011. **416**: p. 75-79.
4. M. Mochizuki, M. Hayashi and T. Hattori. *Numerical analysis of welding residual stress and its verification using neutron diffraction measurement*. in *Transactions of the ASME*. 2000.
5. P.S. Prevey, *X-ray diffraction residual stress techniques.* Metals Handook, 1986. **10**: p. 380-392.
6. *Assessment of the integrity of structures containing defects*, in *R6 Revision 4*. British Energy: Gloucester.
7. O. Muránsky, C.J. Hamelin, V.I. Patel, V. Luzin and C. Braham, *The influence of constitutive material models on accumulated plastic strain in finite element weld analyses.* International Journal of Solids and Structures, 2015. **69-70**: p. 518-530.
8. O. Muránsky, M. Tran, C. J. Hamelin, S. Shrestha and D. Bhattacharyya, *Assessment of welding-induced plasticity via electron back-scatter diffraction.* International Journal of Pressure Vessels and Piping, 2017.
9. J.M. Dulieu Barton, *Thermoelastic Stress Analysis*, in *Optical Methods for Solid Mechanics*, Wiley-VCH, Editor. 2012. p. 345-366.
10. A.F. Robinson, *Assessment of residual stress using thermoelastic stress analysis*, in *Faculty of Engineering and the Environment*. 2011, University of Southampton.
11. S. Quinn, J.M. Dulieu-Barton and J.M. Langlands, *Progress in thermoelastic residual stress measurements.* Strain, 2004. **40**: p. 127-133.
12. J.A. Francis, H.K.D.H. Bhadeshia and P.J. Withers, *Welding residual stresses in ferritic power plant steels.* Material Science and Technology, 2007. **23**(9): p. 1009-1020.
13. H.-L. Ming, Z.-M. Zhang, P.-Y. Xiu, J.-O. Wang, E.-H. Han, W. Ke and M.-X. Su, *Microstructure, Residual Strain and Stress Corrosion Cracking Behavior in 316L Heat Affected Zone.* Acta Metallurgica Sinica, 2016. **29**(9).
14. R.A. Cottis, *Guides to good practice in corrosion control Stress Corrosion Cracking*. 2000, NPL.
15. A.F. Mark, J.A. Francis, H. Dai, M. Turski, P.R. Hurrell, S.K. Bate, J.R. Kornmeier and P.J. Withers, *On the evolution of local material properties and residual stress in a three pass SA508 steel weld.* Acta Materialia, 2012. **60**: p. 3268-3278.
16. *Practical Heat Treating*. Second edition ed. Vol. Second Edition. 2006: ASM International.
17. W.D. Callister, and D.G. Rethwisch, *Materials Science and Engineering*. Eighth Edition ed. 2011: John Wiley & Sons, Inc.
18. K. Suzuki, I. Kurihara, T. Sazaki, Y. Koyoma and Y. Tanaka, *Application of high strength MnMoNi steel to pressure vessels for nuclear power plant.* Nuclear Engineering and Design, 2001. **206**: p. 261-278.
19. *R5. Assessment procedure for the high temperature response of structures*, *Issue 3*. 2003, British Energy: Gloucester.
20. *R6 Revision 4. Assessment of the integrity of structures containing defects*. 2004, British Energy: Gloucester.

21. P.J. Withers, M. Turski, L. Edwards, P.J. Bouchard and D.J. Buttle, *Recent advances in residual stress measurement.* International Journal of Pressure Vessels and Piping, 2008. **85**: p. 118-127.
22. P.J. Bouchard, and R. A. W. Bradford, *Validated axial residual stresses profiles for fracture assessments of austenitic stainless steel pipe girth welds*. 2000, British Energy Generation Ltd.
23. A.A. Scaramangas, R.F.D. Porter Goff and R.H. Legatt, *On the correction of residual stress measurements obtained using the centre-hole-drilling method.* Strain, 1982. **18**(3): p. 88-97.
24. F.A. Kandil, J.D. Lord, A.T. Fry and P.V. Grant, *A review of residual stress measurements obtained using the centre-hole method*, in *NPL Report MATC(A)04*. 2001: Teddington.
25. P.V. Grant, J.D. Lord and P.S. Whitehead, *Measurement Good Practice Guide No. 53 - Issue 2: The Measurement of Residual Stresses by the Incremental Hole Drilling Technique*. 2006, National Physical Laboratory.
26. P.J. Withers, and H.K.D.H. Bhadeshia, *Residual stress. Part 1 - Measurement techniques.* Material Science and Technology, 2001. **17**(4): p. 355-365.
27. *Measurement of Residual Stresses by the Hole-Drilling Strain Gage Method*. 2010, Micro-Measurements.
28. D.J. Smith, P.J. Bouchard and D. George, *Measurement and prediction of residual stresses in thick-section steel welds.* Journal of Strain Analysis, 2000. **35**: p. 287-305.
29. A. Elmesalamy, J. A. Francis and L. Li, *A comparison of residual stresses in multi pass narrow gap laser welds and gas tungsten arc welds in AISI stainless steel.* International Journal of Pressure Vessels and Piping, 2014.
30. F. Hosseinzadeh, J. Kowal and P.J. Bouchard, *Towards good practice guidelines for the contour method of residual stress measurements.* The journal of engineering, 2014.
31. M.C. Smith, and A.C. Smith, *NeT bead-on-plate round robin: Comparison of residual stress predictions and measurements.* International Journal of Pressure Vessels and Piping, 2009. **86**: p. 79-95.
32. M.C. Smith, P.J. Bouchard, M. Turski, L. Edwards and R.J. Dennis, *Accurate prediction of residual stress in stainless steel welds.* Computational Materials Science, 2012. **54**: p. 312-328.
33. O. Muránsky, C. J. Hamelin, M. C. Smith, P. J. Bendeich and L. Edwards, *The effect of plasticity theory on predicted residual stress fields in numerical weld analyses.* Computational Materials Science, 2012. **54**: p. 125-134.
34. O. Muránsky, C. J. Hamelin, M. Tran, C. Braham and M. C. Smith. *Assessment of welding-induced plasticity in austenitic steel weldments*. in *Proceedings of the ASME 2016 Pressure Vessels and Piping PVP2016*. 2016. Vancouver, British Columbia, Canada.
35. M. Turski, J.A. Francis, P.R. Hurrell, S.K. Bate, S. Hiller and P.J. Withers, *Effects of stop-start features on residual stresses in a multipass austenitic stainless steel weld.* International Journal of Pressure Vessels and Piping, 2012. **89**: p. 9-18.
36. W. Park, H. Kobayashi, H. Nakamura and T. Koide. *Measurement and evaluation of welding residual stresses for austenitic steel by X-ray diffraction method*. in *Proceedings of the 1994 annual meeting of JSME/MMD*. 1994.
37. H. Ilker Yelbay, I. Cam and C. Hakan Gür, *Non-destructive determination of residual stress state in steel weldments by magnetic Berkhausen noise technique.* NDT&E International, 2010. **43**: p. 29-33.
38. E. Tanala, G. Bourse, M. Fremiot, J.F. de Belleval, *Determination of near surface residual stresses on welded joints using ultrasonic methods.* NDT&E International, 1995. **28**: p. 83-88.

39. Y. Ueda, H. Murakawa and N. Ma, *Welding deformation and residual stress prevention*, ed. Elsevier. 2012, Waltham, USA.
40. H.D. Hibbitt, and P.V. Marcal *A numerical, thermo-mechanical model for the welding and subsequent loading of a fabricated structure.* Computers & Structures, 1973. **3**(5): p. 1145-1174.
41. L.-E. Lindgren, *Computational welding mechanics thermomechanical and microstructural simulations*. 2007: Woodhead Publishing.
42. J.R. Chukkan, M. Vasudevan, S. Muthukumaran, R. Ravi Kumar and N. Chandrasekhar, *Simulation of laser butt welding of AISI 316L stainless steel sheet using various heat sources and experimental validation.* Journal of Materials Processings Technology, 2015. **219**: p. 48-59.
43. T.L. Teng, P.H. Chang and W.C. Tseng, *Effect of welding sequences on residual stresses.* Computers and Structures, 2003. **81**: p. 273-286.
44. J.L. Hansen, *Numerical modelling of welding induced residual stresses*, in *Department of manufacturing engineering and management*. 2003, Technical University of Denmark.
45. S.K. Bate, R. Charles and A. Warren, *Finite element analysis of a single bead-on-plate specimen using SYSWELD.* International Journal of Pressure Vessels and Piping, 2009. **86**: p. 73-78.
46. C.J. Hamelin, O. Muransky, M.C. Smith, T.M. Holden, V. Luzin, P.J. Bendeich and L. Edwards, *Validation of a numerical model used to predict phase distribution and residual stress in ferritic steel weldments.* Acta Materialia, 2014. **75**: p. 1-19.
47. X.K. Zhu, and Y.J. Choa, *Effects of temperature-dependent material properties on welding simulation.* Computers & Structures, 2002. **80**(11): p. 967-976.
48. N. O'Meara, S.D. Smith, J.A. Francis and P.J. Withers. *Development of simplified empirical phase tranformations model for use in welding residual stress simulations*. in *Proceedings of the ASME 2014 Pressure Vessels and Piping Conference*. 2014. Anaheim, California, USA.
49. E. Hinton. *NAFEMS: Introduction to nonlinear finite element analysis*. in *Nafems*. 1992.
50. J. Goldak, A. Chakravarti and M. Bibby, *A new finite element model for welding heat sources.* Metallurgical and Material Transactions B, 1984. **15**(2): p. 299-305.
51. L.D. Cozzolino, *Finite element analysis of localised rolling to reduce residual stress and distortion*, in *School of applied sciences, Welding Engineering and Laser Processing Centre*. 2013, Cranfield University.
52. M.C. Smith, and A.C. Smith, *NeT bead-on-plate round robin: Comparison of transient thermal predictions and measurements.* International Journal of Pressure Vessels and Piping, 2009. **86**: p. 96-109.
53. A.H. Eslampanah, M.E. Aalami-aleagha, S. Feli and M.R. Ghaderi, *3-D numerical evaluation of residual stress and deformation due welding process using simplified heat source models.* Journal of Mechanical Science and Technology, 2015. **29**(1): p. 341-348.
54. I.F.Z. Fanous, M.Y.A. Younan and A.S. Wifi, *3-D Finite element modelling of the welding process using element birth and element movement techniques.* Journal of Pressure Vessels Technology, 2003. **125**(2): p. 144-150.
55. X.Y. Shan, M.J. Tan and N.P. O' Dowd, *Developing a realistic FE analysis method for the welding of a NET single-bead-on-plate test specimen.* Journal of Materials Processings Technology, 2007. **192-193**: p. 497-503.
56. J.M.J. Mc Dill, A.S. Oddy, J. Goldak and S. Bennison, *Finite element analysis of weld distortion in carbon and stainless steels.* Journal of Strain Analysis for Engineering Design, 1990. **25**(1): p. 51-53.
57. O. Muránsky, M. C. Smith, P. J. Bendeich, T. M. Holden, V. Luzin, R. V. Martins and L. Edwards, *Comprehensive numerical analysis of a three-pass bead-in-slot*

weld and its critical validation using neutron and synchrotron diffraction residual stress measurements. International Journal of Solids and Structures, 2012. **49**: p. 1045-1062.

58. S. Quinn, Dulieu-Barton, J. M., J. Eaton-Evans, R.K. Fruehmann and P.J. Tatum, *Thermoelastic assessment of plastic deformation.* The Journal of Strain Analysis for Engineering Design, 2008. **43**: p. 451-468.
59. N. Instruments. *Measuring Strain with Strain Gauges*. 2016 03/10/2017]; Available from: www.ni.com/white-paper/3642/en/.
60. efunda. *Strain gauge rosette for strain measurement*. 2017; Available from: http://www.efunda.com/formulae/solid_mechanics/mat_mechanics/strain_gage_rosette.cfm.
61. A.J. Wilkinson, and D. J. Dingley, *Quantitative deformation studies using electron back scatter patterns.* Acta metallurgica et Materialia, 1991. **39**(12): p. 3047-3055.
62. M. Kamaya, A. J. Wilkinson and J. M. Titchmarsh, *Measurement of plastic strain of polycrystalline material by electron backscatter diffraction.* Nuclear Engineering and Design, 2005. **235**: p. 713-725.
63. M. Kamaya, *Measurement of local plastic strain distribution of stainless steel by electron backscatter diffraction.* Materials Characterization, 2009. **60**: p. 125-132.
64. R. Yoda, T. Yokomaku and N. Tsuji, *Plastic deformation and creep damage evaluations of type 316 austenitic steel by EBSD.* Materials Characterization, 2010. **61**: p. 913-922.
65. M. Kamaya, A. J. Wilkinson and J. M. Titchmarsh, *Quantification of plastic strain of stainless steel and nickel alloy by electron backscatter diffraction.* Acta Materialia, 2006. **54**: p. 539-548.
66. T.M. Angeliu, E. L. Hall, J. Sutliff, S. Sitmen and P.L. Andresen. *Strain and microstructure characterization of austenitic stainless steel weld HAZs*. in *NACE International*. 2000.
67. V.C.M. Beaugrand, L. S. Smith and M. F. Gittos. *Subsea dissimilar joints: failure mechanisms and opportunities for mitigation*. in *Corrosion 2009*. 2009. Atlanta, Georgia, USA, March 2009.
68. R.V. Martins, C. Ohms and K. Decroos, *Full 3D spatially resolved mapping od residual strain in a 316L austenitic steel weld specimen.* Materials Science and Engineering A, 2010. **527**: p. 4779-4787.
69. J.M. Dulieu-Barton, and P. Stanley, *Development and applications of thermoelastic stress analysis.* Journal of Strain Analysis, 1998. **33**: p. 93-104.
70. R.C. Tighe, G.P. Howell, J.P. Tyler, S. Lormor and J.M. Dulieu-Barton, *Stress based non-destructive evaluation using thermographic approaches: From laboratory trials to on-site assessment* NDT&E International, 2016. **84**: p. 76-88.
71. J.M. Dulieu Barton, and F. Pierron. *Handbook of Experimental Mechanics*. in *Experimental Mechanics Course*. 2014. Southampton.
72. A.K. Wong, J.G. Sparrow and S.A. Dunn, *On the revised theory of the thermoelastic effect.* Journal of Physics and Chemistry of Solids, 1988. **49**(4): p. 395-400.
73. R.J. Greene, E. A. Patterson and R. E. Rowlands, *Thermoelastic Stress Analysis*, in *Springer Handbook of Experimental Mechanics*, Sharpe, Editor. 2008. p. 743-768.
74. T.R. Emery, and J. M. Dulieu-Barton, *Thermoelastic Stress Analysis of damage mechanics in composite materials.* Composites Part A: Applied Science and Manufacturing, 2010. **41**(12): p. 1729-1742.
75. N. Sathon, and J. M. Dulieu-Barton, *Evaluation of Sub-Surface Stresses using Thermoelastic Stress Analysis.* Applied Mechanics and Material, 2007. **7-8**: p. 153-158.

76. J.M. Dulieu Barton, T. R. Emery, S. Quinn, and P. R. Cunningham, *A temperature correction methodology for quantitative thermoelastic stress analysis and damage assessment.* Measurement Science and Technology, 2006. **17**(6).
77. P.a.J.M.D.-S. Stanley, *Determination of crack-tip parameters from thermoelastic data.* Experimental Techniques, 1996. **20**(2): p. 21-23.
78. P. Stanley, and W. K. Chan. *Mode II crack studies using the SPATE technique*. in *International Conference of Experimental Mechanics*. 1986. New Orleans.
79. G.P. Leaity, and R. A. Smith, *The use of SPATE to measure residual stresses and fatigue crack growth.* Fatigue and Fracture of Engineering Materials and Structures, 1989. **12**: p. 271-282.
80. A.K. Wong, S.A. Dunn and J.G. Sparrow, *Residual stress measurement by means of the thermoelastic effect.* Nature, 1988. **332**: p. 613-615.
81. A.K. Wong, R. Jones and J.G. Sparrow, *Thermoelastic constant or thermoelastic parameter?* Journal of Physics and Chemistry of Solids, 1987. **48**(8): p. 749-753.
82. A.F. Robinson, J. M. Dulieu-Barton, S. Quinn and R. Burguete, *The potential for assessing residual stress using thermoelastic stress analysis: a study of cold expanded holes.* Experimental Mechanics, 2013. **53**: p. 299-317.
83. T.G. Ryall, and A.K. Wong, *Determining stress components from the thermoelastic data - A theoretical study.* Mechanics of Materials, 1988. **7**(3): p. 205-214.
84. E. Patterson, Y. Du and D. Backman. *A new approach to measuring surface residual stress using thermoelasticity*. in *Proceedings of SEM XI International Congress and Exposition*. 2008. Orlando, Florida, USA.
85. J.M. Dulieu Barton, and P. Stanley, *Applications of thermoelastic stress analysis to composite materials.* Strain, 1999. **35**(2): p. 41-48.
86. P.R. Cunningham, J.M. Dulieu-Barton, A.G Dutton and R.A. Shenoi, *The Effect of Ply Lay-Up upon the Thermoelastic Response of Laminated Composites.* Key Engineering Materials, 2001. **221-222**: p. 325-336.
87. A.K. Wong, *A non-adiabatic thermoelastic theory for composite laminates.* Journal of Physics and Chemistry of Solids, 1991. **52**(3): p. 483-494.
88. P. Zhang, and B. I. Sandor, *Thermographic analysis of stress concentration in a composite.* Experimental Mechanics, 1989. **29**: p. 121-125.
89. G. Pitaressi, M. S. Found and E. A. Patterson, *An investigation of the influence of macrosopic heterogeneity on the thermoelastic response of fibre reinforced plastics.* Composites Science and Technology, 2005. **65**(2): p. 269-280.
90. G.Y. Gyekenyesi, *Thermoelastic stress analysis: The mean stress effect in metallic alloys*. 1999, NASA: University of Akron, Akron, Ohio.
91. S.W. Boyd, J.M. Dulieu-Barton and L. Rumsey, *Stress analysis of finger joints in pultruded GRP materials.* International Journal of Adhesion and Adhesives, 2006. **26**(7): p. 485-510.
92. A.K. Wong, T.G. Ryall and M.J. Richmond. *Structural Assessment of the Orion P3 Leading Edge Using a State-of-the-Arte Thermal Imaging System*. in *International Aerospace Congress 1995: Proceedings Pacific International Conference on Aerospace and Technology; Sixth Australian Aeronautical Conference*. 1995.
93. A.F. Robinson, J.M. Dulieu-Barton, S. Quinn and R.L. Burguete, *Paint coating characterization for thermoelastic stress analysis of metallic materials.* Measurement Science and Technology, 2010. **21**: p. 11-21.
94. G.P. Howell, M. Achintha and J.M. Dulieu-Barton, *Identification of Plastic Strain using Thermoelastic Stress Analysis*, in *Faculty of Engineering and the Environment*. 2017, University of Southampton.
95. J. Rosenholtz, and D. Smith, *The effect of compressive stresses on the linear thermal expansion of magnesium and steel.* Journal of Applied Physics, 1950. **21**: p. 369-399.

96. A.R. Rosenfield, and B.L. Averbach, *Effect of stress on the expansion coefficient.* Journal of Applied Physics, 1956.
97. J.C. Lippold, and, D.J. Kotecki, *Welding metallurgy and weldability of stainless steels*. 2005: Wiley.
98. M.C. Smith, A. C. Smith, R. Wimpory and C. Ohms, *A review of the NeT Task Group 1 residual stress measurement and analysis round robin on a single weld bead-on-plate specimen.* International Journal of Pressure Vessels and Piping, 2014. **120-121**: p. 93-140.
99. M.F. Ashby, and M. Smidman, *Materials for nuclear power systems.* Granta, 2010.
100. K. Suzuki, *Neutron irradiation embrittlement of ASME SA508, Cl.3 steel.* Journal of Nuclear Materials, 1982. **108-109**: p. 443-450.
101. K. Sangho, I., Young-Roc, L. Sunghak, L. Hu-Chul, O. Yong Jun and H. Jun Hwa, *Effects of alloying elements on mechanical and fracture properties of base metals and simulated heat affected zone of SA 508 steels.* Metallurgical and Material Transactions A, 2001. **32A**: p. 903-911.
102. N. O'Meara, H. Abdolvand, J. A. Francis, S. D. Smith and P. J. Withers, *Quantifying the metallurgical response of a nuclear steel to welding thermal cycles.* Materials Science and Technology, 2016.
103. M.V. Li, D. V. Niebuhr, L. L. Meekisho and D. G. Atteridge, *A computational model for the prediction of steel hardenability.* Metallurgical and Material Transactions B, 1998. **29**: p. 661-672.
104. D.P. Koistinen, and R.E. Marburger, *A general equation prescribing extent of austenite-martensite transformation in pure Fe-C alloys and plain carbon steels.* Acta Metallurgica, 1959.
105. N. O'Meara, *Private communication on the SSPT modelling in SA508 Gr.3 Cl.1 steel*, E.C. Chevallier, Editor. 2017.
106. ASTM, *Standard test method for determining Average grain size,* in *E112 - 13* 2013.
107. K.H. Ho, S.T. Newman, *State of the art electrical discharge machining (EDM).* International Journal of Machine Tools & Manufacture, 2003. **43**: p. 1287–1300.
108. K.K. Singh, *Strain hardening behaviour of 316L austenitic stainless steel.* Material Science and Technology, 2004. **20**(9): p. 1134-1142.
109. C.J. Hamelin, O. Muránsky, P. Bendeich, K. Short and L. Edwards, *Predicting solid-state phase transformations during welding of ferritic steels.* Materials Science Forum, 2012. **706-709**: p. 1403-1408.
110. F. Dunne and N. Petrinic, *Introduction to Computational Plasticity*. 2005: OUP Oxford.
111. *Measurement of residual stresses by the hole drilling strain gage method,* S.g.a. instruments, Editor. 2010, Tech Note TN503.
112. M.T.a.H.M. Flaman, *Determination of Residual Stress Variation with Depth by the Hole Drilling Method.* Experimental Mechanics, 1985. **25**: p. 205-207.
113. W.R. Delameter, and T. C. Mamaros, *Measurements of residual stresses by the Hole-drilling method.* 1977, Sandia National Laboratories Report SAND-77-8006. p. 27.
114. E. Procter, and E. M. Beany, *Recent Developments in Centre-hole Technique for Residual-stress measurements.* Experimental Techniques, 1982. **6**: p. 10-15.
115. Y.L. Sun, M. J. Roy, A. N. Vasileiou, M. C. Smith, J. A. Francis and F. Hosseinzadeh, *Evaluation of Errors Associated with Cutting-Induced Plasticity in Residual Stress Measurements Using the Contour Method.* Experimental Mechanics, 2017. **57**: p. 719-734.
116. D.B. Darmadi, *Validating the accuracy of heat source model via temperature histories and temperature field in bead-on-plate welding.* International Journal of Engineering & Technology, 2011. **11**(5): p. 12-20.